Zirconium Doped Zinc Oxide Thin Films Deposited by Atomic Layer Deposition

STEPHANIA HERODOTOU

PhD Thesis

The University of Liverpool

School of Engineering

Faculty of Science and Engineering

June 2015

To my mother and my late father who I never met but he was always my inspiration for every step of my life.

Acknowledgments

I express my gratitude to everyone who supported me throughout the course of this PhD study. I would like to thank my supervisors Dr. R. Potter and Prof. G. Tatlock for their support and guidance. I would also like to thank Dr. K. Abrams from the NanoInvestigation Centre in Liverpool for providing TEM images of the current samples, and Dr. R. Treharne along with Prof. K. Durose from Stephenson Institute for Renewable Energy for providing guidance and the equipment for the spectrophotometer measurements. I express my warm thanks to the academic and technical staff of the Material Science team, who help me and provided me with the facilities being required for this research. I would also like to thank SAFC Company for providing the ALD precursors for my study.

I am very grateful to my family and friends for their support all those years that motivated me to strive towards my goals. At the end I would like to express appreciation to my mother for all of the sacrifices that she made on my behalf since I was born.

Abstract

Doped zinc oxide is of interest as a transparent conductive oxide (TCO), due to the abundance of its major constituents, its low resistivity, high transparency and wide bandgap. The current work focuses on the properties required for TCO applications including resistivity of $\leq 10^{-3}\ \Omega\cdot cm$, carrier density of $\geq 10^{20}\ cm^{-3}$, and transparency >80% in the visible light. Zirconium (Zr^{4+}) was chosen as the dopant in the current work due to its abundance, comparable ionic size to Zn and because it can act as a double donor providing up to two extra free electrons per ion when substituted for Zn^{2+}. The doping process can be controlled using atomic layer deposition (ALD), with the doped films resulting in an increased conductivity. The films in the current work resulted in a minimum resistivity of $1.44\times10^{-3}\ \Omega\cdot cm$ and maximum carrier density of $3.81\times10^{20}\ cm^{-3}$ for films <100 nm thickness, having 4.8 at.% Zr concentration. The resistivity was further reduced after reducing the interfacial and grain boundary scattering (i.e. increase grain size), by increasing the overall film thickness. The resistivity of $7.5\times10^{-4}\ \Omega\cdot cm$, carrier mobility of $19.6\ cm^2V^{-1}s^{-1}$ and carrier density of $4.2\times10^{20}\ cm^{-3}$ were measured for a 250 nm thick film with 4.8 at.% doping. The tuning of the carrier density via doping offers control over the optical gap due to the net effect of Burstein-Moss effect and bandgap renormalisation. This resulted to an increase of the optical gap from 3.2 eV for the un-doped ZnO to 3.5 eV for 4.8 at.% Zr-doped films. The average optical transparency in the visible/near IR range was as high as 91% for 4.8 at.% doped films. The thickness increase also resulted in a grain orientation shift from perpendicular to the substrate (i.e. polar c-plane orientation) to parallel (i.e. non-polar m-plane) due to the strain

increase that forced the films to grow at a low strain energy direction. This offers the possibility of growing non-polarised films that show no piezoelectric field charge observed in polar oriented films. Therefore, controlling the grain size through the number of ALD cycles can effectively result in mobility and preferred orientation control, while the doping concentration controls the resistivity, optical bandgap and transparency of the films.

Table of Contents

Acknowledgment……………………………………………………………………
Abstract…………………………………………………………………………..
Table of Contents ....
List of publications……………………………………………………………….
Notation…………………………………………………………………………..
Chapter 1 ....
Introduction 1
Chapter 2 ....
Literature Review 6
2.1 Properties of Zinc Oxide 6
2.1.1 Crystal structure 7
2.1.2 Electrical and Optical properties..9
2.1.2.1 Optical emission background..9
2.1.2.2 ZnO bandgap...13
2.1.2.3 ZnO stimulated emission 14
2.1.2.4 ZnO defects...16
2.2 Applications of ZnO...17
2.2.1 LED..19
2.2.2 UV photodetectors 19
2.2.3 Metal-Insulator-Semiconductor 20
2.2.4 Solar cells..21
2.2.5 TCOs..22
2.3 Growth techniques 26
2.3.1 CVD..26
2.3.2 Magnetron Sputtering 27
2.3.3 MBE..28
2.3.4 Sol-gel 28
2.3.5 PLD..29
2.4 Doping in ZnO 30
2.4.1 Doped ZnO films 30
2.4.1.1 N-type doping 32

2.4.1.2 Co-doping 34
2.4.2 Zirconium doped ZnO films by different techniques 34
2.5 Atomic Layer Deposition 38
2.5.1 ZnO deposited by ALD 43
2.5.2 Doped ZnO deposited by ALD 47
2.5.3 Zirconium in ALD 47
Chapter 3 ....
Experimental processes 49
3.1 Introduction 49
3.2. Ellipsometer 49
3.3. Atomic Layer Deposition 54
3.4. Four-Point probe 61
3.5. Hall Effect measurements 64
3.5.1. Background information 64
3.5.2. Measurement information 68
3.6. Photoluminescence 71
3.6.1. Background information 71
3.6.2. Measurement information 72
3.7. UV-Vis Spectroscopy 77
3.7.1. Background information 77
3.7.2. Measurement information 82
3.8. X-ray Diffraction 83
3.8.1. Background information 83
3.8.2. Measurement information 89
3.9. X-ray Photoelectron Spectroscopy 92
3.10. Transmission Electron Microscope 98
3.11. Atomic Force Microscope 101
Chapter 4 ....
Effects of Zr doping on the microstructure of ZnO films 105
4.1. Introduction 105
4.2. Effect of growth temperature on un-doped ZnO 106
4.3. Zr-doped ZnO microstructure 113
4.3.1 Growth rate 113

4.3.2 Microstructure 115
4.3.3 Higher XRD peak intensity with doping 129
4.4 Orientation shift 133
4.4.1 Orientation shift by strain 137
4.4.2 TEM study of the thicker doped film 143
4.5. Conclusion 147
Chapter 5 ....
Electrical properties and chemical state of ZnO and ZnO: Zr 149
5.1 Introduction 149
5.2 Zr-doped ZnO films electrical properties 154
5.2.1 Resistivity, carrier density and mobility of the ZnO: Zr films 154
5.2.2 Carrier density increase at low Zr doping levels 156
5.2.3 Carrier density decrease at high Zr doping levels 159
5.2.4 Carrier mobility reduction with Zr doping 160
5.3.2 Refractive index 163
5.2.5 Improvement of electrical properties 164
5.3 Degeneracy of the ZnO films 168
5.4 Chemical state 172
5.4.1 XPS spectrum analysis 173
5.4.2 Chemical shift 179
5.6 Conclusion 182
Chapter 6 ....
Optical properties of ZnO and Zr-doped ZnO films 184
6.1 Introduction 184
6.2 Spectrophotometry 185
6.2.1 Transmittance 185
6.2.2 Drude model calculations 191
6.2.3 Optical bandgap calculation 193
6.2.4 Conclusion of the Spectrophotometry results 195
6.3 Photoluminescence 195
6.3.1 PL on un-doped ZnO films 195
6.3.1.1 Growth Temperature effect on the un-doped ZnO films 195
6.3.1.2 Excitation energy dependence on the PL signal of the un-doped films 198

6.3.1.3 Low temperature measurements on ZnO films 204
6.3.1.4 Substrate effect on the PL signal 208
6.3.2 PL on ZnO: Zr samples 212
6.3.2.1 The PL peaks origin 218
6.3.2.2 Thickness effect in the PL emissions 224
6.3.2.3 Energy increase of the dominant emission in doped films 225
6.3.2.4 Optical gap modification 227
6.3.3 PL Conclusion 232
Chapter 7 .....
Conclusion 233
7.1 Main outcome 233
7.2 Future work 236
References 238

List of publications

Herodotou, S., Treharne, R. E., Durose, K., Tatlock, G. J., & Potter, R. J. (2014). The effects of Zr doping on the optical, electrical and microstructural properties of thin ZnO films deposited by ALD. Submitted paper to Thin Solid Films as a 'SI: TCM 2014 article'.

Notation

Arabic

A	Absorbance	(%)
A_w	Atomic molecular weight	(g/mol)
B	Magnetic Field	(Telsa)
d	Lattice spacing	(Å)
D	Grain size	(nm)
e	Electron Charge	(C)
E_α	Activation energy in thermal quenching (eV)	

E_F	Fermi level energy	(eV)
E^f	Formation energy	(eV)
F	Structure factor	(unit-less)
F_C	Texture coefficient	(unit-less)
ħ	Planck constant	(Js)
I	Intensity	(MW cm^{-2})
I_0	Integrated intensity	(a.u.)
I_C	Electric Current	(A)
m*	Effective mass	(kg)
m_0	Electron mass	(kg)
m_0*	Effective mass at the bottom of the CB (kg)	
m_{eh}*	Reduced effective mass	(kg)
m_h*	Hole effective mass	(kg)
N_A	Avogadro's number	(1/mol)
N_C	Mott critical density	(cm^{-3})
n_e	Electron Carrier Concentration	(cm^{-3})
R	Reflectance	(%)
Rs	Sheet Resistance	(Ω/□)
S	Surface energy	(Jcm^{-2})
r_0	Exciton distance	(Å)
r_s	Radius ratio of Bohr over exciton	(unit-less)
t	Thickness	(nm)
t_C	Critical thickness	(nm)
T	Temperature	(°C)
T_r	Transmittance	(%)
TU	Optical Thickness	(Å)
U	Strain energy	(Jcm^{-2})

V	Volume	(cm^3)
V_H	Hall voltage	(V)
Z	Atomic number	(unit-less)

Greek

α	Absorption coefficient	(unit-less)
α_r	Bohr radius	(Å)
α_0	Hydrogen Bohr radius	(Å)
α_m	Monolayer thickness	(Å)
α_{np}	Non-parabolicity parameter	(eV^{-1})
α_{Zn}	Auger parameter for Zn	(eV)
ε	Strain	(%)
ε_0	Vacuum permittivity	(Fm^{-1})
θ	Bragg's diffraction angle	(°)
λ	Wavelength	(nm)
μ	Carrier mobility	($cm^2V^{-1}s^{-1}$)
ρ	Resistivity	(Ω·cm)
ρ_d	Density	(kg cm^{-3})
τ	Relaxation time	(s)
Φ	Work function	(eV)
ω_p	Plasma frequency	(cm^{-1})

Acronyms

4PP	Four Point Probe
AAO	Aluminium Oxide

AFM	Atomic Force Microscopy
ALD	Atomic Layer Deposition
ALE	Atomic Layer Epitaxy
AZO	Al-doped ZnO
BGN	Bandgap narrowing
BM	Burstein-Moss
CB	Conduction Band
CDS	Chemical Database Service
CVD	Chemical Vapour Deposition
DC	Direct Current
DEZ	Diethylzinc
DFT	Density Functional Theory
DSSC	Dye Sensitised Solar Cells
ECR	Electron Cyclotron Resonance
EDS	Energy Dispersive Spectrometry
EHP	Electron-Hole plasma
EPES	Elastic Peak Electron Spectroscopy
FESEM	Field Emission Scanning Electron Microscope
FET	Field-Effect Transistor
FFT	Fast Fourier Transform
FIB	Focused Ion Beam
FTO	Fluorine doped Tin Oxide
FWHM	Full-Width at Half Maximum
GZO	Ga-doped ZnO
IMFP	Inelastic Mean Free Path
ITO	Indium Tin Oxide
LCD	Liquid Crystal Display

LED	Light Emitting Diodes
LD	Laser Diode
LPCVD	Low Pressure Chemical Vapour Deposition
MBE	Molecular-Beam Epitaxy
MEMS	Micro-Electro-Mechanical Systems
MOCVD	Metal-organic Chemical Vapour Deposition
MQW	Multiple Quantum Wells
MIS	Metal-Insulator-Semiconductor
MSM	Metal-Semiconductor-Metal
NA	Numerical aperture
OLED	Organic Light Emitting Devices
PE-ALD	Plasma Enhance Atomic Layer Deposition
PECVD	Plasma Enhanced Chemical Vapour Deposition
PET	Polyethylene Terephthalate
PL	Photoluminescence
PLD	Pulse-Laser Deposition
PV	Photovoltaic
QCM	Quartz Crystal Microbalance
QD	Quantum Dot
QDSSC	Quantum-Dot-Sensitized Solar Cell
QW	Quantum Well
RF	Radio Frequency
RHEED	Reflection High Energy Electron Diffraction
RTA	Rapid Thermal Annealing
SAD	Selected Area Diffraction
SAW	Surface Acoustic Wave
SC	Solar Cell

SEM	Scanning Electron Microscope
STM	Scanning Tunnelling Microscope
TCO	Transparent Conductive Oxide
TDMAZ	Tetrakis-dimethylamino-zirconium
TEMAZ	Tetrakis-ethylmethylamino-zirconium
TFT	Thin Film Transistors
TEM	Transmission Electron Microscope
TMA	Trimethylaluminium
UHV	Ultra High Vacuum
UV	Ultraviolet Light
VB	Valence Band
XPS	X-ray Photoelectron Spectroscopy
XRD	X-ray Diffraction

Chapter 1

Introduction

Zinc oxide is a very popular intrinsically n-type semiconductor due to its low toxicity, low price to obtain as it is earth abundant, and also its properties can be controlled through doping. It is used in applications such as thin film transistors (TFT) [1]-[3], laser diodes [4]-[5], light emitting diodes (LEDs) [6]-[8], transparent conductive oxides (TCO) [9]-[10], dye sensitised solar cells (DSSC) [11]-[12], etc. Applications of TCOs include solar cells [13], flat panel displays [14], organic light emitting devices (OLED) [15], etc, which require high conductivity and high transparency. For such applications, the use of doped ZnO is preferred rather than intrinsic ZnO, as it can be readily doped to degeneracy providing even higher conductivity. Degenerate materials behave as metals in terms of conductivity due to their high carrier density. However, degenerate materials are avoided in some applications such as TFTs, as the material used as the connection between the source and the drain parts of the transistor (Figure 1) must have high carrier mobility to allow fast switching from on and off, and also low carrier density to allow faster switching off.

The complexity in forming stable p-type ZnO makes it very difficult to manufacture p-n homojunctions based LEDs and UV laser diodes, so it is not commercially

available yet. Heterojunctions though have been realized using ZnO as the n-type layer combined to p-type materials such as Si, GaN, CdTe, etc. [16].

Doped zinc oxide used as TCO offers low resistivity (≤10^{-3} Ω·cm), high transparency (>80%) and wide bandgap (3.37 eV [17]). Additionally, it is an attractive alternative to indium tin oxide (ITO) that contains earth-scarce indium, due to the abundance of zinc and hence low cost of its major constituents. In order to compete with ITO, doped ZnO must have resistivity in the order of 10^{-4} Ω·cm [18], transparency higher than 85% [18]-[20], and optical gap higher than 3.1 eV to allow full transmission of the visible light.

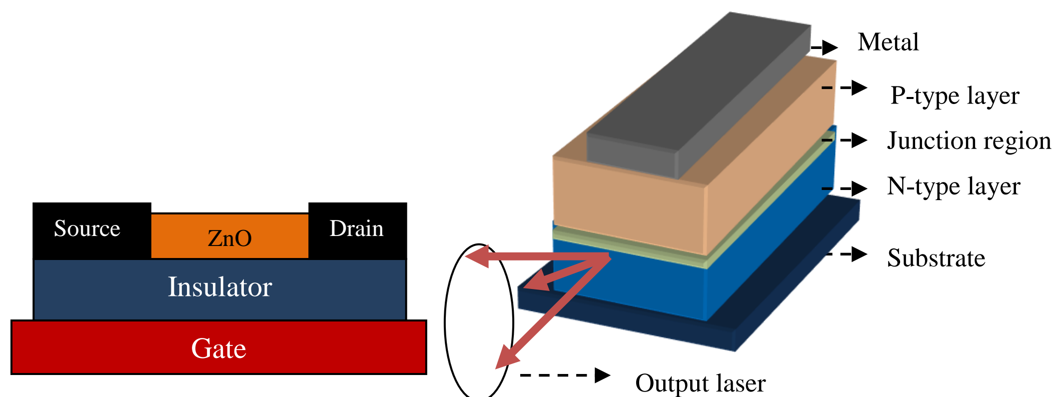

Figure 1: Schematic of a simple layer arrangement in a) TFT and b) laser diode.

The dopants used to achieve those target values should be shallow donors that provide extra ionized electrons to the system. A wide range of different dopants has been extensively studied such as B [10],[21], In [22]-[23], Co [24], Zr [25]-[26], Ge [27], Hf [28], Sn [29], while the group-III dopants Al [30]-[34] and Ga [35]-[38] are preferred as they lead to more conductive and transparent films. Al-doped ZnO (AZO) is reported to have

high conductivity and transparency, although it shows limitations such as lattice distortion, it is highly reactive to oxygen causing oxidation [39]. Also, it could be placed in interstitial positions due to its small ionic radius [40], eliminating in that way one of the intrinsic donors in ZnO (i.e. interstitial Zn). Ga-doped ZnO (GZO) is also a very effective n-type dopant and it is preferred to Al in some devices as it is less oxygen reactive and its larger ionic radius minimises the lattice deformations [41]. Both dopants offer three ions to the system, while transition elements could offer more. One such donor dopant used for ZnO is zirconium.

Zirconium was chosen as the dopant in the current work which is focused on the development of degenerate doped films in order to improve the properties required for TCOs. The dopant selection was based on zirconium abundance, its comparable ionic size to zinc, and because it can act as a double donor providing up to two extra free electrons per ion when substitutes to Zn^{2+} [42]. The close match between the ionic size of Zr^{4+} compared to Zn^{2+} [43] (i.e. 0.745 Å for Zr and 0.740 Å for Zn [42]) should help minimize the lattice distortion, which is often observed with other dopants such as Al [29]. Its large radius favours its placement as substitutional to Zn^{2+}, avoiding the interstitial positions and thus the reduction of zinc interstitials. An additional advantage of using Zr as a dopant is that it does not readily bond with Zn atoms, hence is unlikely to form secondary intermetallic phases [44], proving a stable form of doped ZnO. A number of publications report on Zr-doped ZnO deposited by spray pyrolysis [26],[45]-[47], low temperature coprecipitation method [48], sol-gel method [28],[49]-[50], direct current (DC) magnetron sputtering [51]-[54], microwave irradiation [55], radio frequency (RF) magnetic sputtering [56]-[57], pulse laser deposition (PLD) [58], and atomic layer deposition (ALD) [25]. ALD was the method used in the current study to produce modulated (delta) doped ZnO during the

deposition itself, which is considered an advantageous method for accurate control of the carrier concentration, an essential property for efficient TCOs. The self-limiting nature of ALD also provides excellent control over film thickness, good uniformity and conformality, while the relatively low growth temperature permits the use of temperature sensitive substrates such as polymers.

At the time of writing, only one publication of Zr-doped ZnO is reported using ALD [25], with questions regarding the doping effects that cause changes in the films' microstructure, the optical and the electrical properties. Hence, the current study attempts to cover most of those aspects using a range of different doped films grown by ALD, providing characterisation on how the texture is changing, how the electrical properties are affected at low and heavily doping, and finally how the optical properties are altered regarding their transparency and photolumisenscence (i.e. optical bandgap). In parallel, the effect of different film thickness is covered in order to evaluate how the properties of the doped films can be improved.

In order to evaluate the effect of zirconium doping in zinc oxide films, a literature review is first presented in chapter 2, while an overview of the equipment used throughout this research is presented in chapter 3. This study's experimental outcomes are presented in three different chapters divided in the main three property categories of microstructural, optical and electrical. The first one (chapter 4) presents initially the microstructure changes of the un-doped films using different thickness and growth temperatures during the ALD deposition. Those optimum growth conditions are the ones selected for depositing the doped films. In the same chapter, any changes in texture are shown as the doping concentration alters, in addition to the texture changes at different film thicknesses. The results show suppression of the grains growth as doping increases, while the thickness of the film results in larger

grains. However, the strain induced in the thicker films causes preferred orientation shift from c-axis to a-axis, which can be predicted using a graph comparing the surface and strain energies in the system (i.e. the dominant force is driving the orientation). By establishing the grain growth relation to doping and film thickness, the electrical properties are measured and presented in chapter 5. The resistivity decreases at low doping levels and high film thickness, while it is increased for the heavily doped films. The reason for this increase is allocated to the grain growth suppression and the ionised impurity scattering increase that led to the carrier mobility reduction. The conductivity of the films was found to be related to their transparency as presented in chapter 6, with the most transparent films being the most conductive. In the same chapter, the photon emission energies are found to be related to the doping concentration as the increased carrier density induces band filling effects and so the optical gap is increased. The final chapter (chapter 7) of conclusion highlights the main findings in this study and refers to possible future work.

Chapter 2

Literature Review

2.1 Properties of Zinc Oxide

Zinc Oxide is a naturally n-type semiconductor, which has been the focus of many studies in recent years due to its fundamental properties. ZnO has been the focus of significant research, since it has been studied for a century now along with other semiconductors after the invention of the transistor [19]. The first X-ray investigation by Aborn in 1930 [59], and an analysis of the lattice dimensions of the ZnO hexagonal crystal structure by Bunn in 1935 [60], were some of the first thorough studies on ZnO. In recent years, interest has grown due to the development of advance technological growth techniques that allow controllable doping. Doping is the key for the development of controllable and more conductive ZnO, which is the main aim in using doped ZnO films for optoelectronic applications such as TCOs. Its wide bandgap (3.4 eV) allows light transmission up to UV region, which is preferred in many optoelectronic applications, in contrast to GaAs, a very conductive semiconductor with narrow bandgap (1.4 eV). Its high exciton binging energy (60 meV) also allows higher efficiency in the luminescence of excitons at room temperature, which is even higher than GaN (28 meV).

2.1.1 Crystal structure

ZnO is a II-VI compound semiconductor [61], which is formed in three crystal phases. In all phases both zinc and oxygen have tetrahedrally oriented bonds, in other words each ion is connected to four neighbouring ions. The most stable phase under ambient conditions is hexagonal wurtzite, but it can also crystallise in cubic zincblende and rocksalt structures [62]. ZnO has high bond polarity and this is considered to be the driving force behind the formation of wurtzite crystal structure, as the zincblende structure is favoured for lower polarity bonds such as GaAs [61]. The formation of ZnO with zincblende crystal structure can only be successful by epitaxial growth on cubic substrates such as ZnS and GaAs [63]. The rocksalt structure on the other hand, is a metastable cubic phase of the wurtzite hexagonal structure formed at pressures higher than 6 GPa and the transition is reversible after decompression [64]. It has 17% less volume than the hexagonal phase [65] and it is an unstable cubic structure [19].

The high bond polarity of ZnO is the result of the large difference between the electronegativity of Zn and O, which is defined as the power of an atom to attract electrons [66]. This difference in the attraction power creates an ionic energy shown by the ionicity level [67], causing the transfer of electrons from the least electronegative to the most electronegative atom. The electronegativity of Zn is 1.49 [68] in Pauling's scale [66]-[70] and for O is 3.5 [66], leading to the relatively high ionicity of 0.6 (i.e. in the Philip's scale with range 0-1 [70]). Hence, the main elements can be considered to be ionised into Zn^{2+} and O^{2-} with ionic radius of 0.740 Å and 1.4 Å respectively [61].

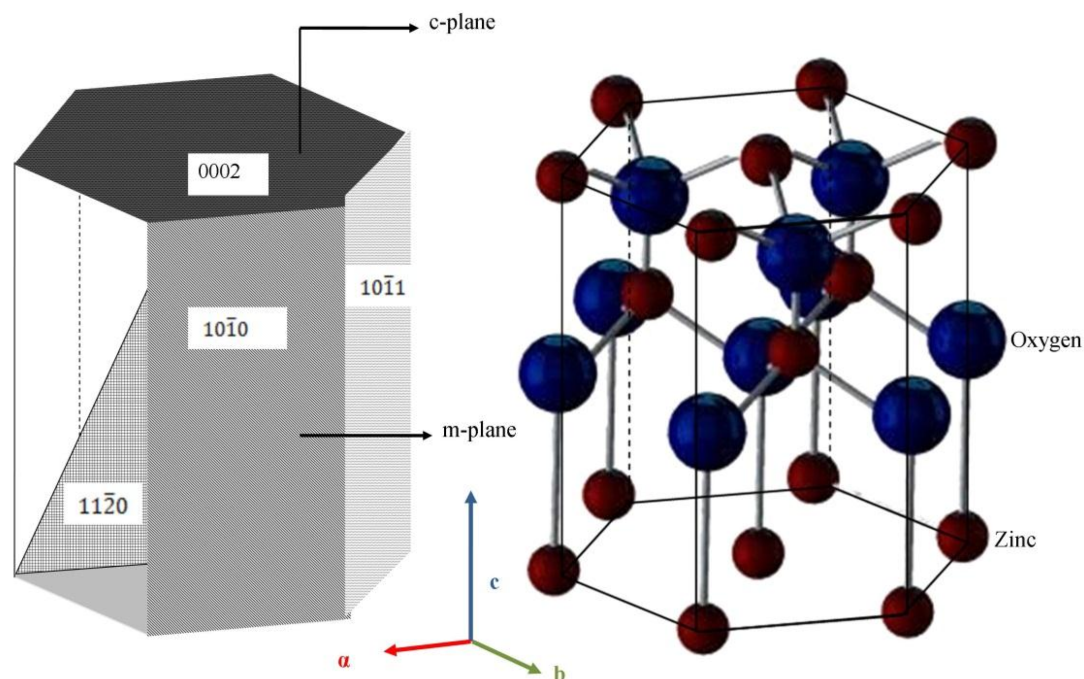

Figure 2: Hexagonal wurtzite ZnO structure.

A schematic diagram of the wurtzite ZnO structure is shown in Figure 2. The 4-axis system illustrated along with the Miller-Bravais indices system can be used to identify the polarity of the crystal, the planes and vectors in different directions [71]. The polar Zn (i.e. Zn terminated plane) is found in the (0001) plane and O in the ($000\bar{1}$) plane. The most common non-polar planes (i.e. terminated with both elements) are the ($10\bar{1}0$), ($11\bar{2}0$), and ($10\bar{1}1$) planes [72]. The planes in the direction of the 'c' constant (vector) are referred to as c-axis oriented (i.e. (0001), (0002), etc), and the planes perpendicular to the c-axis are referred as a-axis oriented (i.e. ($10\bar{1}0$), ($10\bar{1}1$), etc). The hexagonal shape of the ZnO crystal indicates that 'a' and 'b' lattice constants (i.e. vectors in a-axis and b-axis), are equal and ideally symmetrical related to c constant by $c/a=\sqrt{8/3}$. However, electrostatic forces cause a small distortion of the hexagonal symmetry resulting in an actual axis ratio of c/a=1.602 [61]. The lattice parameters based on the references are a=3.2495Å and c=5.2069Å [72].

2.1.2 Electrical and Optical properties

2.1.2.1 Optical emission background

The transition between two energy states is completed by three possible processes. The first is the absorption of radiation by electrons that excite them to a higher energy level due to the obtained energy. The stimulated emission is the opposite process, in which the electrons at high energy state will be forced by irradiation to emit radiation (i.e. photons) in order to fall to a lower state. The third transition is not an externally forced process as it occurs without apparent provocation and is called spontaneous emission from a high energy state to a lower one by emitting photons [73]. This electron-hole recombination occurring during stimulated and spontaneous emissions is either radiative or non-radiative. The radiative recombination releases energy as electromagnetic radiation, while the non-radiative recombination releases thermal energy rather than radiation, in the form of lattice vibrations (i.e. phonons) [74]. For non-radiative recombination there are several processes such as Auger recombination, surface recombination, recombination through defects and phonon emissions [73]. The Auger recombination leads to degradation of the emission intensity as it causes very rapid non-radiative recombination when the energy of recombination is transferred to another carrier and does not lead to photon emission [75]. The carriers with the gained energy are 'hot' carriers and emit photons at a second radiative recombination with high energy [73].

There are three possible radiative recombination possibilities; the band-to-band recombination, the exciton recombination, and the recombination through impurities'

states [74]. The band-to-band recombination is the simplest form of electrons combined to holes between the conduction band minimum (CBM) and the valence band maximum (VBM). This is the fundamental bandgap. The fundamental bandgap can be modified by doping through inducing lattice strain, which increases (compressive strain) or decreases (tensile strain) the bandgap. The strain causes changes in the distribution of the density of states [73], leading to electron rearrangement into higher energy state under compression strain (i.e. increase of the energy gap), and reversibly under tensile strain (i.e. lower state and reduced gap).

Excitons are electron-hole pairs bound together due to Coulomb interaction between them (i.e. exciton binding energy). Therefore, if the Coulomb interaction is strong, exciton recombination will occur from free-excitons or bound excitons. Free excitons are electron-hole pairs created by intrinsic transitions. Their binding energy decreases with increased carrier density, due to the reduced Coulomb interaction overshadowed by the additional electron-hole pairs. At carrier density equal to the Mott density (i.e. the critical value for carrier density when the Fermi level moves above the CBM [76]), the Coulomb interaction is weakened and hence the exciton binding energy is fixed at higher carrier densities [17]. The Fermi level is the highest available energy level at absolute zero temperature (0K), and it can only be occupied by two electrons with opposite spins in each state based on Pauli's exclusion principle [73]. In degenerate materials, the Fermi level is shifted at high energy due to the occupancy of energy states by the high number of electrons (i.e. located in the CB).

In ZnO the Mott density is fixed at 4×10^{18} cm^{-3} [17] and is not affected by temperature. Therefore, the exciton binding energy in ZnO is fixed at 60 meV, which

is higher than the thermal energy gained at room temperature (i.e. 25 meV) allowing excitonic transitions. The binding energy is higher than GaN (28 meV [77]), which has similar geometry and electronic properties to ZnO. The difference is attributed to the near-gap states formed at the CB edge, where ZnO has a larger CB minimum due to oxygen sites, while GaN does not [77].

Bound excitons are related to extrinsic transitions as they are excitons connected to defects and impurities [78]. Hence, the free-exciton recombination has a higher energy than the bound excitons, due to the binding energy losses during their binding to the impurities or defects. Thus, energy states are created within the bandgap, consisting of molecular states for excitons connected to donors or acceptors, or they form molecular ion states when they are connected to ionised carriers [78].

The impurity transitions occur within the intrinsic and impurity defects states formed within the bandgap. With the addition of donor impurities, neutral donor excitons are formed at lower energy than the free-excitons, and ionised donor excitons are formed at energy lower than the donor energy state below the CB minimum [79]. Consequently, any radiative emission within the impurity states or exciton states will result in lower energies than the band-to-band transition due to the position of the impurity formed energy level, which is always within the bandgap. However, band filling effects are formed in degenerate films causing the expansion of the donor available states above the CBM, leading to higher energy recombinations than the band-to-band transition (Burstein-Moss effect) [80].

The optical gap is the one observed between the maximum available states. Hence, it can be increased by a degenerate band filling effect referred as the Burstein-Moss effect [80]. Burstein was the first to observe the gap widening phenomenon,

suggesting that the shift of the absorption limit is based on the changes in effective mass and not to the impurities added to the material [80]. Thus, by examining the Fermi level shifts, the optical energy gap is equal to the energy between the unfilled band in the CB and the VB maximum [80]. The optical gap is only equal to the actual bandgap when the electron density is lower than the critical value (i.e. not a degenerate semiconductor). For degenerate films, the high carrier density fills the lower CB levels with electrons leaving only high energy states available, thus the optical gap is larger than the bandgap.

Wolff established that degenerate films exhibit many-body perturbation [81]. The many-body effect is caused by the carriers scattering against ionised impurities, leading to bandgap renormalisation (narrowing) [82].This was confirmed later by Roth et al., who suggested that above the critical value for carrier density (Mott critical level) when the Fermi level is above the CBM, the optical gap is not only shifting due to BM effect, but the bandgap simultaneously narrows (BGN) [83].

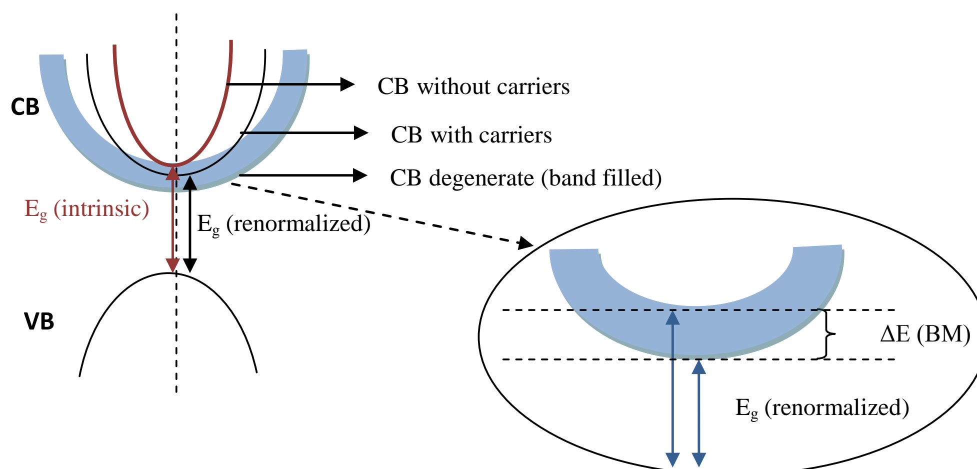

Figure 3: Schematic of the band structure during different carrier filling possibilities in the CB.

Figure 3 illustrates the initial state of the CB minimum without carriers (high energy), the reduction of the CB minimum as carriers are increased (renormalized), and the broadening of the CB when the carrier density reaches degeneracy. It has to be noted that the optical bandgap measured by photon emission (e.g. photoluminescence) is smaller compared to the optical bandgap measured by the absorption (e.g. spectrophotometer). This is due to the energy difference between the excitation state (absorption) and the relaxation state (emission) referred as Stokes shift.

2.1.2.2 ZnO bandgap

ZnO is a direct wide gap semiconductor with bandgap of 3.437 eV at 4.2 K [80] for the wurtzite crystal structure. However, as temperature increases the bulk bandgap red-shifts to a lower energy, which is 3.37 eV (λ=368 nm) at room temperature [85]. The bandgap of ZnO is within the near-UV region (300-400 nm) as shown in Figure 4, hence it allows light of higher wavelength to be transmitted through, making it highly transparent in visible/near infrared region.

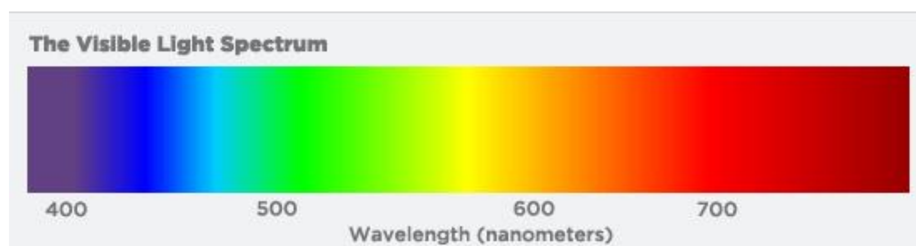

Figure 4: Solar spectrum diagram [86].

The gap can be engineered and controlled via doping in order to achieve higher or lower values. An increased gap can be achieved by doping ZnO with MgO, which has a very large bandgap of 8.4 eV (λ=148 nm), and can result in an enlarged doped ZnO bandgap of up to 3.87 eV (λ=320 nm) [87]. On the other hand, by doping with CdO, which has a bandgap of 2.5 eV (λ=496 nm), the ZnO bandgap can be reduced down to 3.04 eV (λ=408 nm) [88].

2.1.2.3 ZnO stimulated emission

Stimulated emission involves exciton transitions and electron-hole plasma recombinations, as shown in Table 1 and Figure 5 for ZnO emissions using photoluminescence (PL). The dominant PL emission is presented at 3.26 eV (λ=380 nm) corresponding to the optical bandgap [99]-[100], and it is usually referred as the near-band-edge (NBE) emission. The value expands in a range of 3.21-3.24 eV for ALD fabricated ZnO films as the emissions occurs between band tail states [101]. The NBE expresses the recombination of free excitons between the VB maximum (O 2p orbital) and the CB minimum (Zn 4s orbital) [102], consisting of negatively charged carriers (O^{2-}) and positively charged carriers (Zn^{2+}) respectively. With the addition of Zr atoms, a defect level (donor) will be created above the CB minimum, corresponding to Zr 3d orbital [42]. This is due to the shallower 3d orbital energy of Zr compared to Zn 4s [42]. As a result, the Fermi level is expected to move higher in the CB with Zr doping, causing higher NBE energy.

Low temperature PL measurements reveal emissions such as donor acceptor pairs (DAP) [73], bound excitons (BE) [17], and donor-excitons (D^0X) [109]. At high

excitation intensity the emissions are usually due to electron-hole plasma at 3.15 eV (λ=394 nm) [106], which may cause amplified spontaneous emissions at 3.26 eV [113]. Further discussion on the stimulated emissions of ZnO is carried out in chapter 6.

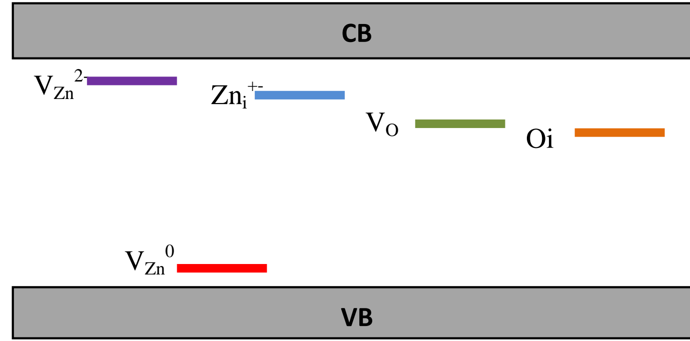

Figure 5: Schematic of the defects states in ZnO within the bandgap.

Table 1: Emission energies for different pairs based on literature.

Emission	Transition	Energy (eV)	
NBE	**CBM→VBM**	**3.21 [101] – 3.26 [99]-[100], (3.29 [104])**	
V_O	V_O→ V_{Zn}^0	1.85-2.0	[99],[101],[104]
	V_O→VBM	2.23-2.35	[99], [105]
Oi	O_i →VBM	2.15-2.25	[99], [101]
Zn_i^+	Zn_i^+ → V_{Zn}^0	2.58-2.65	[99]
	Zn_i^+→VBM	2.62	[99]
V_{Zn}^{2-}	V_{Zn}^{2-} →VBM	2.76	[99]
V_{Zn}^0	CBM →V_{Zn}^0	3.02-3.14	[99], [101]
EHP	EHP (HI)[1]	3.12-3.16	[106]-[107]
E-E, E-el, E-(LO)	Excitons (RT)[2]	3.18, 3.2, 3.26	[100], [106],[108]
DAP	Excitons (LT)[3]	3.22	[73]
(D^0X)	Excitons (LT)	3.28-3.33	[109]
BE	Excitons (LT)	3.28-3.35	[17]
(e, A^0)	Excitons (LT)	3.31	[110]
FE	Excitons (RT)	3.26, 3.31	[100],[107]
BSF	(LT)	3.32	[111]
Deep BE (Y)	Excitons (LT)	3.33-3.35	[109]
(A^0X)	Excitons (LT)	3.33-3.36	[109]
(D^+X)	Excitons (LT)	3.36-3.375	[109]
FE	Excitons (LT)	3.38	[109]

[1] Measurement under high excitation intensity
[2] Measurements under room temperature
[3] Measurements under low temperature

2.1.2.4 ZnO defects

As an intrinsically n-type semiconductor, ZnO is extremely difficult to convert into p-type by adding impurities (acceptors) mainly due to the large acceptor activation energies and the existence of hydrogen impurities acting as shallow donors, found in all films once exposed to atmosphere [73]. According to Van de Walle, in ZnO H^+ (donor) has lower formation energy than H^0 (neutral) and H^- (acceptor) in any Fermi level position, indicating that hydrogen always acts as a shallow donor and contributes to the n-type behaviour (i.e. increased conductivity) [89]. However, this concept is still in dispute since the conductivity of claimed H-free ZnO samples was still measured at very high values [90].

The n-type behaviour is also attributed to the intrinsic defects of oxygen vacancies and interstitial zinc atoms, which act as donors [65],[72]. Oxygen vacancies are the most populated defects due to their low formation energy [91] and are believed to be deep donors, while Zn interstitial defects act as shallow donors [92]. The concept of oxygen vacancies acting as donors was in fact referred as one of the difficulties for achieving p-type, and hence the aim was to use dopants substituting the vacancies and reduce their concentration [92]-[93]. However, in recent years the theory that oxygen vacancies drive the n-type behaviour is less accepted as it was shown that when the Fermi energy is near the conduction band minimum, the oxygen vacancies have neutral charge, hence acting as deep donors [85]. On the other hand, zinc interstitials have low ionisation energy [94] thus act as shallow donors, but are not stable at room temperature. Their stability as shallow donors was reported as Zn interstitials formed complexes with nitrogen impurities [95]. Due to the instability of zinc interstitials at room temperature conditions (resistivity measurements) and the

doubts over their effect in unintentional n-type conductivity [85], it is believed that the room temperature resistivity measurements in the current study will not be affected by those defects.

Zn vacancies are considered as acceptors, and are used to reduce conductivity by favouring their formation through the reduction of OH bonds [96]. Their low formation energy for n-type materials (i.e. decreases as Fermi level increased) allows them to exist in highly n-type materials [85]. Additionally, zinc vacancies are considered as deep level acceptors and so are responsible for electron trapping effects at high irradiation (i.e. high irradiation induced defect production in zinc sub-lattice [97]). As a result, the formation of neutral defects in degenerate materials can be attributed to the high concentration of zinc vacancies.

2.2 Applications of ZnO

ZnO offers the possibility for engineering bandgap, tuning its n-type character of ZnO, and even trying to succeed stable p-type behaviour to achieve homogeneous p-n junctions. Those are the main aspects of researching possible applications of ZnO in thin films and 3D nanostructures, as reviewed in this section.

The piezoelectric properties of ZnO are due to the strong bond polarity [61], which is applied in surface acoustic wave (SAW) transducer used in radar and telecommunications [114]. They operate when an insulating wave travels across the ZnO surface at the acoustic velocity and then is detected at the end of the film [19].

Other applications include ZnO piezoelectric sensors, such as thin film pressure transducers by using Micro-Electro-Mechanical Systems (MEMS) technology [115], strain sensors for measuring displacement, force, torque, or even as flexible strain sensors made by ZnO nanostructure in a paper matrix [116]-[118].

ZnO is also studied for varistors, which are variable resistors sensitive to voltage change, and are usually used as solid state switches for devices in the case of excessive voltage supply [19],[61]. Varistors show non-linear current-voltage performance, with highly ohmic (i.e. resistive) behaviour at relatively low current and voltage (i.e. linearly depended) [119]. This characteristic can be found in $SrTiO_3$, TiO_2, SnO_2, ZnO, etc. [119]. ZnO varistors were first developed in early 1970s by Matsuoka et al. [120], and the physical and electrical properties of conductive ZnO grains used in varistors are best known by study [121].

The direct wide bandgap of ZnO led to research over LEDs, photodetectors, photoconductive detectors and diode lasers applications [122]. The advantage of ZnO to other wide bandgap semiconductors is the large exciton-binding energy of 60 meV [122] providing thermal stability at room temperature (i.e. thermal energy 25 meV [112]). In more detail, excitons do not have enough energy to travel in any state other than the bound electron-hole state with the thermal energy gained at room temperature, and so the excitons are restricted at a narrow energy range allowing the construction of devices with more discrete energy states such as UV lasers. The exciton binding energy can be also tuned according to a study that changes the width of Quantum Wells (QW), indicating increased values of up to 115 meV [11].

2.2.1 LED

LED technology has rapidly developed due to the low power consumption and hence the environmentally friendly performance [123]. An example of their efficiency is their use as the replacement for liquid crystal display (LCD) technology for panel displays [19]. Diodes use p-n junctions with the most common pairs of heterojunctions using n-type ZnO and a p-type semiconductor such as Si, GaN, AlGaN, NiO, Cu_2O, SiC, and GaAs [16]. Additionally, engineering bandgap can be applied and develop heterostructured color-tunable LEDs by doping ZnO, using dopants such as Cu [6], Ga [7], and Er [8]. There have been reports of homojunctions by using nitrogen doped p-type ZnO [124]-[126] and arsenic doped p-type ZnO [127].

2.2.2 UV photodetectors

UV photodetectors are also widely used devices using the photoconductivity property of ZnO. ZnO is very sensitive to UV light exposure, which makes it suitable of having 0-1 states by detecting whether UV light is present or not [128] (i.e. 1 state indicates the illumination of UV light, and 0 its absence). The light effect on the ZnO surface can be used on different approaches such as a switch in photodetectors [128],[129] and for thin film transistors (TFT) [1],[129],[130]. Another approach is the use of high aspect ratio structures (e.g. nanowires) in order to increase the surface detecting the light and therefore reduce the time response, resulting in higher device efficiency [131].

2.2.3 Metal-Insulator-Semiconductor

Metal-insulator-semiconductor (MIS) is a structure that can be formed by homogeneous ZnO layers as it does not require the use of p-type layers [16]. This is due to the use of n-type layers and insulating layers (Figure 6) formed by bandgap engineering via doping. Doped ZnO was easily used as the n-type layer in heterojunctions, with insulation layers such as SiO_2 for producing MIS photodetector [132]. However, heterojunctions showed that the two layers interfere with each other and resulted to leakage [133]. Therefore, homostructural MIS was proposed with P-doped ZnO as the insulation layer for the development of high voltage MIS diode [133]. Post-metal deposition annealing at 250°C was reported to enhance the heterojunctions performance [134].

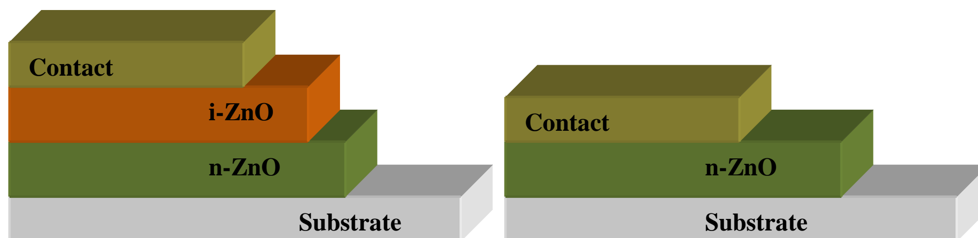

Figure 6: Schematic of the a) MIS and b) MSM material layers.

A similar structure developed before MIS is the Metal-semiconductor-metal (MSM), which does not include an insulation layer (Figure 6). The junction had low efficiency in photodetectors due to the low photocurrent [135]. Therefore, it was

proven that the most effective improvement was the inclusion of an insulator layer in the middle, which led to the development of the more efficient MIS [132], [136].

2.2.4 Solar cells

Considerable interest in solar cells (SC) resulted in applying ZnO in a number of studies. High charge carrier mobility, wide bandgap and the possibility to create 3D nanostructures for higher efficiency are a few of ZnO properties which qualify for SC development [137].

Of great interest are the vertically-aligned ZnO nanostructures that can be used to enhance the SCs efficiency by their large surface. However, based on a review study [138], the synthesis techniques (e.g. hydrothermal method, MOCVD, CVD) have not yet perfectly establish reproducibility of the alignment due to the high sensitivity of the synthesis conditions. A different approach is the use of ZnO nanoparticles, which were first applied to hybrid SCs by Beek et al. in 2004, with impressive ultra-fast charge transfer during excitation of the electrons, which resulted in highly efficient SC [139].

ZnO has also been applied to Grätzel-type SCs [12],[140]-[141], called dye sensitised solar cells (DSSC), which in 1991 came as an alternative and economical solution to single Si crystal SCs [142]. The device required an n-type semiconductor, which produced current after the photons were absorbed by the covering dye, exciting electrons that were then injected to its conduction band [142]. Furthermore, nanowires were combined to quantum dot sensitized solar cells (QDSSC), were quantum dots

(QD) came as a replacement to the dye by having the flexibility to provide different energy gaps by changing the dots size, and therefore capture a wider range of photons [143].

The reduction in typical SC cost led to the development of thin film solar cells, which use transparent conductive oxides (TCO) as electrodes [13]. ZnO is a perfect candidate for the applied oxide, however doping is necessary due to the high conductivity requirements for better efficiency [72]. The results of Al doping for example gave a very efficient SC and were the start of further development [13].

2.2.5 TCOs

Transparent conductive oxides (TCOs) are oxides that conduct electricity as metals and simultaneously are highly transparent due to their wide bandgap. Their use started in 1907 with the first thin film TCO of cadmium oxide produced by Badeker [144]. TCOs are used as transparent electrodes using n-type and even p-type semiconductors of either polycrystalline, amorphous or single crystals, targeting the minimum resistivity and the maximum transparency in the visible range. The most common applications are as electrodes in optoelectronic devices (e.g. photovoltaics), and also as low emissivity coatings used in IR-efficient architectural window applications [39]. The heat efficient windows consist of TCOs (e.g. tin oxide) that reflect the light in the infrared range, and visible transparency is of much higher importance than low resistivity [144]. On the other hand, for optoelectronic devices the requirements for n-type TCOs focus on the high carrier density in the order of 10^{20} cm^{-3} or higher, resistivity in order 10^{-3} $\Omega \cdot cm$ or lower, and wide optical gap of

3.1 eV or higher in order to allow transparency higher than 80% in the range 400-700 nm [35],[145]. In order to achieve such high carrier densities and therefore low resistivity, the material must be doped to degeneracy so that the Fermi level moves into the conduction band. Based on the high transparency and low resistivity, the performance of TCOs is measured by the figure of merit proposed by Haacke [146] (see relation in section 6.2.1). The use of p-type TCOs aims the fabrication of fully transparent devices such as metal-oxide-semiconductor (MOS), using materials such as NiO, $CuInO_2$, and $CuMO_2$ [15].

The carrier density also influences the transparency range. The transparency range expands from the bandgap wavelength of the material to the plasma edge, which is the point that the material starts to absorb the light. This wavelength is defined by the plasma frequency, which is the frequency that the charge oscillates depending on the carrier density and the effective mass. The plasma edge has to be in higher wavelength than the short wave IR region (i.e. λ>1400 nm) in order to avoid having a narrow transmission range. This requires control over the optical properties as the plasma edge is shifted to lower wavelength when the carrier density is very high. Thus, doping to degeneracy is typically used to control the transparency range by expanding or reducing the plasma edge, and by widening the optical gap through the Burstein-Moss effect.

The films grown at high temperatures have low thermal stability, as the surfaces of the substrates and the films could be easily damaged [147]. The selection of the temperature also limits the use of polymer substrates for applications such as photovoltaics (PV) and thin film transistors [148]. This is the reason of developing amorphous films in recent years that can be grown at low temperatures, including

room temperature deposition [148]. Amorphous TCOs offer high mobility as the absent of grain boundaries allows less carrier scattering in comparison to the crystalline films. However, lower resistivity is still recorded for crystalline films grown at temperatures higher than 200°C [39] (e.g. indium oxide crystallises at 150°C [144]). Nevertheless, crystalline materials are not selected for applications requiring low temperature deposition, such as Si-based SCs [39], and thus amorphous films are preferred (e.g. amorphous indium doped ZnO).

The most universally used n-type materials are indium tin oxide (ITO), fluorine tin oxide (FTO), and n-type doped ZnO. ITO is the most common TCO used commercially, manufactured using scale-up DC magnetron sputtering system [144], applied in solar cells, heat-reflecting mirrors, antireflection coating, gas sensors and flat panel displays [147]. It is widely used as it offers the best performance in terms of low resistivity (i.e. ~10^{-4} Ω·cm) and high transparency (i.e. >90%), it has a wide bandgap (i.e. 3.5-4.3 eV [147]), it is environmentally stable with reproducible properties, and has good surface morphology [144]. The high carrier density of ~10^{21} cm^{-3} is attributed to the oxygen vacancies and substitutional tin dopants [147]. However, indium is an earth-scarce element and so the fabrication of ITO is expensive. An alternative TCO is the FTO, which consists of inexpensive raw materials and it can be easily deposited using chemical methods that have low cost [39]. It is used commercially as window coating for low emissivity glasses, but it is not preferred for PV applications as it requires high processed temperatures (i.e. 450°C) that limit the use of different substrates [39]. Another alternative developed in recent year to replace ITO, is doped ZnO, often using Al and Ga dopants. Doped ZnO is preferred as it can be grown at low temperatures, its major constituents are earth abundant elements thus the production cost is low, it is non-toxic, and it can be

readily grown into 3D nanostructures such as nanowires that could enhance the PV performance. For the replacement of ITO, the transparency has to be higher than 85% [15],[18],[20],[149], and resistivity in the order of 10^{-4} Ω·cm [18]. The doped ZnO is preferred over the intrinsic ZnO as it offers better stability and better control over its properties (i.e. instability at high temperatures and undetermined n-type conductivity origin for the un-doped ZnO).

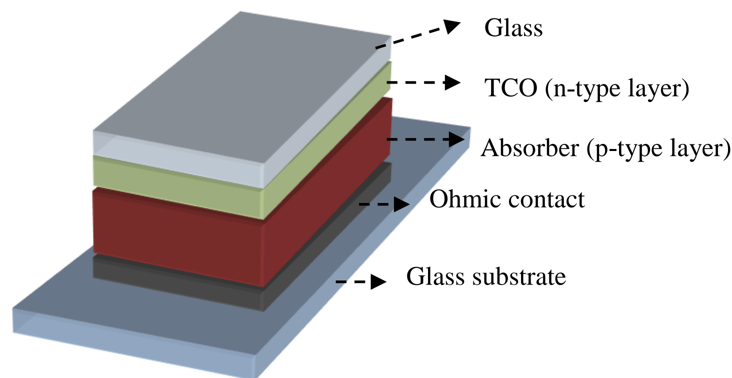

Figure 7: Schematic of a typical thin PV structure.

For photovoltaic applications (Figure 7), TCOs are used as the n-type conductor (electrode) and must be chosen to have band alignment to the absorber by controlling the work function of TCO [150]. This requires a higher Fermi level for the TCO to match the absorber's Fermi level in order to help the electrons transfer from the first to the latter one. On the other hand, the difference between the two VBs has to be as large as possible in order to avoid the transfer of holes from the absorber to the conductor [151]. The most commonly used absorber is CdS with bulk bandgap 2.4 eV [152], which has 1.4 eV difference with the VB of ZnO [150]. The VB is fixed for ZnO but the optical gap can be wider by degenerate doping (i.e. Fermi shift). As a result,

the high carrier density could enhance the performance for PVs applications, by improving the Fermi level alignment for ZnO and CdS.

2.3 Growth techniques

The intense research activity focused on ZnO, has involved a variety of growth techniques such as screen printing, thermal oxidation of the films, spray pyrolysis, sol gel synthesis, magnetron sputtering, chemical vapour deposition (CVD), metal-organic CVD (MOCVD), molecular-beam epitaxy (MBE), pulse-laser deposition (PLD), atomic layer deposition (ALD), etc [72]. A few of those techniques are reviewed in the following sections.

2.3.1 CVD

Chemical vapour deposition (CVD) is a vapour reaction technique, which takes place on the substrate surface and forms the layer when precursors' doses are introduce to the chamber reacting or decomposing close to the substrate's surface [137]. The most common types of CVD are the low pressure CVD (LPCVD) and plasma enhanced CVD (PECVD) [153] forming nanostructures such as thin films, nanowires, nanorods and nanocombs. For the nanostructures, it was reported that adjusting the growth rate of the CVD process could control the diameter of highly oriented ZnO nanorods [154].

Metal-organic CVD (MOCVD) is another form of CVD process, which uses metal-organic precursors to achieve the surface reaction that forms the film or 3D nanostructure (e.g. nanowires) [137]. As a process for high-quality films deposition, it is used in industrial mass production [155].

2.3.2 Magnetron Sputtering

Magnetron sputtering has been widely used method of industrial coatings for many years, and it has been used to produce wear-resistant coatings, corrosion resistance coatings and coatings for enhancing the electrical and optical properties [156]. The process consists of plasma-generated energetic ions bombarding a target plate forcing the plate's atoms to be removed (i.e. sputtering) and then be condensed on the substrate creating the thin film [156]. By this process the target material and the distance to the substrate can play a significant role on the film properties. There are two main types of magnetron sputtering, the direct current (DC) driven by a constant voltage usually applied when the target is a conductor, and the radio frequency (RF) using an alternative current frequency that prevents the current built up in the case of insulator targets. Hence, usually for doping, the RF method is used to allow a wider range of target materials. The disadvantages of magnetron sputtering using either source type are mainly the low deposition rates, inability to precisely control the growth temperature [157] and the overheating of the substrate (i.e. not feasible of using low temperature melting substrates) [156].

2.3.3 MBE

Molecular-beam epitaxy (MBE) is a highly controllable technique at the atomic-layer scale, offering precise control over composition using reflection high energy electron diffraction (RHEED) that precisely monitors the growth during deposition. MBE operates under ultra-high vacuum (UHV), where the material sublimated or evaporated from the heated effusion cells forms a molecular beam of atoms that travels through the vacuum and grows a film as the atoms impinge on the heated substrate. For the deposition of nitrides or oxides, the gases can be activated using electron cyclotron resonance (ECR) plasma source. The amount of material deposited is controlled via shutters at the opening of the effusion cells. The growth temperature is relatively high at 450-750°C for ZnO [106], but can be exploited to deposit single crystal epitaxial films.

2.3.4 Sol-gel

Sol-gel methods have also been used in many publications as there are simple, inexpensive techniques that can be readily applied over large area substrates [158]. Sol-gel methods can be used to prepare multi-component materials with stoichiometric control. It uses a mixture of solvent and stabilizer to form a solution by a process of stirring and cooling the mixture at room temperature, following by a repeatedly spin coating. After the spin coating the solution is heated up to remove residual by-products [158]. The term sol refers to liquid particles used to prepare the solution, and aerosol to gas phase particles.

2.3.5 PLD

Pulse laser deposition (PLD) is a method similar to MBE and can be used for rapid prototyping of high quality thin films and heterostructures [159]. The process uses a pulsed laser to ablate the target materials (plates) and induce plasma plume that condense on the substrate to form the film. For epitaxy, PLD operates at high growth temperature (e.g. 800°C), which is possibly the reason for the observed high Zn interstitial concentration, leading to very conductive doped ZnO films in comparable levels to ITO with resistivity in the order of 10^{-5} Ω·cm [14]. However, low temperature grown Al-doped ZnO films were also reported, using different laser energy density at room temperature [160].

The lowest resistivity doped ZnO films were grown by PLD [58],[161],[162]. Its effectiveness was the subject of a study that compared the electrical and optical properties of un-doped ZnO films grown by atomic layer deposition (ALD) and PLD using annealing processes and photoluminescence (PL) to determine the defect states [163]. The results indicated that the conductivity of the PLD films was driven by the high Zn interstitial concentration acting as intrinsic shallow donors, in contrast to ALD films that showed low concentration of both zinc interstitials and oxygen vacancies. The mechanism favouring the formation of zinc interstitials in PLD that lead to much higher carrier densities is the effect of the laser energy during deposition that possibly causes atomic peening [163]. Nevertheless, the need for producing films for large scale mass production led to the use of different methods such as ALD, which is a highly scalable process. ALD is a precise, controllable growth technique, allowing low temperature deposition on various substrates due to

the advantage of using gas phase semiconductors. In this study, ALD is the only growth technique used, and it is reviewed in section 2.5.

2.4 Doping in ZnO

2.4.1 Doped ZnO films

The properties of ZnO can easily be altered via doping, and there is significant interest in improving the n-type behaviour as well as ongoing interest in the challenging and controversial issues of p-type doping. Dopants acting as donors or acceptors are elements with low ionisation energy (i.e. the energy needed to remove an electron from the nucleus attraction). Hence, as shown in Figure 8, donors will have low ionisation energy below the CBM (i.e. E_D), and by gaining that energy their electrons will be ionised into the CB and contribute to conductivity. Acceptors on the other hand, will have low ionisation energy above the VBM (i.e. E_A), and by gaining an electron from the VB, a hole is generated.

The dopants selected for ZnO are generally categorised into their element groups. Elements from group I are generally considered to act as acceptors with recent reports on p-type materials of K and Li doping [164]. However, recent research has shown that Li and Na actually produce semi-insulating material [72], due to the formation of stable neutral complexes from dopants acting as donors when placed in interstitial positions and as acceptors when substitute on zinc sites [85]. This is avoided with group V elements as they tend to substitute to oxygen vacancies.

Nitrogen is the most studied and most promising candidate for p-type ZnO as it is reported to have the smallest ionisation energy (i.e. hence it should act as a shallow acceptor [16],[72],[165]), and also its similar atomic size to oxygen favours its substitution on oxygen sites [85]. However, according to a study by Lyons et al. [166], nitrogen has higher ionisation energy than the VB maximum of ZnO, thus it is expected to act as a deep acceptor.

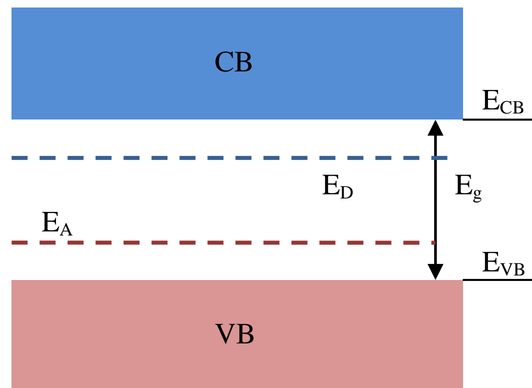

Figure 8: Schematic of a band energy structure showing the donor and acceptor ionisation energies.

Elements from Group III are widely used as donors to increase n-type conductivity as they provide extra electrons in relation to Zn^{2+} after ionisation, hence substituting to zinc sites will offer more carriers to the material. The most common elements used include Al^{3+} [167]-[169] and Ga^{3+} [38],[162]. Other dopants from the same group including B [10],[21] and In [22]-[23], have also been reported. Group IV elements such as Sn [29], Si [170] and Ge [27], have been recently used for donor doping as they act as shallow donors (i.e. low ionisation energy). Transition metals have also been used as dopants, such as Ti [171], Mn [158], Co [24], Ni [172]-[173], Cu [174], Zr [25],[28],[48], Ag [174],

and Hf [3],[28],[175], which all showed reduced resistivity at low doping levels. A detailed discussion on n-type dopants is given in section 2.4.1.1.

2.4.1.1 N-type doping

One of the most commonly used dopants is Al, introduced by different growth methods such as RF magnetron sputtering [176]-[179], CVD [180]-[181], spin coating technique [182], ionised deposition [183], sol-gel method [184], spray pyrolysis [185], and ALD [33]-[34],[167]-[169],[186]-[188]. The selection of Al as a dopant is based on its low cost over large scale applications and on its electrical and optical properties when added to ZnO. In more detail, Al^{3+} provides one extra carrier when ionised and substitutes to Zn^{2+} leading to high carrier density and thus to lower resistivity. In addition, Al^{3+} has smaller ionic size (0.57Å) than Zn^{2+} (0.72Å) [185] and thus could occupy both interstitial and Zn positions in the film [40].

The resistivity values of ALD films [33],[186]-[187] were slightly higher than spray pyrolysis [185], magnetron sputtering [176]-[177] and much higher than PLD [161] as shown in Table 2. However, the resistivity of the ALD films was reported lower when using sapphire as the substrate (i.e. from 3.0×10^{-3} Ω·cm on glass to 7.7×10^{-4} Ω·cm on sapphire), attributed to the c-axis textured grains formed on sapphire resulting in less scattering than the random oriented grains on glass [34].

Gallium is another widely used dopant for ZnO films in TCO replacements of ITO, since Ga is economical and more abundant than indium. It also offers less grain reduction in comparison to other dopants such as In, Zr and Sn [29], and it is placed as

substitutional to Zn in the lattice [40]. The Ga-doped films often show lower resistivity and higher transparency than Al-doped films, and are preferred due to their resistance to oxidation and the fact that Ga is less reactive to Zn rather than Al [189]. Comparable studies between Al and Ga dopants showed higher carrier density for Ga (5×10^{20} cm^{-3}) compared to Al (3×10^{19} cm^{-3}) [40]. ALD deposited films showed comparable resistivity (8.0×10^{-4} Ω·cm [38]) to the Al-doped films [34], but still much higher than the one reported for PLD films (8.12×10^{-5} Ω·cm) [162].

Table 2: List of published doped ZnO films using different dopants and growth techniques.

	Growth method	Resistivity (Ω·cm)	Carrier density ($\times10^{20}$cm^{-3})	Carrier mobility (cm^2/Vs)	Transparency	Optical gap (eV)	Growth T (°C)	Film thickness
Al	SP[1] [185]	7×10^{-4}	3.6	25	88%	3.7	450	1.4 µm
	RF MS[2] [176]	4.6×10^{-4}	7.2	18.8	90%	-	250	130 nm
	RF MS (H-annealed at 300°C) [177]	8.3×10^{-4}	8.86	9.7	90%	3.7	-	-
	PLD [161]	8.5×10^{-5}	15.4	47.6	88%	-	230	280 nm
	ALD [33]	3.2×10^{-3}	1.4	14.3	-	-	200	45 nm
	ALD [186]	2.4×10^{-3}	-	-	>80%	3.5	150	180 nm
	ALD [187]	4.4×10^{-3}	1.7	8	92%	3.73	150	100 nm
Ga	RF MS (annealed at 550°C) [189]	1.5×10^{-3}	1.4	29.4	-	-	-	1.4 µm
	PLD [162]	8.1×10^{-5}	146	30.96	90%	3.5	300	200 nm
	ALD [38]	8.0×10^{-4}	1.1	18	-	-	300	-
In	SP [22]	5.6×10^{-1}	-	-	90%	3.3	450	600 nm
	RF MS [23]	4.4×10^{-3}	18	10.1	>80%	-	-	1.5 µm
	ALD [192]	3×10^{-3}	6	20	>85	-	200	180 nm
Ti	ALD [171]	8.9×10^{-4}	6.2	10	>80%	3.4	200	100 nm
Ni	Sol-gel [173]	4.8×10^{-4}	-	-	91.2%	-	200	-
Hf	ALD [28]	6×10^{-4}	3.7	20	>80%	3.56	200	200 nm

[1] Spray pyrolysis
[2] RF magnetron sputtering

A direct comparison between Al, Ga and In showed that In resulted in the highest carrier density [190], possibly due to the formation of oxides, as In substitutes to Zn

and combines to O interstitials [191]. However, indium is not preferred as a dopant for ZnO as the aim for using doped ZnO as TCOs is to replace ITO due to In scarcity.

2.4.1.2 Co-doping

Co-doping of ZnO films has been developed in the recent years, to either enhance n-type conductor or to explore p-type ZnO. Most of the reported studies are theoretical predictions, as it is very difficult to experimentally achieve stable and improved properties with co-doping. The experimentally reported studies are under dispute for their accuracy of films with stable properties. An approach for p-type ZnO films is the use of dual acceptor co-doping [193], such as Li-Ni co-doped by PLD [195], or even donor-acceptor co-doping, such as Al-N co-doped ZnO by ALD [194], and Li-Zr co-doped ZnO by aqueous solution [196]. On the other hand, donor-donor doping could enhance further the electrical n-type properties by improving structural defects caused by a single dopant. An example is the surface degradation caused by Ga doping, which was shown to be avoided with the introduction of In, showing reduced resistivity of 7.4×10^{-4} Ω·cm compared to GZO with resistivity of 1.04×10^{-3} Ω·cm [197]. Other combinations of donor co-dopants include Co- Al [198] and Co-Ga [199].

2.4.2 Zirconium doped ZnO films by different techniques

Zirconium was chosen as the dopant in this work due to its high abundance in Earth's crusts and because it acts as a shallow donor in ZnO providing two extra free

electrons when substitutes to Zn^{2+}. Zirconium is also a transition element and it is considered to be a good doping candidate based on its comparable ionic size to Zn [43] (i.e. 0.745 Å for Zr and 0.74 Å for Zn [42]). This helps to minimize lattice distortion usually observed with other dopants when substituting for Zn^{2+} (e.g. Al) [29] that could affect the mobility, the electron distribution and the band structure. The minimisation of the lattice changes does not correspond to zero changes, in contrast, Zr-doped ZnO studies showed a small increase in the d-spacing of the lattice when adding Zr [26],[56]. An additional advantage is the reluctance of Zr to bond with Zn atoms, avoiding the formation of secondary (inter-metallic) phases and therefore enhancing the stability of the target phase [44].

The use of Zr provides the extra electrons required to increase the carrier density and so enhance the n-type conductivity. However it is expected to result in a small mobility reduction due to its tendency to cluster into the grain boundaries which reduces the grains size [29],[48],[57]. This suppression of grain growth is more intense at high doping when ZrO_2 molecules are formed and placed at grain boundaries [49],[57]. The mobility and grain size reduction could both be used as an indication of the dopant segregation at grain boundaries in the current study, which can exists in epitaxial films without the formation of clusters due to the dopants mobility within the grain boundaries.

A number of publications using Zr-doped ZnO were reported using different deposition techniques, such as spray pyrolysis [26],[45]-[47], low temperature coprecipitation method [48], sol-gel method [29],[49],[50],[200], DC magnetron sputtering [51]-[54], RF magnetic sputtering [56], microwave irradiation [55], low temperature gel-combustion [201], PLD [58], and ALD [25]. The number of related studies is much lower

than for other dopants such as Al and Ga, and thus various gaps remain in the understanding of Zr doping. In particular for ALD growth, there is only one published study for Zr-doped ZnO thin films [25] reporting conductive and transparent films, but also leaves scope for further research which is addressed in the current study. The findings of the published ALD study and the research gaps identified are discussed in the zirconium in ALD section (2.5.3).

A theoretical study by Wang et al. [43] using first principle calculations, reported the most likely position of Zr in the ZnO lattice based on the calculated formation energies. This study suggests Zr is likely to be substituted onto Zn sites as this arrangement has the lowest formation energy and causes the lowest lattice distortion (due to ionic radius similarity). According to those calculations, Zr_{Zn} will result in Fermi level shift into the CB and thus the conductivity will be increased.

Experimentally, Zr-doped ZnO films were shown to reduce the resistivity compared to the un-doped ZnO films, with the most effective doping being typically between 1-5 at.% Zr. Films prepared by sol-gel showed resistivity of 7.2×10^{-2} Ω·cm at a low doping level of 1.5 at.%, and increased again as the doping increases further [49]. In the same study, possibly due to the low carrier density (1.5×10^{19} cm^{-3}), the optical measurements showed no Burstein-Moss effect and the bandgap was found to reduce with increasing doping. In another study using the same deposition technique, ZnO nanoparticles with Zr doping, showed enhanced oxygen vacancies concentration with doping that resulted in room temperature ferromagnetism while pure ZnO showed paramagnetism [200]. Different nanostructures with Zr doping have also been reported using a low temperature coprecipitation method [48]. It showed that the

bandgap can be manipulated by controlling the morphology of the material (i.e. nanoflakes, nanorods, spherical nanoparticles).

DC magnetron sputtered films were also reported, including a study of thick doped films (450 nm) that showed high transparency up to 92% with resistivity of 9.8×10^{-4} Ω·cm after vacuum post-annealing (300°C) [53], more conductive than a study using RF magnetron sputtering of 300 nm thick films (2.1×10^{-3} Ω·cm) [57]. Polymer substrates of polyethylene terephthalate (PET) were also used by DC magnetron sputtering, showing low resistivity up to 1.8×10^{-3} Ω·cm and transparency up to 86% [51]. Spray pyrolysis method resulted in higher resistivity films (100 nm) of 6.7×10^{-2} Ω·cm, reduced to 2×10^{-3} Ω·cm after vacuum annealing at 400°C [26]. The most conductive Zr-doped films were reported using PLD, with resistivity of 5.6×10^{-4} Ω·cm for a 200 nm film, and optical transmittance of 84% [58].

According to Paul et al. [49], the grain orientation was initially random for the un-doped films, then formed a-axis preferred orientation $(10\bar{1}1)$ at 1 at.% before shifting to c-axis orientation (0002) at 2 at.%, which is enhanced as doping increased further to 3 at.% [49]. The increase of c-axis preferred orientation with increasing doping was also observed by Bahedi et al. using spray pyrolysis [45]-[47]. Other studies of Zr-doped ZnO films, reported increase of amorphization as doping increases using RF magnetron sputtering [56] and spray pyrolysis [26]. This trend was explained by Gokulakrishnan et al. as the effect of Zr being placed in interstitial positions and not to zinc sites [26]. This suggests that increase of c-axis alignment corresponds to Zr being placed in zinc sites, with the cause being discussed in chapter 4.

The larger ionic size of Zr atoms was reported to result in larger lattice constants according to Tsay et al. [50] and Zhang et al. [200] using sol gel method [50], Khan et al.

using gel-combustion method [201], Wang et al. using RF magnetron [56],and Gokulakrishnan et al. using spray pyrolysis [26]. As a result, it can be said that chemical mixing methods result in increased lattice constants with the addition of Zr atoms.

The structural properties of Zr-doped ZnO films compared to other dopants such as Ga, In and Sn were studied by Tsay et al. using sol-gel [29]. This study showed that Ga and In doped ZnO exhibited the lower resistivity due to the formation of larger grains in comparison to Zr and Sn doped ZnO, ultimately resulting in lower grain boundary scattering [29]. The same effect of grain size difference was also reported when compared to Al-doped films, where Zr was reported to show slightly higher resistivity (6.1×10^{-4} Ω·cm) than Al-doped films (5.7×10^{-4} Ω·cm) deposited by DC magnetron sputtering [54]. The reduction of grain size due to Zr doping is yet to be published for ALD, thus this is also investigated in this thesis.

2.5 Atomic Layer Deposition

Atomic layer deposition (ALD) is an atomic layer-by-layer growth technique, which uses self-limiting surface chemistry to controllably deposit thin films, with monolayer precision (i.e. few Å) [202]. ALD was first developed in the 1970s in Finland, with the name atomic layer epitaxy (ALE) by Suntola et al [203]. ALE was presented as a closely related method to MBE, with the initial experiments focused on growing II-IV compound films on glass [204]. Later this process became well

known to other researchers, who developed, analysed and renamed the process as atomic layer deposition (ALD) [205].

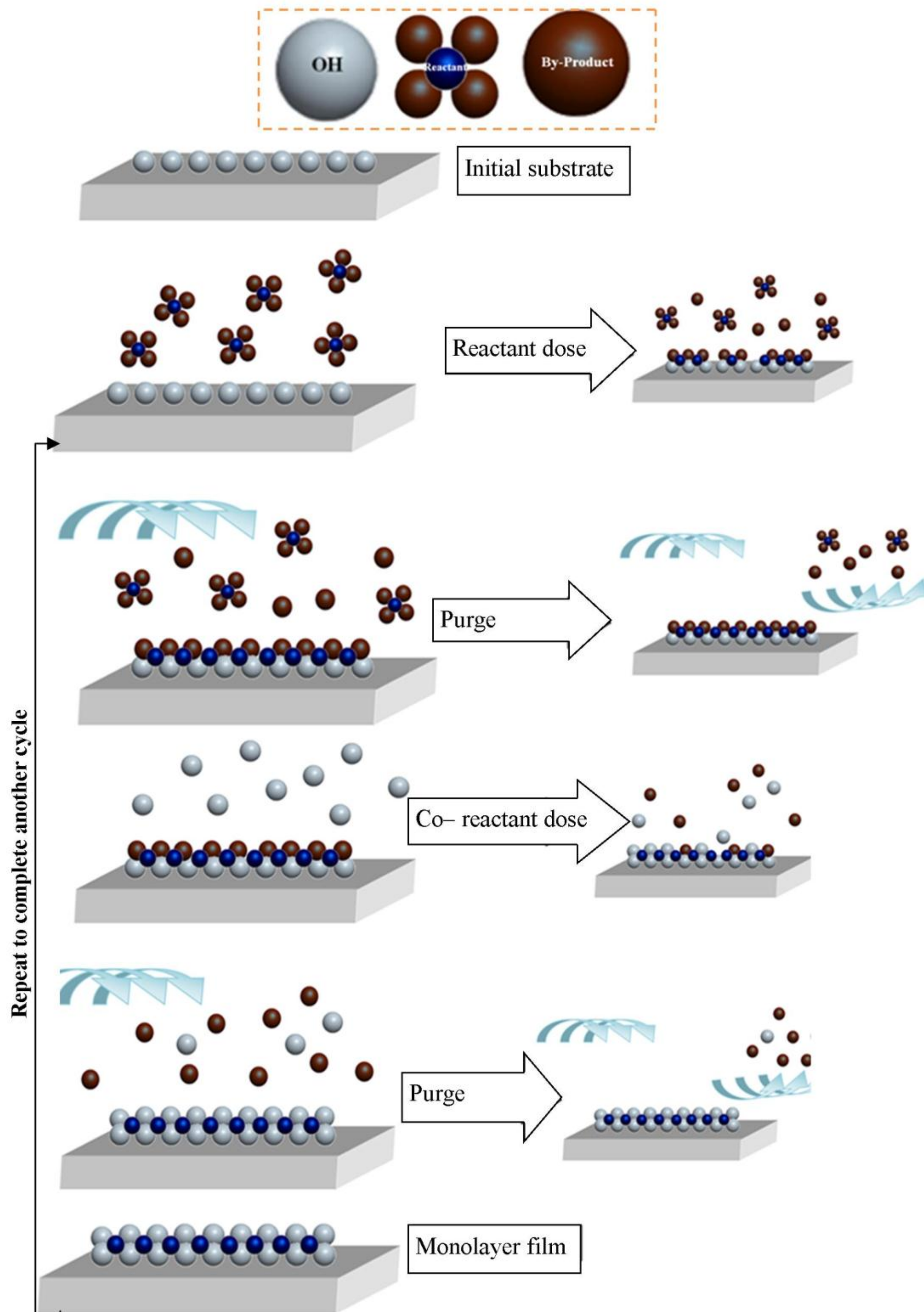

Figure 9: Schematic of ALD process using self-limiting surface chemistry.

The gas-solid reactions formed from the sequential steps of a process, led to the self-limiting behaviour and the precise control of the thickness [202]. Based on its gas phase nature, ALD is suitable for coating on many surfaces providing uniformity and conformal deposition [206]. In fact, it is believed that no other thin film technique produces coating on high aspect ratio structures with such high conformality [205], such as nanowires and nanorods [206].

The success of ALD is based on the surface chemistry, since in two stages a layer can be formed after the reaction of two precursors (i.e. reactant and co-reactant) [207] under high vacuum conditions in the order of mTorr. The operation of ALD (Figure 9) is based on four simple steps: precursor (reactant) exposure, precursor purge, co-reactant exposure, co-reactant purge.

The precursor exposure is the step introducing the selected precursor, into the reaction chamber. The dose time length is typically very short (i.e. volatile precursors introduced in ms) so that the precursors do not react in the volume of the chamber but only to the adsorbates on the sample surface [208]. Thus, the dose time depends on the vapour pressure, the reactor geometry, the sample geometry (i.e. if the sample has high aspect ratio it will require longer dose), and how well the precursor adheres to the substrate. The precursor doses are separated using inert gas purges in order to remove the remaining by-products left after the surface reactions. The co-reactant exposure forms the bonds that are metal-oxygen in the case of oxides. The by-products are then again purged in the fourth step, leaving OH groups for H_2O doses that react on the next cycle's precursor dose producing another layer. The end of a cycle leaves a monolayer of typically 1 or 2 Å thickness, and under self-limiting growth conditions this value is fixed per cycle. Those growth

parameters such as doses times and substrate temperature are controllable via software interface for most ALD systems, operating in a sequence of steps defined by the user (recipes). Therefore, the thickness of the deposited layer is precisely controllable as the film thickness is linearly proportional to the number of ALD cycles completed.

ALD is used to deposit metal oxides such as ZnO, metal nitrides such as TaN, sulfides such as ZnS, and phosphides such as GaP [205]. Each ALD process requires a suitable combination of precursors and co-reactants, which have to be volatile, reactive with each other, and thermally stable in either solid, gas or liquid form [209]. Precursors can be initially classified as reactant (metal) and co-reactant (non-metal), with the co-reactant precursors such as H_2O and NH_3, being used for depositing oxides and nitrides. The reagents are often inorganic precursors, in which metal atoms are connected to organic ligands groups in order to increase the volatility of the metal at low temperatures. Highly volatile precursors are introduced into the chamber typically using short pulses, while for some involatile precursors it is necessary to bubble gas through the precursor to increase the pickup of vapour into the gas stream.

One of the most important advantages of ALD is the deposition of highly reactive precursors at low temperature. The reactions in thermal ALD are usually carried out in the 150°C to 350°C temperature range [210]. The growth temperature is always set higher than the precursor heating temperature by at least 20°C to assure equilibrium between the surface chemical reaction and the physical absorption/desorption [208]. Note that highly volatile precursors such as diethylzinc precursor are left at room

temperature, but less volatile sources such as tetrakis-ethylmethylamino zirconium precursor, are heated to increase the vapour pressure.

The ‘ALD window’ (Figure 10) is shown at the temperature range where the growth rate is fixed (i.e. saturation region). At lower temperatures the reactions cannot occur due to lack of thermal energy, and thus the bonds are not formed (i.e. incomplete reaction) leading to decreased deposition rate. In some cases, condensation may occur at low temperatures leading to an apparent increase in growth rate. If the temperature is higher than the ALD window, the excess thermal energy may induce desorption of the precursor (i.e. break the formed bonds out of the lattice) leading to a reduction in growth rate. Another possibility is the precursor may thermally decompose at high temperatures, leading to CVD-like condensation of growth and hence to an actual increase in growth rate.

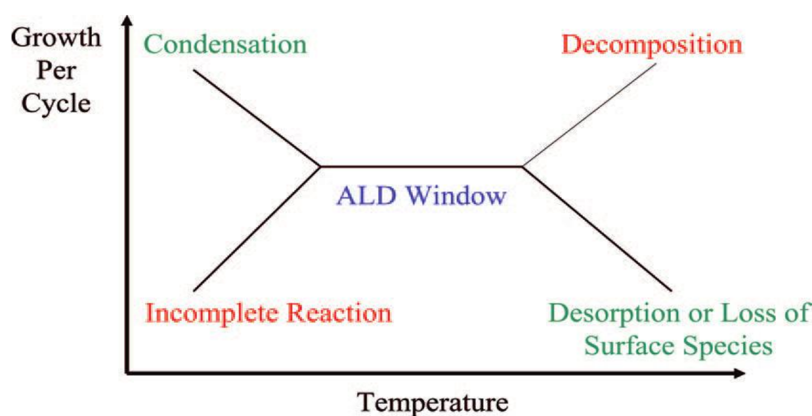

Figure 10: Schematic of possible behaviour for the ALD growth per cycle versus temperature [205].

ALD is divided into two main types; the thermal ALD and plasma enhance ALD (PE-ALD). Thermal ALD simply uses thermal energy to induce reactions, whether

PE-ALD uses plasma as a source of additional energy for reactions that are not feasible with low energy [205]. Hence, plasma can be used at lower growth temperature compared to thermal ALD, which could be particularly useful for temperature sensitive substrates. However, all of the studies mentioned in this report are based on thermal ALD, which could also use low growth temperature and could be more easily used to deposit on high aspect ratio structures.

2.5.1 ZnO deposited by ALD

ALD of ZnO has been extensively studied by many research groups over the last decade [208]-[209],[211]-[217]. Alkyls are the most commonly used precursors for zinc oxide, however, it is reported that these can leave carbon and hydrogen residues [202]. The most commonly used zinc sources are diethylzinc (DEZ) and dimethylzinc (DMZ), with water mostly used as the co-reactant [209], since it allows deposition at temperatures as low as room temperature (i.e. partially crystalline films) [218]. The use of low temperature (90°C) with DEZ allowed deposition of ZnO films on plastic-based polymer solar cells leading to 4.1% power conversion efficiency [211]. DMZ was reported to result in faster growth rate (i.e. up to 3.7 Å/ cycle) than DEZ (i.e. up to 2.1 Å/ cycle) due to shorted ligand of ethyl compared to methyl (i.e. smaller steric hindrance) [212].

DEZ consists of ethyl groups, which make it highly volatile, giving it a high vapour pressure even at room temperature. DEZ also has high reactivity at temperatures lower than 200°C. This is considered a great advantage as it enables deposition on a variety of applications such as organic substrates and polymers [214]. At temperatures

higher and lower than the ALD window, the growth rate decreases, due to desorption and incomplete reaction respectively [212]-[213]. The use of DEZ in thermal ALD is reported to result in growth rate of 1.9-2.0 Å/ cycle within the ALD window [215]-[217]. However, when it is used in a PE-ALD the growth rate is higher at 2.8 Å/ cycle due to the high reaction when using oxygen plasma rather than water reactant [217]. The comparison between the two methods also showed higher carrier density for the thermal ALD at low temperatures, while interstitial oxygen sites were formed at low temperature PE-ALD (i.e. <300°C) that acted as electron compensators, making the plasma grown films more suitable for TFT applications [217]. The effect of chamber pressure was also studied and showed that at high pressure of 760 Torr the growth rate increased compared to 2 Torr, attributed to the excess water that remained at the film surface after the water purge step at high pressure, but it is suggested that increased gas velocity can resolve this issue [213].

Similarly to PLD, the increase of zinc interstitials was found to reduce the resistivity [163], hence in ALD it was found that at high temperatures the population of those defects increases, leading to higher carrier concentration [219]. The effect of growth temperature on the electrical properties was also studied for low growth temperature at 100°C, which showed low carrier concentration suitable for use in Schottky diodes [220]. The mobility on the other hand could be increased by increasing film thickness via ALD, as increasing the overall thickness will lead to grain enlargement and hence to the reduction in interfacial and grain boundary scattering [214].

ALD deposited ZnO is usually polycrystalline with peaks of $(10\bar{1}0)$, (0002), $(10\bar{1}1)$, $(10\bar{1}2)$ and $(11\bar{2}0)$, found even from ultrathin films (10 nm) [221]. The preferred orientation of such films is usually in the (0002) plane (polar orientation) [222]-[223] as

it has the lower surface energy and so grains grow in that direction to minimise the system's energy. However, studies also reported films of $(10\bar{1}0)$ preferred orientation (non-polar) [216],[224]-[227]. In those studies, the growth conditions were different than the standard ALD deposition of ZnO films, including the use of short DEZ doses and short water purge steps [224], the growth at low temperatures (i.e. 150-220°C) [225], and the use of thick films [216],[226]-[227]. The most recent study showing the thickness effect on the grain orientation suggested that the preferred orientation shifted from (0002) to $(10\bar{1}0)$ direction as the thickness increased [226] (further analysis on the reasons of that change is carried out in chapter 4). Hence, ALD offers the opportunity to set different preferred orientation in ZnO films by changing the film thickness without altering any other growth parameters. A schematic of the crystal structure for both polar and non-polar surface is shown in Figure 11.

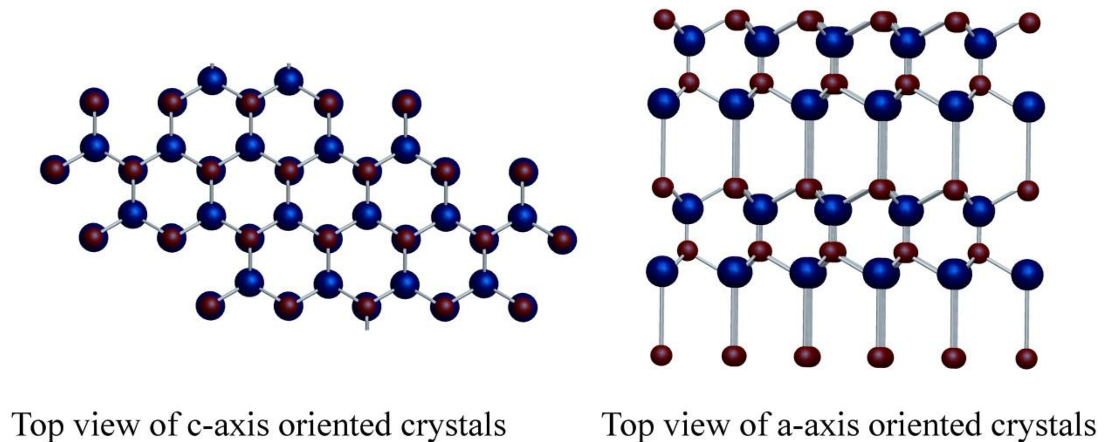

Figure 11: Schematic of the top views for polar (c-axis oriented crystals) and non-polar (a-axis oriented crystals) surfaces. The red spheres show zinc atoms and the blue ones show oxygen atoms.

Non-polar ZnO films are of interest, in order to avoid electrostatic instability created in the polar surfaces. Polar surfaces lead to spontaneous polarization [228], which creates a non-zero dipole moment that forms macroscopic electric field with perpendicular direction to (0001) plane [229]. This electric charge causes reduction of electron-hole recombination probability and reduces the photons generation [228]. To avoid this effect, non-polar films are more favourable for more efficient optoelectronic devices, such as LEDs and LDs [228],[230]. It was also found important for electrical properties according to Fujimura et al. [231], who stated that $(10\bar{1}0)$ oriented films were more conductive compared to $(11\bar{2}0)$ and (0001) oriented films. This was also seen by Illy et al., who reported improved photovoltaic performance when the orientation is at $(10\bar{1}0)$ orientation rather than (0002) plane [232].

ALD can be used to grow ZnO films on various substrates such as flexible polyethylene terephthalate (PET) [215], glass slides [217],[220],[227],[233], sapphire substrates [220], and on Si substrates [217],[220]. The ability of ALD to coat high aspect ratio structures also allowed the use of coating 3D ZnO structures, such as nanowires for dye sensitised solar cells (DSSC) [234] and for field-effect transistor (FET) [235]. Based on this advantage, ZnO was used as the coating on several other 3D structures such as anodic aluminium oxide (AAO) templates [236], TiO_2 nanoparticles [237]-[238], multi-walled carbon nanotubes [239], and high surface area silica gel [240]. Additionally, ZnO nanowires can be grown using hydrothermal growth on deposited ALD films [241].

2.5.2 Doped ZnO deposited by ALD

Doping can be easily achieved by ALD using a “delta doping method” (i.e. using one doping cycle in a series of ZnO cycles), such as the one used in this study. As a result, a variety of dopants have been studied using ALD, with focus on producing improved n-type films as shown by some examples in Table 3.

Table 3: List of published doped ZnO films deposited by ALD using different dopants.

	Resistivity (Ω·cm)	Carrier density ($\times10^{20}cm^{-3}$)	Carrier mobility (cm^2/Vs)	Transparency	Optical gap (eV)	Growth T (°C)	Film thickness	Ref
Al	9.7×10^{-4}	-	-	>80%	-	200	-	[242]
	3.2×10^{-3}	1.4	14.3	-	-	200	45 nm	[33]
	2.4×10^{-3}	-	-	>80%	3.5	150	180 nm	[186]
	4.4×10^{-3}	1.7	8	92%	3.73	150	100 nm	[187]
Ga	8.0×10^{-4}	1.1	18	-	-	300	-	[38]
Ge	$6\text{-}7\times10^{-3}$	2.14	5	>80%	3.62	250	100 nm	[27]
In	3×10^{-3}	6	20	>85	-	200	180 nm	[192]
Ti	8.9×10^{-4}	6.2	10	>80%	3.4	200	100 nm	[171]
B	6.9×10^{-4}	~4	~20	-	-	136	-	[247]
Hf	6×10^{-4}	3.7	20	>80%	3.56	200	200 nm	[28]
Zr	1.3×10^{-3}	2.2	19.7	92%	3.27	180	100 nm	[25]

2.5.3 Zirconium in ALD

Zirconium is used in ALD to form nitrides and oxides [202], such as ZrO_2 layers proposed as high-k dielectrics [248]. The precursors used are tetrakis-dimethylamino zirconium (TDMAZ) [249] and tetrakis-ethylmethylamino zirconium (TEMAZ) [25]. TEMAZ (used in the current study) was reported to vaporise at 120-150 °C and grow at 150-300°C with growth rate at 1.1 Å/cycle [250]-[251].

There is only one publication to date establishing the effect of Zr doping concentration on the resistivity of the ~100 nm thick ZnO films, showing the lower resistivity of 1.3×10^{-3} Ω·cm and maximum carrier density of 2.2×10^{20} cm^{-3} when doped with 2 at.% Zr (mobility of 19.66 cm^2/Vs) [25]. The maximum transmittance was of 92% within the range 390 to 900 nm, while the optical gap was found to be increased with the Zr doping concentration, from 3.23 eV for the un-doped film to 3.35 eV for the 8 at.% Zr-doped film [25]. Additional data were presented regarding the increase of crystallinity as the 4 at.% Zr-doped film was annealed at 900°C, and also photoluminescence studies showed electron-hole plasma emission at high excitation intensities. Therefore, further analysis could be carried out to cover the microstructural effects as doping increased, on how they affect the conductivity, identify the causes for the optical gap increase, prove that Zr is in the state of Zr^{4+} when doped in the films, and finally to identify any defects generated as doping alters. The current study will focus on those topics by carrying out an overall characterisation of the ALD grown films with a systematic doping alternation.

Chapter 3

Experimental processes

3.1 Introduction

This chapter addresses the experimental methods used for sample preparation and characterisation. ALD growth is explained in section 3.3, by establishing the growth and sample preparation of all films presented in this thesis. The thickness of these films was then measured by ellipsometry (section 3.2) and confirmed by TEM (section 3.10). TEM was also used to analyse the microstructure of the films, together with XRD (section 3.8) and AFM (section 3.11). The electrical properties of films deposited on glass were characterised using a four-point-probe (part 3.4) and Hall effect measurements (section 3.5), while the chemical state was assessed by XPS (section 3.9). Finally, the optical properties were investigated using photoluminescence (section 3.6) and spectrophotometry (section 3.7).

3.2. Ellipsometer

Ellipsometry is an optical technique that provides information such as the refractive index, through illuminating and analysing polarised light. The ellipsometer used in this study, uses polarised light with fixed wavelength to illuminate a sample surface,

and then analyse the reflected elliptically polarised light as shown in Figure 12. The physics behind this technique followed the wave theory of light (Hooke 1660), the polarisation of light theories (Faraday mid 1840s), and the theory of electromagnetic waves (Maxwell 1873) [252]. The development of the first ellipsometer is attributed to Paul Drude (1902). His models are still used today, mostly in spectroscopic ellipsometry, to relate the carrier density with plasma frequency obtained through reflection/transmission as discussed in section 3.7.1.

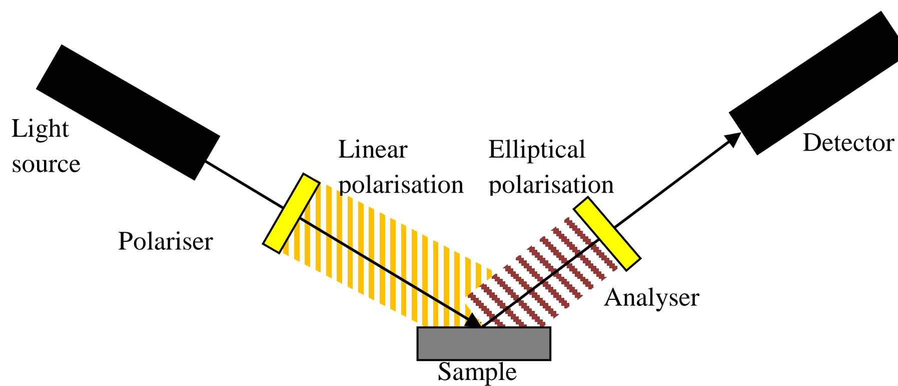

Figure 12: Schematic of ellipsometer setup.

In ellipsometry two parameters are measured during the scan, the angles Ψ and Δ, which present the light amplitude change and phase change after reflection respectively [252]. From the change in polarisation with ellipse shape (Figure 13), the reflected polarised light consists of two components, the parallel (r_p) and the perpendicular (r_s). The numerical components are presented in Equation 1 and Equation 2, which result in the refractive index (n) calculation in Equation 3.

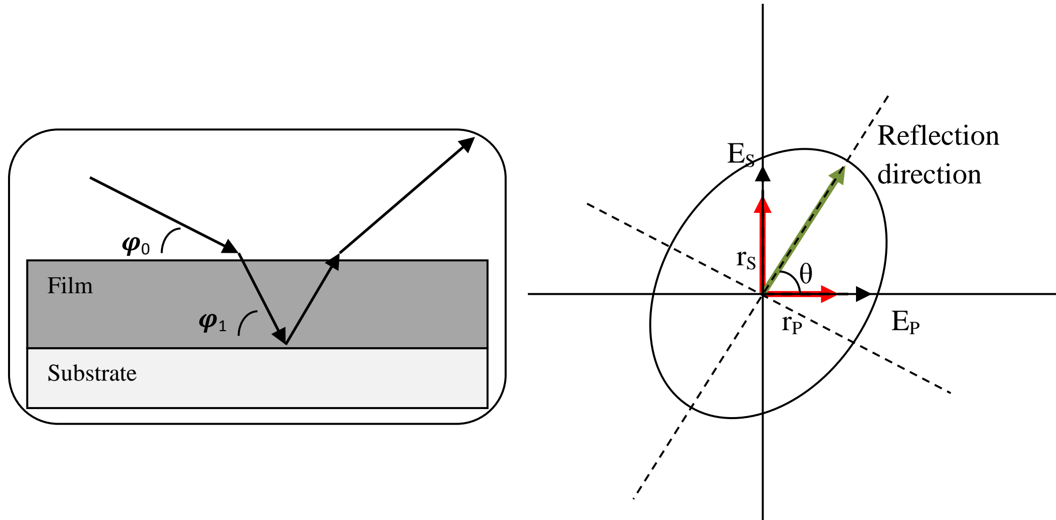

Figure 13: a) Angles during reflection in ellipsometer, and b) Schematic of the elliptical polarised light reflected from the sample surface.

Equation 1, Equation 2

$$r_P = \frac{\tilde{N}_1 \cos\varphi_0 - \tilde{N}_0 \cos\varphi_1}{\tilde{N}_1 \cos\varphi_0 + \tilde{N}_0 \cos\varphi_1} \qquad and \qquad r_S = \frac{\tilde{N}_0 \cos\varphi_0 - \tilde{N}_1 \cos\varphi_1}{\tilde{N}_0 \cos\varphi_0 + \tilde{N}_1 \cos\varphi_1}$$

Equation 3

$$\tilde{N} = n + ik$$

where $\tilde{N}$ is a complex number and k is the absorption index. By knowing the complex components and the incident angle, the phase factor β can be calculated using Equation 4 providing the thickness of the film (L). The value β is calculated using the Fresnel equations [252], based on the parallel and perpendicular polarised components.

Equation 4

$$\beta = 2\pi \left(\frac{L\sqrt{\widetilde{N_1^2} - N_0^2 \sin^2\varphi_0}}{\lambda} \right)$$

The measured angles of Ψ and Δ are related to parallel and perpendicular components as given by Equation 5 [252], which presents the ellipsometry variable ρ.

Equation 5

$$\rho = \frac{r_p}{r_s} = \frac{|r_P|\exp(i\delta_P)}{|r_S|\exp(i\delta_S)} = \tan\Psi\, e^{j\Delta}$$

where Ψ and Δ are given by the following equations:

Equation 6

$$\tan\Psi = \frac{|r_P|}{|r_S|} \qquad and \qquad \Delta = \delta_P - \delta_S$$

As a result, when the thickness increases, the angle Ψ increases and angle Δ decreases. A simulation model called ellipsheet [253] represents this relation, and shows that as the refractive index and thickness varied for a range of Ψ and Δ, the relation is presented as loop. As a result, it is possible to have the same values of Ψ and Δ for different film thicknesses. When the thickness of the film is too small, the accuracy of the ellipsometer thickness reading is reduced since it may give different numbers of refractive index for Ψ=10° [253].

The ellipsometer was used as the technique to determine the optical thickness and refractive index of the films deposited on Si wafer substrates. A Rudolph Research Auto-EL-IV ellipsometer was used in the current study. It uses light at three different wavelengths of 633 nm, 576 nm, and 405 nm. The wavelength used for all measurements presented in this study was the 633 nm (single point program 20-20). The use of this program is based on the assumption that all films have one refractive index (i.e. no internal reflections). For the doping set, the films were assumed to be flat and have uniform refractive index.

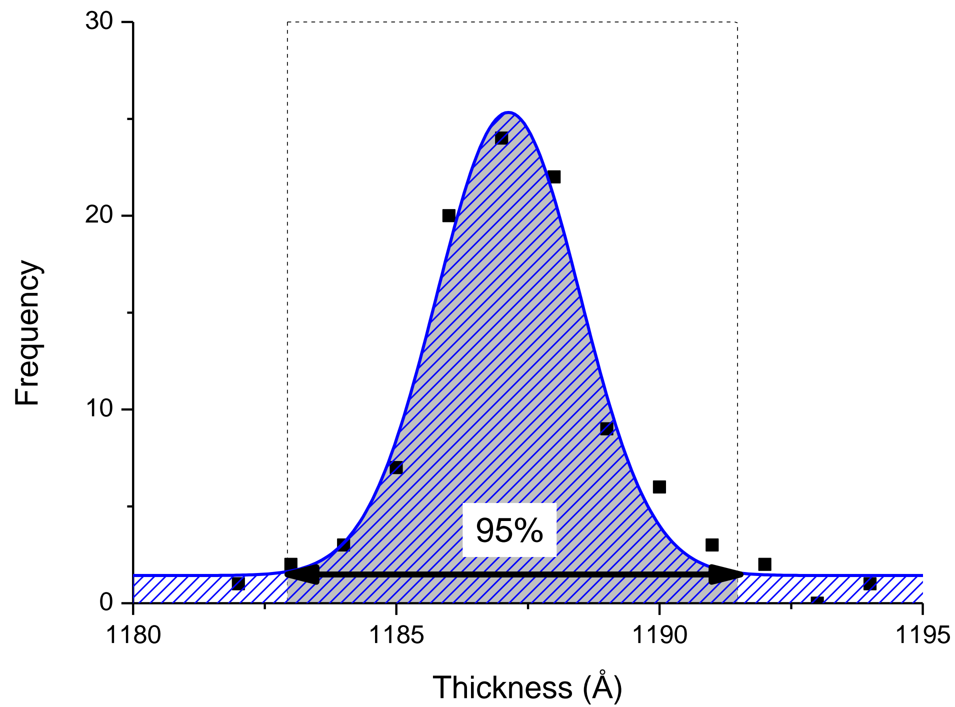

Figure 14: Standard deviation showing the 95% error margin for the ellipsometer thickness readings.

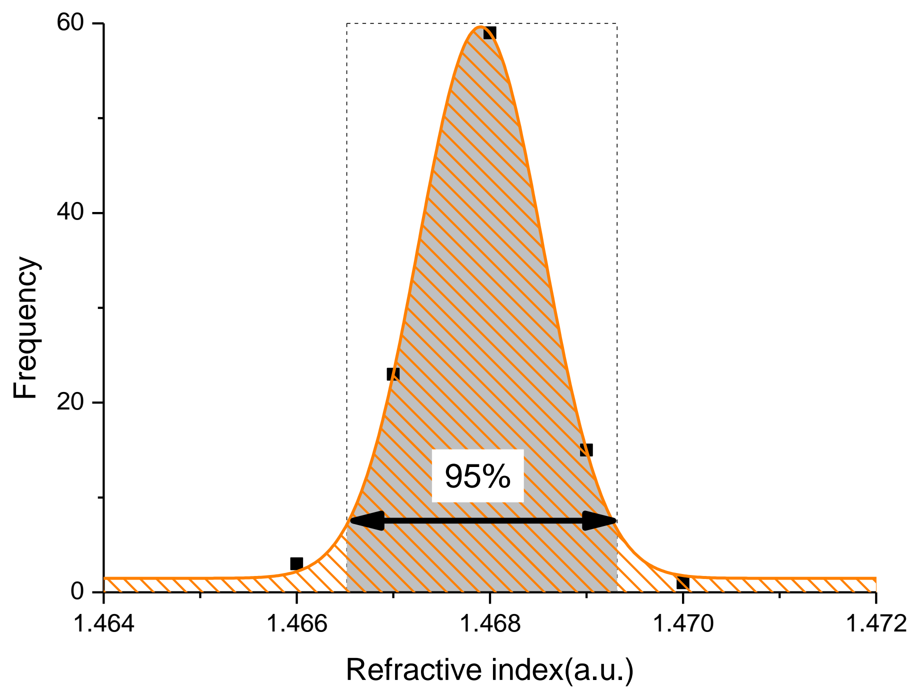

Figure 15: Standard deviation showing the 95% error margin for the ellipsometer refractive index.

The measurements of a reference sample were taken for setting the error margins (i.e. 1178 Å standard 4″ initialisation wafer of silicon single crystal), which was used for calibrating the ellipsometer every day. The standard deviation was then plotted for the thickness (Figure 14) of 100 readings, showing thickness error margin of ±8.5 Å within the 95% of the total area (1183-1191.5 Å). The 95% acceptance margin for the refractive index (Figure 15) was found between 1.466-1.469 (unit-less), hence the refractive index error margin is set at ±0.003 (unit-less).

3.3. Atomic Layer Deposition

Atomic Layer Deposition was used to grow all the films presented in this thesis using an Oxford OpAL ALD reactor arrangement schematically shown in Figure 16. There are three precursor lines (one not shown) and one co-reactant line. The co-reactant line is the H_2O source, and the other three lines are connected to zinc, zirconium, and aluminium sources.

There are two main gas lines on the ALD reactor, the dose line (shown as blue line in Figure 16) used for flowing argon into the bubblers in order to increase the pickup of vapour and to carry it into the chamber. When volatile precursors are used, this line is not required and precursor is dosed using vapour draw. The purge line (shown as red line in Figure 16), forces argon through the dose line (above the dose valves) at the end of each dose step in order to clean the line and purge the chamber. The argon flow was kept constant at 200 sccm during deposition to maintain a stable chamber pressure of around 200 mTorr. As a result, 200sccm were directed by the Fill valve during the dose steps, and re-directed back to the purge valves during purge.

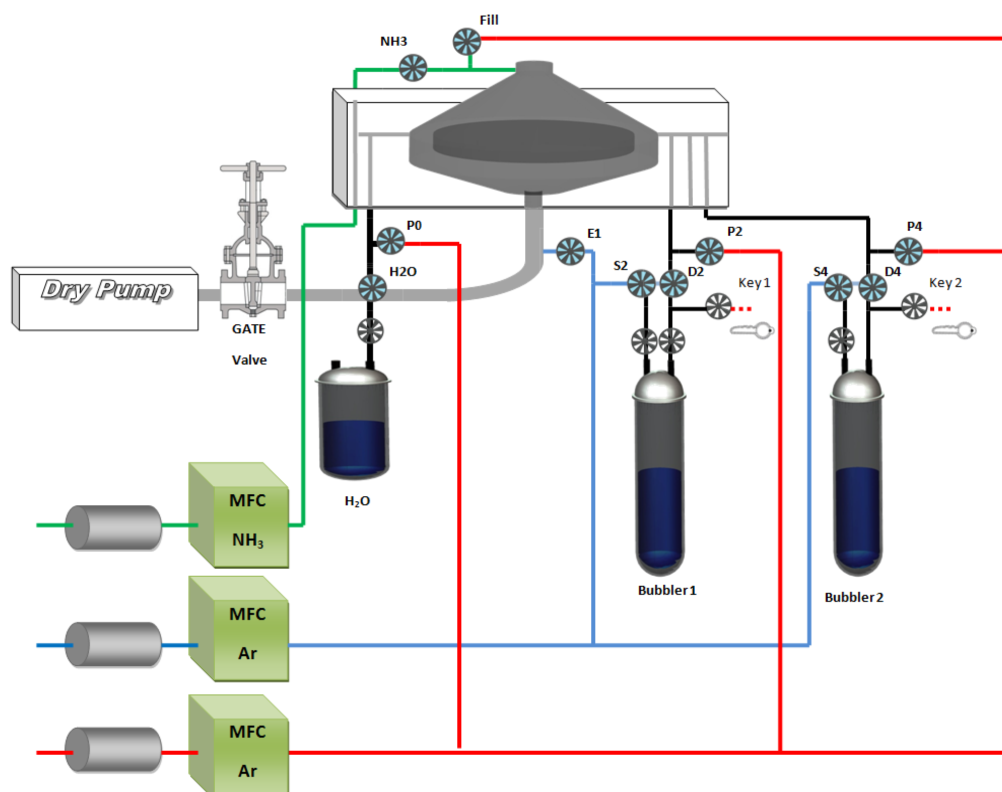

Figure 16: Schematic of the ALD OpAL kit operational lines (i.e. blue is the dose line and the red one is the purge line).Note that D=dose valves, S=source valves, P=purge valves, E1=exhaust valve, and the white-gray valves show the manual valves.

For the runs used in this study, the precursor purge valves and the water purge valve were used during the main processes, while the Fill valve was used at the beginning of the run to stabilise the pressure. The precursors used in this study were the organic diethylzinc (DEZ) and tetrakis-ethylmethylamino zirconium (TEMAZ) as Zn and Zr sources respectively (both supplied by SAFC Hitech). Deionised water was used as the co-reactant throughout the process, with argon (BOC research grade) as the purge gas. Each precursor was delivered via vapour draw, with DEZ and H_2O source held at room temperature and TEMAZ heated at 95°C. In more detail, the main precursor chemical reaction is shown in Equation 7 for the DEZ precursor [254],

where the ethyl groups of the precursor bonded to Zn sites react to water and form ZnO bonds and C_2H_6 as the by-products.

Equation 7

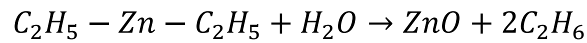

$$C_2H_5 - Zn - C_2H_5 + H_2O \rightarrow ZnO + 2C_2H_6$$

The deposition temperature was set at 200°C following initial temperature tests presented later in this section. Trimethyl-aluminum (TMA) and H_2O were also used to deposit 2-3 nm Al_2O_3 buffer layers at the same temperature with the precursor held at room temperature. This was done to improve nucleation of the ZnO and achieve better optical measurements as it provides transverse optical confinement with minimum absorption loss due to its wide energy bandgap [255].

Two types of substrates were used in each deposition run in order to satisfy the sample restrictions of the characterisation processes. Films were deposited on standard sodalime glass microscope slides and on virgin test grade n-type Si (100) wafers. The glass substrates were used for optical measurements as it required transparent substrates, they were also used for electrical measurements as it was important of having a non-conductive substrate to prevent parallel conduction in the substrate. The glass slides were carefully cleaned with isopropanol prior of the deposition, by using drops on the surface and then drying them out using nitrogen air. Samples grown on Si wafers were mostly used for microstructure analysis and for optical thickness estimation using ellipsometer in order to isolate the refractive index of the film (e.g. ellipsometry is more sensitive when using high refractive index substrates, such as silicon wafers).

The temperature on the deposited surface was slightly different than the one set by the controlled ALD software due to the conduction and conversion heat transfer in

the chamber (Figure 17). Due to the different substrates used with different thermal conduction coefficients, the sample surface had slightly different temperature. By experimentally measuring the sample's surfaces under growth conditions using a low mass thermo couple (i.e. under vacuum at 200°C table temperature with 200sccm argon flow), the surface of the glass substrate was repeatedly measured at 181°C and on Si wafer at 186°C. The temperature difference between the two types of substrates is unlikely to have an effect on the films properties.

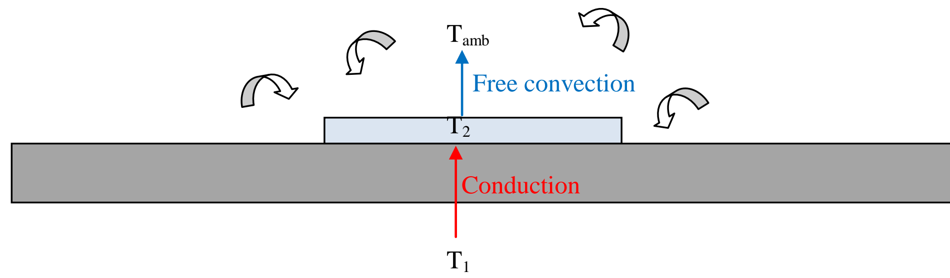

Figure 17: Schematic of Heat transfer in a sample heated on the ALD chamber plate.

A typical ALD cycle of ZnO is shown in Figure 18 which is repeated X times to create a film of X number of cycles. The step times and ALD temperature windows for ZnO were initially investigated to establish suitable growth conditions for the doping study. All the resultant plots are shown in Figure 19.

For the tests some standard parameters were set such as a low table temperature at 150°C, with DEZ dose at 30 ms, water dose at 50 ms pulses and purge times at 5 s. The number of cycles was kept constant at 300. For each plot, only the variable changed in each run with the above parameters being fixed. The growth rate graphs

do not show any error bars related to the error margin set for ellipsometer, due to the very small uncertainty.

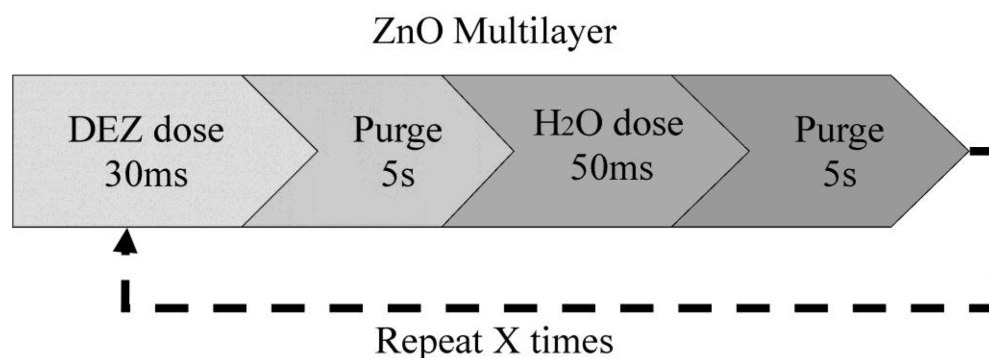

Figure 18: Schematic of the ALD process to deposit ZnO films.

The first parameter tested was the precursor dose, and as DEZ is highly volatile, only very short doses were applied. From the growth rate plot (Figure 19a), the ALD window began at 20 ms with 2±0.1 Å/cycle growth rate. Thus, the optimum precursor time was set at 30 ms for all subsequent runs. The co-reactant (H_2O) pulses showed saturate growth starting at very short pulses of 10 ms, which is the shorter time allowed by the Swagelok ALD valves. A run without co-reactant showed no growth, hence confirming that the growth is only ALD. The abundance of this precursor allowed selecting a longer pulse time, set at 50 ms. The purge time (Figure 19c) showed slightly higher growth rate at the shorter step of 1s, suggesting lack of by-products removal. The growth rate then showed a saturated region between 3-12 s, and at 15 s the growth rate was reduced, possibly indicating desorption of the precursor due to the prolong purge. The optimum value was at 5 s in order to keep the run times to the minimum.

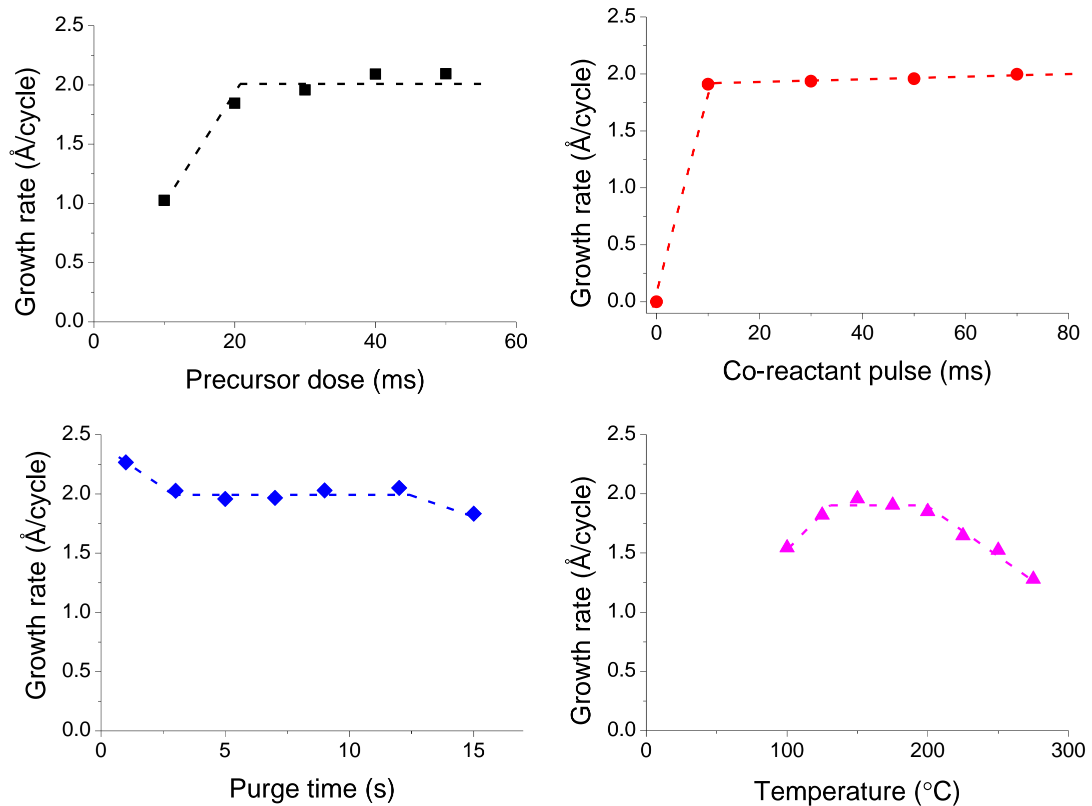

Figure 19: ZnO growth rate by varying the a) precursor dose (150°C), b) co-reactant dose (150°C), c) purge time (150°C), and d) temperature.

As reported by Rueter et al., the DEZ adsorbs on the Si (100) surface at temperature lower than -73°C [256], thus deposition was expected at very low temperatures. Indeed growth is shown even at 100°C with the ALD window found within 130-200°C. Below 130°C the growth rate was low indicating desorption as not all the bonds could be formed due to lack of thermal energy. At temperatures above 200°C, there was a decrease in growth rate consistent with the literature suggesting desorption of DEZ [257]. This is related to zinc metal desorption at relatively low temperature (277°C) leaving adsorbed ethyl groups on the substrate [256]. As a result, the selected temperature for the main set of samples was set at 200°C based on the resulted lower resistivity of the films as shown in section 5.2. One cycle using the selected parameters gives a growth rate of 1.87 Å/cycle.

The full characterisation process of zirconium oxide was not conducted for the TEMAZ precursor due to the limited quantity of precursor available for this study. Thus, the ALD temperature window was obtained from the literature. According to study [250], TEMAZ precursor with higher vaporise temperature (120-150°C) reacting with H_2O, resulted in a ALD window between 150°C and 300°C with growth rate at 1.1 Å/cycle. The same growth rate was reported for PE-ALD using O_2 plasma, with the temperature window starting from 150°C to at least 250°C (no higher temperature growth was presented) [251]. Hence, the selected temperature of 200°C from the ZnO study is within this ALD window. TEMAZ was heated at 95°C and the dose time was set at 1 s, giving a growth rate of 0.65 Å/cycle. The precursor temperature was selected based on Becker et al. study [258], which was applied in the current work and resulted in uniform and repeatable film growth.

In this study a fixed number of 500 cycles was used for the doping study. In addition, a range between 300 and 1500 cycles was used to examine the film thickness effect. The doping process shown in Figure 20 had an extra step at the end of the standard ZnO sequence, for the deposition of zirconium oxide. This is an ALD 'delta' doping methodology similar to the one reported by Chalker et al. [27]. During this method, only one doping cycle of ZrO_2 was added per period of the main loop, and the doping percentage was altered by changing the number of repeats of the ZnO cycle. The total number of cycles was again kept fixed, with $(Y+1)\times X$ be equal to 500. The doping concentration (i.e. atomic percentage) cited throughout this study is based on the cycle ratio and the number of atoms. In more detail, this estimation was based on the assumption that during the zirconium process, Zr-O bonds are formed similarly to monoclinic ZrO_2 (formed at low temperatures [259]). Hence, for the doped layers we assume that there are two O for every Zr, while for ZnO it was assumed

that there was one O for every Zn atom. For example with X=50, Y=1, the corresponding doping concentration was estimated to be 4.8 at.% and the doping percentage cycle as 10%. Unfortunately, it was not possible to prove this experimentally using XPS as is believed to give layers of Zr rich material rather than homogeneous defects. As a result, the surface sensitivity of XPS dominates and discards the measurements. Nevertheless, the gradual change of the properties as doping increased such as resistivity supported the fact that ZnO films were controllably doped by Zr.

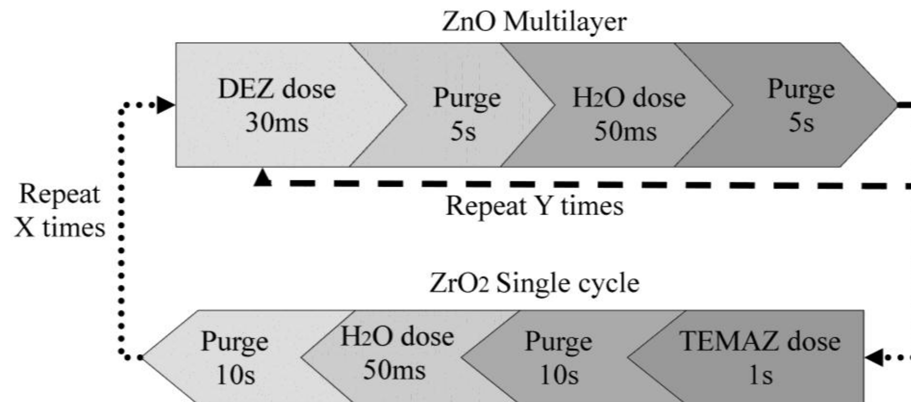

Figure 20: Schematic of the ALD process to deposit Zr-doped ZnO films

3.4. Four-Point probe

Resistivity measurements were carried out on films deposited on glass using a four point probe (4PP). 4PP uses four in-line probes of equal spacing (1.3 mm) placed on the films surface. Electrical current is applied between the first and fourth probe (see Figure 21), and the resulting potential difference is measured by the two middle probes (2 and 3).

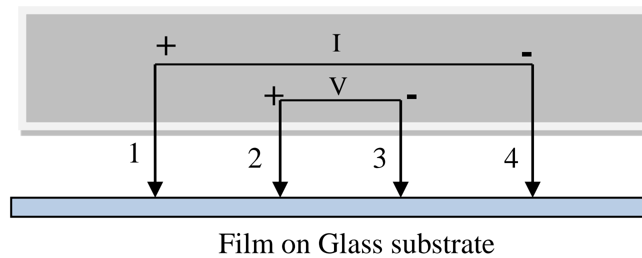

Film on Glass substrate

Figure 21: Schematic of the four-point-probe configuration, with the 4 probes on the film surface.

The principle of this method is based on Ohm's law stating that the resistance is proportional to the potential difference (V) and inversely proportional to the current (I) flowing across the sample (i.e. R=V/I). The resistance is expressed by the resistivity and the geometry of the sample. Resistivity is the property of the film corresponding to the degree of electrons mobility (Equation 8) [260].

Equation 8

$$\Delta R = \rho\left(\frac{dx}{A}\right)$$

For bulk materials where thickness (t) is much higher than the probe distance (s), the current penetrates spherically into the sample and hence the affected area is $A=2\pi x^2$. As a result the resistivity (ρ) is calculated by Equation 9 [260].

Equation 9

$$\rho = 2\pi s\left(\frac{V}{I}\right)$$

For very thin films where t is much smaller than s (t<<s), current rings are formed that change the penetrated area into A=2πxt. This changes the resistivity formed given by Equation 10 [260].

Equation 10

$$\rho = \frac{\pi t}{\ln 2}\left(\frac{V}{I}\right) = 4.532\, t\left(\frac{V}{I}\right)$$

Sheet resistance (R_S) is the resistivity without taking into account the thickness of the film (Equation 11). The sheet resistance is calculated by taking the slope of the voltage to current relation obtained by the four-point-probe data. The slope must pass though zero and should be linear for semiconductor materials. The resistivity of the film is then calculated by multiplying the film thickness (Equation 12).

Equation 11

$$R_S = 4.532\left(\frac{V}{I}\right)$$

Equation 12

$$\rho = R_S \times t$$

The home built 4PP system used in this work comprised of a Lucas Signatone Corp SP4 Probe head and a Keithley Series 2400 Sourcemeter. The probes were made from tungsten carbide with a 0.13 mm tip radius, and 1.3 mm tip spacing. For the measurements the sample was placed on a flat insulating surface and the probes were lowered to touch the sample surface. The tips on spring loaded to give a set load per tip, thus the load must not be high. The sources rates were controlled using computer software, in which the current range, current step and step speed were set and the

data were logged. The resultant slope of the I-V plots was used to determine the sheet resistance (Ω/square) and from this the resistivity value (Ω·cm).

The potential difference measured by the 4PP is between 200 mV and 200 V. Hence, the current must be always set higher than 10 mA for very conductive films in order to obtain a measurable potential difference. The current was set at 10^{-7} A for very resistive films, as the high resistance leads to high potential difference (V) that might overcome the measurable voltage limit. For the conductive films the current was set at 10^{-4} A. The samples in the current study were all set at range $\pm 2\times10^{-5}$ A with steps of 2×10^{-6} A.

The error for 4PP is very small for thin and low resistivity films. Repeatability tests estimated the error margin at ± 4.8 Ω/square. For example, a 100 nm film of resistivity in the order 10^{-3} Ω·cm will have an error margin of $\pm 4.8\times10^{-5}$ Ω·cm.

3.5. Hall effect measurements

3.5.1. Background information

For further analysis of the electrical properties, Hall measurements were undertaken by using the van der Pauw method. This can also be used to determine resistivity to verify the 4PP results. The most important aspect though was the use of Hall effect to establish the carrier density and mobility, which is especially useful for doped films as it reveals the majority carriers type and hence allows classification of the semiconductor as n-type or p-type.

The technique is based on the Hall effect principle discovered by E. H. Hall in 1879, which refers to the phenomenon of potential difference generation across a conductor when it is placed under the influence of a magnetic field (B) with a current flow (I) along its length. This is expressed by Equation 13 [261]

Equation 13

$$V = R_H IB$$

where V is the electron drift velocity and R_H is the Hall resistance of the sample. The potential acts in the transverse direction to the electric field and perpendicular to the magnetic field as illustrated in Figure 22.

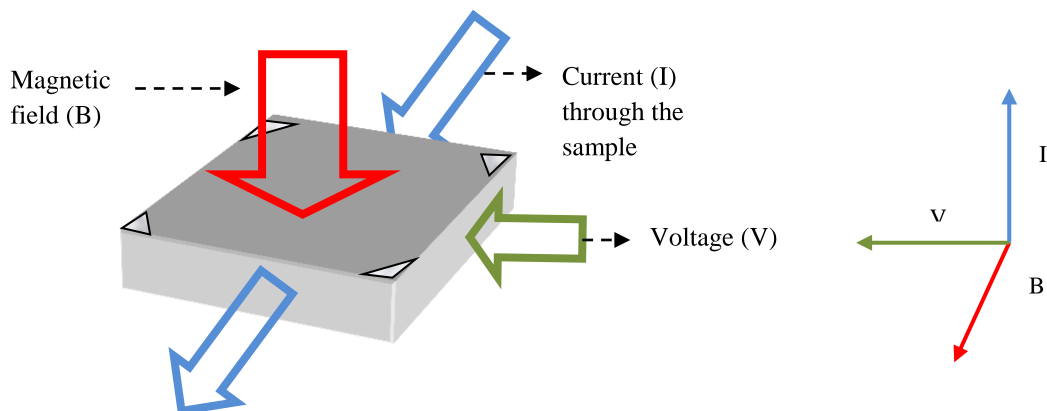

Figure 22: Hall Effect arrangement (left) and current-voltage-magnetic field directions (right).

Later on van der Pauw specified a configuration that resulted in an accurate measurement of the generated Hall voltage (V_H). This configuration has limitations in the sample geometry and the contacts applied. According to van der Pauw [262] the film thickness has to be homogeneous and on a flat substrate with no gaps in the film (i.e. all grains are in contact). Additional requirements are that the contacts are

applied at the top of the surface and are small compared to the circumference of the sample. The use of triangular contacts was found to be most effective by Chwang et al. [263]. As a result, the easiest and most accurate sample shape followed over the years is the perfect square with symmetrical ohmic triangular contacts at the corners as shown in Figure 22. The sheet resistance is specified in the van der Pauw configuration as the component of vertical (R_v) and horizontal (R_h) resistances (i.e. the resistances measured across the x and y direction of the sample). Two vertical and two horizontal sheet resistances are measured across each side of the sample (Equation 14 [264]). The values are then applied in Equation 15 stated by van der Pauw [262] to be solved numerically for the total sheet resistance Rs.

Equation 14

$$R_V = \frac{R_{12,34} + R_{34,12}}{2} \qquad and \qquad R_h = \frac{R_{23,41} + R_{41.23}}{2}$$

Equation 15

$$e^{-\pi R_v/R_s} + e^{-\pi R_h/R_s} = 1$$

After measuring and calculating the resistivity of the sample with thickness (t), the Hall mobility (μ_H in cm^2/Vs) can be calculated by experimentally measuring the Hall voltage (V_H). The Hall voltage is generated under the influence of a magnetic field (B) and electric current (I) as expressed by Equation 16 [262].

Equation 16

$$V_H = \frac{\mu_H I B \rho}{t}$$

The majority carrier density (cm^{-3}) can be also calculated (Equation 17) in relation to the electron charge ($e=1.6 \times 10^{-19}$ C). The majority carrier type can be determined from the polarity of the Hall voltage.

Equation 17

$$n_e = \frac{1}{\mu e \rho}$$

The carrier mobility is related to carrier collisions within the structure (scattering). There are different scattering mechanisms that could occur within a thin film, such as interfacial scattering, ionized and neutral impurity scattering, surface scattering, acoustic phonon scattering, piezoelectric scattering, scattering by dislocations, and scattering in the grain boundaries. Some of those mechanisms do not apply in the current films, such as neutral impurity scattering, which only occurs at very low temperatures [265].

The interfacial scattering is related to the film thickness, and it increases at low film thicknesses. Hence, by increasing the overall thickness, this parameter is limited until it gets to the bulk mobility value (i.e. mobility increases initially linear and then sublinear as a function of thickness).

The ionized impurity scattering is related to the number of ionized shallow-donor impurities, and it is correlated to the electron energy loss after inelastic scattering with donor ions [265]. As a result, scattering is expected to increase with doping concentration due to the high concentration of ionized donors. Additionally, impurity mobility is inversely related to the effective mass given by the relation $\mu_I=e \cdot \tau_i / m^*$, where τ_i is the relaxation time and m^* is the effective mass. At high carrier density the effective mass increases due to the increase of screening effect, which reduces

the forces affecting the electrons movements. The increase of the effective mass causes an increase of the ionized impurity mobility scattering.

The acoustic phonon scattering is related to the thermal vibrations in the lattice, and so it contributes substantially to the electron mobility at high temperatures [265]. The lattice scattering increases as the temperature increases. For a fixed temperature, the thermal vibrations are expected to be the same for each film measured under the same conditions. Hence, the acoustic phonon scattering is considered to have little effect on the mobility differences measured in the current study.

The piezoelectric scattering applies to polar semiconductors with crystal inversion symmetry, which causes electrons to be scattered by acoustical phonons [265]. However, it was found to have very little influence on the electrical properties in comparison to the other factors [265].

3.5.2. Measurement information

For this study, Hall effect measurements were carried out using a Keithley Series 2400 Sourcemeter attached to a BioRad Hall probe station with a 0.3 T fixed magnet. The BioRad Hall probe station consisted of four needle probes which can be positioned onto the four contacts (Figure 23). The probes were connected to the source via a switching box. I-V was measured between contacts 1-4 and 2-3 to give an average. When the Hall measurement was made, I-V was measured diagonally across the sample between contact 1 and 3, and also between 2 and 4, both with and

without the magnetic field applied. The measurement for both sides is carried out for better accuracy and assures that the film is electrically uniform.

For the Hall effect, the voltage was zeroed before applying the magnetic field. Hence, the measured voltage under the magnetic field was the Hall voltage. The current used for those measurements was 1 mA, as lower values resulted in very low potential out of the measurable limits. Note that all measurements were taken under room light and room temperature conditions.

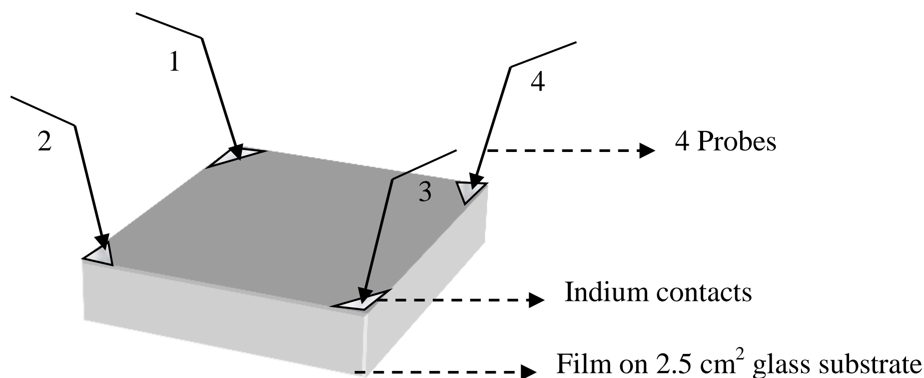

Figure 23: Van der Pauw configuration for square glass substrate with In contacts as used in the current study.

One of the biggest issues for accurate Hall voltage measurements were the ohmic contacts. Due to the required geometry, the sputter coater was initially used to apply gold contacts with the use of an aluminium mask. The coater uses plasma energy to deposit gold, and so the sample was exposed to high temperatures. As a result, the electrical properties of the samples were altered after contacts were deposited due to sample annealing. To prevent this annealing, indium contacts were subsequently used, applied using a soldering iron (Figure 23). The samples used were squared of 2.5×2.5 cm^2 and the triangular contacts had approximately 3 mm wide edges.

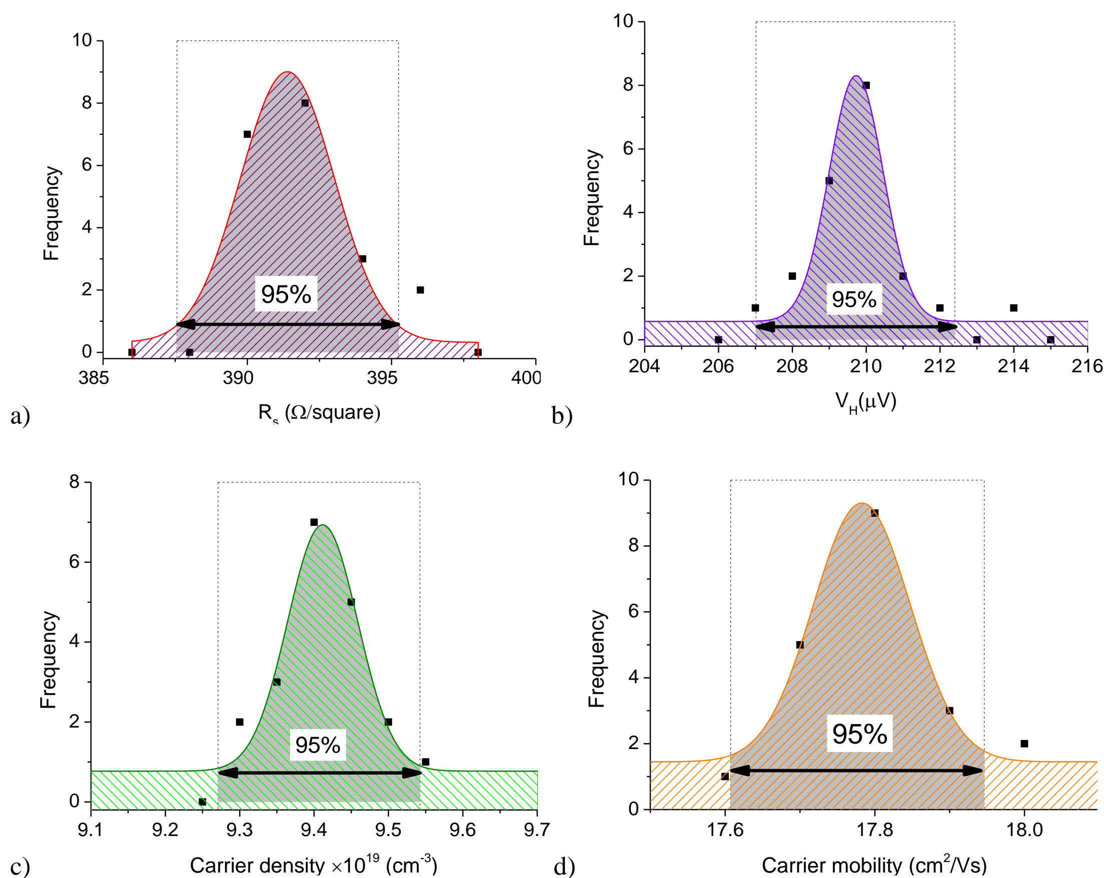

Figure 24: Standard deviation showing the 95% error margin for the Van der Pauw measurements of the a) sheet resistance, b) Hall voltage, c) carrier density and d) carrier mobility.

Propagation of error was estimated by using 20 measurements of the same un-doped sample. Those measurements were used to calculate the 95% experimentally acceptable margin for sheet resistance, Hall voltage, carrier density and mobility (Figure 24). The error margin for the sheet resistance was set at ±7.6 Ω/square, which showed that the 4PP was a more accurate technique for resistivity measurement. The margin of 95% for the Hall voltage was found at ±5 μV. Finally, for the carrier density it was found at $\pm 2.7\times 10^{18}$ cm^{-3}, and for the mobility at ±0.35 cm^2/Vs.

3.6. Photoluminescence

3.6.1. Background information

Photoluminescence (PL) provides information about the optical properties by examining the photons emission under radiation. The emitted photons are shown as peaks at a certain wavelength, revealing information about the defect states (λ >400 nm) and the band to band emission (for ZnO is λ<400 nm). Therefore, the optical gap can be measured by PL, typically shown as the highest energy peak. Tests by varying the experimental temperature and excitation intensity can also reveal the origin of the emissions by examining the emission intensity and energy as the conditions change.

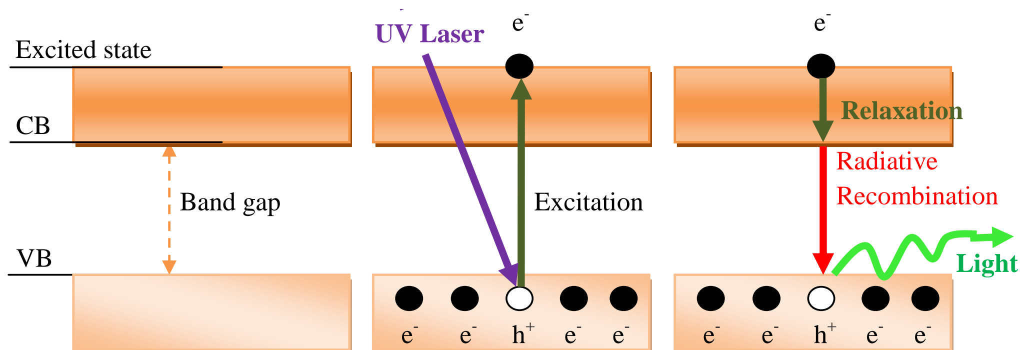

Figure 25: Schematic of the PL excitation and photon emission process.

PL involves the photoexcitation of semiconductors by irradiation with monochromatic light usually from a laser. This results in photon emission during carrier recombination with energy equivalent to the optical bandgap, as shown in the schematic in Figure 25. The process consists of photon absorption that excites

electrons from the valence band (VB) to the excited electronic state in the conduction band (CB) [266]. However, the excited states are unstable, and hence the electrons tend to 'relax' at the bottom of the CB. The excited electrons can radiativly recombine with holes in the VB, resulting in either non-radiation emission (heat) or radiative emission of photons with lower energy than the absorbed light. The higher emission energy represents the optical gap energy and any lower energy emissions show recombinations between defect states. The relaxation process occurs much faster (i.e. picoseconds) than the radiative recombination (i.e. nanosecond) [267], therefore the electrons typically recombine from the relaxation state under normal conditions. Note that hot electrons can be formed in conditions such as elevated measurement temperature, and recombine from the excitation state.

3.6.2. Measurement information

The PL measurements were carried out using a Horiba JY LabRam HR HR800 confocal Raman microscope fitted with a Kimmon IK series He-Cd UV laser (325 nm, 20 mW power), schematically shown in Figure 26. Two different microscope objectives were used during this study, the OFR MicroSpot Focusing Objective LMU-40×-NUV (f_2 =5 mm) used for most of the measurements, and the ThorLabs microscope objective LMU-15×-NUV (f_2=13 mm) used for low temperature measurements. The detection of the full spectrum is carried out using a CCD detector (i.e. a Si based multichannel array detector [269]), ranging from UV to 1.5 μm [267]. In order to avoid seeing laser lines in the sample emission energies, an edge filter rather than a notch filter is used, available for UV lasers. The confocal

hole can be set from 100 nm to 1000 nm, and its adjustment may change the emission intensity and the detection of the reflected photon arrays, as shown in Figure 27. Measurements at low temperature were carried out using a Linkam TSM 94 temperature controlled stage, providing control over high and low temperatures between 600°C and -196°C. The nitrogen filled chamber used for those measurements restricted the sample size, thus films on 1 cm^2 Si substrates were used.

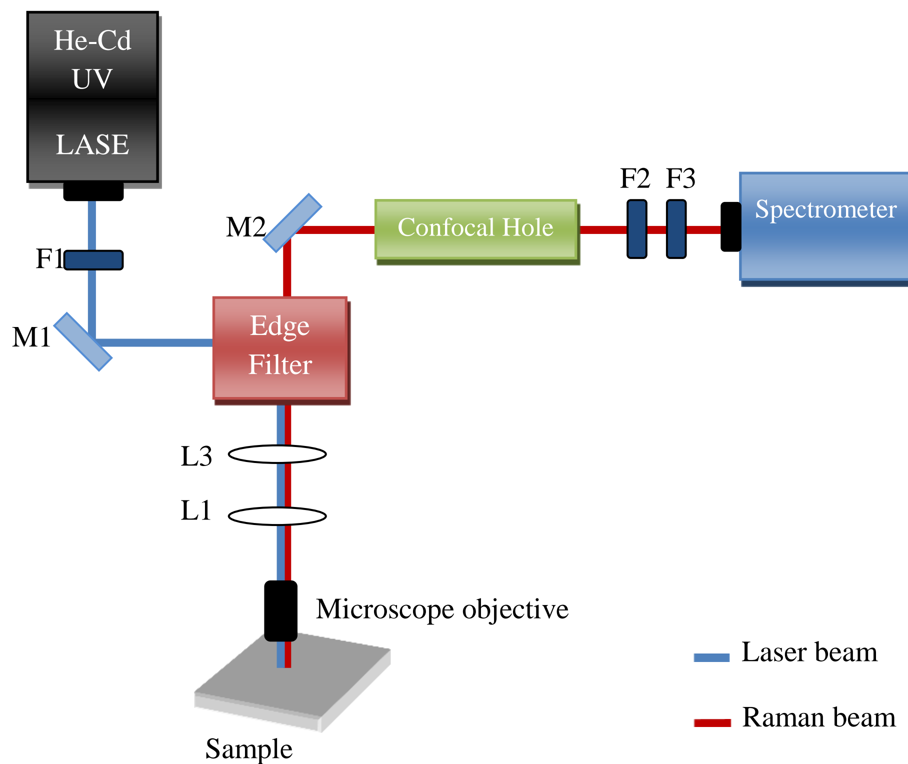

Figure 26: Schematic of the PL experimental setup [267]-[268].

The samples in those tests were on either glass or on silicon in order to examine any emission changes caused by the substrates. The PL tests were carried out for un-doped ZnO films first in order to separate the effects caused by doping. Those included growth temperature effects, excitation intensity effects, and low

temperature effects. The same tests were subsequently carried out for the Zr-doped ZnO films (thin and thicker films). The penetration depth for direct bandgap semiconductors is in the order of 1μm and diffusion occurs in the range 1-10 μm [270], thus in the current study the photons penetrate through all the films with thickness up to 250 nm.

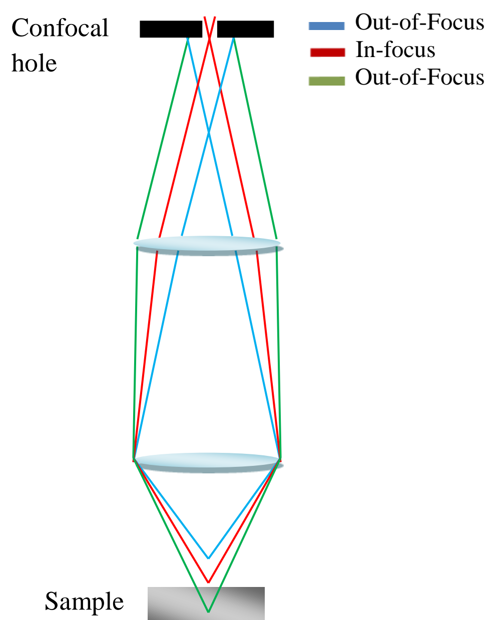

Figure 27: Schematic of the reflected photon arrays of focus and out-of-focus sample placement as they try to pass through a small confocal hole.

The user has to adjust the stage position in μm accuracy (XYZ motorised stage) using a camera connected to the LabSpec software, in order to focus on the sample's surface. By using the software it is possible of adjusting the main parameters such as the confocal hole (100-1000 μm), the filter controlling the incident light intensity from 0.01-100%, and finally the acquisition parameters to set slower measurements. The collected PL signal was automatically plotted between 330 nm and 600 nm wavelength range for the current films. Calibration was conducted prior of each set

of measurements using the zero-order diffraction of a white light source to set the zero of the spectrometer, and using the 520 cm^{-1} Raman emission of a silicon calibration sample to calibrate the linear coefficient. The precision has to be better than two pixels (i.e. one pixel is 0.14 meV) for an accurate calibration [267], thus the uncertainty within that range is estimated at ~ ±0.3 meV.

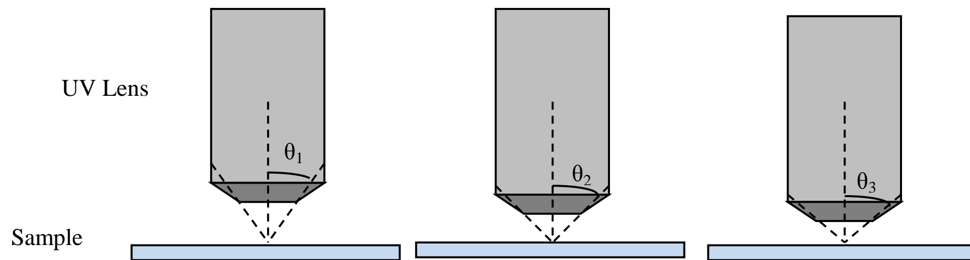

Figure 28: Schematic of the angle apertures for different sample positioning in regard to the lens.

The resolution and depth of focus for each lens depends on the numerical aperture (NA), which is proportional to the angle created between the sample and the lens (i.e. angular aperture). Therefore, if the lens is placed closer to the sample the angle would increase, leading to an increase in the NA. This is shown by Equation 18 [271], where n is the refraction rate of the medium (i.e. for air is 1), and θ is the angle created by the refractive light on the sample and the centre of the objective lens.

Equation 18

$$NA = n \cdot \sin\theta$$

Therefore, practically NA could change as the stage positioning is altered. For example, when the motorised stage is closer to the lens the numerical aperture

increases as illustrated in Figure 28. From the diagram $\theta_1 < \theta_2 < \theta_3$, hence it results to $NA_1 < NA_2 < NA_3$. This will have a great effect on the focus to the film surface and could alter the emission properties (shift in intensity and position). For that reason, focus calibration to the surface was done at the beginning of each scan on every sample.

The resolution (R) defined by the smaller distance between two separately scanned points, can be also calculated using the NA as given by Equation 19 [269].

Equation 19

$$R = \frac{0.61\lambda}{NA}$$

This relationship shows that at shorter laser wavelength and higher NA, the resolution improves. Based on the manufacturers' specifications for the numerical aperture of the lenses, the lower resolution will be for the LMU-40×-NUV lens at 396.5 nm (NA=0.5 unit-less), in comparison to the LMU-15×-NUV lens with a resolution 619.5 nm (NA=0.32 unit-less).

The excitation intensity of the He-Cd UV laser using the LUM-40×-NUV objective can be calculated by the power of the laser and the spot radius of the focused beam after it exits the objective. The power (P) is 20 mW and the focused spot radius (α) can be calculated using Equation 20, where λ is the laser wavelength (=325 nm), f is the focal length of the lens, and r is the lens entrance aperture radius

Equation 20

$$a = \frac{\lambda f}{\pi r}$$

For the LMU-40×-NUV lens the entrance aperture has a diameter of d=5 mm and the LMU-15X-NUV lens has d=8.5 mm. Therefore, α is equal to 0.21 μm and 0.32 μm respectively. The excitation intensity (I) radiated at the focused spot area is given by Equation 21.

Equation 21

$$I = \frac{P}{\pi a^2}$$

The excitation intensity is equal to 14.87 MW/cm^2 for the LMU-40×-NUV and 6.36 MW/cm^2 for the LMU-15×-NUV. The excitation intensity could be reduced by applying filters blocking the full beam power. The ones used to examine the intensity effect on the PL emission were at 10% (1.49 MW/cm^2), 25% (3.72 MW/cm^2), 50% (7.44 MW/cm^2) and full intensity at 100% filter. For both lenses the damage intensity is at 50 MW/cm^2 according to the manufacturers.

3.7. UV-Vis Spectroscopy

3.7.1. Background information

UV-Vis spectrophotometers measure the light absorbed by samples as a function of wavelength. The spectral range for those measurements includes UV, visible and near infrared light. When the photon energy is greater than the optical gap, the photons are absorbed, while at lower energies they are transmitted.

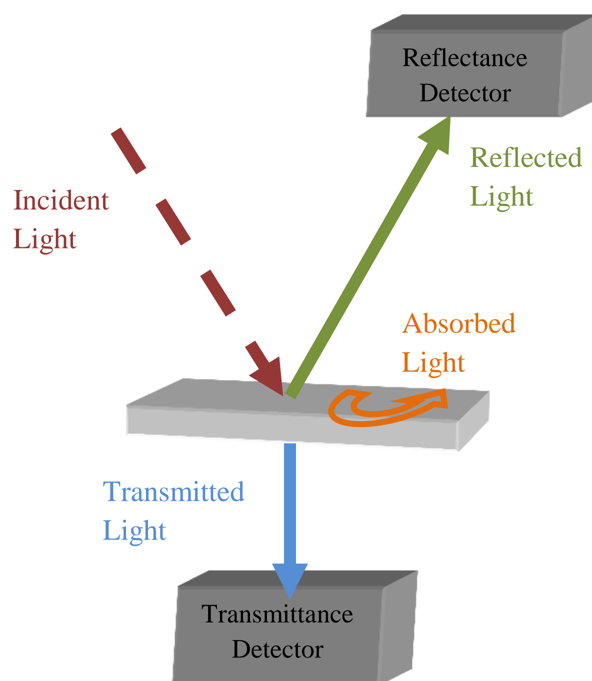

Figure 29: Schematic of the light directions reaching the sample's surface during a spectrophotometer measurement.

Three different graphs can be obtained from a single scan, consisting of absorbance, reflectance and transmittance. All three are directly related as shown in Figure 29. The transmittance (T_r) is determined by the ratio of light passing through the sample (I) over the incident light intensity (I_0), as shown in Equation 22 [272].

Equation 22

$$T_r = \frac{I}{I_0}$$

The reflectance is then directly related to transmittance as shown in Equation 23. The relation shows that as transmittance increases the reflectance decreases.

Equation 23

$$T_r = (1 - R)^2$$

The absorbance spectrum corresponds to the light absorbed by the sample. The relation of the absorbance (A) to transmittance is given by Equation 24 [273].

Equation 24

$$A = -\log T_r = -\log \frac{I}{I_0}$$

The reflectance is also related to the refractive index (n) of the film, as shown in Equation 25. The reflectance is expected to be higher in a film with high refractive index, which in turn reduces the transparency.

Equation 25

$$R = \frac{(n-1)^2}{(n+1)^2}$$

The spectrophotometer scans provide raw data of transmittance percentage over a range of wavelength, which can be used to plot a graph such as the one showing in Figure 30. The graph shows two of the 4.8 at.% doped samples with different thicknesses in order to illustrate the information gained from this technique. Firstly, the average transmittance for each region is taken by the integrated area within the spectrum regions of the visible light at 380-780 nm [274], the near infrared at 780-1400 nm, and the short wave IR range at 1400-2000 nm. The values are then normalised with respect to uncoated glass substrate transparency (i.e. 91% at visible and 90% at near IR). For n-type TCOs high transparency in the visible region [144] (shown in the red covered area in Figure 30) is required.

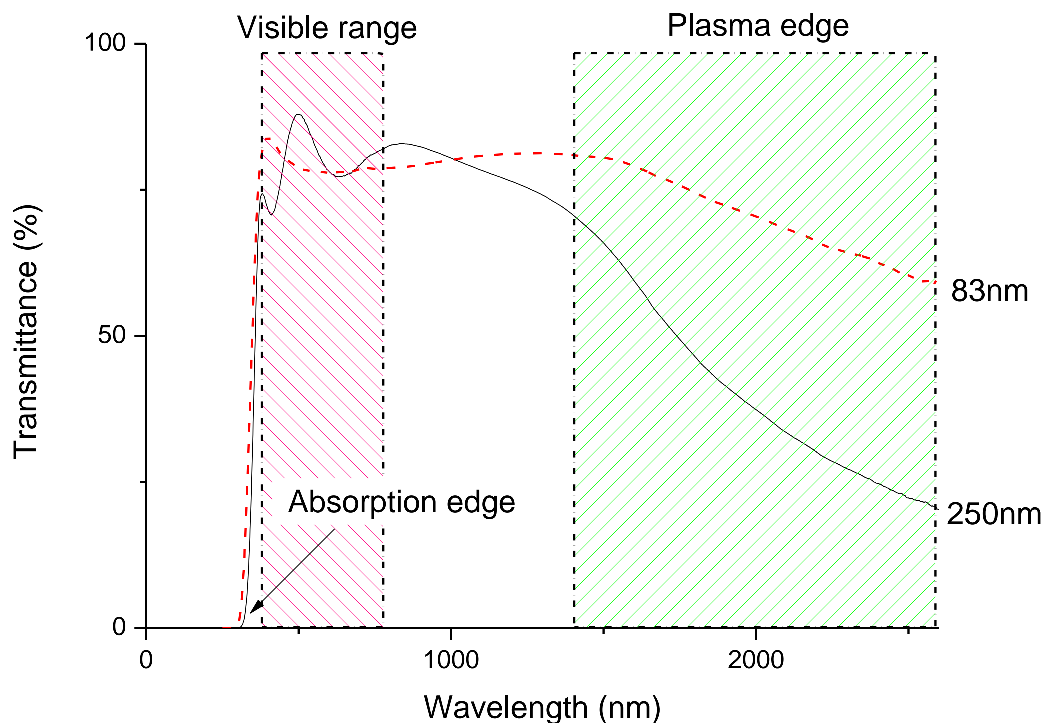

Figure 30: Transmittance spectra of 83 nm and 250 nm thick films with 4.8 at.% doping, used for explaining the main four data points obtained from a transmittance graph.

The oscillations in the short wavelength region which are denser in thicker films correspond to interference of the reflected light between the film-surface and film-substrate interface. Hence, thicker films have more internal reflections and higher interference causing increased frequency oscillations. The increase of oscillations in the visible range will result in higher transmittance area and therefore to increase of the visible transmittance, which is more desirable for n-type TCOs.

The final two points are the absorption edge and plasma edge indicating the start and the end of the transmittance range respectively. The absorption edge shows the wavelength at which the sample is starting to transmit light, so it is related to the optical gap. For TCOs the absorption edge needs to be in the UV region in order to enable full transmission from the UV to near IR wavelength [39], so the optical gap

should be higher than 3.1 eV (< 400 nm). Numerical optical gap values are obtained by applying the absorption range in the Tauc relation (see chapter 6).

The plasma edge on the other hand, relates to the carrier density of the film as the line slope is proportional to the plasma frequency which in turn is proportional to the carrier concentration based on the Drude model (i.e. $n_e \propto \omega_p^2$). For TCOs the plasma edge has to be at the short wave IR region (>1400 nm as shown in the green area in Figure 30) in order to secure high transmittance in visible and near IR spectra. This is always the main issue for degenerate films since the plasma edge is shifting to shorter wavelength as the carrier density increases.

The Drude model was developed by Paul Drude at the beginning of the 20th century and is based on some assumptions. Those include the assumption that electrons do not interact with each other, that electrons scattered in time τ, and that electrons mobility is based on the free electron equation [276]. However, the changes in the effective mass as a result of the high carrier concentration may cause differences between the model and Hall effect data if a fixed value is used. For the Drude model calculations the conductivity effective mass (m^*) is used as a constant in order to estimate the carrier concentration (n_e) using vacuum permittivity (ε_0) and electron charge (e) in Equation 26 [276].

Equation 26

$$n_e = \frac{\omega_p^2 \, m^* \, \varepsilon_0}{e^2}$$

The carrier mobility was estimated using the Drude model through the damping factor. The damping factor was used to specify the relaxation time (τ) corresponding to the time between the carrier scattering elastic collisions, which is linearly

proportional to the mobility of the film (Equation 27). As a result, the resistivity can be calculated at this stage using Equation 28.

Equation 27

$$\mu = \frac{e\,\tau}{m^{*}}$$

Equation 28

$$\rho = \frac{1}{\eta_{e}\,\mu\,e}$$

3.7.2. Measurement information

In this thesis, the UV-Vis transmission was carried out using a Shimadzu Solid Spec-3700DUV dual beam spectrophotometer, with a resolution of 0.1 nm [275]. The measurements had 4.7 nm steps and a wavelength range of 250-2600 nm. The transmittance and reflectance raw data were analysed using SCOUT 3.0 spectrum simulation software which enables line fitting to the raw data and provided data such as the absorbance spectra (absorption coefficient), plasma frequency (ω_p), and the damping factor. From those data, the carrier concentration, carrier mobility and the film's resistivity could be estimated with the use of the Drude model. The effective mass of ZnO used as fixed at this point was $0.4m_0$*.

From the manufacturer details, the wavelength error margin for UV/Visible spectrum is ±0.2 nm, and for near IR spectrum is ±0.8 nm [275]. Therefore, by applying those shifts in the wavelength, the bandgap measured by the Tauc relation was calculated

to be shifted by ±0.04 nm, thus it is set as the error margin for those calculations. The stray light specified by the manufacturer is less than 0.00008% for UV and less than 0.005% at the end of the measured range [275]. Therefore, the error margin for the transmittance percentage is very low and can be neglected. Nevertheless, an error margin of ±0.3% was accounted after measuring the visible transmission by using different spectrum ranges (e.g. 400-800 nm, 390-700 nm, etc) found in published studies.

3.8. X-ray Diffraction

3.8.1. Background information

X-ray Diffraction (XRD) is widely used as a reliable and quick scan technique (i.e. no special sample preparation), used to provide information about the microstructure of samples. With the use of X-rays the lattice planes diffract the rays in a way that shows if the planes are aligned and comply with the Bragg's law. Bragg's law states that diffracted rays from parallel planes are in phase and hence amplify the detected intensity [277], while if the planes are aligned randomly the diffracted intensity is cancelled out. The Bragg's law occurs at a specific diffracted angle (2θ), which is unique for a set of crystalline planes direction. Hence, the crystalline phase can be identified using reference card files. Additionally, the dominant peak can reveal the preferred orientation of the grains. Further analysis reveals the crystallite size and the d-spacing between the planes indicating if there is any strain in the lattice.

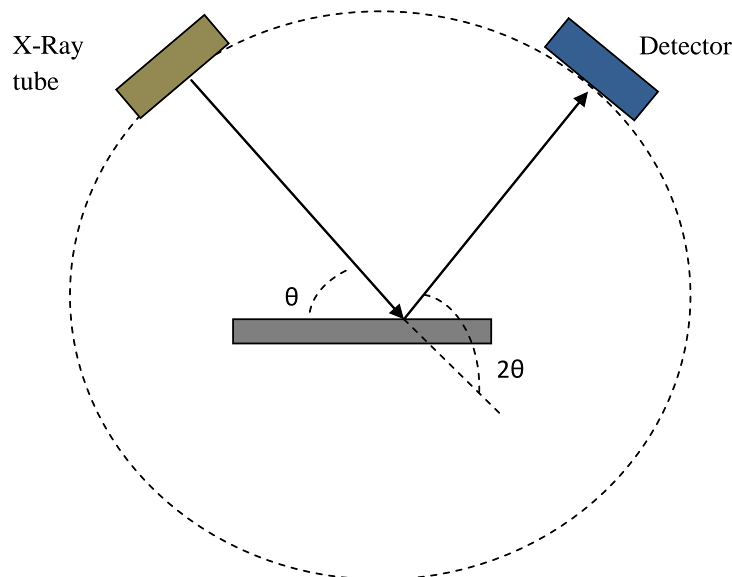

Figure 31: Bragg-Brentano geometry.

The X-rays are generated when electrons are emitted by a heated cathode, and then accelerated by a large electric field between the cathode and the anode of a vacuum tube, and finally fall at the target material at the anode to knock electrons in K and L shells releasing radiation. The most commonly used material is copper, in which the accelerated electrons knock out K-shell electrons resulting in X-rays from Kα and Kβ radiation. In order to have monochromatic X-rays, the Kβ and all other radiation is suppressed by an added filter, thus the generated X-rays create diffraction of wavelength 1.54 Å. The wavelength must be a few Å so that it is the same order of magnitude as the interatomic spacing of atoms in the lattice.

The monochromatic diffraction allows the use of the Bragg-Brentano geometry (Figure 31) so that with fixed X-rays wavelength the incident angle can be varied. Based on this geometry, the X-ray tube position is fixed, and the sample's holder is

driven by the same mechanical drive system as the detector (the detector moves 2° for every 1° of the sample). The rotation follows a circular axis resulting in a variable incident angle 'θ' (diffracted angle is 2θ). The condition for this geometry is that the rotation path must be always fixed (measured curvature), and the sample's surface must always align to the holder and be flat.

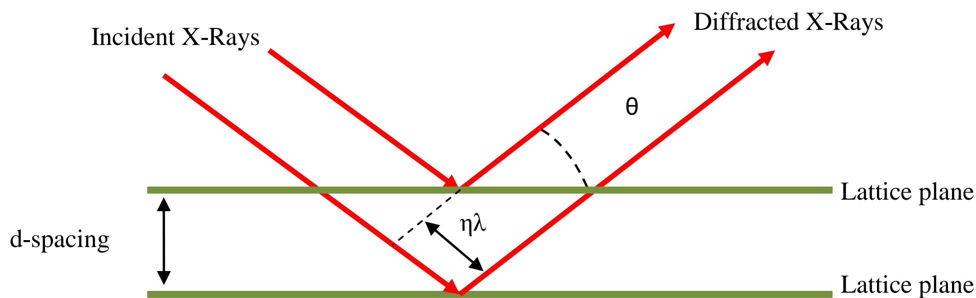

Figure 32: Bragg's law.

The distance between the planes (d-spacing) in relation to the X-rays wavelength (λ) can be calculated by the Bragg's law (Figure 32) given in Equation 29 [278].

Equation 29

$$n\lambda = 2d \sin\theta$$

Information about the crystal structure and unit cell dimensions can be obtained from the diffraction pattern. The lattice constants for a-axis and c-axis can be calculated using Equation 30 and Equation 31 respectively, for hexagonal structures such as the ZnO wurtzite.

Equation 30

$$a = \frac{\lambda}{\sqrt{3}\sin\theta}\sqrt{h^2 + hk + k^2}$$

Equation 31

$$c = \frac{\lambda}{2\sin\theta} l$$

Based on those, the d spacing for each plane can be calculated using Equation 32-35 for (0002), $(10\bar{1}0)$, $(10\bar{1}1)$ and $(11\bar{2}0)$ planes.

Equation 32 &Equation 33 &Equation 34 & Equation 35

$$d_{0002} = \frac{c}{2} \qquad d_{10\bar{1}0} = \frac{\sqrt{3}}{2} a \qquad d_{10\bar{1}1} = \frac{1}{\sqrt{\frac{4}{3}a^2 + \frac{1}{c^2}}} \qquad d_{11\bar{2}0} = \frac{a}{2}$$

The strain value can be estimated by calculating the relation between the idealised d-spacing value (d) and the difference between the d value and the recorded for d-spacing values (Δd), using Equation 36.

Equation 36

$$\varepsilon_0 = \frac{\Delta d}{d}$$

The full width half maximum (FWHM) of the peak (B), the crystal size (L) and the constant of proportionality (i.e. K=0.94) can be used to calculate the grain size using the Scherrer equation (Equation 37) [278]. The assumption for this relationship is that the crystals have uniform size and shape, with grains smaller than 200 nm. The instrumental peak broadening is larger than the broadening due to grain size for crystallites smaller than 20 nm, hence, the size cannot be accurately calculated using

this method for grains smaller than 20 nm. According to the data obtained by AFM and TEM on the current films, the grains have needle-like shape crystallites and in very thin films (<100 nm) the grains are smaller than 20 nm in width. Thus the method was not used in this study as not all films can be accurately compared, instead AFM was used.

Equation 37

$$B_{size} = \frac{K\lambda}{L\cos\theta}$$

The peaks' intensity consists of parameters affecting the crystal characteristics of the sample. For example, the heavier elements (i.e. high atomic number) will result in high structure factor (F_{hkl}) that could enhance the diffracted intensity. Other parameters are the multiplicity factor (M_{hkl}) based on the number of similar planes that could contribute to the reflection (e.g. for (0002) it is 2 and for $(10\bar{1}0)$ it is 6), the Lorenz-Polarization factor based on the geometry of the crystal and its correction value for the un-polarised incident beam. Finally the temperature factor (e^{-2M}) that takes into account any unit cell expansion due to thermal vibration. The relation for reflection (hkl) with intensity ($I_{(hkl)a}$), is given by Equation 38 [277] with the Lorenz-Polarization factor given in the parenthesis and the temperature factor's M exponential given in Equation 39.

Equation 38

$$I_{(hkl)\alpha} = I_0 e^{-\mu d} M_{(hkl)} \left|F_{(hkl)\alpha}\right|^2 \left(\frac{1+\cos^2 2\theta}{\sin^2\theta\cos\theta}\right)_{hkl} e^{-2M}$$

Equation 39

$$M = B\left(\frac{\sin\theta}{\lambda}\right)^2$$

where the factor B is the isotropic temperature factor and is usually neglected [277]. Nevertheless, the resulting value for the total temperature factor in our data is close to 1 (i.e. 1.03 with ±0.0001 uncertainty due to angle shifts), which indicates negligible effect due to thermal expansion of the unit cell.

The structure factor expresses the sum of atoms' interferences in the unit cell (Equation 40 [277]). This depends on the atoms positions in the crystal along with their individual atomic scattering factor (*f*). Therefore, in some cases the atoms are placed at out of phase planes and cause extinction. In other words, those reflections are forbidden by the structure factor and they are not visible in XRD patterns [279].

Equation 40

$$F_{hkl} = \sum_{j=1}^{N} f_j \cos\{2\pi(hx + ky + lz)\} + i\sum_{j=1}^{N} f_j \sin\{2\pi(hx + ky + lz)\}$$

The atomic scattering factor represents the amount of coherent and incoherent atomic electron scattering (photoabsorption) of a material when exposed to X-rays [280]-[281]. Those values can be found in the International Tables of Crystallinity [280] for each element at different scattering angles. The denser atoms have higher scattering factor (i.e. Zr). Thus, if the structure factor calculation indicates that Zr atoms are located at an in phase plane, then the structure factor would be altered as doping increases, and may cause differences in the XRD peak intensities (see analysis in chapter 4).

3.8.2. Measurement information

XRD was carried out using a Rigaku Miniflex Diffractometer in the Bragg-Brentano geometry with Cu Kα X-ray source (1.54 Å, 40 kV, 50 mA). The samples were placed in the metallic holders and were carefully aligned to the horizontal top edge of the holder. The scan parameters such as the angle range and the speed scan were set using the “Standard Measurement” software. Based on the equipment arrangement, all scans must start higher than 5° as the X-ray tube is fixed at 5° higher than the sample holder. Hence, the range of the scan was always set between 20°-60°, covering all the primary planes of ZnO that start from 31° (above 60° the secondary diffraction planes appeared, such as the $(20\bar{2}0)$ plane at 67°), and avoids a very strong feature of the (400) plane of the Si substrates at around 70°. The speed for each scan was set at one degree per minute, which is a quick scan as the films showed high signals in relation to noise. The background noise was then removed from the patterns obtained using the “Peak Search” software, and then for further analysis the Gaussian function was used for peak fitting using OriginPro8.6. From the analysis the d-spacing of each plane along with the strain in the lattice were obtained for films on silicon and glass substrates.

The experimental patterns were compared to reference card files from the chemical database service (CDS) in order to specify the phase of the sample and identify the corresponding plane for each peak. An example of an experimental pattern is shown in Figure 33 for ZnO randomly oriented powder, in addition to the Si wafer pattern. The Si pattern was later on used in XRD patterns of the films (chapter 4) to exclude the peaks originating from the substrate. However, the powder was not used as a reference due to possible errors in peak position by its alignment to the holder (i.e.

placed below the top edge of the holder). Note that the intensity ratio was not affected by that factor, and so it was used for peak intensity normalisation. The normalisation factors are summarised in Table 4.

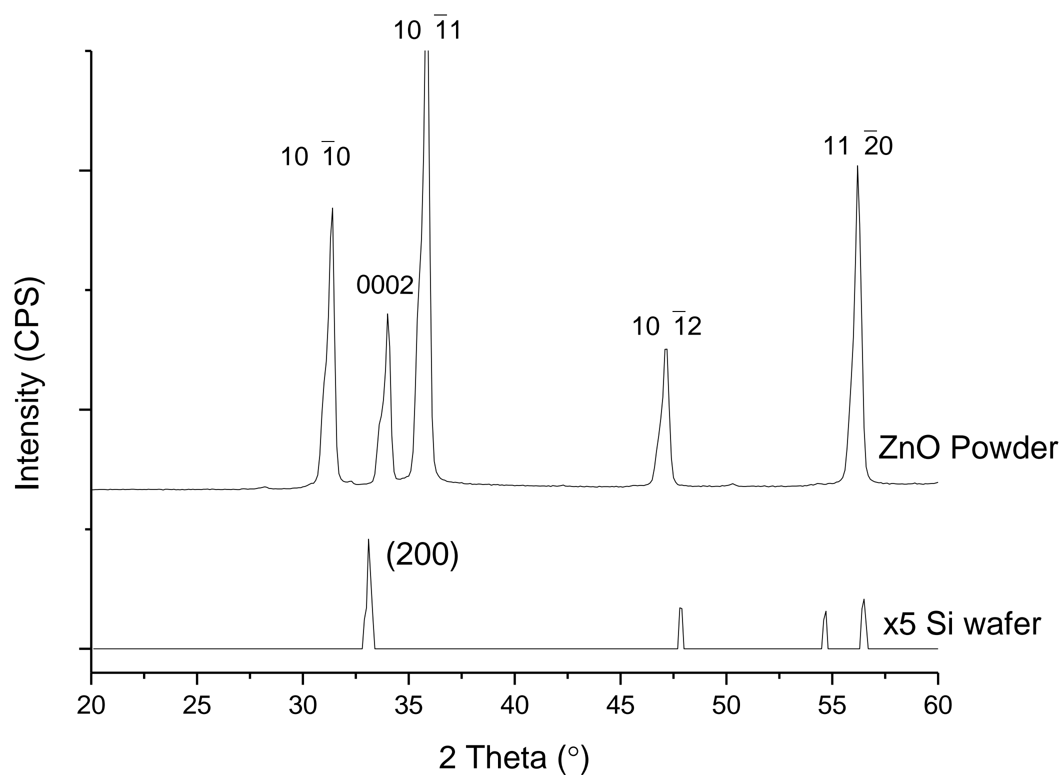

Figure 33: XRD pattern of ZnO randomly oriented powder and Si substrate (the intensity was increased by 5 times for better visual comparison).

The Si (100) wafers used as substrates for the ZnO films, caused the appearance of a peak at 33° corresponding to the (200) plane. As the peak did not appear in every scan, several scans were undertaken and concluded that the peak appeared only when the Si sample was in the middle of the holder and precisely horizontally aligned to the holder. As a result, the patterns with the Si peak were preferred for the analysis since it proved accuracy in sample placement.

Table 4: Normalisation factors based on the measured intensity of ZnO randomly oriented powder.

Peak	Normalisation factors
$(10\bar{1}0)$	0.55
(0002)	0.32
$(10\bar{1}1)$	1.00
$(10\bar{1}2)$	0.29
$(11\bar{2}0)$	0.65

The errors based on the Rigaku manual include the sample displacement that could result in 0.01° peak shift for every 60 μm higher or lower to the holder alignment. Other factors may also affect the accuracy of the data, including very large grains, axial diverge and preferred orientation. The latter one affects the intensity of the peaks by favouring the one in which the grains are aligned, suppressing all the other deflections.

Table 5: Error margins set for the three main peaks.

Plane	Peak shift (°)	Lattice spacing (Å)	Strain (%)
$(10\bar{1}0)$	±0.02	±0.0032	±0.07
(0002)	±0.02	±0.0015	±0.06
$(11\bar{2}0)$	±0.20	±0.0032	±0.13

Based on multiple measurements on the same sample (Zr-doped one), the error margins by peak shifts (repeatability error) were set for each one of the main peaks. Thus, the margins corresponding to peak shift, lattice spacing and strain are shown in Table 5.

3.9. X-ray Photoelectron Spectroscopy

Einstein's equation for the photoelectric effect was the initial theorem which was subsequently used by other researchers to develop the electron spectroscopy. Kai Siegbahn and his team in the late 1950s developed a high resolution beta-ray spectrometer, where each peak corresponded to a specific electron shell and chemical bonding effects could be derived [282]-[283]. The Electron Spectroscopy for Chemical Analysis subsequently developed by the same team [284], and along with the vacuum chambers advanced at that time it was developed into the X-ray photoelectron spectroscopy (XPS) device as known today.

XPS is used in semiconductor research in order to study chemical composition and bonding states. During the process, the sample's surface is irradiated with photons from a soft X-ray source or a synchrotron [285]. Poorly conductive materials readily become charged during XPS, resulting in meaningless results. An ion gun can be used to resolve this issue by neutralising the surface charge.

The equipment used is a FISONS VG Escalab MKII Scientific XPS, with Al Kα radiation as the X-ray source and photon energy of 1486.6 eV. For each sample a full survey scan was recorded over the binding energy (BE) range from 0 to 1286 eV, and then four extra scans were completed over the main core-level elements for Zn, O, Zr and C (the carbon is used for referencing). The step size was 0.1 eV, and the constant pass energy was 50 eV for the full scan and 20 eV for the individual elements scans.

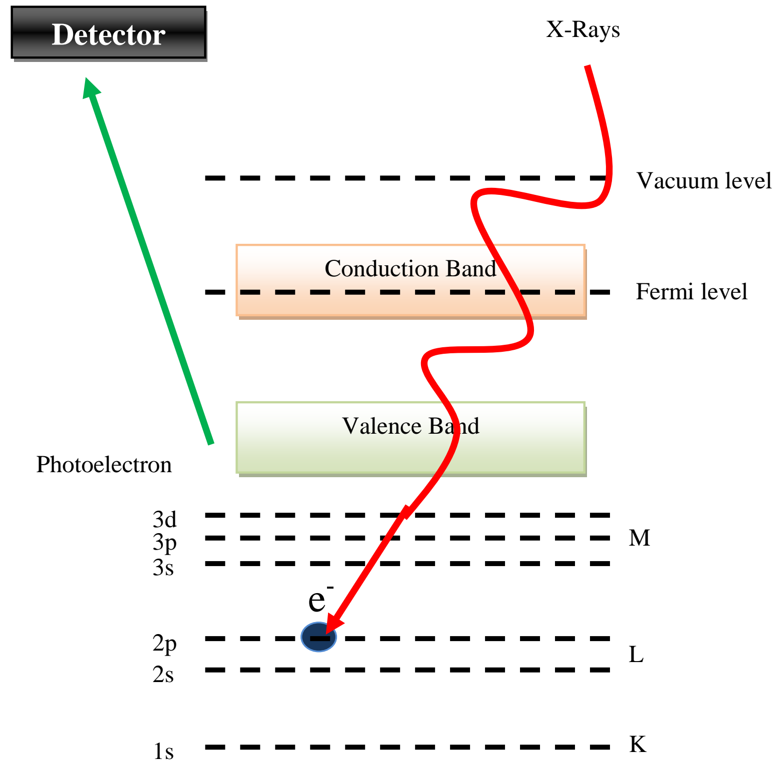

Figure 34: Schematic of the XPS radiation and photoelectron excitation process.

During this process (Figure 34), the photon energy (hv) from the incident X-rays is absorbed by electrons from different inner shells and ionized, resulting in ejecting photoelectrons [286]. All measurements must be carried out in ultra-high vacuum (i.e. 10^{-7} Pa) to prevent scattering by air molecules. The X-rays penetrate up to 1µm depth, but the electrons that are ejected from the sample are only coming from atoms closer to the surface (up to 10 nm) because electrons from deeper can't escape as they are inelastic scattered.

By assuming no loses in the process, the X-rays' photon energy (hv) is equal to the sum of the BE, the work function (Φ) and the kinetic energy (KE) of the ejected photoelectron measured by the detector (Equation 41). The binding energy is the energy needed to ionise and emit the electron from the shell up to the Fermi level.

The BE is unique for each element, hence it is used to specify the composition and the atoms chemical bonding. The sample's work function, which is the energy up to the vacuum level, is aligned to the spectrometer work function (Φ_{spec}) and hence the latter energy is used. The BE can then be estimated by measuring the kinetic energy of the ejected electrons. The data obtained are in the form of peaks corresponding to BE of individual atoms. The peaks originating from each core levels may exhibit double peaks due to spin orbit splitting.

Equation 41

$$KE = hv - BE - \Phi_{spec}$$

Photoelectrons in the solid may interact with other electrons, resulting in an electronic transition which causes energy loses to the photoelectrons [286]. The loss is known as inelastic scattering and it is shown as background noise. Inelastic scattering is one of the main issues of XPS as it limits the extraction information to only the top surface layer. In more detail, the photons from Al Kα have energy enough to insure accurate results only up to 2 nm deep in the film. However, the minimum path estimated without inelastic scattering is referred by the term inelastic mean free path (IMFP) estimated separately for each element [285]. The calculation of IMFP can be done theoretically with the use of Equation 42 [287], and experimentally with the use of elastic peak electron spectroscopy (EPES). The elastic electron backscattering ratio of intensities is used to calculate IMFP experimentally. The surface roughness has no effect on the IMFP [288].

Equation 42

$$\lambda_m = \frac{538}{KE^2} + 0.41(aKE)^{\frac{1}{2}}$$

The IMFP (Equation 42) is therefore related to the kinetic energy (KE) of a specific element. IMFP is converted into nm when is multiplied by the monolayer thickness (α_m). To calculate the monolayer thickness in nm Equation 43 [287] is used.

Equation 43

$$a_m{}^3 = \frac{A_w}{\rho_d n N_A} \cdot 10^{24}$$

where A_w is the atomic molecular weight, n is the number of atoms in the molecule, N_A is Avogadro's number, and ρ_d is the bulk density in kg/m^3. For the current ZnO films the value α is estimated as 0.23 nm.

The IMFP calculation is based on the assumption that the electrons signal travel in straight lines and the sample is atomically flat [287],[289]. This leads to a different approach, where the attenuation length (AL) is used instead of the IMFP, and it is relative to the atomic number (Z) of the elements by Equation 44 [289].

Equation 44

$$\lambda_{AL} = 0.316\alpha^{3/2} \left\{ \frac{KE}{Z^{0.45}[\ln\left(\frac{KE}{27}\right) + 3]} + 4 \right\}$$

IMFP or AL is used in the quantitative analysis, which can be completed by two methods. The first one is the comparison of each element's intensity by including standard sensitivity factors established by bulk materials. However, the method is not considered as the most accurate, due to the difference in contamination between the samples and the reference [290]. The second method is the comparison of intensities by using first principles, in which the photoelectron current is proportional to elements' concentration [290]. The first principle approach involved

the use of independent parameters for each element, including IMFP (or AL) and the subshell photoionisation cross-sections established by Scofield (i.e. Scofield factor) [291]. The atomic percentage could be then estimated by the peaks intensity of each element (I), the IMFP (λ_n), and by the Scofield factor (S) using Equation 45.

Equation 45

$$at.\% = \frac{\left(\frac{I_i}{S_i\lambda_{ni}}\right)}{\left(\frac{I_i}{S_i\lambda_{ni}}\right) + \left(\frac{I_j}{S_j\lambda_{nj}}\right) + \left(\frac{I_k}{S_k\lambda_{nk}}\right)}$$

The limitation of this approach is that it assumes that the surface is uniform and that the scan is only from the top monolayer [290]. Therefore, the roughness of the surface layer may affect the quantitative results. This was first introduced by Fadley et al. [292], who examined the correlation of the photoelectron angular distribution and surface roughness, and found that the surface intensity is reduced by surface roughness, most probably by photoelectron scattering. Hence, this method had limited accuracy for rough surfaces, since photoelectron scattering increases when protrusion areas recapture the photoelectrons injected [288]. The roughness effect at different angle scans was the subject of several studies, where mainly it was specified that at low angles the surface topography affects the detected signal [293]. Therefore, it was suggested that X-ray beams remain perpendicular to the faces of the rough surface, so that the photoelectrons emitted in a relative angle to the X-rays will be less disrupted, providing more accurate results [294].

The photoelectron recapture effect may affect the XPS measurements in this study. Hence, although the dopant may be effectively deposited around the ZnO grains, the XPS may not be able to identify it due to the protrusion areas created by the grains

size and shape. In order to explain this, Figure 35 schematically illustrate how the incident X-rays reaches the surface and how the photoelectrons path is affected by the surface morphology. The image shows that the film with large grains and low surface roughness is causing less obstructing to the photoelectron path compared to the mixture of small and large grains. As the grains became narrower, the restricted photoelectron path is again affected, and thus it is possible to see lower XPS peak intensities. As a result, the morphology differences in the current data do not allow obtaining accurate composition of the films with XPS due to the photoelectron scattering effects.

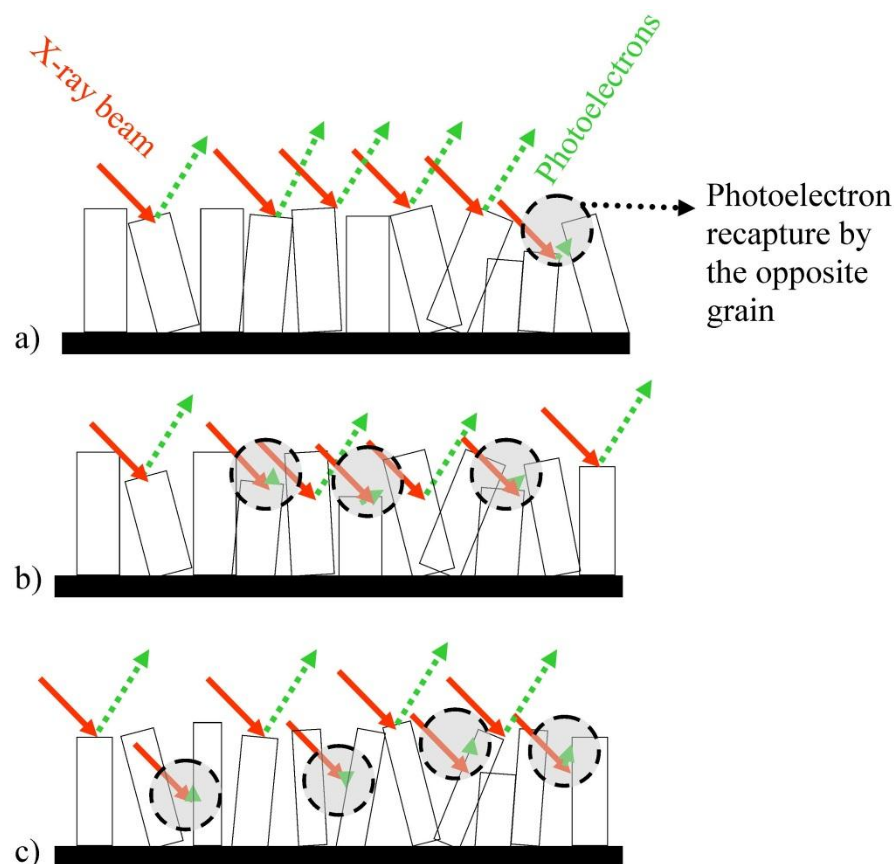

Figure 35: Schematic of the photoelectron scattering effects for a) low roughness surface, b) high roughness surface, and c) for films with narrow grains. The red arrows indicate the incident X-rays and the green arrows the excited photoelectrons, which some of them are absorbed (grey circle) by the grains located in the path.

3.10. Transmission Electron Microscope

Transmission electron microscope (TEM) is a technique that uses an electron beam to create an image of the target, rather than light that is used in the optical microscopes. As a result, the images can achieve a much higher magnification and resolution due to the low wavelength of the electron beam (i.e. in 10^{-3} nm). The images obtained by TEM can achieve near atomic resolution and hence enable observation on crystal planes. TEM is widely used in material science to study crystalline microstructures (e.g. identify lattice patterns or find lattice defects such as stacking faults). It can also provide elemental analysis using energy dispersive spectrometry (EDS). The main limitation for TEM is that it requires very thin films (<100 nm) as the images are obtained by transmitting the electron beam through the sample, which is not possible with thicker samples. There are some fundamental differences between TEMs and light microscopes. Firstly, the electron beam path must be in vacuum to avoid electrons scattering. Additionally, the lenses used are always electromagnetic due to the inability of electrons passing through common glass objective lenses [295]. Hence, the formation of TEM images is the result of focusing the incident electron beams by using those EM-lenses.

A graphical example is shown in Figure 36, illustrating the three main planes in TEM including the image plane, focal plane of objective lens and specimen plane [296]. As shown by the arrows direction, the incident beam is transmitted through the specimen plane, and then the transmitted and diffracted beams are focused to the back focal plane with the use of magnetic objective lenses. The beams in phase form bright spots and the out-of-phase ones cancel each other. The screening of the

diffraction area is presented as reciprocal lattice points for the diffracted orientations [297]. Those are diffraction dots and for polycrystalline samples they form diffraction rings. This results in the formation of an electron diffraction pattern. A mathematical algorithm known as the fast Fourier transform (FFT) is used to generate the diffraction pattern from a real space image of the lattice. An FFT consists of bright dots representing planes, in an arrangement based on the crystal structure and orientation. The image is obtained after changing from the diffraction mode to the image mode by using the intermediate lens [298]. The change is carried out when the focus of the intermediate lens changes from the back focus plane of the objective lens to the image plane of the objective lens.

The use of FFT images is an accurate method of measuring the lattice spacing by taking the distance between the dots (planes). The FFT patterns are well defined for each crystal direction, and so any lattice distortions can be identified by comparing the measured values to literature. Another method to measure the lattice spacing is the use of an intensity profile plot obtained from the real space image of the lattice. The dominant orientation in a sample can be identified by using the electron diffraction patterns, which corresponds to the brighter diffraction rings. The rings order is the same as the XRD peaks, corresponding to $(10\bar{1}0)$ orientation for the inner ring, then the next one to (0002), etc. For ZnO, the electron diffraction patterns have been studied since 1935 [299].

EDS can be used to analyse the sample composition, it uses a range of X-ray wavelengths to identify the elements in a sample [298]. This is similar to the method used to generate X-rays in XRD, although with EDS the anode target is the sample itself. As a result, when the accelerated electrons hit the atoms and knock a K or L shell electron, X-rays are generated and emit radiation with energy unique for each

atom. This technique is more accurate and sensitive for atoms with an atomic number higher than 10 as they have both K and L shells and releasing radiation at two wavelengths. Therefore, two peaks provide a more definite identification than just a single peak.

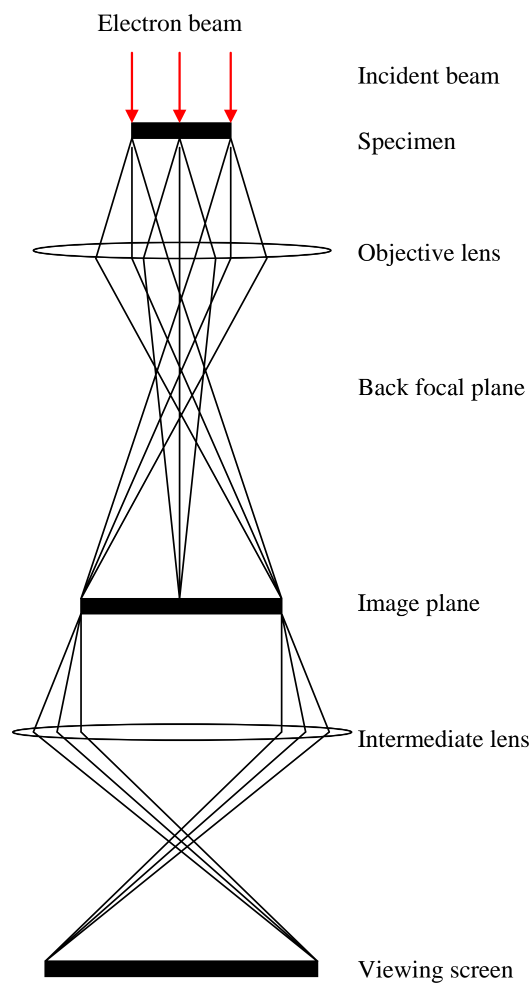

Figure 36: Schematic of the TEM ray paths, based on [296],[298]

For this study a JEM-2100 LaB6 TEM was used to analyse a small number of films on Si. The samples were polished to 2 μm^2 area and 10 μm depth using a focused ion

beam (FIB) (FEI Helios 600i FIB dual beam SEM). Briefly, with the sample tilted perpendicular to the ion beam (52° with respect to the electron beam) a protection layer of carbon was deposited onto the sample surface. Ga^+ ions of a specific accelerating voltage were then utilised to remove material at a controllably rate from the bulk, and then the exposed cross-section was polished with a recipe of reducing energies until the finer features were revealed. The polished samples were then mounted on TEM grids for microscope analysis. The images were used for thickness estimation, identification of the grains' orientation, and lattice spacing calculation. All the TEM images and FIB polishing were conducted by Dr. Kerry Abrams.

3.11. Atomic Force Microscope

Atomic force microscope (AFM) was first developed by Binnig and Quate [300] in 1985, as a method of scanning samples with inter-atomic forces between single atoms. The use of an optical technique to detect the position of the tip on the sample surface allows AFM to image non-conductive as well as conductive materials in atomic scale, which is ideal for samples charging up in electron microscopes. The small forces moving the cantilever beam (i.e. 10^{-18} N) [300] provide high sensitivity in relation to other methods such as scanning tunnelling microscope (STM).

The configuration consists of a flexible cantilever beam connected to a sharp tip, a laser source, a detector system, and an XYZ position control stage on which the sample is placed (Figure 37). The sample moves under the tip and the features on the sample cause movement of the tip and the cantilever attached. The laser beam is

focused onto the back of the cantilever and then it is reflected onto a split optical sensing system (photodiode detector). Hence, the movements of the cantilever cause changes of the laser beam position and a differential voltage is generated as the position of the laser beam changes on the photodiode. Hence, the differential voltage is used to obtain information about the deflections of the cantilever. The data provide surface height information over small (e.g. 500 nm^2) or larger areas (e.g. 5 μm^2).

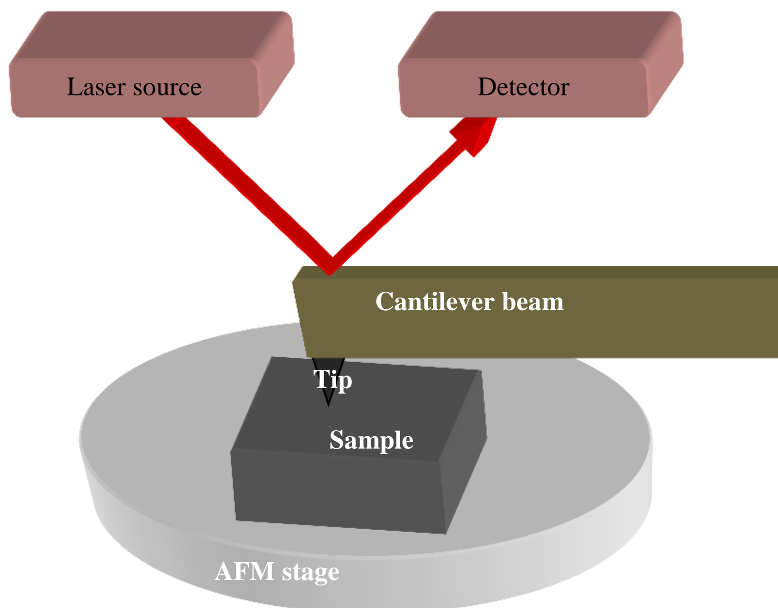

Figure 37: Schematic of the AFM main components arrangement.

The information obtained by AFM is strongly affected by the properties of the spring (flexible part of the cantilever) and the tip [301]. The spring should have high resonant frequency in order to reduce the vibrational noise effect, which can be controlled via a high and unvarying ratio of the spring constant k and spring effective mass m_o [300].

High aspect ratio tips are also suggested to avoid electrostatic cantilever-sample interaction, which may result in a capacitive force [302].

AFM operates in typically two modes, the contact mode and tapping mode. The contact mode consists of the tip contacting the sample's surface, with finite forces that deform the tip and sample [301]. The tapping mode on the other hand consists of forces that deflect the tip in a constant distance from the sample's surface at 40-50Å [301], hence, it is preferred for scanning 'soft' materials such as organic materials.

The AFM used in this project was the Bruker Multimode 8, which was connected to NanoScope software that controlled the scanning parameters, such as the frequency of cantilever (scanning speed), image quality, etc. Noise turbulence was a great issue in obtaining good quality images, although the vibration disruptions are partially minimised by the vibration absorbed floor and through an acoustic isolated environment with the use of a foam cover. Using the foam cover did not show a difference in the images, hence it was not used. The parameters providing the best quality images were at frequency 1 Hz and 1024 pixel image using the ScanAsyst mode, since the contact mode was highly affected by the noise vibrations. The ScanAsyst mode is an improved technology of tapping mode developed by Bruker to help the users obtaining better quality images by automatically adjusting the scanning parameters and eliminating the cantilever tuning. This mode uses precise controlled force curves to generate an image, protecting in that way delicate films [303]. The tip radius used for this mode is 2-12 nm, indicating the resolution of the scan.

From the software, the topographic images showed the surface scanned height and tip friction along the surface, although in this project only the height related images

will be analysed. Those were later on analysed to obtain the root mean square roughness (RMS), the average roughness (R_a), the maximum height, and the image surface area. The RMS and R_a are widely used terms that express the roughness of the surface, with the calculation formulas being the only difference between them. The numerical value of RMS is higher than R_a as it uses the square root of the sum of height difference, and so a large height feature will affect more the RMS value. The R_a uses the average of individual heights. Most of the studies related to the current work used the term RMS to express the level of surface roughness, hence, RMS data are the only data presented in this study in order to compare them with literature. RMS is expressed by Equation 46 [304], where z is the grains height and N is the number of grains. From the relation is shown that RMS is high with larger or sparse grains. However, the relation was not actually used for calculations since the RMS values were automatically estimated by the NanoScope Analysis software.

Equation 46

$$R_q = \sqrt{\frac{1}{N}\sum(z_i - z_{ave})^2}$$

Chapter 4

Effects of Zr doping on the microstructure of ZnO films

4.1. Introduction

This chapter focuses on the microstructure of both Zr-doped and un-doped ZnO films. Microstructure plays an important role in determining the optical and electrical properties of TCOs and it is therefore essential to understand how it is affected by doping, film thickness and also by growth conditions. The microstructure in this work has been investigated using XRD, AFM and TEM to reveal information about the grains preferred orientation and the crystallite size.

Particular focus is given to the preferred orientation of the crystallites and how it is affected by the film thickness. Recently, Singh et al. reported orientation shift in ZnO films deposited by ALD, from c-axis to a-axis as the film thickness increased [226]. The current work will analyse this effect further by identifying the thickness at which the orientation is shifting to a-axis by using different thickness films and using mathematical models of the surface and strain energies that drive the preferred orientation. This analysis is carried out using un-doped and Zr-doped ZnO films.

4.2. Effect of growth temperature on un-doped ZnO

The microstructure of un-doped ZnO thin films was investigated as a function of growth temperature. AFM was carried out on ZnO films grown at 150°C, 200°C, 250°C and 275°C with 500 cycles of ALD. Figure 38 shows detailed area (500 nm^2) scans of these samples (excluding 150°C as it is very similar to the 200°C result). The height topography across selected cross sections is shown as dotted lines in the figures.

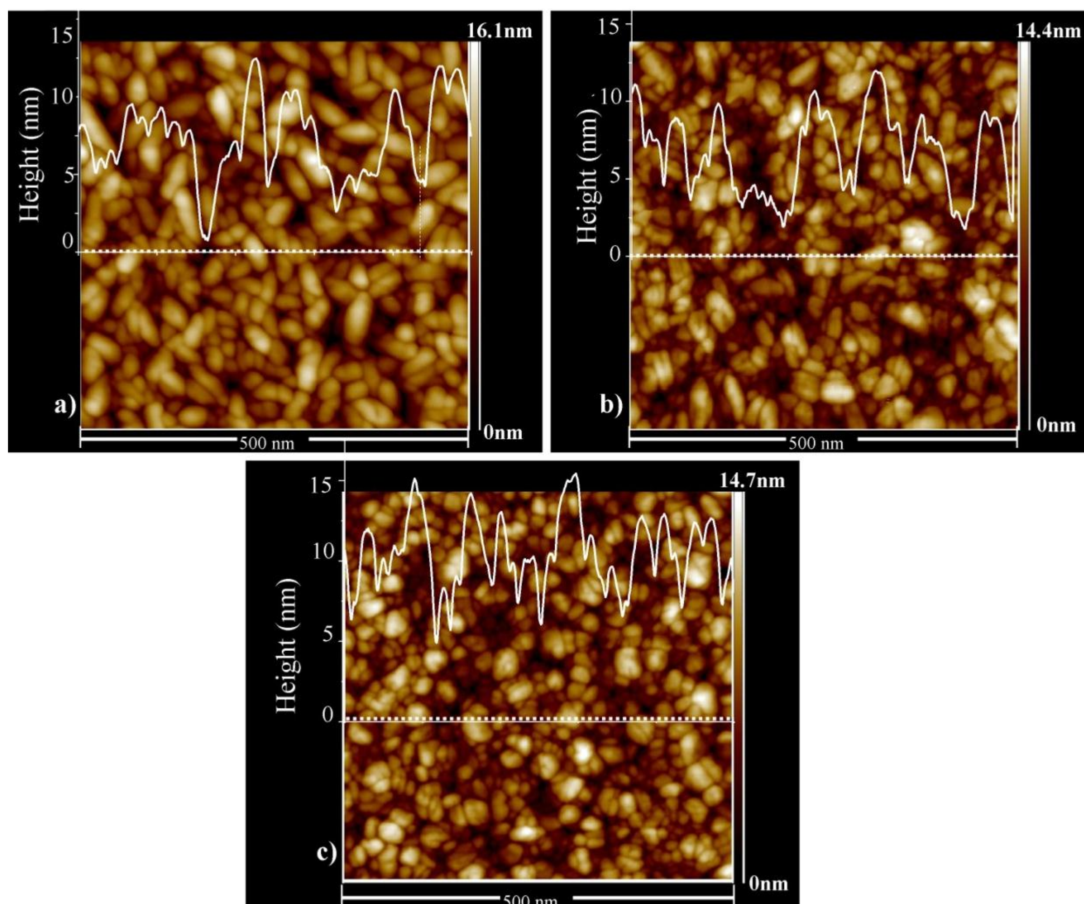

Figure 38: AFM images of un-doped films grown at a) 200°C, b) 250°C, and c) 275°C. The dotted line section shows the height changes of the surface map, which was used to estimate the length of one grain in each image.

The root mean square (RMS) values obtained using the NanoScope Analysis software, do not show much variation, ranging from 2.25 nm (250°C) to 2.34 nm (275°C), with the 200°C film having RMS=2.31 nm. The small variation indicates negligible changes in surface roughness as temperature increased, although the grains appear different in shape. From the three films, the grains appear as needle shaped at the low temperature with features of 50-60 nm length. It is assumed that the length of the needle shaped grains is the c-axis and their width is the a-axis. The grains in films grown at 275°C appear rounder in shape compared to the ones at 200°C, while the grains at 250°C appear both elongated and round. The round grains could be elongated grains oriented perpendicular to the substrate. It is difficult to accurately assess the length of the grains along the c-axis using AFM as the orientation of individual grain is unknown. It is, however, possible to estimate the width of each grain along the a-axis by measuring the shortest dimension of the AFM features.

The a-axis dimensions at low temperature are approximately the same as the width of the round feature at high temperature after measuring the average dimensions of the grains using AxioVision Rel. 4.8 software (i.e. 24.7 nm width at 200°C and 23.2 nm at 275°C). The grains' height on the other hand presented by the plotted peaks shown on the AFM images, was shown to increase at 275°C indicating possible transition of the grains orientation. As a result, the surface topography indicates that as the temperature increases the grains become more perpendicular to the substrate (i.e. grains lie perpendicular to the image angle and so appeared rounder, but are still needle shaped).

In order to support the AFM data and specify the grains orientation, XRD measurements were carried out on the same samples. The measurements are displayed in Figure 39, consisting of XRD diffraction patterns of 99-62 nm films grown from 150-275°C (i.e. thickness reduced with temperature increase as the number of cycles was kept fixed but the growth rate was decreased). The graph also shows the reference patterns of hexagonal wurtzite ZnO by space group P63mc [305] and the diffraction pattern from uncoated Si wafer substrate.

All the films are polycrystalline, with the highest intensity peak typically indicating a preferred orientation in that plane. The current films grown at low temperatures show dual orientation (two peaks are dominant) with a rise of (0002) and $(10\bar{1}0)$ peaks corresponding to the c-axis and a-axis orientation respectively. At high growth temperature the (0002) orientation is the most favourable as the $(10\bar{1}0)$ peak gradually suppresses and disappears. The $(10\bar{1}1)$ peak is very small and broad in all films, although in the reference pattern it has the strongest signal. The $(10\bar{1}2)$ peak does not appear, but the $(11\bar{2}0)$ diffraction appears as a very small peak up to 225°C. From the reference pattern the $(10\bar{1}2)$ peak has the lowest intensity of all diffractions, hence, it is very difficult to be seen, especially when its related peak $(10\bar{1}1)$ is very low. The suppression of the planes in the z-direction such as $(10\bar{1}1)$ and $(10\bar{1}2)$ suggests that the grains are closed packed as grown horizontally or perpendicularly to the substrate, hence, there is no much space for grains to grow in other directions. Note that the existence of both (0002) and $(10\bar{1}0)$ peaks do not correspond to planes of the same unit cell as the cells oriented in the c-axis do not allow diffractions of a-axis planes. Therefore, the a-axis diffractions refer to grains oriented in the a-axis and the c-axis to grains oriented in the c-axis direction.

XRD results are therefore consistent with AFM, with the 200°C film showing elongated grains corresponding to a-axis oriented grains, and with the 275°C film showing smaller round features corresponding to c-axis oriented grains (i.e. vertical to the substrate). Additionally, as shown in AFM the elongated grains were reduced in number at 250°C, which agrees with the intensity reduction of the $(10\bar{1}0)$ peak, while the rounder features increased accordingly to the (0002) XRD peak intensity. As temperature reach its maximum of 275°C, no elongated grains appeared in AFM which corresponds to the disappearance of the $(10\bar{1}0)$ peak in XRD. The data agreement between the two techniques at this stage suggests that the grains at low temperature grow parallel to the substrate, while as temperature increased the grains gradually grow in direction perpendicular to the substrate.

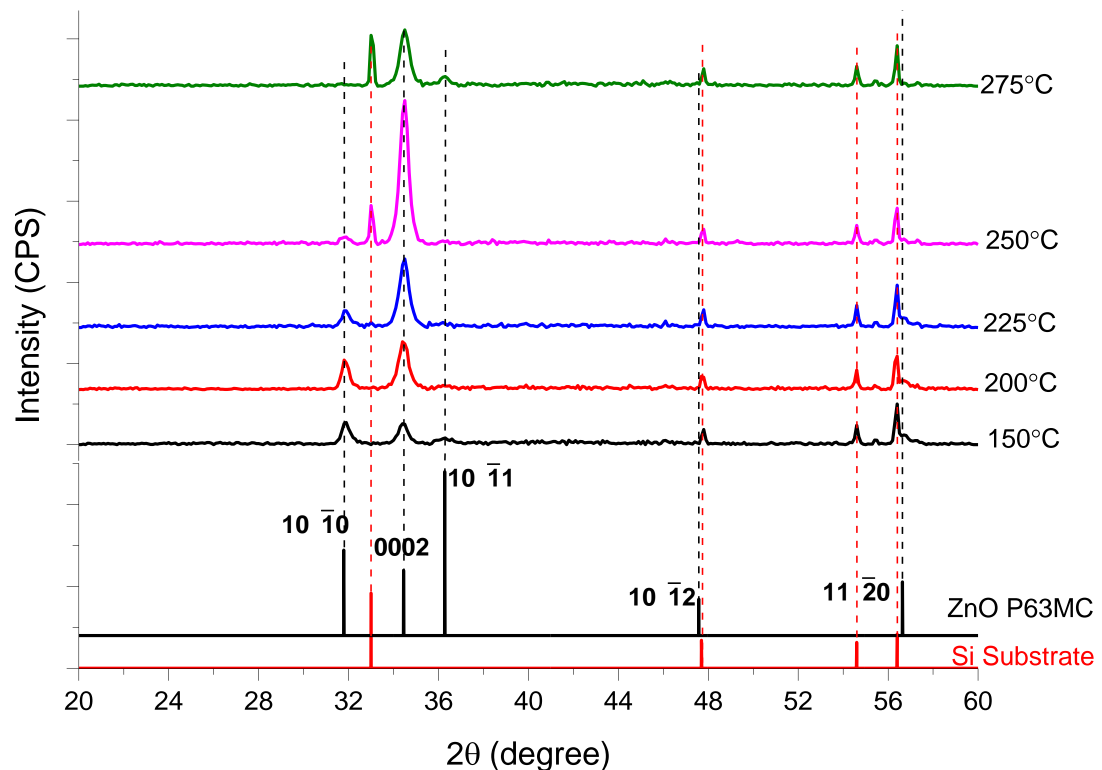

Figure 39: XRD patterns of ZnO films (500 ALD cycles), with reference patters displayed for comparison to Si substrate pattern (see chapter 3) and ZnO pattern of space group P63mc [305].

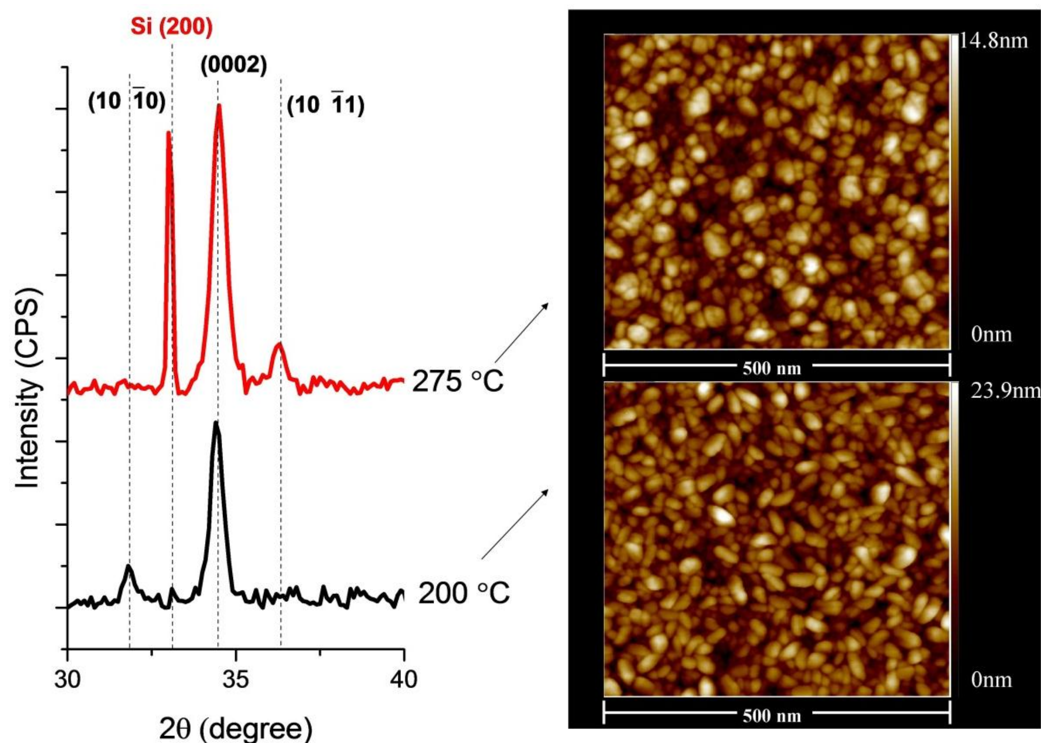

Figure 40: XRD and AFM data comparison of similar thickness films (55-62 nm) grown at 200°C and 275°C respectively.

The growth temperature appears to affect the degree of orientation shown by the increased XRD intensity. However, it has to be examined whether this is an effect of having different film thickness. A direct comparison of XRD and AFM data is shown in Figure 40 for films grown at different temperatures both with similar thickness (i.e. 55-62 nm). From the AFM data the grains were found to be narrower and longer for the 200°C film compared to the 275°C film, with their length to width ratio of 1.9 and 1.3 respectively (i.e. 39.9/21.3 nm at 200°C and 31.0/23.2 nm at 275°C). The image shows a-axis oriented grains at 200°C, consistent with XRD data showing a small $(10\bar{1}0)$ peak. The round features showing in the 275°C film indicate c-axis oriented grains, consistent with the high XRD intensity of the (0002) peak, while the appearance of the $(10\bar{1}1)$ peak suggests the existence of a few a-axis

oriented grains. The higher (0002) peak intensity for the 275°C film indicates the formation of larger crystallites at high growth temperatures. Hence, regardless the film thickness, the films grow at both a-axis and c-axis directions at low temperatures, while at high temperatures the grains preferred growing in the c-axis direction. Further analysis is necessary to specify whether the orientation shift in preferential growth (dual or c-axis) depends on the thickness, as the peaks intensity changes between the 55 nm (Figure 40) and 95 nm (Figure 39) films grown at the same temperature.

The reason for the grain size increase at high temperature is found within the lattice changes during the growth. In particular, the grain growth occurs by the movement of the grain boundaries and the diffusion of atoms from the one side of the boundary to the other [306]. The boundaries movement is driven by the tendency to reduce the grain boundary energy as the total energy increases, which is done by reducing the boundary area when the grains are larger. Therefore, at high growth temperatures where the total energy is raised, the grain boundaries energetically prefer to be reduced in size by the formation of larger grains. In addition, the atoms mobility increases with increased temperature expressed by Boltzmann transport model (i.e. kinetic energy increases due to the gained thermal energy). Therefore, at high growth temperatures the atoms are expected to move into larger grains, forming very large grains and much smaller ones. This is consistent with the AFM images, as there are many large features and a few small ones in the film grown at 275°C.

In comparison to previously reported studies on ZnO films grown by ALD, the temperature effect is consistent with a selected-area-diffraction (SAD) study of ZnO films grown by ALD using DEZ, showing a higher degree of orientation and larger

grains at high temperature [307]. The low temperature film in [307] also showed dual orientation similar to the data in the current study.

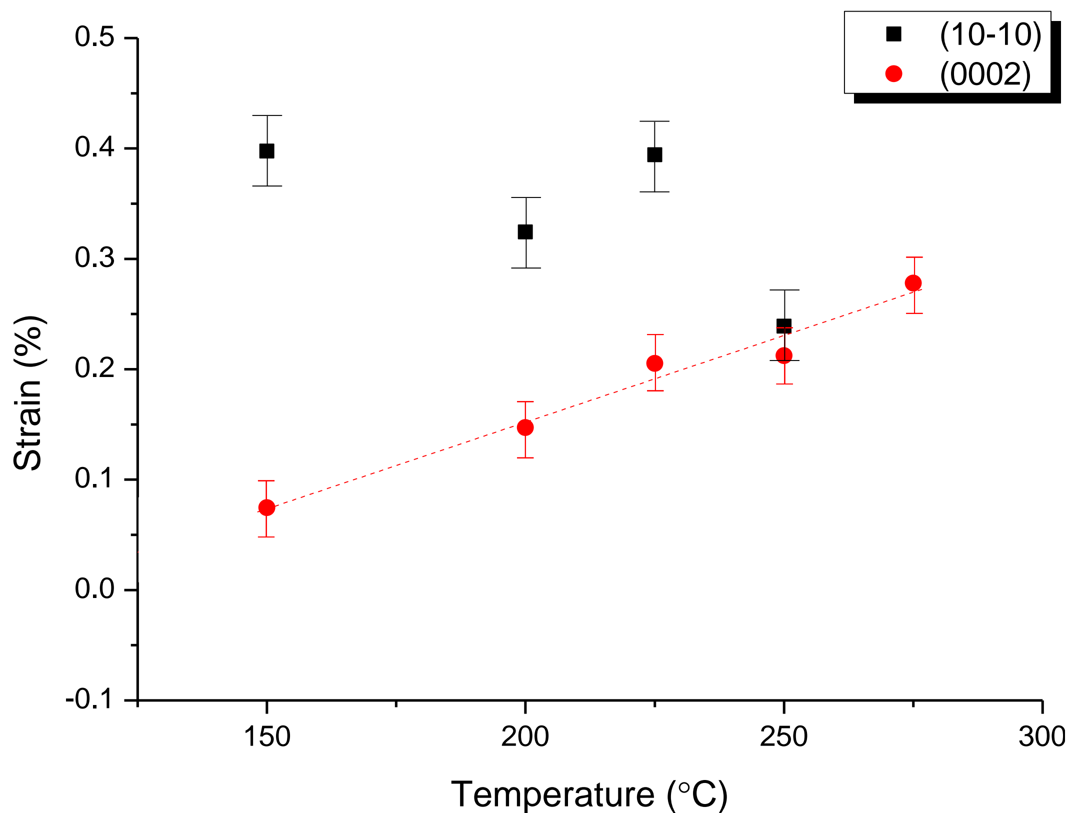

Figure 41: Temperature dependence of lattice strain dependence for ZnO films.

From the XRD data it is also useful to analyse the lattice strain and observe any effects of altering the deposition temperature. The lattice strain (Figure 41) was obtained by comparing the measured d–spacing to literature values of $d_{(10\bar{1}0)}$=2.815 Å and $d_{(0002)}$=2.604 Å [17]. The results show a linear increase in tensile strain in the c-axis as temperature increases, corresponding to $d_{(0002)}$ spacing decrease. The strain in the a-axis (i.e. $(10\bar{1}0)$ peak) shows an overall reduction with temperature, although there is some scattering due to the low signal from the plane.

This suggests that as temperature increases the c-axis oriented grains are under more tensile strain and the grains in the a-axis preferred direction are under less tension.

4.3. Zr-doped ZnO microstructure

4.3.1 Growth rate

The growth rate of ZrO_2 (0.65 Å/cycle for self-limiting ALD) is significantly lower than the growth rates of ZnO (1.87 Å/cycle) and hence increasing doping levels would be expected to reduce the film thickness if the overall number of ALD cycles is kept constant. An estimation based on the growth rates in comparison to the experimental measurements (ellipsometer) are shown in Figure 42. As shown in the graph, the film thickness clearly decreases as doping increases showing that the thickness is dependent on the doping concentration being targeted. However, the decrease is found to be more rapid than expected (as shown by the red line in Figure 42). This decrease could be due to a number of possible mechanisms such as no nucleation of the dopant cycles, the dopant cycles may not nucleate in the growth rate expected for a ZrO_2 film, and the difficulty in nucleating ZnO films after the dopant cycle.

The change at electrical properties due to doping and the ionic Zr^{4+} in the films shown by XPS, suggest that dopants are indeed deposited in the film. Therefore, the two most likely cases are the problems in nucleation in either the ZrO_2 or ZnO cycles, but with the available experimental resources it was not possible to specify

which layers had the problem. The use of quartz crystal microbalance (QCM) can reveal the cause by showing the changing in growth during each deposition step.

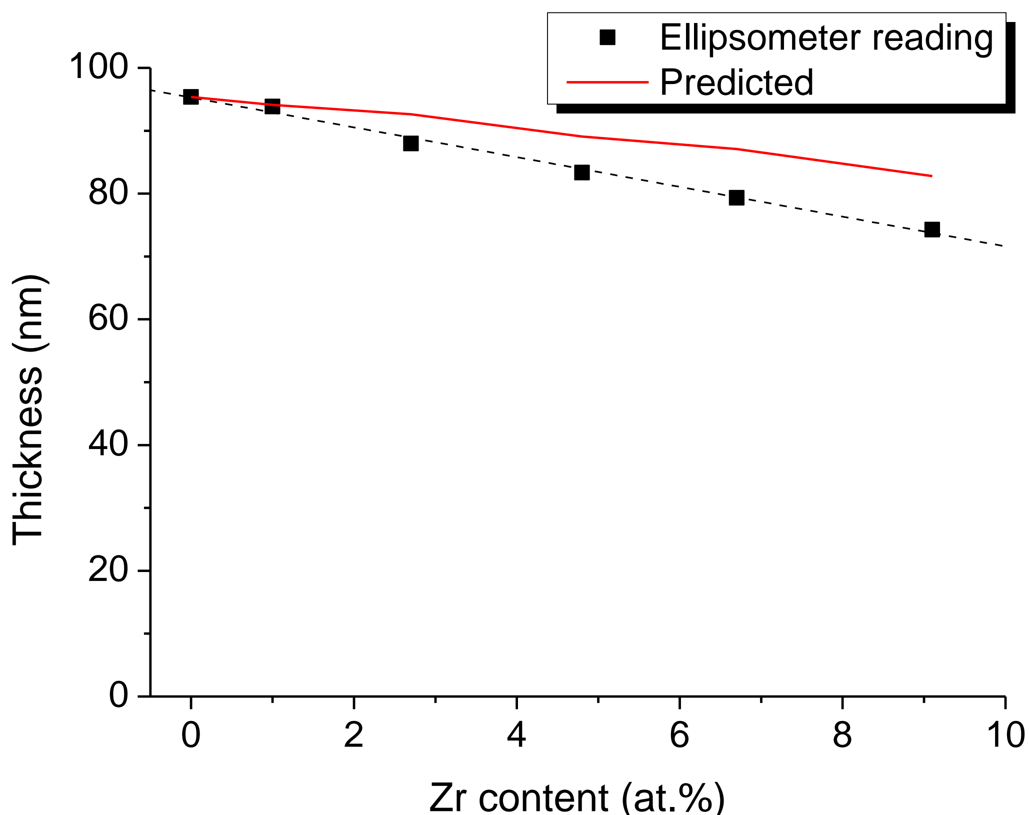

Figure 42: Zr doping dependence of film thickness.

The thickness difference between the un-doped and 9.1 at.% doped film is 21 nm. In future experiments a fixed thickness for all the samples should be targeted. Hence, the current analysis avoided issues involving the thickness difference by comparing similar thickness films, such as the undoped (234 nm) and 4.8 at.% doped (250 nm) films. The analysis on the thinner set is mostly carried out for comparable film thickness films of the undoped (95 nm) and 4.8 at.% doped (83 nm) samples.

4.3.2 Microstructure

In order to examine the microstructure of doped films, AFM measurements were carried out for all samples, from which three are shown in Figure 43.

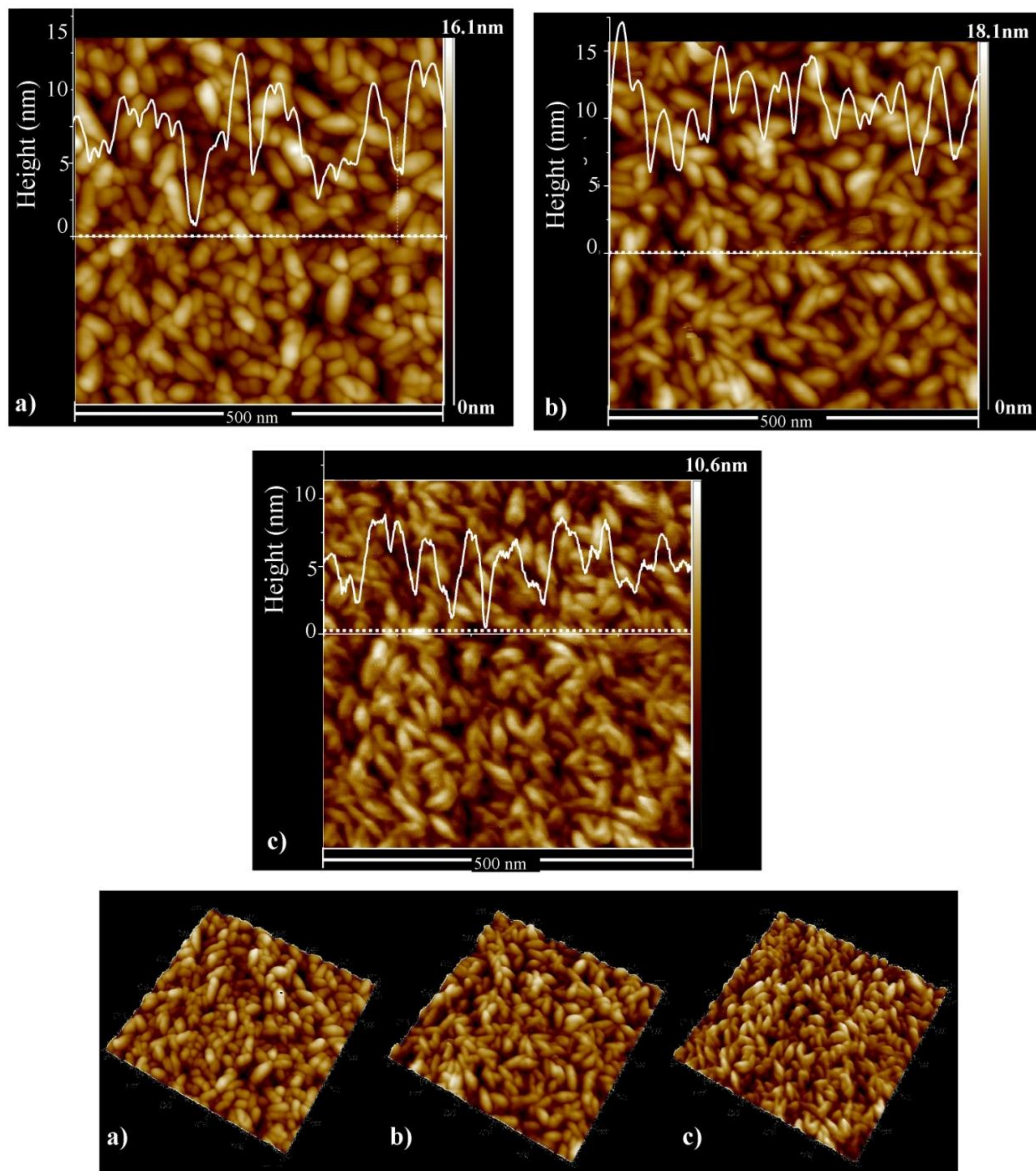

Figure 43: AFM of a) 0at. %, b) 4.8 at.% and c) 9.1 at.% doping, with the top images showing 2D images of greater details and the bottom images of the same samples in 3D.

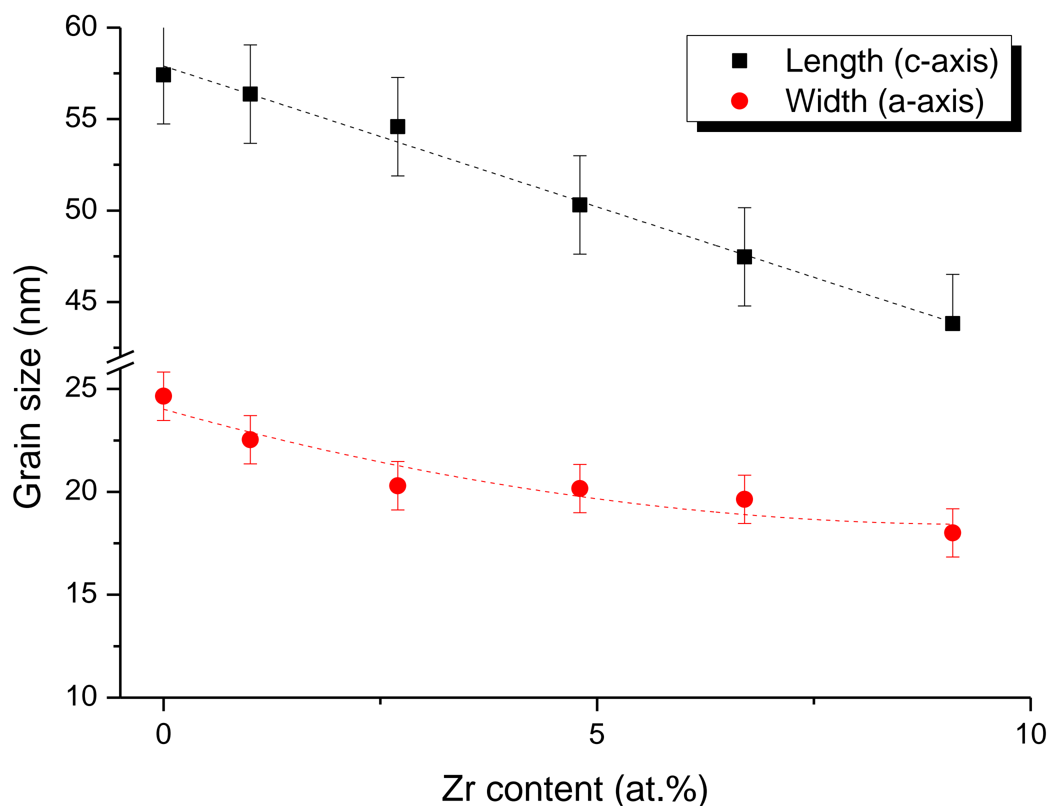

Figure 44: Zr doping dependence of grain size measured by the AFM images.

As shown in Figure 43, the grains are again found to be needle shaped, and as doping increases they become increasingly perpendicular to the substrate. The grains height illustrated by the white line plots for the dotted line area, increases at 4.8 at.% doping and then decreases again at 9.1 at.% doping. The increase is believed to be due to the shift towards a preferred c-axis orientation, similarly to the case of high temperature un-doped films shown earlier in the chapter. The heavier doped film reduces in height, possibly due to the reduction in grain size associated with the film thickness reduction.

The features size was calculated from the AFM images using AxioVision Rel. 4.8 software. The average values are shown in Figure 44, with the error bars

corresponding to standard deviation for each value with scaling factor 0.5. From the plot the grains are shown to be reduced in size as doping increases in both length and width. The reduction of the width is a more comparable measurement as it is not dependable on the orientation of the grains (i.e. length is possibly smaller due to tilting of the grains). The reduction trend is similar to the thickness reduction, suggesting that it is possibly driven by the thickness changes. To evaluate whether this reduction is due to doping effect, one doped and one un-doped film of similar thickness are compared in Figure 45. The average length was measured approximately the same for the doped (39.6 nm) and the un-doped (39.9 nm), while the width was smaller for the doped film (17.2 nm) compared to the un-doped (21.3 nm). Therefore, the grains are shown to be reduced in size with doping, a fact expected to affect the electrical properties as the enlarged grain boundaries might increase the carrier scattering.

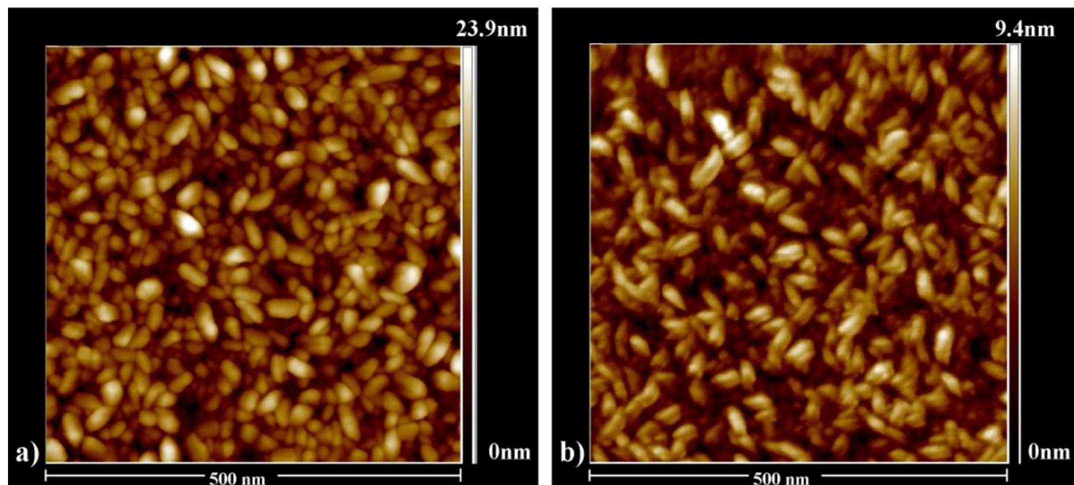

Figure 45: AFM of a) un-doped (55 nm) and b) 4.8 at.% doped (50 nm) films.

The feature lengths mostly reflect the size of the grains having a-axis preferred orientation. Hence, the reduction of the features length simultaneously to the shift of orientation in the c-axis suggests that the length reduction cannot be accurately attributed to the doping effect. However, the reduction of the features width can reveal the effect of doping. The width of a grain with preferred orientation in c-axis is restricted by the surrounding grains oriented in the same direction. The width reduction observed for similar thickness films reveals that the grain size decrease is in fact affected by the doping.

The grain size reduction with Zr doping is consistent with literature, for a range of growth methods including spray pyrolysis [26],[46], microwave irradiation [55], low temperature co-precipitation method [48], and radio frequency magnetron sputtering [57]. One proposal is that doping has a tendency to reduce grain size due to segregation of Zr atoms into grain boundaries, causing crystal disorder that led to the decrease of grain size [57]. The finer grains as a result of Zr doping were reported to result in less conductive films compared to Ga and In doped ones, due to the increased carrier scattering [29]. Nevertheless, dopant segregation is not only observed for Zr-doped systems, but also for degenerate doping materials using dopants such as Al, Ga, In and Sc [308]. This is due to the higher energy state of the dopant atoms compared to the grain boundary energy [306]. Therefore, the high number of impurities tends to cause dopant segregation at the boundaries, and it is likely that this is more distinctive when using Zr doping.

The RMS data representing the surface roughness is shown as a function of doping in Figure 46. The values following a linear trend range around 2.3-2.6 nm up to 6.7 at.% doping, and peak at 2.7 at.% doping with the lower value of 1.6 nm for the heaviest doped film. The difference between the first five samples is within the error

margin and so is showing that doping is not affecting the surface roughness. This is due to the increase of the grains height as they become more perpendicular and smaller as doping increased, leading to a balance change in RMS relation (see chapter 3). The heavier doped film shows lower RMS due to its lower thickness.

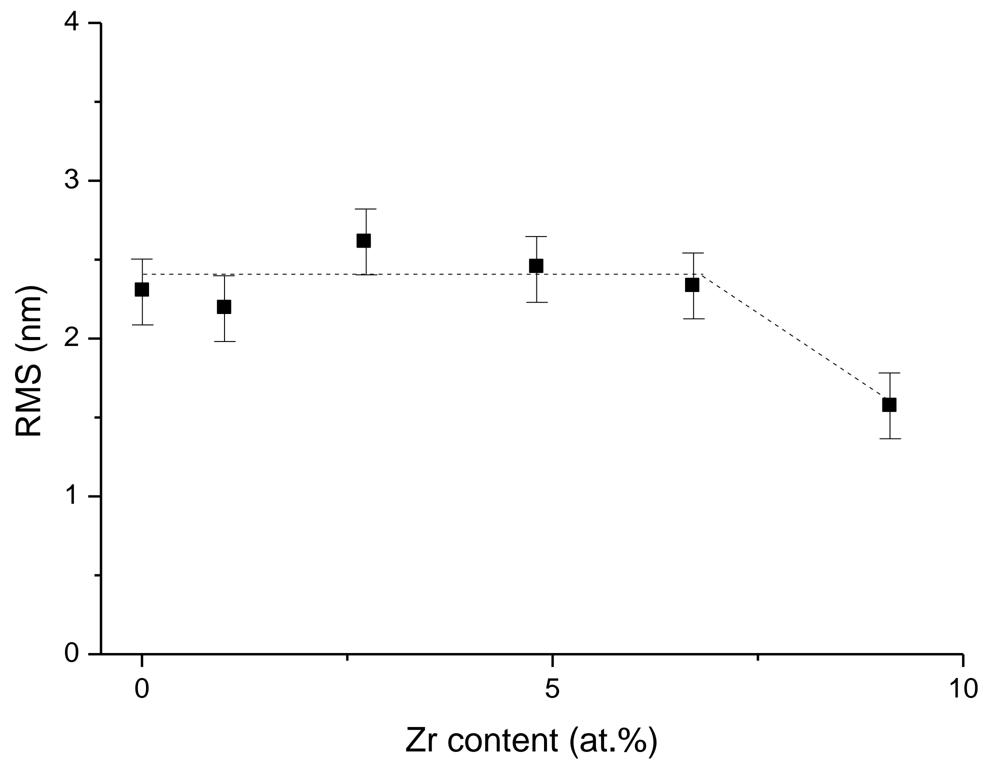

Figure 46: RMS data from AFM analysis, in relation to Zr doping with error bars set as ±0.6 nm.

In order to evaluate if RMS is thickness dependent, the RMS of a range of different thickness 4.8 at.% doped and un-doped films were measured. RMS (Figure 47) linearly increases with film thickness. The doped and un-doped films follow the same increasing trend within experimental errors, implying that Zr doping is not affecting the roughness of the films. This is consistent with an un-doped ZnO study that showed a similar linear RMS dependent on thickness [309].

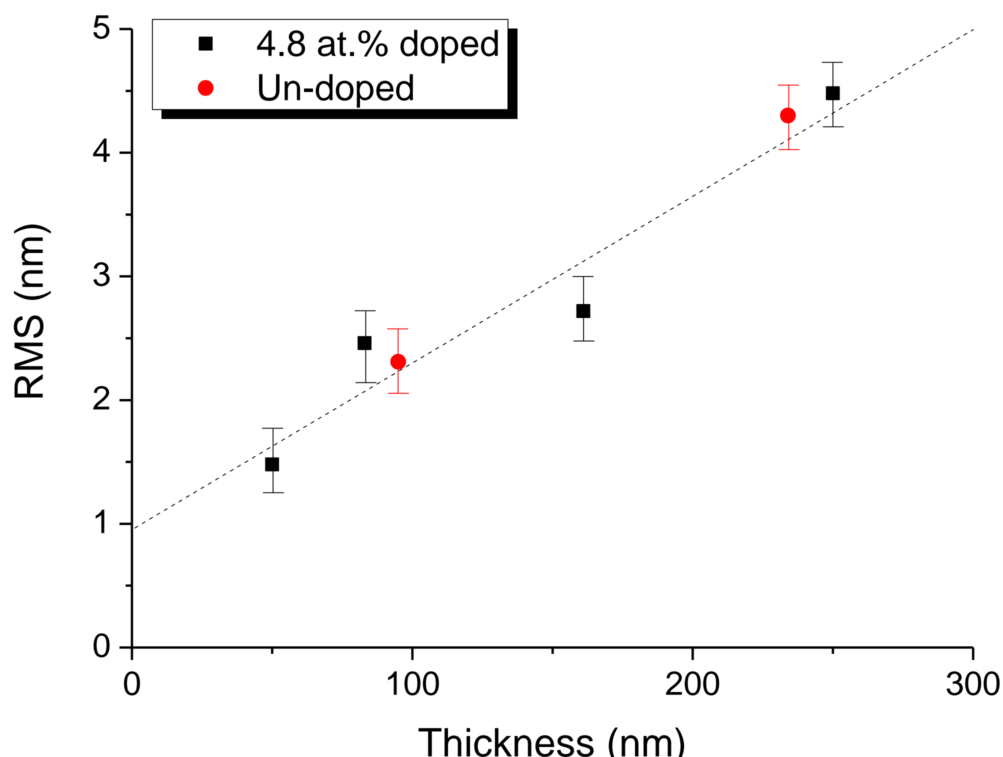

Figure 47: Thickness dependence of the RMS for films doped with 4.8 at.% Zr.

The surface roughness can be considered as an advantage in terms of electrical properties, as it can reflect on large grains, which result in reduction of the grain boundary scattering. This is supported by the comparison of the current data and the values reported by Tsay et al. [29], who reported smoother 210 nm thick ZnO: Zr films (RMS=2.55 nm) using sol-gel growth method on alkali-free glass, compared to the current films of similar thickness (RMS=4.5 nm). The lower roughness was due to the smaller crystallites of 12 nm [29], compared to ≥50 nm long grains in the current work. The current films resulted in lower resistivity of at least six orders of magnitude compared to the study in reference [29] (see chapter 5). In comparison to other techniques, ALD provided much smoother films than spray pyrolysis on glass substrates that showed 11 nm RMS for Zr-doped ZnO films of 100 nm thickness [26], and even higher values were reported using spray pyrolysis of RMS=65 nm [46].

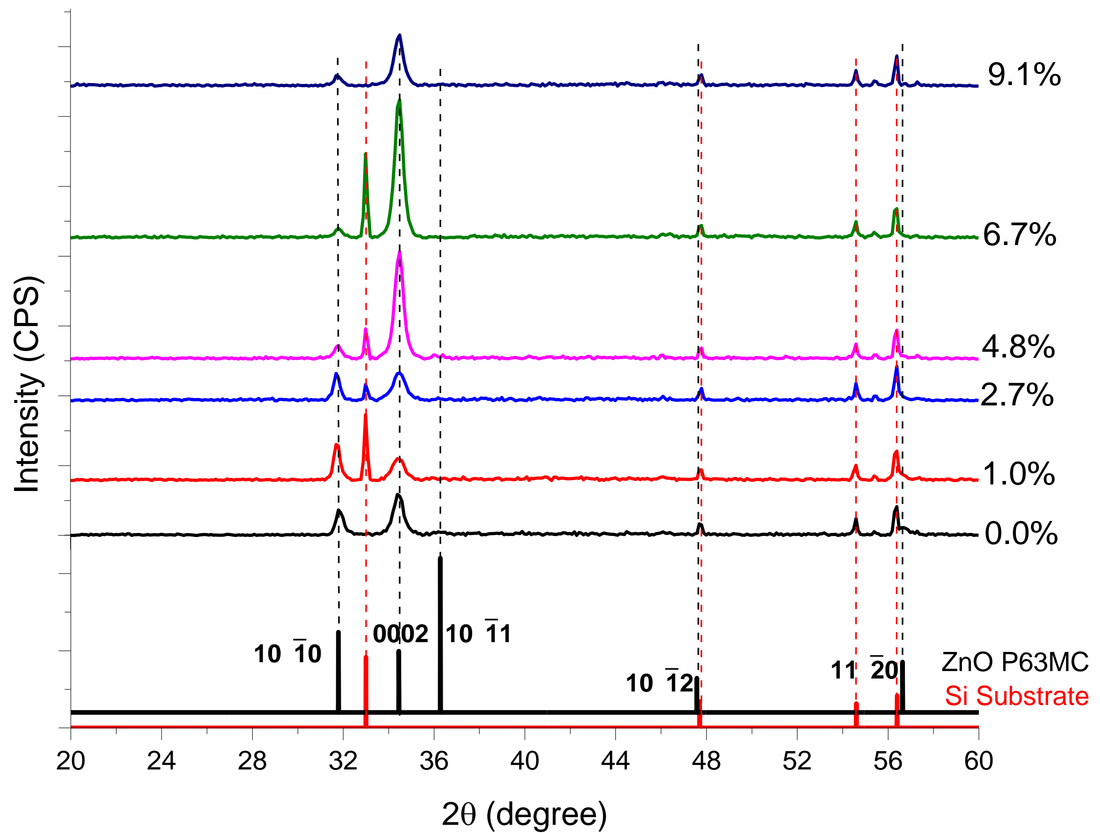

Figure 48: XRD patterns of Zr-doped ZnO films on Si (100) substrates.

In comparison to other dopant studies involving ALD, the current RMS values are higher than films with similar film thickness and grain orientation using dopants such as Al of 100 nm thickness on quartz glasses (1.25 nm) [187] and of 200 nm thickness on sapphire substrates (2.38 nm) [34]. The decreased roughness in these doped films is believed to be driven by the smaller grain size, but as no grain size was reported in these studies, it is not possible to carry out a direct comparison to the current data. However, the un-doped RMS values recorded in the current study, are comparable to a study of un-doped ZnO films by ALD [309] with RMS=2.4 nm (~100 nm film), and RMS=5.5 nm of ~250 nm thick film.

To further investigate the doping effect on the grain orientation, XRD measurements were carried out (Figure 48). The films are polycrystalline with strong $(10\bar{1}0)$ and

(0002) peaks for no or low doping. However, as the doping level increases above 2.7 at.%, the (0002) feature increases in intensity while the $(10\bar{1}0)$ feature is suppressed. For the highest doping level the dominant peak is remaining the (0002), although its intensity is reduced compared to the samples with slightly lower doping (4.8 at.% and 6.7 at.%). The $(10\bar{1}1)$ and $(11\bar{2}0)$ peaks have very low intensity in all samples. Therefore, the doped films show preferential orientation similar to the un-doped films (section 4.2) in two planes (i.e. $(10\bar{1}0)$ and (0002) planes).

The increase in the intensity of the (0002) peak indicates that the long-range crystalline c-axis ordering increases with higher doping concentration (at least up to 6.7 at.%). This increase implies that Zr^{4+} is substitutional to Zn^{2+}, since placement at interstitial positions is expected to result in amorphization [26]. The reduction in intensity for the heavily doped film is consistent with previous c-axis oriented Zr-doped ZnO films, in which the intensity of the (0002) peak was reported to be reduced at high doping due to high dopant segregation [26],[46],[57].

The lattice changes can reveal the expansion of the lattice due to the larger atoms of Zr. Hence, the lattice constants in both a-axis and c-axis preferred oriented grains are measured based on the XRD peak shifts. The literature values for pure ZnO are $d_{(10\bar{1}0)}$=2.815 Å and $d_{(0002)}$=2.604 Å [17]. The measured lattice constants on glass substrates for the un-doped films are $d_{(10\bar{1}0)}$=2.814 Å and $d_{(0002)}$=2.608 Å, and for the 4.8 at.% doped film are $d_{(10\bar{1}0)}$=2.822 Å and $d_{(0002)}$=2.608 Å. Therefore, an increase of the lattice constant will lead to compressive strain and a reduction to tensile strain. The lattice constants in the c-axis show a reduction as doping increases, while the constant in the a-axis is increased (Figure 49). This suggests that the slightly larger Zr atoms (0.745 Å) compared to Zn atoms (0.740 Å) [42] are added

in the a-axis oriented planes and increase the d-spacing. This is consistent with reported studies on Zr-doped ZnO [26],[56],[200]. The decrease in the c-axis can be related to the grain boundaries increase as doping increases, which apply more pressure to the lattice. The reduction of only the c-axis preferred oriented grains suggests that their positions in the film is more affected, and are most likely basal grains. The increase in the a-axis preferred oriented grains suggests that they are less affected and are most possibly at the top of the film. TEM was used to specify their position as discussed in section 4.4.2.

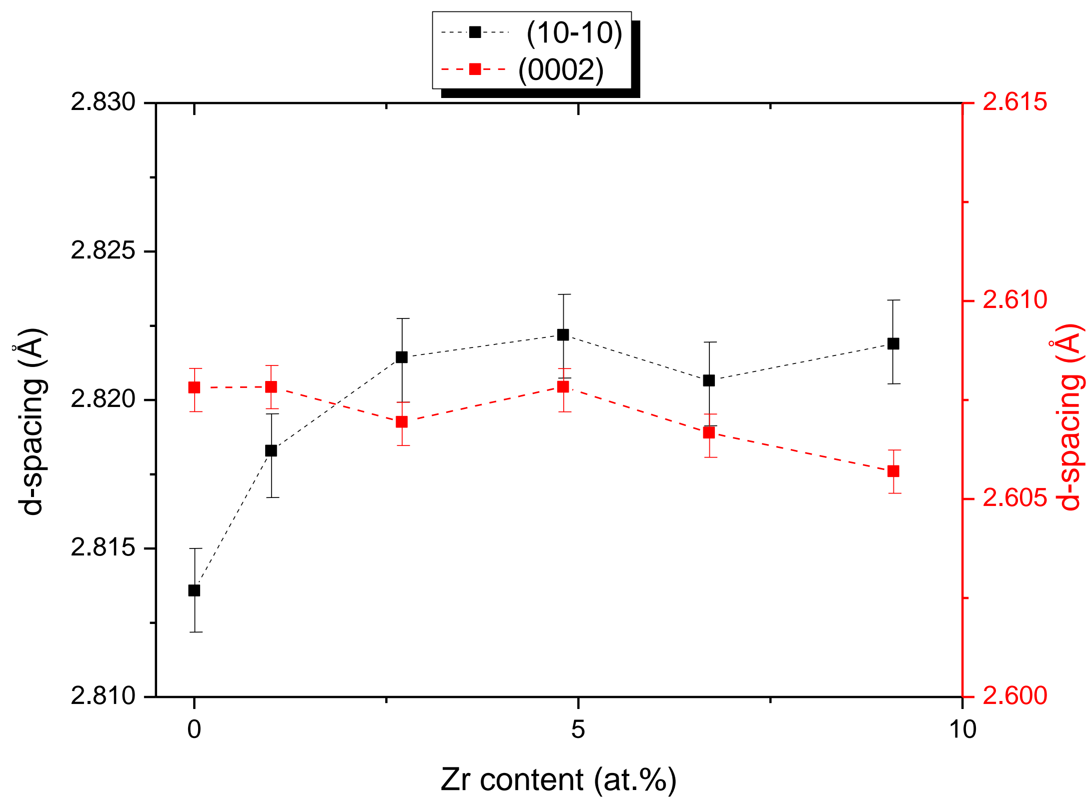

Figure 49: Zr doping effect on d-spacing for $(10\bar{1}0)$ *and* (0002) *orientated crystallites on glass substrates.*

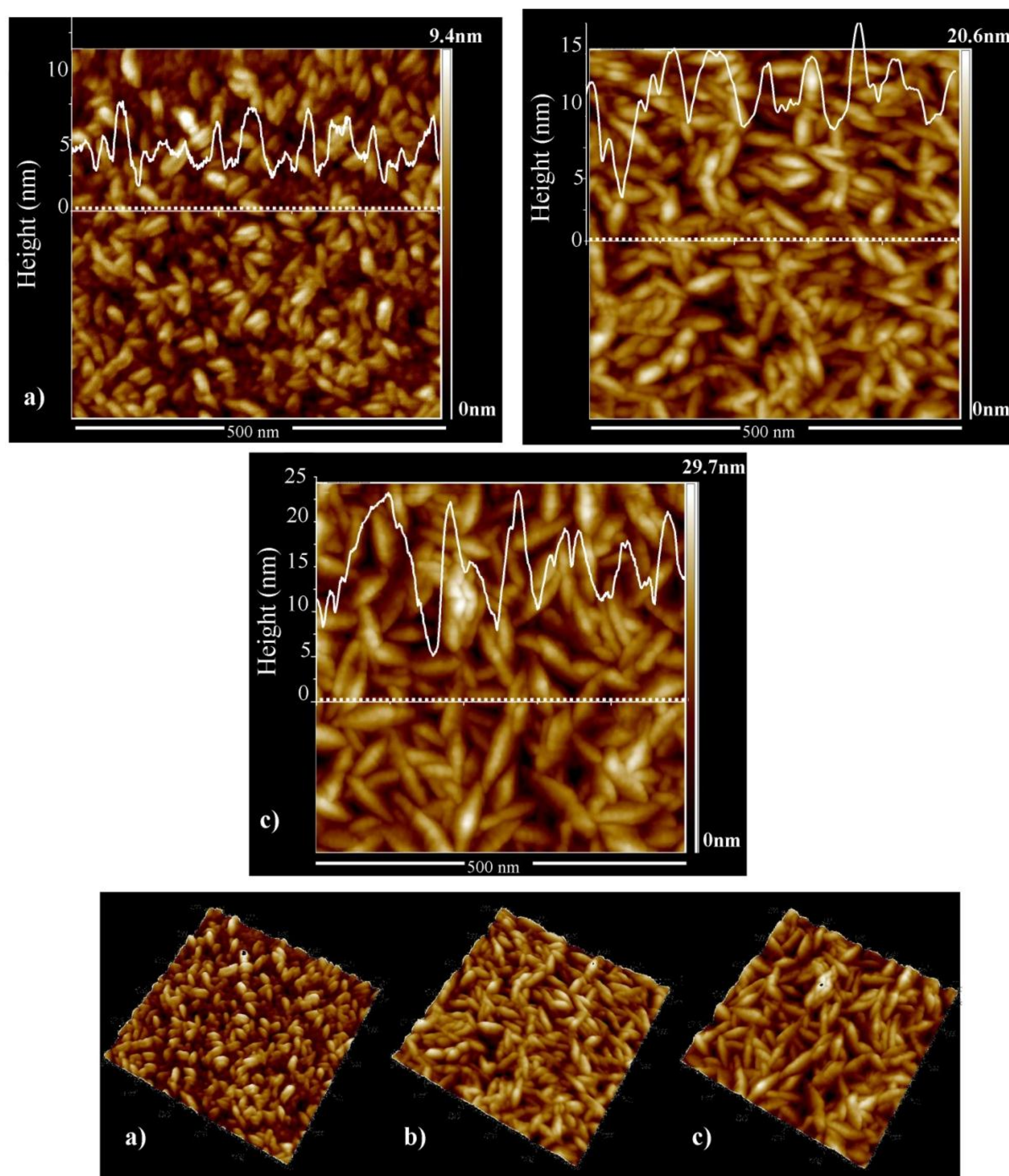

Figure 50: AFM of 4.8 at.% doped films of a) 50 nm, b) 161 nm and c)250 nm thickness.

The thickness effect on the surface topography is shown in Figure 50, illustrating larger grains as thickness increases. The features size was then measured by AxioVision software and is shown in Figure 51. Its shows a linear increase of the length (i.e. ~40-90 nm) and a linear increase of the grain width (i.e. ~18-30 nm) as the thickness increases. For thinner films, the AFM features are mostly rounded in

appearance as the long axis of each crystallite is perpendicular to the substrate; the grains are mostly c-axis orientated with respect to the substrate surface. As film thickness increases, the features become more needle-like in shape, which is indicative of a-axis orientated grains. The gradual changes to thickness increase suggest that the orientation is shifting from c-axis to a-axis preferential orientation as the film thickness increases.

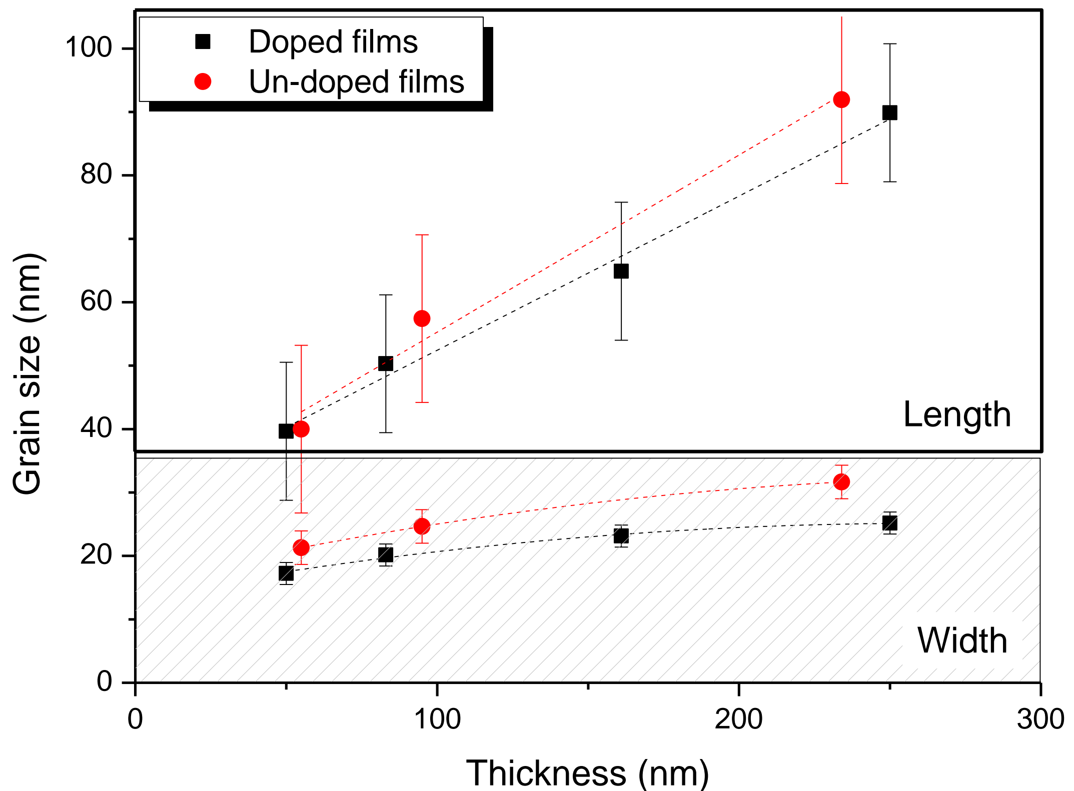

Figure 51: Average grain size measured by the AFM images as a function of film thickness (4.8 at.%).

In order to investigate whether the changes in grain orientation are influenced by doping, a direct comparison of thick films for 4.8 at.% Zr-doped and un-doped films is shown in Figure 52. Both films show needle shaped grains oriented in a-axis,

consistent with reported films of the same orientation using ALD [32],[216],[224]. The grains size was measured as 89.9/25.2 nm for the doped and 91.9/31.7 nm for the un-doped film, with the difference attributed to the doping effect on the grain growth established earlier. Hence, the grains orientation transition appears the same for doped and un-doped films, suggesting that it is driven by thickness rather than doping.

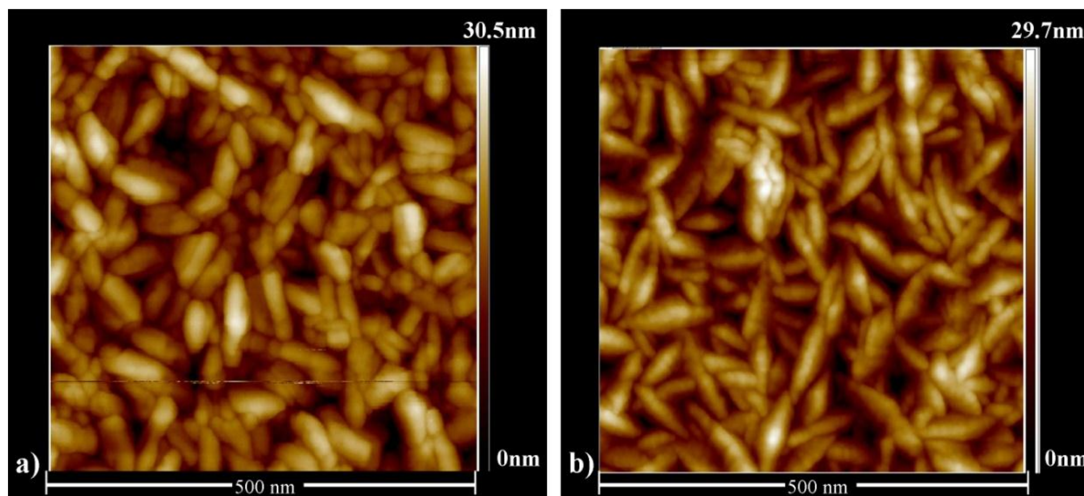

Figure 52: AFM images comparison of a) un-doped (234 nm) and b) 4.8 at.% doped (250 nm)

The effect of film thickness on XRD is shown in Figure 53. The diffraction patterns show three different crystal orientations, with the first one being preferred orientation in c-axis for the thinner film, then dual preferred orientation at slightly thicker films, and finally a-axis preferred orientation for the thicker films. The (0002) peak is dominant for the thinner film, and as the thickness increases, both diffractions of $(10\bar{1}0)$ and (0002) are dominant for the doped and un-doped films. With further thickness increase the pattern is dominated by $(10\bar{1}0)$ planes,

indicating a-axis preferred orientation. In each case, this is consistent with the AFM data, hence, both methods show that increase in thickness drive the orientation from c-axis preferential to a-axis, with a transition range for intermediate thicknesses.

This orientation shift is also consistent with XRD results obtained for films grown on glass substrates (Figure 53). The peak ratio of the two main peaks is similar regardless of the substrate, with the only exemption being the 83 nm film, where the peak ratio is lower than the film on Si substrate. This is possibly due to the formation of more randomly aligned grains on the amorphous substrates. The similarity in peak ratios between the two substrates suggests that the orientation shift in this study is not affected by the substrate used.

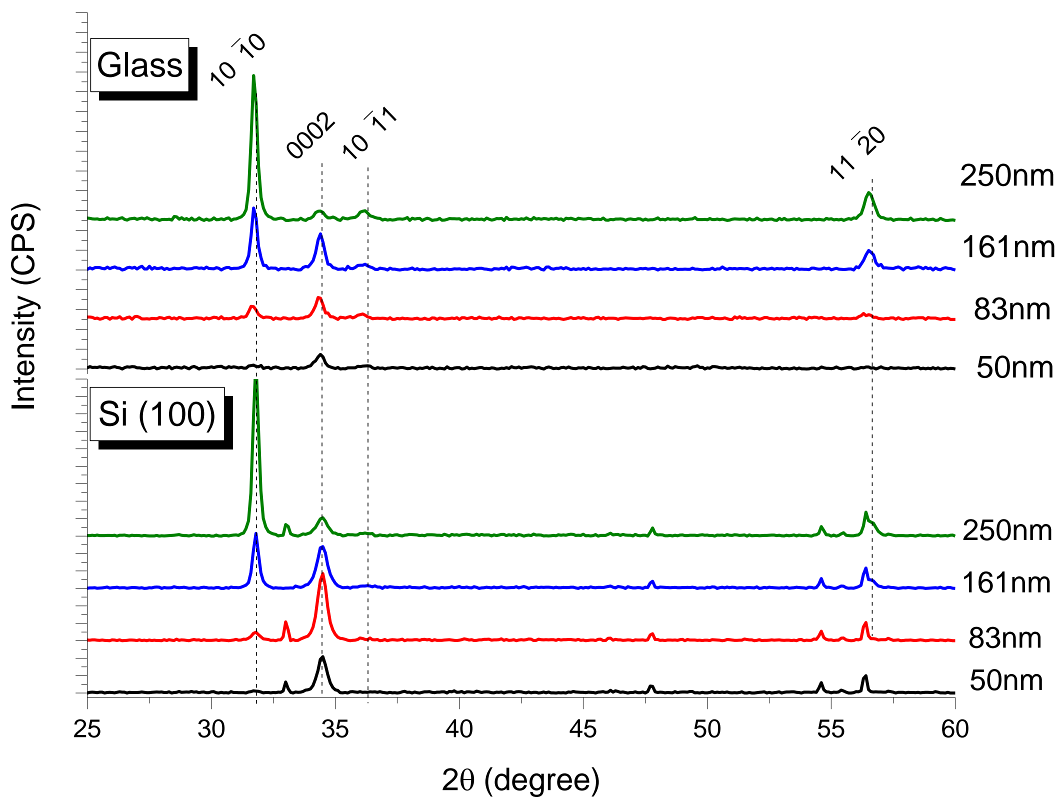

Figure 53: XRD of different thickness 4.8 at.% Zr-doped films on Si (100) and glass substrates.

The XRD peaks from films on glass substrates are shifted to slightly lower angles in comparison to films on silicon (Figure 54). The shift of the peak to the right indicates smaller lattice constants for films on Si substrates as it shows tensile strain (i.e. smaller lattice) when it is compared to literature constants [17], while the ones on glass show compressive strain (i.e. larger lattice). Both peaks are shifted in the same direction indicating that the lattice spacing in either a-axis or c-axis oriented films is larger on glass substrates. The tensile strain is believed to have been caused due to the nucleation of deposited films on a wider (i.e. 3.84 Å) cubic lattice in comparison to the ZnO hexagonal lattice (i.e. 2.6 Å).

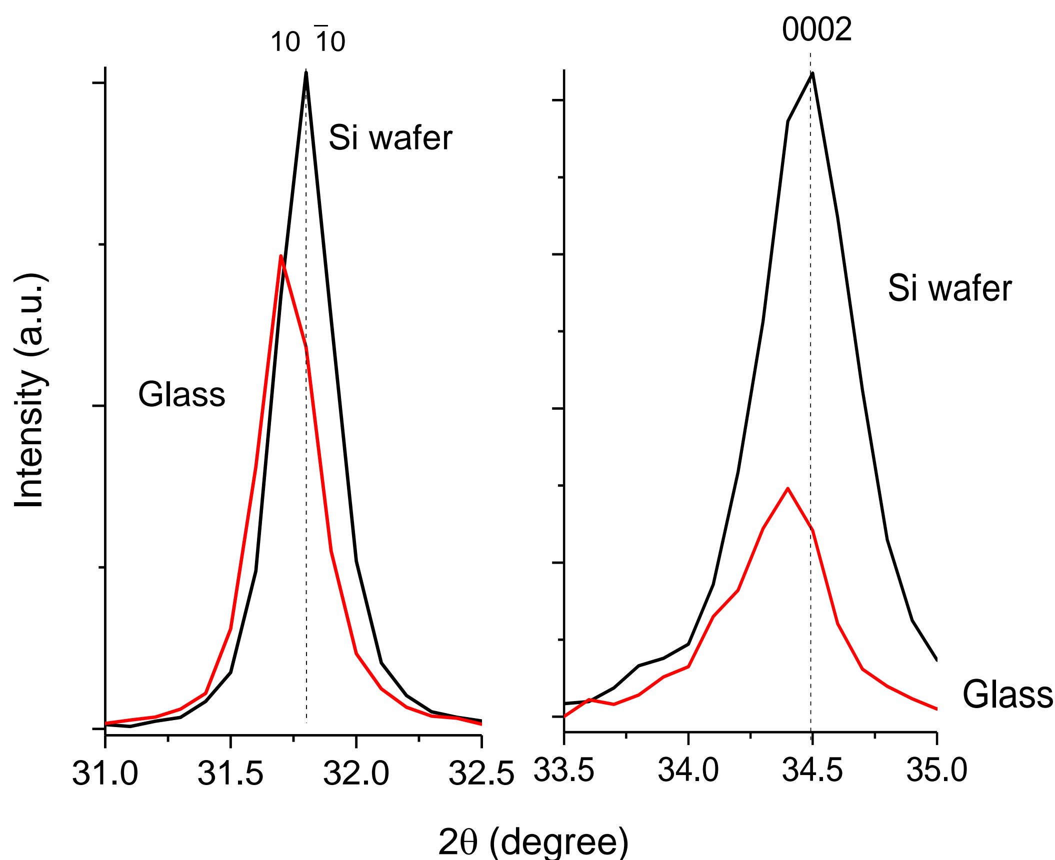

Figure 54: XRD peaks at $(10\bar{1}0)$ and (0002) planes of films on Si and glass substrates (different films are used with preferred orientation in either plane, hence the intensity is on in the same scale).

The general trend from literature is that Zr-doped ZnO films grown by different methods, have preferential c-axis orientation when deposited on crystalline substrates such as quartz with trigonal crystal structure [25],[53], but are usually polycrystalline films without specific preferred orientation when the substrate is amorphous such as glass [29],[49],[50]. Additionally, previous studies showed that as doping increases the c-axis orientation is preferred [46]-[47],[49],[56]-[57]. However, in some cases at heavier doping the (0002) peak intensity is reduced [26],[46],[57], which is attributed to the dopant segregation in grain boundaries [182]. Hence, the current study's data are consistent with the general orientation trend regardless the deposition method, while the preferred direction is the same for both substrates used.

4.3.3 Higher XRD peak intensity with doping

By directly comparing the diffraction patterns of un-doped and Zr-doped films of the same thickness at 95 nm, the (0002) peak intensity is observed to be greater for the doped film indicating increased degree of orientation in c-axis (Figure 55). As a result, it could be said that the addition of Zr dopant in the film results in the improvement of the crystals alignment in their preferred orientation. To support that, a-axis oriented films of thickness ~250 nm show the same tendency of the doped films having higher intensity of $(10\bar{1}0)$ peak than the un-doped films (Figure 55). This is not the case for all other peaks, as the (0002) peak is lower for the doped one, indicating that the higher intensity in the doped films is only observed for the plane in which the grains are preferred orientated. The high intensity in the doped films is

not grain size related as the AFM data showed that the features size is reduced by doping (Figure 52).

This trend for higher degree of crystal alignment with Zr doping is consistent with other studies such as the one by Paul et al. [49], who found a shift in orientation from (0002) to random as doping increased. Other researchers have shown the same trend of higher intensity and the absence of any ZrO_2 phase [45]-[46],[54],[56]. According to those studies, the substitution of Zr^{4+} ions into Zn^{2+} sites results in retention of the hexagonal structure [46],[56]. The increased intensity was reported as self-texturing phenomenon [182] and it was also reported by other techniques when using dopants such as Al [182],[310]-[311], In and Sn [311]. However, Zr dopant was found to result in higher peak intensity when directly compared to Al-doped films in the same study [54].

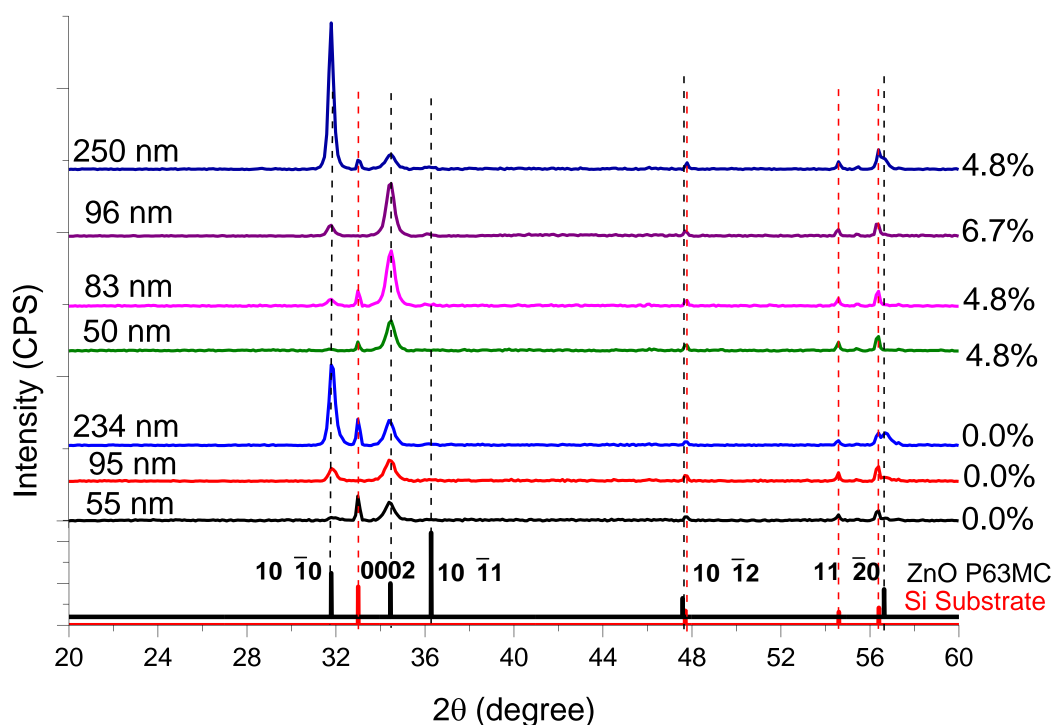

Figure 55: XRD comparison of similar thickness un-doped and Zr-doped ZnO films.

One explanation for this increase could be found through numerical analysis of the parameters contributing to the diffraction intensity. As explained in chapter 3, the peak intensity is affected by a number of geometrical parameters in the films. However, as the films are geometrically similar to each other the main focus will be on the multiplicity factor and structure factor. The multiplicity factor (M) causes higher intensity for the $(10\bar{1}0)$ peak (M=6) in comparison to the (0002) peak (M=2) due to the higher number of similar planes. This will mostly affect the correlation between the different thickness films. The factor that may cause differences between the un-doped and doped films is the structure factor. The structure factor depends on the atomic number of the elements [312], and so it is higher for Zr atoms (Z=40) rather than Zn (Z=30). Based on the relation in chapter 3 (Equation 40), the structure factor depends on the position of each atom in the crystal of *hkl* coordinates.

For a wurtzite structure, the O atoms are located at (000) and $\left(\frac{1}{3}\frac{2}{3}\frac{1}{2}\right)$, while Zn atoms are at $\left(00\frac{3}{8}\right)$ and $\left(\frac{1}{3}\frac{2}{3}\frac{7}{8}\right)$ positions [278]. By assuming that one ZnO unit cell is roughly formed after two ALD cycles, this will mean that Zr atoms were introduced to half unit cell for doping at $1.0\text{ at.\%}$, $2.7\text{ at.\%}$ and $4.8\text{ at.\%}$, while for the samples at $6.7\text{ at.\%}$ and $9.1\text{ at.\%}$ the Zr atoms were introduced after the completion of a unit cell. Therefore, it is assumed that for the heaviest doped samples the Zr atoms were introduced at $\left(00\frac{3}{8}\right)$ positions, while for the lower doped samples they were introduced at $\left(\frac{1}{3}\frac{2}{3}\frac{7}{8}\right)$. As a result, the intensity for the $(10\bar{1}0)$ peak is less affected by the Zr addition for the heavier doped samples due to their position in the crystals. This trend is consistent with the experimental data in which the a-axis peak is suppressed.

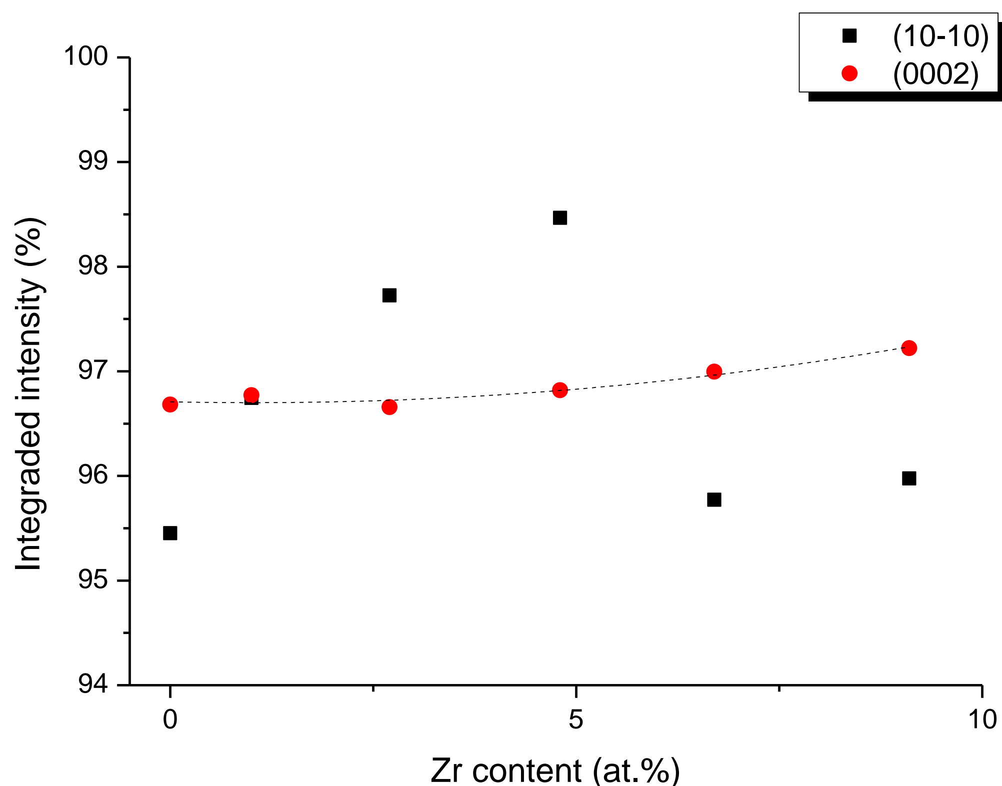

Figure 56: Theoretical integrated intensity data after being normalised to the powder intensities.

The numerical values of the integrated intensities for each doped film were calculated and are shown in Figure 56. The presented values are normalised to the normalisation factors established in section 3.8.2. Based on the graph, the structure factor has a larger effect on the intensity of the $(10\bar{1}0)$ peak compared to the (0002). By comparing the estimated numerical increase at 6.7 at.% doping to the un-doped, the experimental data show a much higher increase of 240% compared to the theoretical increase of only 0.3%, hence, it is unlikely to be the cause of the high peak intensity.

A different approach is to correlate the defects changes due to the addition of Zr atoms, which could contribute to the formation of less distorted hexagonal crystals

and so grains, could grow in better alignment. Those defects are the oxygen vacancies, which could be reduced when Zr is added to the system due to the strong Zr-O bonds leading to high oxygen vacancy formation energy (OVFE) [313]. In order to investigate this experimentally, XPS studies were carried out and showed a reduction of oxygen vacancies as doping increased. This will be discussed in more detail in section 5.4.1.

In summary, a very small fraction of the degree of orientation increase is attributed to the scattering factor, but the main cause is attributed to the reduction of oxygen vacancies (for both orientations) as doping increases.

4.4 Orientation shift

From the previous data it was suggested that as the grain size was increased, the orientation evolved from c-axis preferred orientation to a-axis orientation. In particular the heavier doped samples were highly c-axis oriented as doping induced grain size reduction (Figure 57), while the direct relation of grain size and thickness lead to a linear relation between thickness and orientation change from one direction to another. The data in this plot were analysed further using the texture coefficient given in Equation 47 [95], where F_C is the texture coefficient in *(hkl)* plane and P is the ratio of peak intensity over the sum of peak intensities in the same film. The reference peaks intensities used as P_0 were the peaks obtained from the ZnO powder diffraction pattern (section 3.8.2). The driven force for this change will be specified later in this section after analysing all possible scenarios correlated to literature.

Equation 47

$$F_{C(hkl)} = \frac{P_{hkl} - P_{0_{hkl}}}{1 - P_{0_{hkl}}}$$

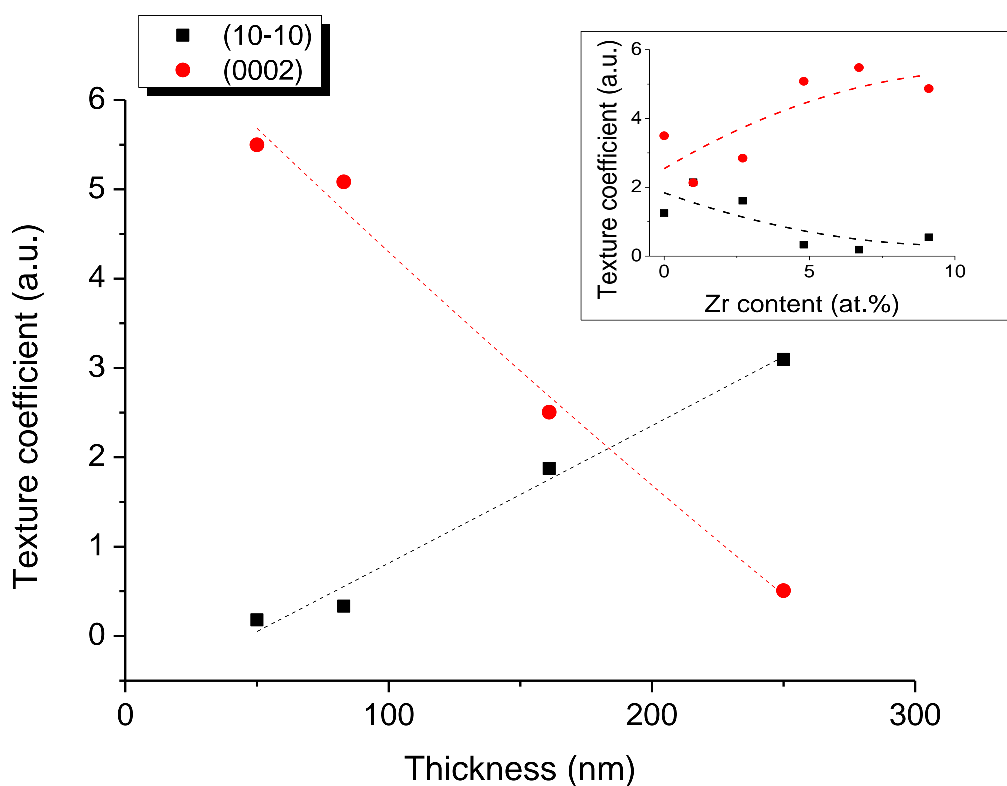

Figure 57: Thickness dependence of texture orientation.

The preferred orientation change in ZnO related to deposition factors was studied early in 1980s, when Murti et al. examined the role of the deposition rate on the crystal growth orientation [314]. The study using RF sputtered films suggested that at slow deposition rate the orientation is at (0002) direction, while at faster rates the orientation shifts to $(10\bar{1}0)$. The thickness of the film was believed to be a neutral factor in determining the orientation while it was stated that the lower deposition rate

corresponds to a higher probability of atoms rearrangement at the surface [314]. Fujimura et al. [231] also reported that the lower deposition rate favours (0002) orientation, adding that this is also the case for high temperature growth using RF magnetron sputtering. According to Nam et al. [315], the deposition rate also affects the crystal orientation in films grown using CVD. The results confirmed that at fast growth rate a-axis orientation is favoured while for slower rates the crystals have more time to be formed and arranged perpendicularly (c-axis) [315]. Those studies refer to growth techniques with tunable deposition rates, however for ALD the growth rate is typically very slow compared to these other techniques. As a result, the deposition rate is not a factor for the current shift.

A different scenario is the difference in growth temperature. Although this was controlled during the ALD process, the thermal resistance could be different for thin and thicker films, as it was stated by Xu et al. [316]. In the same study, the thermal resistance as a function of the film thickness was plotted, which showed higher value for the 250 nm (200×10^{-9} m^2KW^{-1}) compared to a 100 nm film (125×10^{-9} m^2KW^{-1}) [316]. Based on those observations and the fact that at low growth temperature the ALD ZnO films are reported as a-axis oriented [225], it is possible that the thicker films were deposited at a slightly lower surface temperature than the thinner ones. As it was mentioned in chapter 3, the measured temperature during deposition conditions is 186°C on top of a Si wafer. As a result, by applying simple heat transfer calculations and using the thermal resistance values by [316] converted to thermal coefficients, the temperature for the 250 nm film is 178°C compared to around 186°C for the thinner films. A similar surface temperature difference (5°C) was found between the two substrates used, and it was earlier found that it resulted in

the same preferred orientation in the films. Hence, the difference in temperature due to thermal conductivity is also unlikely to be the cause of the orientation shifts.

Other paper suggested that in the ALD the $(10\bar{1}0)$ orientation is favoured by the short purge time [224]. This is explained in terms of anions such as CH_{3-} originating from the source precursors adhering to the positively charge polar (0002) crystals, when the by-products increased in number due to insufficient purging. This theory is supported by the results in a previous report suggesting that the reduced purge time favours the non-polar $(10\bar{1}0)$ and $(11\bar{2}0)$ orientations [317]. Low growth temperature was reported to have the same effect when using DEZ, which is reported to dissociate into group fragments such as CH_{3-} and CH_3CH_{2-} at the same ALD growth temperature used in this study, resulting in non-polar m-plane (a-axis) films of thickness ~600 nm [318]. Nevertheless, this is unlikely to be the case in the current study as the films with a-axis and c-axis preferred orientation were grown using the same deposition parameters, including the purge time and growth temperature.

Pung et al. also stated that the ethyl groups from DEZ were the cause in a-axis orientation for films grown at low ALD temperature [225]. Nevertheless, the fixed number of cycles in that study suggests a variety of film thickness, starting from 240 nm for films within the ALD window that showed dual orientation and then at ~110 nm for the films deposited at much higher temperatures showing c-axis preferred orientation. This orientation is consistent with the current study, in which the temperature was kept fixed. This suggests that the thickness may be the main parameter for controlling orientation in the current study and the studies of [225] and [318]. Additional reports of ALD growths of ZnO have previously reported shift in

orientation as the number of cycles increases [319], and others for $(10\bar{1}0)$ preferred oriented ZnO thick films at the same conditions using a DEZ precursor [317]-[318].

4.4.1 Orientation shift by strain

The correlation of thickness to the changes in orientation, led to an examination of the differences between the two directions. Firstly, c-axis orientation is well established as the lowest surface energy orientation, and therefore the most thermodynamically favoured [215],[320]. More specifically its density of surface energy in (0001) equals 0.099 eV/$Å^2$ which is much smaller than the surface free energy of $(11\bar{2}0)$ plane at 0.123 eV/$Å^2$ and $(10\bar{1}0)$ at 0.209 eV/$Å^2$ [231]. The values were calculated by Fujimura et al. [231] based on the standard latent heat of vaporization (i.e. 3.61 eV/atom), the literature lattice constants and the number of atoms in the wurtzite unit cell. Based on the low surface density it is expected to have a high number of unsaturated bonds of Zn or O ions [315].

According to Fujimura et al., the (0001) orientation always occurs under equilibrium state as the sp^3 hybridized orbit bonding in hexagonal semiconductors spreads along the (0001) direction (i.e. each apex is parallel to the c-axis) [231]. Based on the same study, it was stated that it is only possible to grow other orientations under non-equilibrium conditions that deteriorate the formation of tetrahedral coordination. Nevertheless, this study by Fujimura et al. only takes into account the surface free energy and neglects the influence of strain energy on the system.

The strain energy of the films orientated in the $(10\bar{1}0)$ plane is lower than the ones oriented in the (0002) plane based on the Young's modules in each plane (i.e. E_{0001}=1.44 and $E_{10\bar{1}0}$=1.28 ($\times10^{11}$ N/m^2) [321]). In other orientations the strain is equal to or less than $(10\bar{1}0)$, such as the $(11\bar{2}0)$ plane ($E_{11\bar{2}0}$=1.28$\times10^{11}$ N/m^2) and the $(10\bar{1}1)$ plane ($E_{10\bar{1}1}$=1.19$\times10^{11}$ N/m^2) [321]. Low strain energy offers strain minimisation to the system and hence this might influence the preferred orientation if it is the dominant force. This occurs in films under high strain that could be induced by the enlargement of the grains.

The preferred orientation correlates to the energetic constraints of the surface/interface and strain energy minimisation [322], and the driving force is the one offering the lower energy to the system. Thompson et al. stated that the grain growth can minimise the surface/interface energy through the preferential growth of grains with orientations that offer low surface energy [323]. This happens when the system is under low strain i.e. small grains, and thus according to Carel et al. this is always the driven force for very thin films [322]. On the other hand, the growth of grains may switch to a different orientation to minimise strain energy if the system's strain is increased [324], for example when the grain size increases or when the films grow at low temperatures [325]. The grain size in the current study has been correlated to film thickness, hence, the thinner films are expected to be less strained and will therefore grow in the lowest surface energy orientation of (0002). By increasing the thickness of the films the strain increases and thus the need to minimise the strain energy also increases, hence the preferred orientation shifts to the immediately lower strain energy orientation of $(10\bar{1}0)$, consistent with the experimental data. The same effect was also reported by Singh et al. [226], showing orientation shift at ~200 nm thickness films consistent with the current study, although the current study shows much more

dominant peaks in the preferred orientation for similar thickness films. In conclusion, as the thickness increases the strain must be minimised, thus the orientation will firstly shift to the $(10\bar{1}0)$ or $(11\bar{2}0)$ plane, and when the strain increases further it is expected to shift to the $(10\bar{1}1)$ plane. Films oriented in the $(10\bar{1}1)$ plane grown by magnetron sputtering were shown by Lee et al., having thickness of a few microns [321].

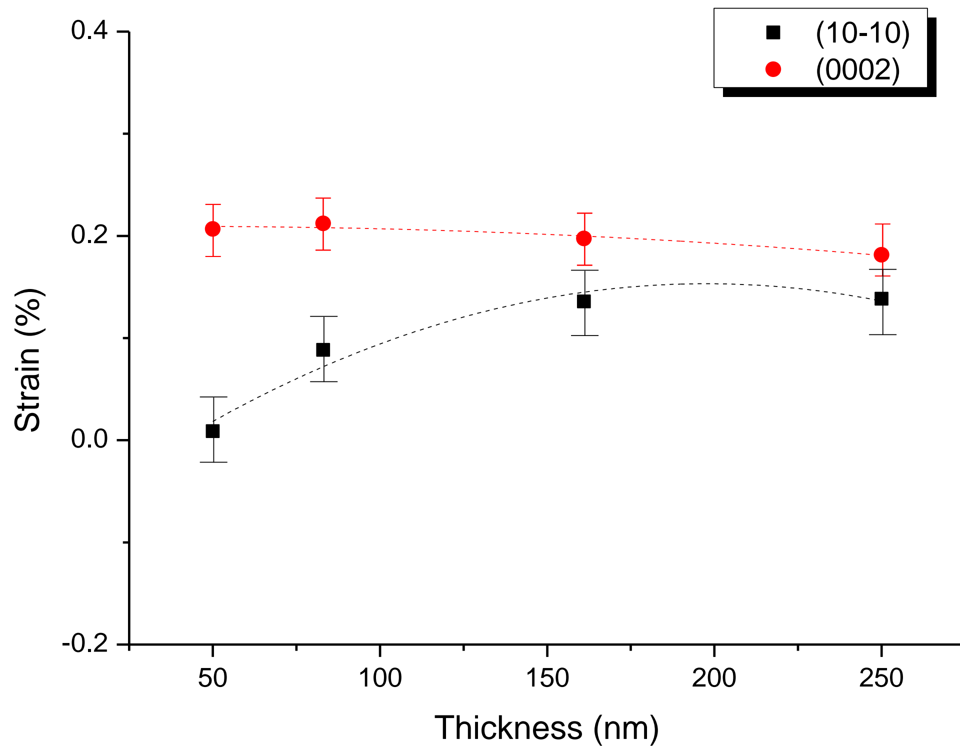

Figure 58: Thickness dependence of strain for $(10\bar{1}0)$ *and* (0002) *planes of 4.8 at.% doped films on Si substrates.*

In order to specify the orientation transition point, the percentage strain needs to be determined for different film thicknesses with fixed doping (Figure 58). The strain in the $(10\bar{1}0)$ and (0002) planes reflects the lattice changes of crystallites orientated in

that direction. The strain values are the results of comparison between the films constants and the pure ZnO values of $d_{(10\bar{1}0)}$=2.815Å and $d_{(0002)}$=2.604Å [17]. The strain analysis on the different thickness films (Figure 58) show almost no difference in the c-axis tensile strain, while the a-axis shows increased tensile strain as thickness increases, as most of the grains are oriented in that direction.

The orientation turning point from the surface energy to strain energy minimisation can be estimated by the thickness critical value within 100-200 Å/strain % (i.e. percentage strain thickness product) [326]. To estimate those points the strain values used were normalised to 100 nm in order to neglect the thickness differences between the samples. Those values were then used in Equation 48 to calculate the critical thickness (t_C) based on the product of 100-200 Å %, which differed for each doping level (Table 6).

Equation 48

$$t_C = \frac{100(or\ 200)}{\varepsilon}$$

Table 6: Critical thickness estimation using the percentage strain thickness product.

Zr contents (at. %)	Normalised Strain (%)	t_C for 100 Å% (nm)	t_C for 200 Å% (nm)	Average t_C (nm)
0.0	0.14	73.5	147.0	110.2
1.0	0.13	79.7	159.4	119.6
2.7	0.25	39.2	78.4	58.8
4.8	0.25	39.3	78.5	58.9
6.7	0.24	41.8	83.6	62.7
9.1	0.22	45.7	91.3	68.5

The strain values used for the calculations are the ones parallel to the c-axis, since this is the initial growth orientation of thin films. The films showing a high strain induced by doping tend to shift to a different preferred orientation at a lower thickness. For example, the 4.8 at.% doped film has a critical thickness of 59 nm, which is much lower than the un-doped film which is expected to shift at around 74 nm. Experimentally, the shifting point for un-doped ZnO is found to be about 60 nm based on the XRD analysis, where the $(10\bar{1}0)$ peak appeared in both films. For the un-doped film the peak appeared as early as 55 nm, which is an indication of having greater strain due to the larger grains in comparison to the Zr-doped films.

In order to establish the point where the strain energy (U) is higher than the lower surface energy (S), the surface and strain energy were calculated at different thicknesses with fixed doping. The sum of the surface and strain energies adds to the total system energy (E_{tot}=S+U). The surface energies for each orientation were already established in [231] as S_{0002}=1.59×10^{-6} Jcm^{-2} and $S_{10\bar{1}0}$=3.3×10^{-6} Jcm^{-2}. The strain energies on the other hand can be calculated by the standard formula shown in Equation 49 [324], where ε is the strain in the plane *hkl*, E is the Young's modules, and V is the volume. By keeping the area as an unknown factor, the energy was calculated in Jcm^{-2} with the use of the film thickness. The corresponding values are shown in Table 7.

Equation 49

$$U_{hkl} = \frac{\varepsilon^2 E_{hkl} V}{2}$$

The calculated data show that the strain energy per unit area is higher for the (0002) plane than for the $(10\bar{1}0)$ plane for all cases, proving the lower strain energy in a-

axis. The increasing strain energy in the c-axis is beyond the surface energy from the 83 nm film, showing that the grains were forced from that point to start growing in the a-axis direction for energy minimisation. The thickness turning point is estimated when all energies are plotted for the 4.8 at.% doped sample in Figure 59.

Table 7: Strain energy for different thickness films with 4.8 at.% doping.

Thickness (nm)	Strain Energy $(10\bar{1}0)$ J/cm^2	Strain Energy (0002) J/cm^2
50	2.46×10^{-9}	1.54×10^{-6}
83	4.15×10^{-7}	2.69×10^{-6}
161	1.90×10^{-6}	4.52×10^{-6}
250	3.07×10^{-6}	5.93×10^{-6}

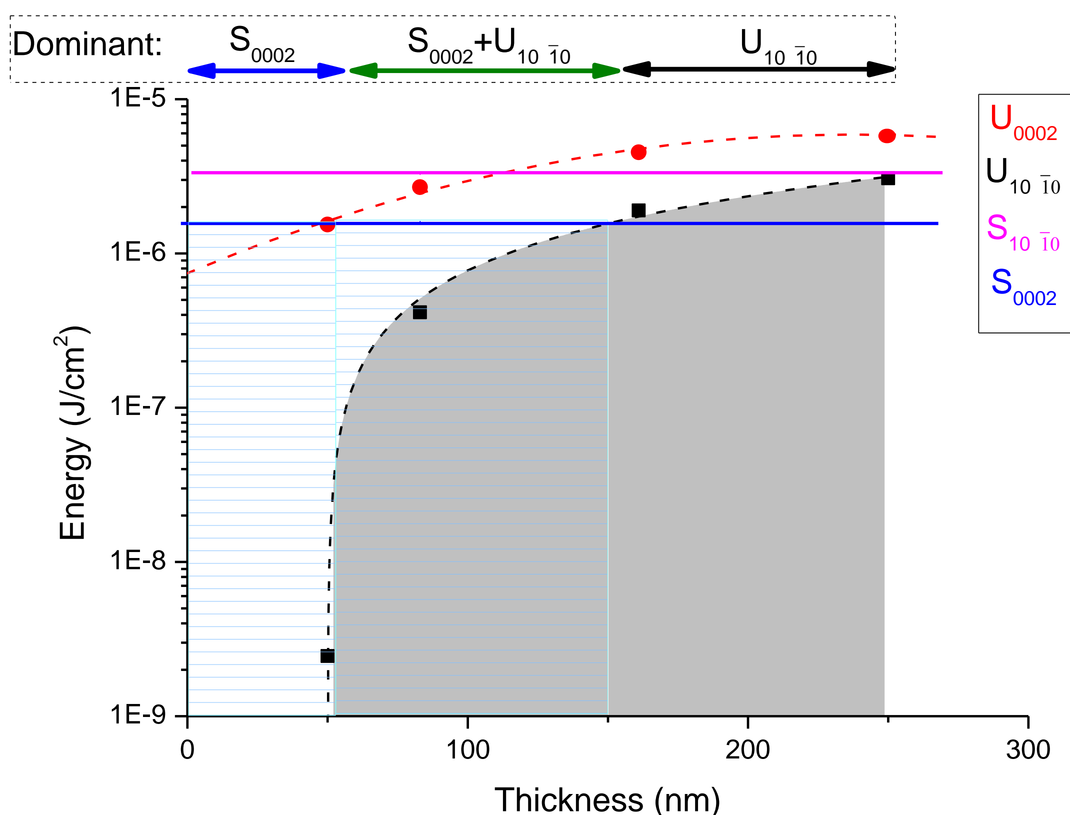

Figure 59: Surface and strain energy components as a function of film thickness with 4.8 at.% doping.

The graph shows the fixed surface energies of the two orientations and the curves of the increased strain energies as thickness increases. The range between 0-53 nm shows that the strain energy (U_{0002}) is lower than S_{0002}, hence the preferred orientation is in (0002) direction to minimise the system's energy. However, above 53 nm the strain energy in (0002) (U_{0002}) increases more than S_{0002}, forcing the grains to start growing in a less energy consuming orientation (i.e. $(10\bar{1}0)$ orientation). The strain energies of both directions are higher than S_{0002} above 150 nm, which is believed to be the point where grains have preffered orientation in a-axis. This is consistent with the XRD data that showed more dominant a-axis orientation starting from 161 nm thickness. The existence of a high intensity (0002) peak in the same XRD pattern is believed to be due to diffraction from the basal planes of c-axis orientation.

4.4.2 TEM study of the thicker doped film

Due to the limited number of samples with thickness around 60-70 nm in which the orientation turning point was estimated, the confirmation of the thickness turning point was only possible using electron microscopy on cross sectionAl-doped films. As a result, TEM was carried out on the 83 nm and 250 nm films with 4.8 at.% doping on Si (100) substrates, as shown in Figure 60. The images illustrate the top interface to Pt which was applied as a conducting layer at the top to allow the TEM scan, and at the bottom is shown the Si substrate with the 2-3 nm buffer layer of Al_2O_3. Both films show large grains of ~60 nm for the 83 nm film, and up to 115 nm long grains for the thicker film, confirming the AFM map that shows grains up to

50 nm and 110 nm respectively. Additionally, the thickness measured is consistent with the ellipsometer readings. Another confirmation was for the roughness of the films earlier stated during the AFM study, showing a much rougher surface for the thicker film compared to the thinner one.

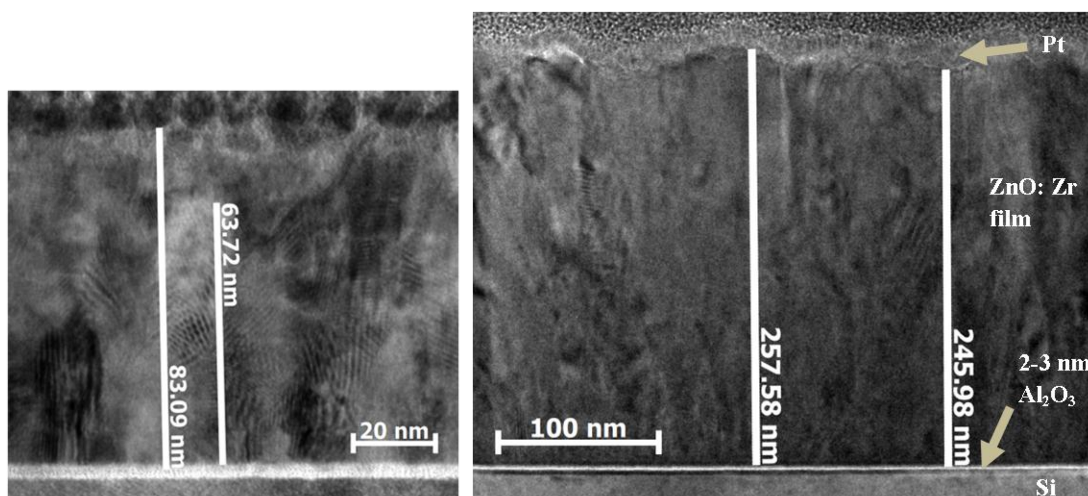

Figure 60: TEM cross section of films a) 83 nm and b) 250 nm thick with 4.8 at.% Zr doping.

The 250 nm film was used to determine the orientation shift point, by measuring the basal planes spacing (Figure 61) and using FFT for the near surface planes (Figure 62). FFT analysis was not possible in the basal planes due to overlapping of the grains (fringes effect). Nevertheless, the planes distance was found to be 2.6 Å in the basal planes consistent with the (0002) d-spacing. The average distance of 10 spacing was measured to be 2.69 Å, which is slightly larger than expected possibly due to the addition of Zr atoms. At the top of the layer, the distance is larger based on the ZnO crystal arrangement pattern in $<01\bar{1}>$ direction applied on top of the obtained FFT. By using the FFT, the distance of 2.9 Å is measured by the half

spacing between $(10\bar{1}0)$ and $(\bar{1}010)$ planes. This distance is in close approximation with the expected $(10\bar{1}0)$ d-spacing.

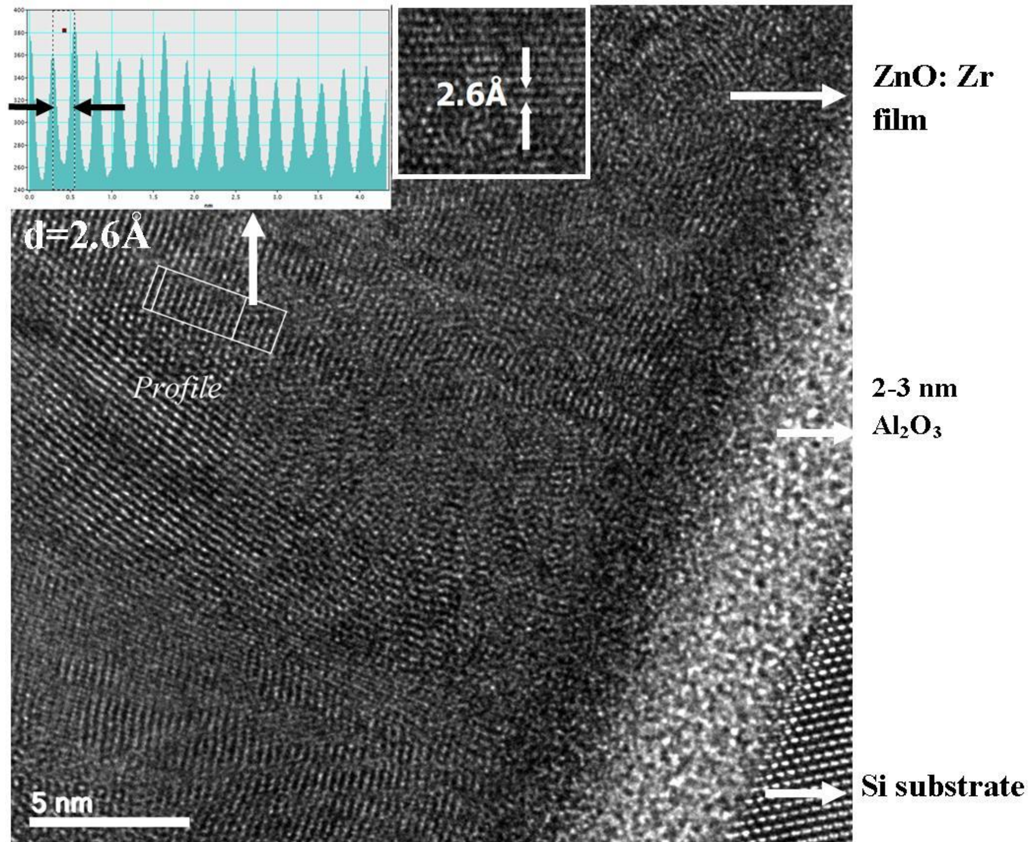

Figure 61: TEM image of 250 nm thick film with 4.8 at.% doping at the Si interface and basal plane.

For further confirmation of the orientation shift with thickness, a bright field cross section TEM image of the 250 nm thick film was taken (Figure 63). As shown the grains are initially columnar and small in size at the first 70 nm of growth. The grain size ranges between 40-90 nm in those basal layers, with an average value of ~57 nm. Above this initial 70 nm, the grains become more horizontally aligned than columnar, shown as cone shaped. The orientation shift is therefore ended at ~70 nm in thickness, in close agreement with the numerical model (i.e. 58 nm on average),

and also to both AFM and XRD data that showed the existence of large grains oriented in parallel to the substrate.

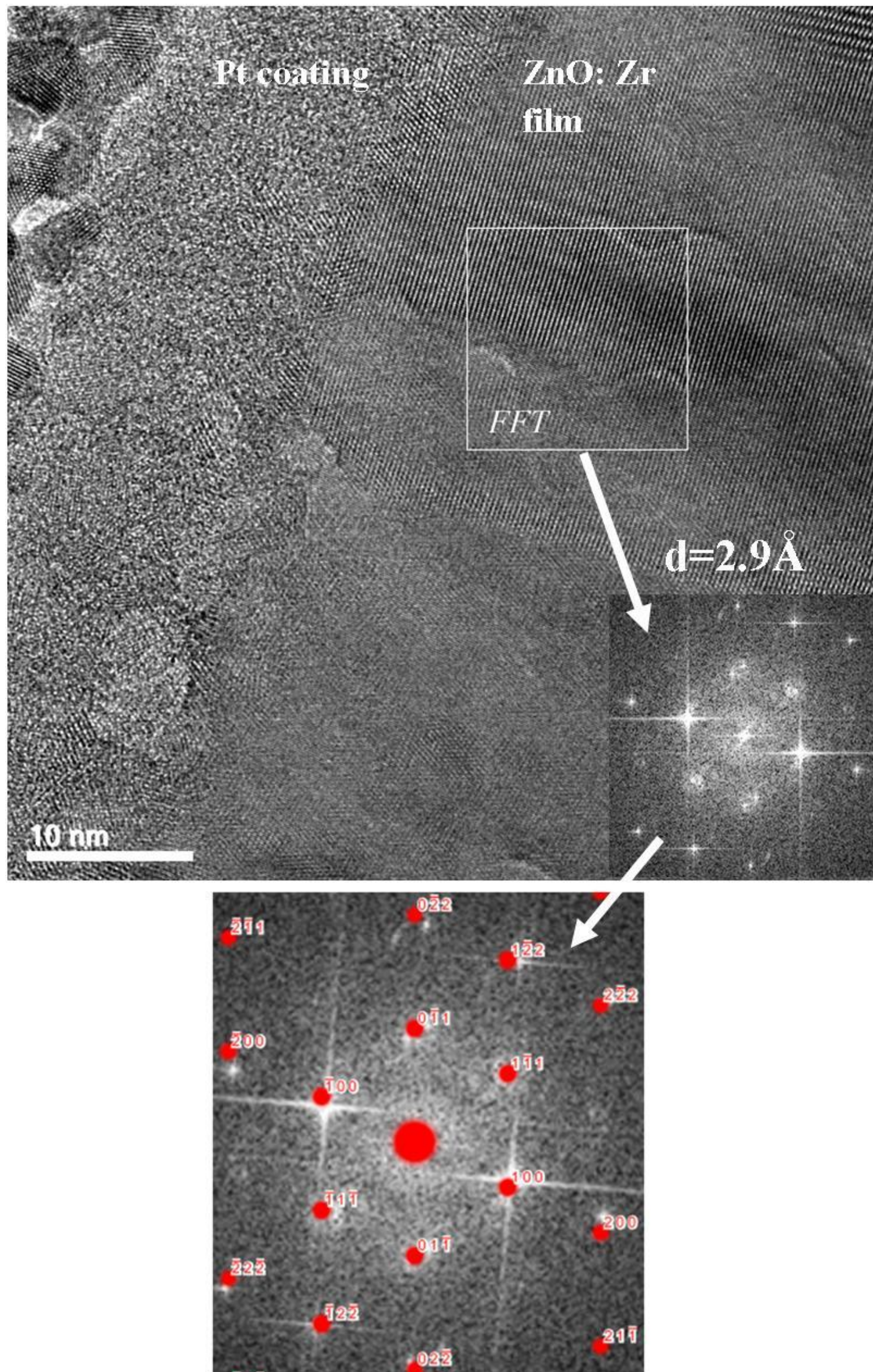

Figure 62: TEM image of 250 nm thick film (4.8 at.% doping) at Pt interface and near surface planes.

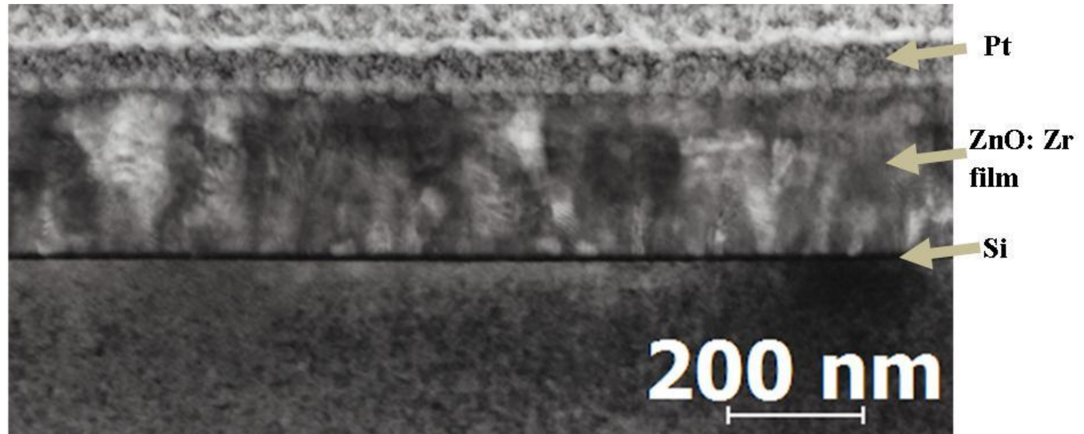

Figure 63: TEM cross section image of 250 nm thick film with 4.8 at.% doping.

4.5. Conclusion

In conclusion, the orientation of the Zr-doped ZnO films were shown to be a function of film thickness. Hence, non-polar m-plane ZnO films were grown at 250 nm thickness, and polar c-plane ZnO films up to ~70 nm. The mechanism behind this was identified as the tendency of the grains to grow in the lowest energy orientation. Therefore, when the grains are small and the strain is low, surface energy controls the orientation resulting in (0002) plane preferred orientation. When the grains are large enough to induce high strain within the structure, the orientation is shifting to a lower strain energy orientation across the $(10\bar{1}0)$ plane. The grain size was found to be reduced proportional to the amount of Zr doping. At high growth temperature the grains were shown to be increased in size. Finally, the grain size was found to be increased as the overall film thickness increases.

The orientation shift due to thickness was confirmed using AFM, which showed at the surface vertically aligned grains at low thickness (<100 nm) and then horizontally aligned grains at high thickness (>100 nm) films. XRD also showed preferred orientation in the $(10\bar{1}0)$ plane for thicker films, while thinner films showed preferred orientation in the (0002) plane. Finally TEM shows that the basal grains in the 250 nm thick film initially grow with a preferred c-axis orientation for around the first 70 nm and then the orientation begins to shift towards an a-axis preferred orientation. This shift can be explained using a theoretical model based on system energy minimisation, which indicates that c-axis is energetically preferential for thicknesses up to around 53 nm. Within this thickness range, surface energy is the controlling factor within the energy model. At thicknesses between 53 nm and 150 nm, the model shows that a-axis starts to become energetically favourable. Within this thickness range, larger crystallites cause an increase in the internal strain energy and as a result, strain energy rather than surface energy becomes the controlling factor within the model. At thicknesses higher than 150 nm, the grains grow preferential in the a-axis orientation.

Doping had no effect on the overall trend of the orientation shift, although the increased strain in the lattice induced the shift to occur at lower thickness. However, doping showed a tendency of higher XRD peak intensity in comparison to the un-doped films due to the removal of defects (oxygen vacancies) that help to retain the hexagonal structure of the crystals. The increase in a-axis lattice constant as doping increased, showed the addition of the larger Zr atoms compared to Zn. The decrease in the c-axis was related to the grain boundaries increase as doping increases, which apply more pressure to the basal crystals. The a-axis preferred oriented grains at the top of the film are less affected by the boundaries pressure.

Chapter 5

Electrical properties and chemical state of ZnO and ZnO: Zr

5.1 Introduction

In the current chapter, the effects of growth temperature, Zr doping concentration and film thickness on the electrical properties of the films are investigated. In this chapter the main focus is to establish and possibly control the electrical properties through 'delta' Zr doping, which is expected to result in high carrier concentration due to their extra electrons compared to Zn. The reduction of resistivity is also targeted through scattering reduction by increasing the film thickness. The resistivity was aimed $<10^{-3}$ Ω·cm and at least 10^{20} cm^{-3} carrier density [14] for better TCO performance. The chemical state is also important to prove that zirconium is indeed incorporated in the lattice by showing that exists on its ionic state (Zr^{4+}). XPS analysis was carried out at the end of this chapter for this purpose.

5.2. Growth temperature of un-doped ZnO

Prior to analysis of doped ZnO, it was essential of establishing the best growth temperature giving the lowest resistivity within the ALD window. This was completed through the un-doped ZnO characterisation of ~40-60 nm thickness films (Figure 64). This graph illustrates the resistivity measured by four-point probe and also the overall film thickness measured by ellipsometer, for films grown between 100°C to 275°C. The thickness reduction for the films grown at high temperatures is attributed to desorption of DEZ beyond the ALD window (see chapter 3), which may have caused the resistivity increase.

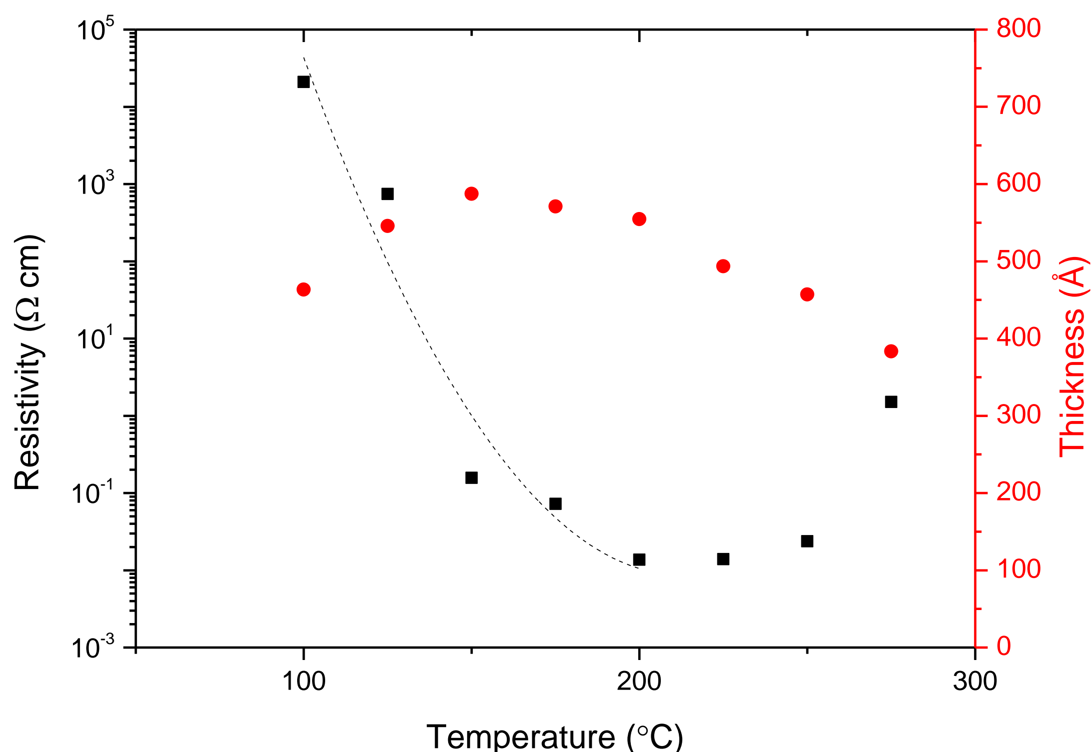

Figure 64: Resistivity and growth rate dependence of growth temperature for un-doped ZnO films grown at 300cycles.

The films within the ALD window (130-200°C) show reduction of resistivity by four orders of magnitude as temperature increases from 130°C to 200°C. At temperatures higher than 200°C, the film thickness changes rapidly and thus resistivity gradually increased by up to two orders of magnitude. Film thickness is known to have a significant effect on the resistivity of very thin films as decreasing thickness causes increasing interfacial scattering, which decreases the carrier mobility and hence increases resistivity. Between 200°C and 275°C, the film thickness decreases from 55 nm to 38 nm, and as a result, resistivity variation with temperature cannot be accurately evaluated and hence the trend line is not extended into this region. Therefore, the growth temperature resulting in the lower possible resistivity within the ALD window (i.e. optimum precursors function) is at 200°C.

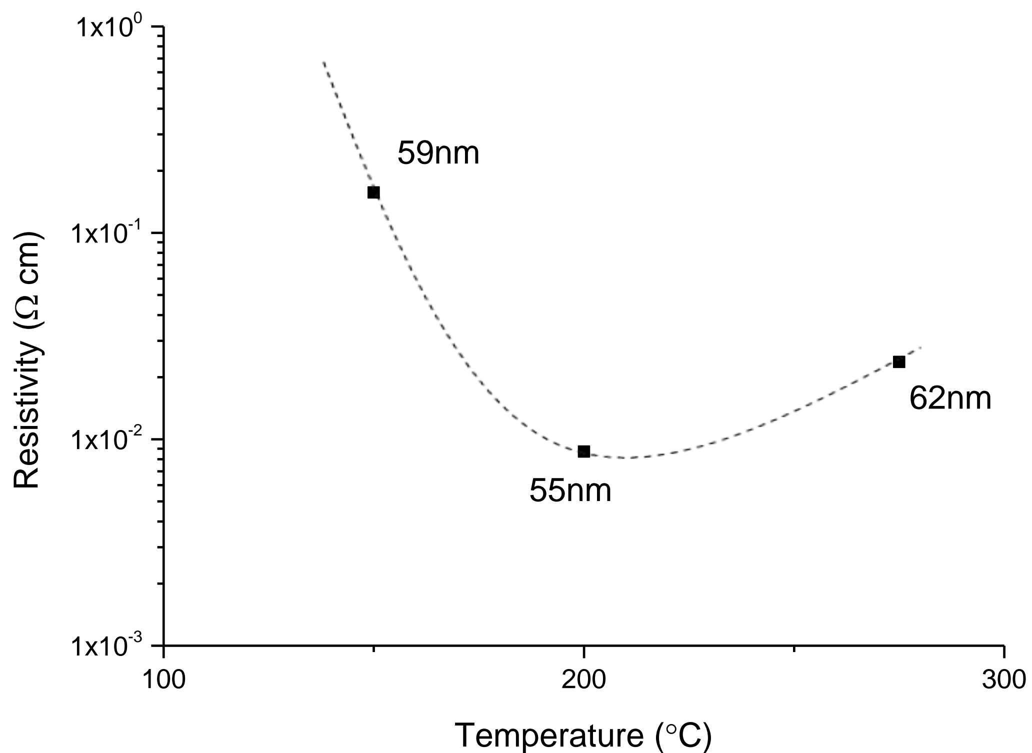

Figure 65: Resistivity dependence on temperature, by comparing similar thickness un-doped films (i.e. 49-62 nm).

In order to evaluate whether higher temperature growth may have resulted in lower resistivity, a comparison with similar thickness films was carried out and is shown in Figure 65. The graph shows again that the 200°C film has the lowest resistivity, even though it has slightly lower thickness (55 nm) than the 275°C film (62 nm). The fitted trend is shown to increase beyond 200°C, which is believed to be due to desorption of DEZ beyond that temperature leading to the reduction of intrinsic ions in the films. Consequently, the comparison data confirmed that the deposition at 200°C results in the lowest possible resistivity.

The findings of this study are consistent with literature, since ZnO ALD films deposited using DEZ tend to be more conductive films when grown at 200°C [34],[217],[257]. The explanation given was that the existence of native defects (i.e. oxygen vacancies or interstitials) with thermal ALD resulted in a resistivity decrease at 200°C [257]. The same explanation was used in another study, trying to explain the high resistivity recorded for the low temperature grown films, suggesting that the intrinsic defects (e.g. oxygen vacancies) were suppressed at low temperature due to the low thermal energy, which was not enough to overcome their activation energy [220]. On the other hand, the lack of extrinsic un-intentional donors may be the cause of resistivity reduction at high temperature, linked to the effect of hydrogen in ZnO. Van de Walle purposed that H^+ acts as a shallow donor to ZnO and it is a source of conductivity [327]. Due to the strong O-H bond, hydrogen has low formation energy in any Fermi level position [327].

The position of hydrogen in ZnO lattice was either interstitial or substitutional to oxygen as it was found by Bang et al. [328]. H was shown to result in concentration decrease from 300°C and diffusion at 475°C, while the interstitial H diffuses much earlier at 125°C, and then it was restored for temperatures between 200°C and 500°C

for 12.5 μm films [328]. The same team showed that the increasingly thickness of the film causes increase of the diffused temperature [329]. As a result, in the current study the diffusion is expected to start at lower temperature for films in the order of 100 nm. Unfortunately, it was not possible to determine the actual position with the available equipment in this thesis as both possibilities are valid at the growth temperature of 200°C, thus both will be considered.

The concept of H acting as donors in ZnO is still in dispute as H-free ZnO samples were reported with high conductivity [90]. Nevertheless, hydrogen doped ZnO films were reported using ALD with hydrogen plasma steps at 200°C [330]. As the hydrogen concentration increased they reported increased carrier density up to one order of magnitude reaching a value of 4.6×10^{20} cm^{-3} [330]. However, at higher temperatures hydrogen was reported to be diffused by using RF sputtering [330]. This was consistent with another study using atmospheric pressure MOCVD where hydrogen was added during the deposition process, which showed that it was difficult to incorporate hydrogen into ZnO films at high temperature [332]. As a result, it is possible that ALD deposition allows H incorporation into ZnO at 200°C and act as un-intentionally dopants. The hydrogen could either come from the H_2O co-reactant or the ethyl groups from the organic precursors used in this study.

Consequently, it is proposed in this study that the defects developed at 200°C favoured higher carrier concentration than any other temperature, due to the formation of intrinsic defects that are suppressed at lower temperatures and due to hydrogen impurities that are suppressed at higher temperatures. Unfortunately, no definite identification of the hydrogen concentration could be shown in this study as XPS does not detect light elements.

5.2 Zr-doped ZnO films electrical properties

5.2.1 Resistivity, carrier density and mobility of the ZnO: Zr films

The effect of doping on resistivity is presented in Figure 66, based on both four-point-probe and van der Pauw measurements. The doping concentration clearly affects the conductivity, with a minimum resistivity in the region between 1-4.8 at.% Zr. The reduction is due to mechanisms discussed later in this section. The lowest resulting value is 1.44×10^{-3} Ω·cm for 4.8 at.% doping, indicating that a further decrease is required to match the ITO resistivity. The lowest value was approximately the same as the previously reported ALD deposited ZnO: Zr films [25], while the effect of doping concentration on resistivity (initial decrease followed by an increase), is widely reported for other doped ZnO systems, such as ZnO: Al [30], ZnO: Ge [27], ZnO: Ga [37] and ZnO: Ni [173].

The majority of carrier concentration and mobility was measured by Hall effect and the results are shown in Figure 67. The carrier concentration increases with Zr doping up to 4.8at. % and then decreases at higher doping, with all doped films showing higher values than the un-doped film. The maximum carrier density is at 3.81×10^{20} cm^{-3} with a corresponding mobility of 10.4 $cm^2V^{-1}s^{-1}$ for the 4.8 at.% sample. Those properties comply with the TCOs requirements of having carrier density in the order of 10^{20} cm^{-3} or higher [14]. The carrier densities are consistent with the resistivity data, suggesting that the same reasons for the resistivity reduction up to 4.8at. % doping also applied for the carrier density increase.

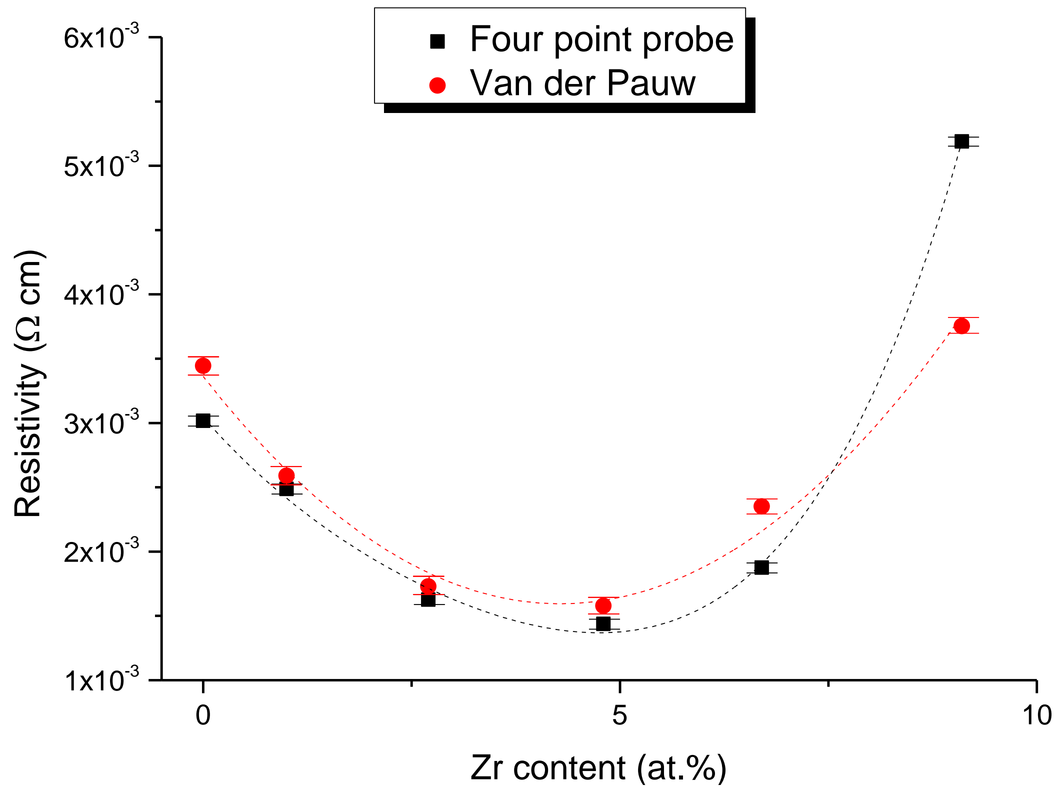

Figure 66: Zr doping dependence of resistivity for films ~85 nm thick.

In comparison to the literature, the value found in the current study for un-doped ZnO of 1.0×10^{20} cm^{-3} is consistent with ALD grown ZnO films at 200°C (200 nm) [208]. On the other hand, the carrier density recorded for ~100 nm thick ALD films doped with 2% of Zr concentration, was lower (i.e. 2.2×10^{20} cm^{-3}) than the current study, but the carrier mobility was higher (i.e. 19.7 $cm^2V^{-1}s^{-1}$) [25]. Carrier density of similar values was also reported for ZnO: Zr films grown by RF magnetron sputtering (300 nm) of 1.95×10^{20} cm^{-3} [57], with mobility of ~15 $cm^2V^{-1}s^{-1}$ again higher than the one of the current most conductive film. The films grown by spray pyrolysis [26] and sol gel method [49] showed a much lower resistivity in the order of 10^{-2} Ω·cm and carrier density in the order of 10^{19} cm^{-3}. This suggests that the carrier density in the current study is high, but scattering mechanisms reduced the carrier

mobility. The resistivity could be reduced further by controlling the scattering mechanisms as discussed in section 5.2.5.

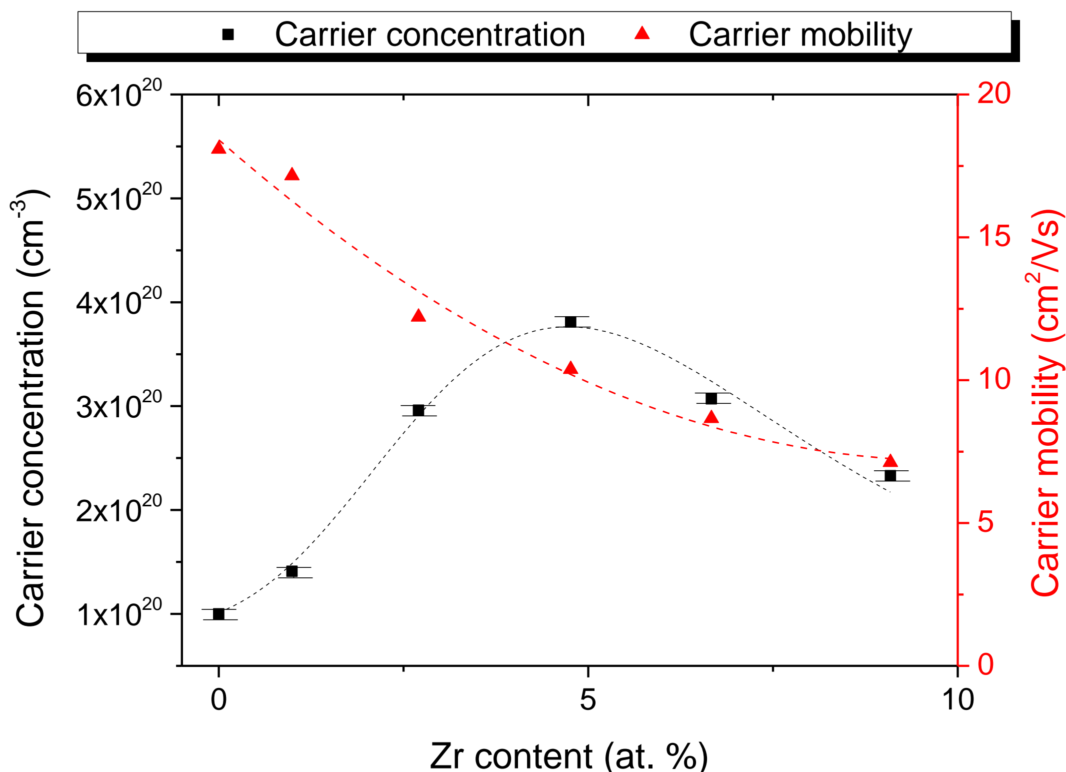

Figure 67: Zr doping dependence of carrier concentration and mobility for films ~85 nm thick.

5.2.2 Carrier density increase at low Zr doping levels

The carrier density increase with Zr doping originates from the placement of Zr atoms within the ZnO film. The Zr ions in ZnO may sit on three possible sites within the crystal lattice; substitution onto Zn sites, substitution onto O sites, and interstitial sites. The placement of Zr at interstitial sites was discussed in section 4.3.2., and was rejected as a likely position due to the increase of the crystal alignment as doping

increased. If Zr was substitutional to oxygen sites, the lattice would have a large lattice distortion due to the repulsive interaction between Zn and Zr ions [43], which would be observed as a larger increase in the d-spacing. The repulsive interaction makes it very difficult to form Zr-Zn bonds, although it was reported to be produced by a long chemical mixing process [333] with bond length of 2.7 Å. As a result, the most likely scenario based on the very small microstructural differences observed with doping in the current work is believed to be Zr substitutional to Zn sites. The carrier density increase is attributed to the additional Zr ions acting as donors. Zr is ionised into Zr^{4+} compared to the existing Zn^{2+}, providing up to two extra electrons per ion [49]. Its ionic state (Zr^{4+}) is experimentally proven by the XPS data presented in section 5.4.1.

The carrier density increase with doping is consistent with the first principle calculation study by Wang et al. [43], who examined the effect of all three placement possibilities. Their study showed that Zr substitution of Zn had the lowest formation energy (E^f) (–3.68 eV) in comparison to placement onto interstitial (i.e. 2.13 eV) and oxygen sites (i.e. 3.28 eV) [43]. The case of Zr substitutional to Zn resulted to an increase in the Fermi energy leading to higher conductivity, while the other two cases showed little impact [43].

The formation energy is related to the impurity concentration (c) in the semiconductor, and hence influences the concentration of donors that are added to the system. The relationship is given by Equation 50 [327]. Based on this, a low activation energy results in a larger number of ionised impurities and as a result to a higher carrier density. The number of available sites is controlled by the doping ratio, which agrees with the experimental data at low doping, but does not explain the observed reduction in conductivity at higher doping level.

Equation 50

$$c = N_{sites} \exp\left(-\frac{E^f}{kT}\right)$$

where N_{sites} are the number of available placements in the lattice, k is the Boltzmann's constant and T is the temperature. Further information about the position of the Zr-O bonds in the structure were given by Pala and Metiu, who suggested that some dopants such as Zr prefer to substitute to Zn sites in the bulk, while others such as Co prefer to substitute to Zn sites at the surface [313].

ZnO consists of ionic bonds between Zn^{2+} and O^{2-}, thus, the ions are shared between them and do not contribute to conductivity. The free electrons causing the n-type semiconductor behaviour originate from the intrinsic donors and hydrogen in the films. By adding Zr^{4+} in the lattice, the extra two carriers per ion will contribute to conductivity. The expected added carriers by 5 at.% Zr doping can be estimated by calculating the total number of atoms in ZnO per cm^3 using the theoretical density calculations (ρ=(number of atoms × atomic weight)/(unit cell volume × N_A)) resulting in 4.1×10^{22} cm^{-3} atoms, from which 5% of the double donor will provide 4.1×10^{21} cm^{-3} extra carriers. This significant difference to the experimental results of 2.8×10^{20} cm^{-3} extra carriers, possibly suggests the formation of defects during doping. Hence, the carrier density increase measured for the Zr-doped films could be attributed to the free electrons by Zr atoms, but not all possible extra carriers act as free carriers.

5.2.3 Carrier density decrease at high Zr doping levels

To confirm that 4.8 at.% Zr gives the most effective doping, a slightly thicker film of 6.7 at.% doping was grown (96 nm compared to 83 nm for 4.8 at.%). The resistivity recorded for the 6.7 at.% film (1.45×10^{-3} Ω·cm) is slightly higher than the 4.8 at.% film (1.44×10^{-3} Ω·cm), and well below the un-doped film resistivity of 3.02×10^{-3} Ω·cm. The similar resistivity between the two doped films is the result of the higher carrier mobility of the 6.7 at.% film (i.e. 11.0 $cm^2V^{-1}s^{-1}$ in comparison to 10.4 $cm^2V^{-1}s^{-1}$) and its lower carrier concentration (i.e. 3.23×10^{20} cm^{-3} in comparison to 3.81×10^{20} cm^{-3} of 4.8 at.%). The reduction of the free electrons concentration at higher doping suggested the formation of neutral defects.

Paul et al. [49] suggested that neutral defects were formed at high Zr doping levels, causing the Zr donors ions to be neutralised. At high doping levels, acceptor defects can be formed that combine to some of the donors (neutralise), causing the reduction of conductivity. The intrinsic defects acting as acceptors are zinc vacancies (V_{Zn}) [95], which have the lowest formation energy of acceptor-type defects in ZnO [85]. In fact, their formation energy decreases as the Fermi energy increases, leading to easier formation in n-type materials compared to p-type ones [85]. V_{Zn} cannot contribute to p-type conductivity as they form deep acceptors. Nevertheless, their formation energy is lowest in oxygen rich conditions [333], leading to the assumption that increased concentration of oxygen in a highly n-type film (i.e. Fermi level high), would favour the formation of more zinc vacancies and thus neutralisation of free donors. The increase of resistivity could also be connected to Zr segregating at grain boundaries as doping increases according to the studies [49],[57]. This has already been suggested in the previous chapter as a possible mechanism for explaining the

observed decrease in grain size with increasing doping. Zr segregation would not only result in carrier scattering at grain boundaries, but also to the carrier density decrease as the segregated dopants will not contribute to the addition of extra carriers in the system.

In this study, it is proposed that the effect of carrier density decrease at high doping is due to a combination of both of these mechanisms. Zr segregation at grain boundaries causes enlargement of the boundaries through decrease of the grain size. As a result, the creation of larger boundary areas is likely to help drive the formation of more zinc vacancies. This is due to the tendency of ions traveling towards the material rather than grain boundaries, which create more vacancies in the boundaries. As a result, the combination of Zr^{4+} and V_{Zn} at the boundaries forms neutral defects and reduces the number of free electrons. This suggestion is supported by the observation of zinc vacancies in the doped films, which are in higher concentration for the two heavier doped films as shown by PL data in section 6.3.2.1.

5.2.4 Carrier mobility reduction with Zr doping

The carrier mobility decreases with doping as shown in Figure 67. This reduction was related to the scattering mechanisms such as interfacial scattering, ionized and neutral impurity scattering, surface scattering, acoustic phonon scattering, piezoelectric scattering, scattering by dislocations, and scattering in the grain boundaries. The mechanisms were discussed in section 3.5.1 and some of those were neglected for the current measurements, such as the neutral impurity scattering, the

acoustic phonon scattering, and the piezoelectric scattering. The surface scattering is also rejected based on the small variations of roughness as the doping increases (see section 4.3.2). The ionized impurity scattering is expected to increase as doping increased in the current films, while the small variation in thickness might cause interfacial scattering increase as doping increases.

The scattering at grain boundaries is directly related to the decrease of grain size, as it increases the boundaries size. Therefore, the decrease of grain size with increasing doping implied an increase of the grain boundary scattering. This is considered as one of the main aspects that contribute to the mobility reduction.

The dislocation density can be estimated as the fraction of the square grain size (i.e. $\delta=1/D^2$) [265], and for the current films resulted in the order of 10^{10}- 10^{11} cm^{-2} (i.e. 1.7×10^{11} cm^{-2} in the a-axis and 3.0×10^{10} cm^{-2} in c-axis based on the un-doped film's AFM data). As a result, the current films were expected to be affected by scattering of dislocations, as they exhibit dislocations higher than 10^8 cm^{-2} [265]. The dislocation scattering was found higher for the heavier doped film (i.e. 3.1×10^{11} cm^{-2} and 5.21×10^{11} cm^{-2}) due to its small grain size, suggesting that dislocations are part of the scattering mechanisms causing the mobility reduction as doping was increased.

The grains' orientation change is also considered as a factor that may affect the carrier scattering as it affects the number of boundaries encountered by the electrons travelling across the film. By taking the two extreme possibilities of films with fully a-axis and fully c-axis oriented grains, the number and length of grain boundaries varies between those directions, and so the scattering across them depends on the electric current's direction. However, this was not the case in the current films as shown by the AFM images (chapter 4), as the grains were randomly aligned in respect to each other in all orientation cases identified. As a result, the number of

boundaries faced is considered comparable in any orientation and so the grains' orientation was believed to have low influence in resistivity.

Some of the scattering effects were simultaneous altered with doping, causing interfacial (thickness reduction), ionized impurity (doping increase), dislocation scattering and grain boundary scattering (grain size reduction). In order to identify the main parameter reducing the carrier mobility, a selection of films is compared.

Firstly, same thickness films of un-doped and 6.7 at.% doped are compared and show that the mobility for the doped films was much lower than the un-doped film (i.e. 18.1 $cm^2V^{-1}s^{-1}$ and 11.0 $cm^2V^{-1}s^{-1}$). The difference suggests that the interfacial scattering was not the dominant scattering mechanism for the mobility reduction due to doping, implying that the small thickness difference across all the doped films had little effect on the electrical properties. However, the grain size reduction observed as dopant was added to the films (chapter 4) could still reduce the mobility. To evaluate that possibility, two films with similar grain size but different thickness are compared between an un-doped (95 nm) and a 4.8 at. % doped film (161 nm), with grain size of 57/25 nm and 65/23 nm respectively. The mobility of the un-doped film is again found to be higher than the doped one, having mobility of 18.1 $cm^2V^{-1}s^{-1}$ in comparison to the doped film of 15.8 $cm^2V^{-1}s^{-1}$. Based on the mobility difference, the effect of grain size difference across the doped set of films (Figure 67) does not appear to be the main reason for the mobility reduction. Consequently, the mobility reduction as doping is added to the films is believed to be driven by ionised impurity scattering. Future experiments on temperature dependence electrical measurements could reveal more information on the cause of the mobility reduction. For example, at high temperature Hall effect measurements the ionised impurity scattering is fixed as the carriers do not need more energy to be excited. At such case, it could be

feasible to observe the mobility shifts at different doped films, as well to determine whether the grain boundary scattering and the dislocation scattering are more dominant than the interfacial scattering.

5.3.2 Refractive index

The refractive index is a property that relates to the optical characterisations of the film. However, it was found to have the same trend as resistivity, suggesting that doping affects the refractive index in the same way as carrier density. The refractive index is the ratio of the speed of light and the light travelling through the sample. For materials allowing the light travelling faster through them, the refractive index is low indicating that most of the incident light is transmitted through the material and it is not reflected. The reflectance is thus low for materials with low refractive index, supported by the mathematical expression given by Equation 25 shown in chapter 3. The variation of the refractive index for the current films measured by the ellipsometer is shown in Figure 68.

It is known that high carrier density can induce an increase of the optical gap, and therefore cause an increase of the absorption and decrease of the reflectance (Lambert-Beer's law). In the current study the optical gap was indeed found to increase up to 4.8 at.% doping (chapter 6), suggesting that the reflectance was reduced at that point due to the gap changes. This reduction was consistent with the refractive index reduction to the same point of 1.87 (unit-less) which is lower than the un-doped value of 1.95. Therefore, the reflectance and refractive index are inversely related to the carrier density of the films. This relation is consistent with

literature, as Bennet et al. suggested that the refractive index is affected by the bandgap widening/narrowing effects, and the free carrier absorption [335].

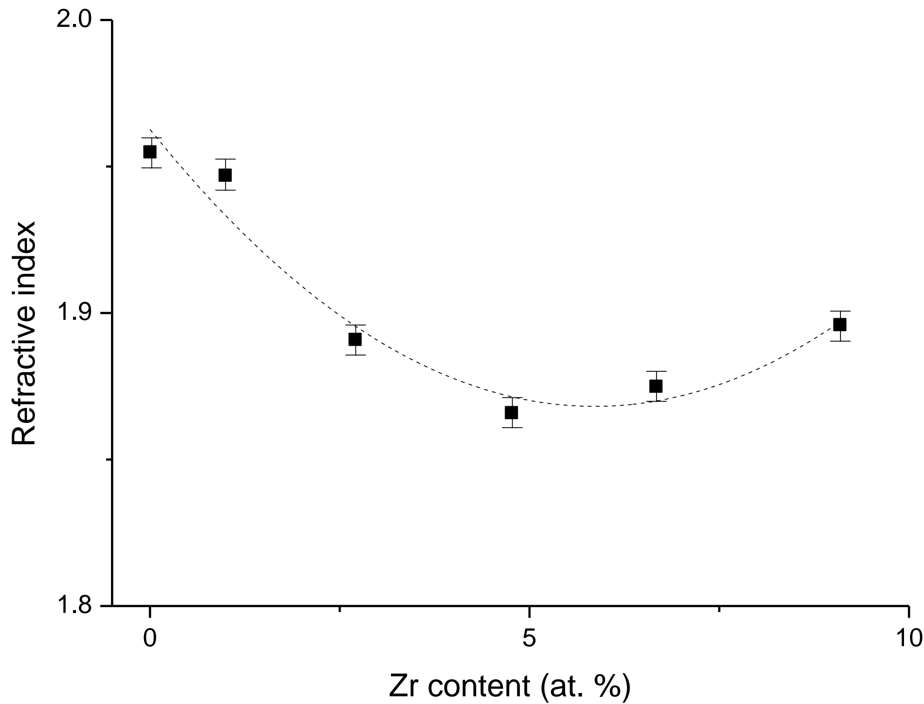

Figure 68: Zr doping dependence of the refractive index for films ~85 nm thick.

5.2.5 Improvement of electrical properties

The resistivity of commercial ITO is about 10^{-4} Ω·cm [14], which indicates that the use of the Zr-doped ZnO films as its replacement requires further resistivity reduction by at least one order of magnitude through controlling the deposition parameters. Based on a review covering the maximum carrier mobility and density published, the lowest resistivity limit for doped ZnO is at 1×10^{-4} Ω·cm due to limitations by ionised impurity scattering [145].

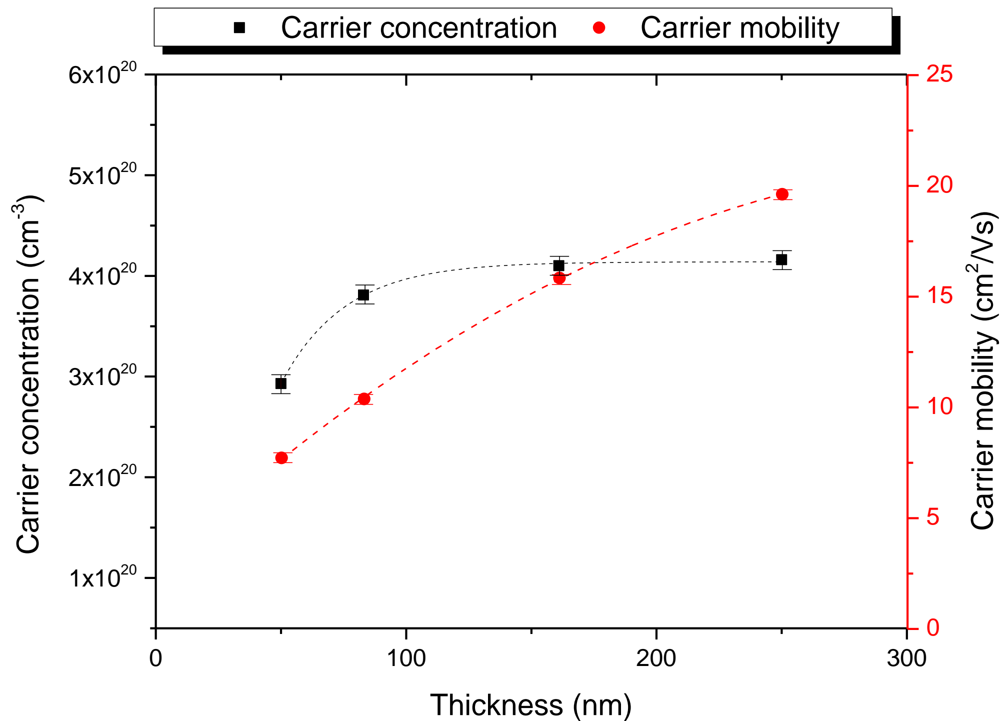

Figure 69: Film thickness dependence of carrier concentration and mobility for 4.8 at.% doped films.

The two ways of reducing the resistivity is the increase of either the carrier concentration or the carrier mobility. With doping the carrier density was shown to increase up to 4.8 at.% doping, which suggests that this is the maximum limit of extra carriers by Zr doping. The resistivity can be reduced through increasing the mobility by measuring the scattering. The dominant scattering effect found earlier (ionised impurity scattering) cannot be reduced as the doping must be kept fixed to maintain the carrier density. As a result, the microstructural related scattering could be reduced through thickness control, which is the most precise parameter controlled in ALD. This was investigated by systematically increasing the film thickness through controlling the number of ALD cycles ranging from 300-1500, and by keeping the recipe fixed for all the other parameters. By increasing the overall film thickness and keeping everything else fixed, the grains increased in size (see chapter

4) resulting in the simultaneous decrease of dislocation scattering (reduction of dislocation density), interfacial scattering and grain boundary scattering. The surface roughness increase was the only parameter that might cause increase in carrier scattering.

The carrier mobility and density as a function of thickness are shown in Figure 69. The mobility trend starts as linear and then sublinear as thickness increases. This is expected as carrier mobility theoretically follows an asymptote line until it gets to the bulk value. This increase shows that the scattering is reduced, but as the grain size and thickness simultaneously increase it is not possible to determine experimentally which scattering mechanism is driving the mobility increase. Nevertheless, based on Vancea and Hoffmann studies [336], the grain boundary scattering is the most dominant when the crystals are in the order of a few nanometres, while the interfacial scattering based on Boltzmann formalism [149] is generally responsible for the resistivity reduction in terms of overall film thickness (i.e. $\rho=\rho_{\infty}[1+G(t^{-1}$, mean free path)] [149]). As a result, the resistivity reduction is often achieved through thickness increase as a method of interfacial scattering reduction, and it is reported to follow an asymptote trend line [36],[149],[330],[337]- [338].

The carrier density was expected to be fixed as the thickness increased, due to the fixed number of impurities added to the films. However, as shown in Figure 69, the carrier density follows an asymptote line with large changes at low thickness and very small changes between the thicker films. This could be associated to strain changes within the films. Strain within the film may shift the distribution of the density of states that affects the arrangement of electrons within the energy states [73]. As a result, compression strain in a lattice could cause electron rearrangement into higher energy states and increase the energy gap while a tensile strain will have the

opposite effect. Therefore, large grains which induce tensile strain in the film are related to a bandgap reduction, while reduction of their size results in compression and the increase of the bandgap. The energy gap changes may affect the population of the bands as the carrier density depends on the energy gap (i.e. $n \propto \exp(-E_g)$) [73]. As a result, in the current films the gap is expected to be reduced as the tensile strain increases with thickness, causing an increase of the carrier density. The strain increase shown in chapter 4 supports this theory as it follows the same trend as the Hall effect measurements shown in Figure 69.

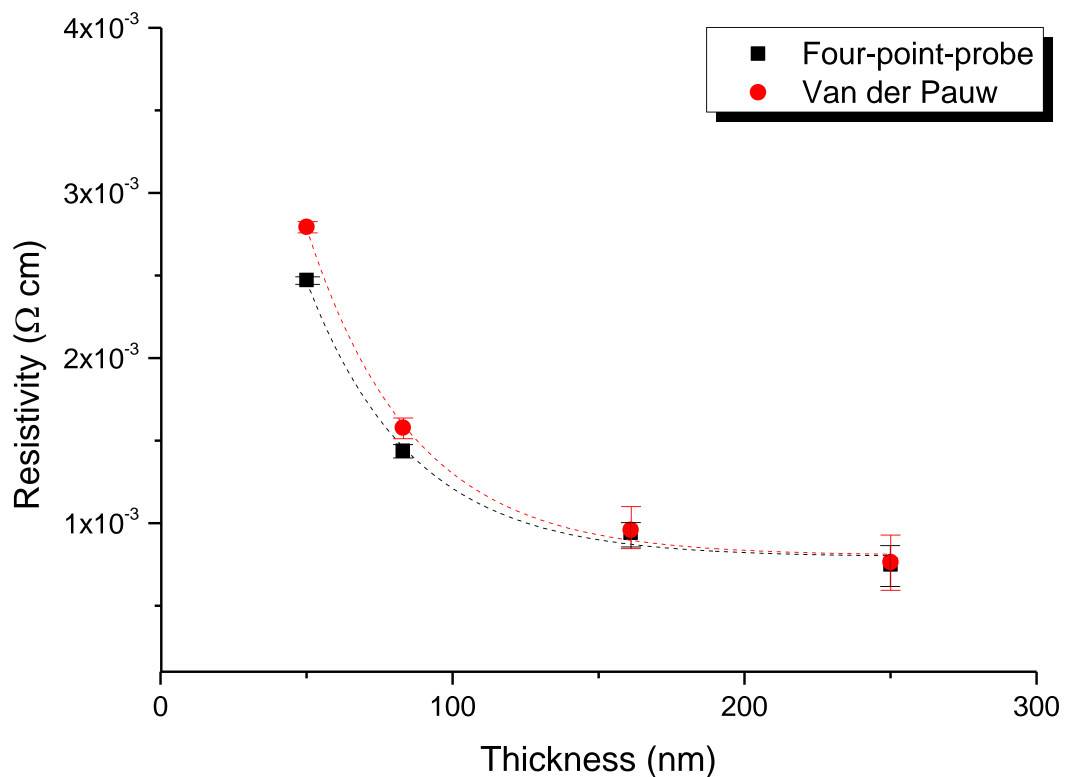

Figure 70: Film thickness dependence of resistivity for 4.8 at.% doped films.

The resistivity decreases asymptotically by a factor of 3 as thickness increases from 50 nm to 250 nm (Figure 70), in a manner similar to the carrier density increase. The

drop-off effect for very thin films (<100 nm) is attributed to the strain sensitivity of very thin films before reaching the bulk thickness. The resistivity recorded is within the required order of magnitude at 7.5×10^{-4} Ω·cm, while the carrier density reaches as high as 4.16×10^{20} cm^{-3} and the mobility up to 19.6 $cm^2V^{-1}s^{-1}$. In comparison to literature, the resistivity found in the current study was even lower than comparable thickness ALD films doped with Al having resistivity of 7.7×10^{-4} Ω·cm [34] and 2.4×10^{-3} Ω·cm [186], as well as for Ga-doped ZnO films having resistivity of 8×10^{-4} Ω·cm [38].

5.3 Degeneracy of the ZnO films

The degeneracy of the films determines the semi-metallic behaviour of the semiconductor. This occurs in heavily doped films such as the ones in the current study, showing very high carrier concentration. In order to determine if the films are degenerate, the Bohr radius has to be compared to the distance between the excitons, as discussed in the following paragraphs.

The Bohr radius is the distance between the nucleus and an electron travelling in the first orbit [339]. This is expressed in relation to the hydrogen first Bohr orbit radius (α_0) equal to 0.53Å, and the dielectric constant of ZnO (ε_{Zn} = 8.49 [340]), as shown in Equation 51 [73].

Equation 51

$$a = \frac{\varepsilon}{m^*/m_0} a_0$$

From the above relation the Bohr radius for ZnO with effective mass (m^*) at the bottom of the parabolic CB ($=0.28m_0$ [62]), is equal to 1.6 nm. The Bohr radius for ZnO is high due to the high dielectric constant and the low effective mass (i.e. naturally high electron density), indicating low Coulomb attraction forces.

The excitons move freely in the material separated with each other by distance (r_0), expressed in Equation 52 [341]. As seen by this relation, the distance is inversely proportional to carrier density (n_e). Therefore, for degenerate semiconductors with very high values for n_e, the distance between the excitons will be very small. When the distance (r_0) is equal to Bohr radius (α), the excitons overlap with each other and the Coulomb interaction is neglected [17].

Equation 52

$$r_0 = \left(\frac{4\pi n_e}{3}\right)^{-\frac{1}{3}}$$

According to Mott-Edwards-Sienko (MES) criterion, if the free carrier concentration overcomes the critical value (Mott density) of overlapping excitons, then the Fermi level is located above the conduction band minimum [76]. This results in the transition of semi-insulating behaviour to semi-metallic in degenerate semiconductors. The transition is related to the filling of the CB minimum, known as the Burstein-Moss effect [342]. During the transition the boson character (quasiparticles) of excitons is reduced and results in electron-hole plasma recombinations. This will lead to bandgap narrowing at high photoexcitation intensity (see chapter 6). To evaluate whether the material becomes degenerate, the dimensionless quantity r_s was calculated. This corresponds to the ratio of the average

electron distance to Bohr radius (i.e. $r_s = r_0/\alpha$). The typical values are 2-5 for metals, while for degenerate materials the value is less or equal to unity [81].

For a direct comparison to the carrier density measured using the Hall effect, the critical density (N_C) is given by Equation 53 [343]. The critical value for the current ZnO is 4.29×10^{18} cm^{-3}, which is comparable to most of the published critical values found in literature (e.g. 3×10^{17} cm^{-3} [113], 5×10^{17} cm^{-3} [100], 1.5×10^{18} cm^{-3} [344] 4×10^{18} cm^{-3} [17], 6.41×10^{18} cm^{-3} [76], and 5×10^{19} cm^{-3} [100]). The carrier concentration for all films is well above this critical value, suggesting semi-metallic behaviour.

Equation 53

$$N_c^{1/3}\alpha \geq 0.26$$

In order to confirm the degeneracy, r_s is calculated for all the doped films. The distance r_0 increases with the carrier density and the Bohr radius of the donors (α_d) increases with the effective mass (related to carrier density) and with the dielectric constant of Zr. The relation is shown in Equation 54 that uses the dielectric constant of zirconium oxide (ε_{Zr} =25 unit-less [345]), and the electron effective mass (m^*) calculated in chapter 6. The increase of Bohr radius leads to the reduction of r_s as shown in Table 8.

Equation 54

$$a_d = \frac{\varepsilon_{Zr}}{m^*/m_0} a_0$$

All films grown for this study have r_s less than unity, confirming that the samples are degenerate. Therefore, the Fermi level always lies above the CB minimum even for

the un-doped film, suggesting that the films might show Burstein-Moss effect and bandgap renormalisation effects at such high densities (see chapter 6).

Table 8: Calculation of quantity r_s for all samples

Zr contents (at.%)	Bohr radius (nm)	r_0 (nm)	r_s (unit-less)
0.0	1.60	1.34	0.83
1.0	3.98	1.19	0.30
2.7	3.65	0.93	0.25
4.8	3.53	0.86	0.24
6.7	3.64	0.92	0.25
9.1	3.77	1.01	0.27

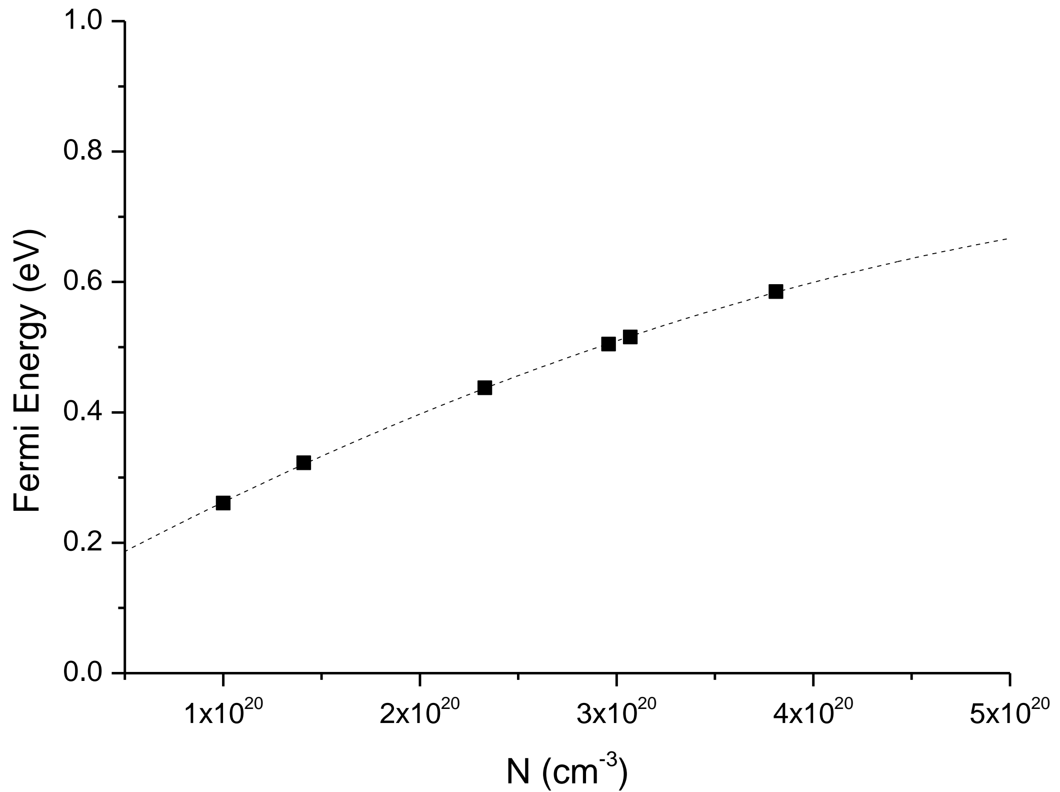

Figure 71: Calculated Fermi energy level above the CB in relation to the carrier concentration.

By knowing the carrier concentration for each film it is possible to estimate the level of Fermi level (E_F). Therefore, E_F with respect to the bottom of the CB is calculated using Equation 55 [346], and Figure 71 shows the Fermi level increase as the carrier density increases. The Fermi level is thus shown to be higher than the CB minimum for all films.

Equation 55

$$E_F = \left(\frac{3n_e}{8\pi}\right)^{2/3} \frac{\hbar^2}{2m_0^*\left[1 + 0.5\left(\frac{m^*}{m_0^*} - 1\right)\right]}$$

5.4 Chemical state

XPS cannot be used for quantitative analysis of rough surface films such as the current films due to the photoelectron scattering effects as it was explained in chapter 3. The difficulties faced to get an accurate composition map were also reported by other studies such as the one by Chen et al. [347], who tried obtaining the Al composition of ZnO: Al films and attributed the reasons to the low Al concentration and the low values of the ionization cross section of Al.

Nevertheless, for the current study an additional difficulty was the doping deposition method (delta method) that restricted the dopants at specific places within the lattice, and as the technique gives accurate information up to 2 nm below surface the dopants might be not detected in their full concentration. Note that although vacuum annealing was carried out at 400°C for some films, the photoelectron scattering effects were causing too much scattering to obtain the full Zr concentration. Those

effects only affected the XPS peak intensities originated from the signal received from each element, but not the binding energy (BE) as it should be only affected by the chemical changes within the film. Consequently, although no accurate composition data can be extracted from XPS, it can be used as a proof of the dopants existence.

5.4.1 XPS spectrum analysis

Zr-doped ZnO thin films were characterised by XPS, with full survey scans in the range of 0–1286 eV. The 4.8 at.% Zr sample with thickness of 250nm is taken as an example of XPS characterisation due to its strong signals from the main elements (Figure 72). The main core-level peaks are observed as high intensity peaks at 1022 eV, 183 eV and 531 eV BE for Zn ($2p_{3/2}$), Zr ($3d_{5/2}$) and O (1s) respectively. The dominant intensity of those peaks indicated that Zr atoms are mostly populated in the 3d orbital and Zn atoms in the 2p orbital. However, electrons from lower and higher orbitals are also photoexcited for Zr and Zn elements respectively, shown by the Zr $3p_{5/2}/3p_{3/2}$ and Zn $3d_{5/2}/3d_{3/2}$ peaks. Those peaks are not analysed further due to their lower intensity to the dominant peaks, but their intensities are directly related to changes observed in the dominant peaks. The peak positions may vary due to energy shifts induced by chemical bonding environment and thus can provide useful information about bonding states.

Any dotted lines in the presented XPS graphs correspond to the reference positions of each peak according to the equipment's manual. The carbon peak associated with hydrocarbon bonds at a binding energy of 285 eV was used to calibrate the energy

scale of the XPS spectra. This calibration corrects for any shifts in the energy scale induced by surface charging.

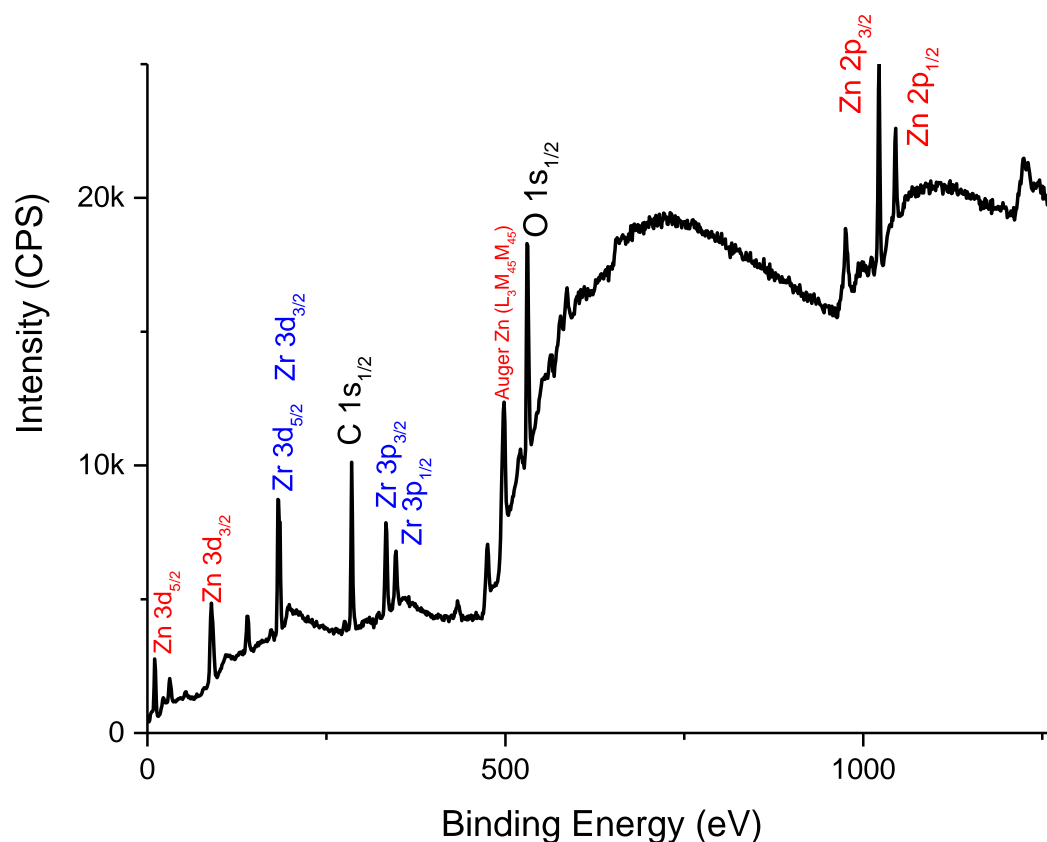

Figure 72: XPS Survey for the 250nm thick film with 4.8 at. % Zr doping.

The doped samples were also scanned in the core-level elements' regions for more accuracy in the peak details. The Zn spectrum for 2p electrons is shown in Figure 73 for the 250 nm 4.8 at.% film and for all the thinner doped films. The peaks are located at 1022 eV and 1045.1 eV for the thicker film (the same as the thinner film with the same doping), which is slightly increased from the un-doped at energies of 1021.5 eV and 1044.6 eV. The corresponding reference peaks were in agreement to the results with energies of 1022 eV and 1045 eV [348]. Nevertheless, other studies

with Zr-doped ZnO films showed lower energies after doping (i.e. 1021.7 eV [57], 1021.8 eV [56]), but are in close approximation to the current study. On the other hand, the low energy peak in the un-doped film is similar to Zn metals binding energy at 1021.5 eV [349]. However, it is not considered as metallic due to the already proven ZnO phase by XRD measurements. The doping effect on the BE induced energy shifts to higher energies, suggesting higher oxidation states for all doped films.

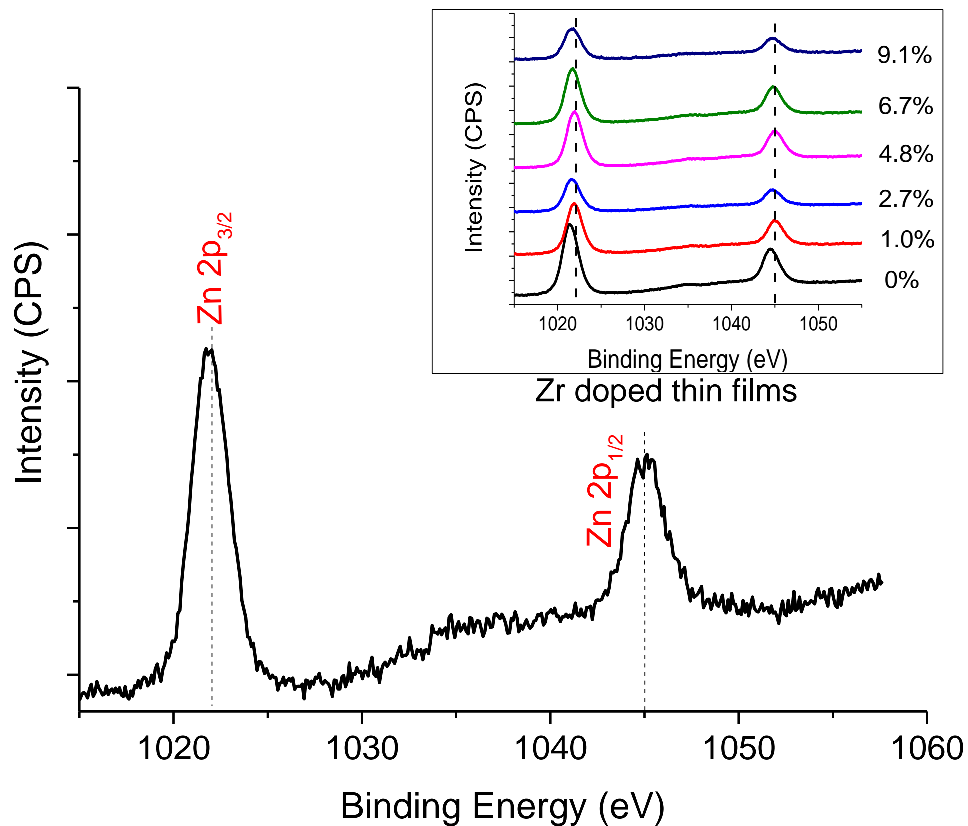

Figure 73: XPS Spectra for Zn 2p peaks for 250nm thick film with 4.8 at. % Zr doping and all doped thin films presented in the smaller window.

The spin-orbit coupling for the p orbital stayed the same as the energy difference between the Zn 2p peaks are at 23.1 eV, indicating that the peaks correspond to Zn^{2+}

in ZnO [200]. The peak area ratio was expected to be at 1:2, which is consistent with the experimental ratio of 0.53 for the un-doped film and it is slightly lower for the doped ones of 0.51–0.52. The small variation is attributed to the different background intensities between the films caused by the shake-up satellite peaks due to the relaxation of valence electrons to higher unfilled levels [348].

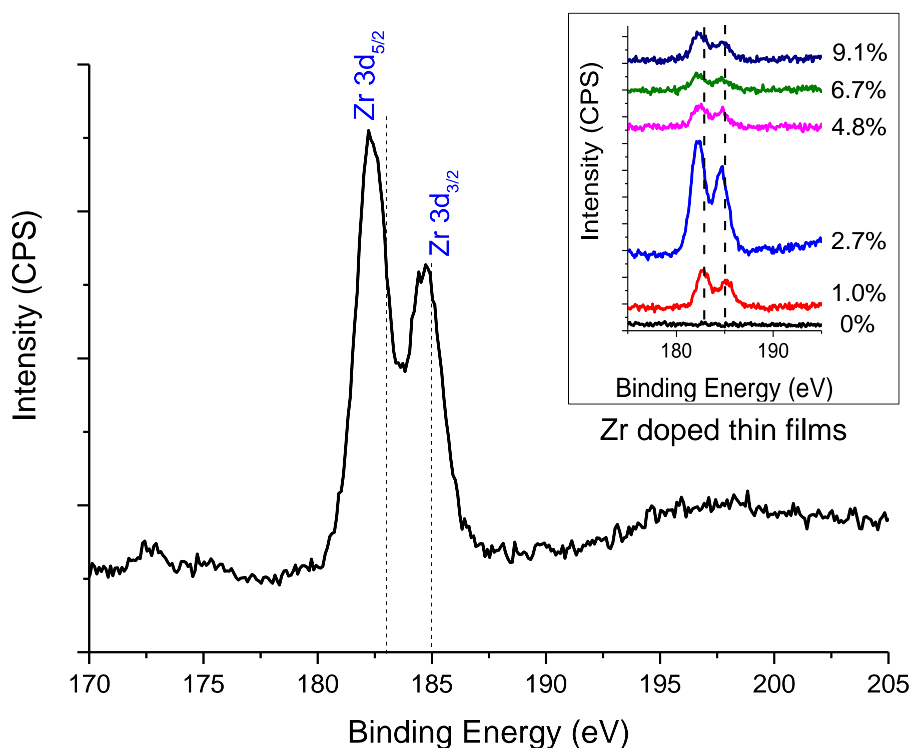

Figure 74: XPS spectrum for the Zr 3d peaks for 250nm thick film with 4.8 at. % Zr doping and all doped thin films presented in the smaller window.

The Zr peaks shown in Figure 74 using the 4.8 at.% doped film, are found at 182.4 eV and 184.7 eV for the Zr 3d spin-orbit double (i.e. Zr $3d_{3/2}$ and Zr $3d_{5/2}$), which are related to Zr^{4+} valence state in the oxide film [350]. This indicates that zirconium is indeed incorporated within the lattice in its ionic state, and does not

exist as separated atoms in metallic form with binding energy of 179 eV. Note that the peak intensity is different between the thin and thicker films with the same doping (i.e. 83 nm and 250 nm), but they show identical peak positions. This suggests that the films are chemically the same. The peak intensity difference though, suggests that XPS is not the appropriate technique for quantitative analysis.

The intensity changes between the films with the same doping are attributed to photoelectron scattering effects, which was more prominent in c-axis orientated grains rather than a-axis preferred orientated grains (i.e. 250 nm film), and so are not corresponding to the overall doping percentage. Consequently, although no composition data were obtained, the Zr peaks existence in all films indicates the existence of Zr atoms in their lattice in its ionic state.

The binding energies for Zr^{4+} are slightly lower than the ones reported in [200] with peaks at 183 eV and 185 eV, but they are slightly higher than the ones reported in [56] with energies at 182 eV and 184.3 eV. The values are similar to the ones reported in [57], with energies at 182.6 eV and 185 eV respectively. The close proximity to the reference indicates the existence of Zr^{4+} in the ZnO lattice. As the Zr 3d peaks are known to have shake-up satellites (i.e. features near core-level peaks), they may have caused the shift in the Zr related energy peaks, similarly to the Zn related peaks.

The spin-orbit splitting indicated by the peaks difference is at 2.3 eV for the films of 1-4.8 at.% Zr doping consistent with reference [56]. As doping increases the BE shifts to lower energies of 181.8 eV and 184.4 eV for 6.7 at.%, with their separation energy to be increased at 2.4 eV for the two heavier doped samples, consistent with the reference [57]. This small difference is attributed to the compressive forces acting on dopants as its concentration increases, causing increase of the spin-orbits distance.

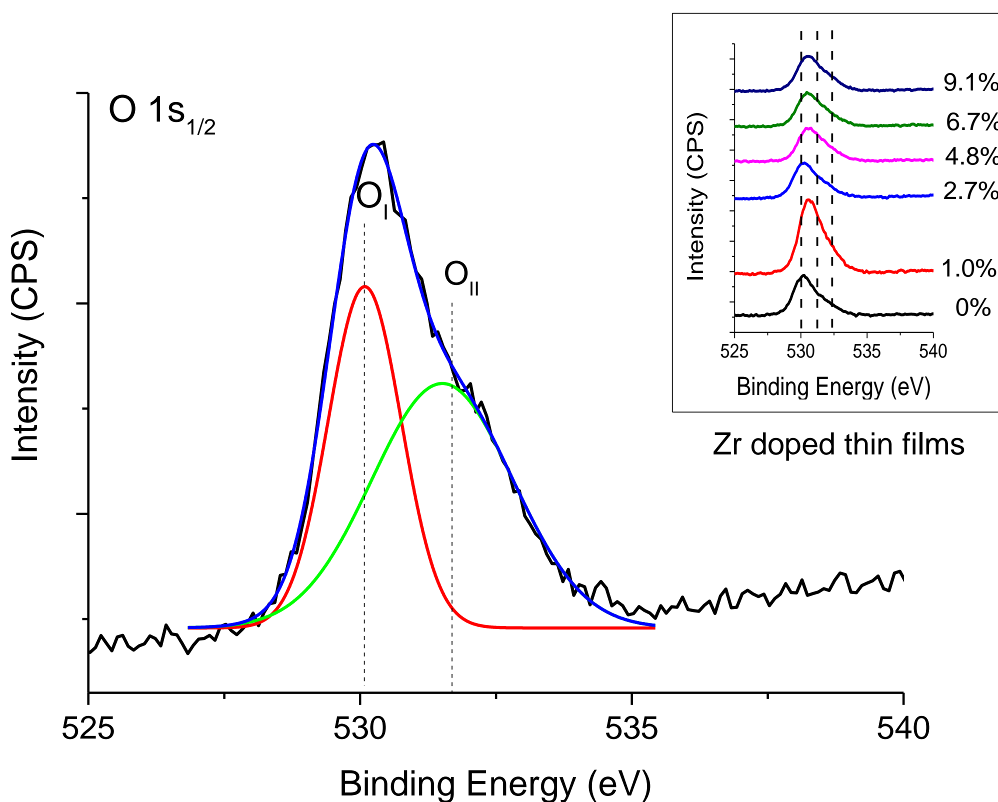

Figure 75: XPS spectrum for the O $1s_{1/2}$ peak for 250nm thick film with 4.8 at. % Zr doping and all doped thin films presented in the smaller window graph.

Figure 75 shows the region covering the oxygen binding energy for the O $1s_{1/2}$ peak with reference the dotted line at 531 eV. The oxygen peak usually consists of three components, although only the first two were identified in the current results. The first component (O_I) is located at 530.1±0.2 eV and corresponds to O^{2-} ions of lattice oxygen bonding within ZnO crystals [31]. The second one (O_{II}) located at 531.3±0.2 eV is associated to the O^{2-} ions [349], representing oxygen vacancies in the structure. The last component (O_{III}) at 532.4±0.2 eV indicates the non-stoichiometric near-surface oxygen atoms in carbonate ions, surface hydroxylation, adsorbed H_2O and absorbed O_2 [200], and it is often associated with OH groups at the surface [290]. In this study only the first two components are detected with the peak analysis of three samples shown in Figure 76 and their peak energy values in Table 9.

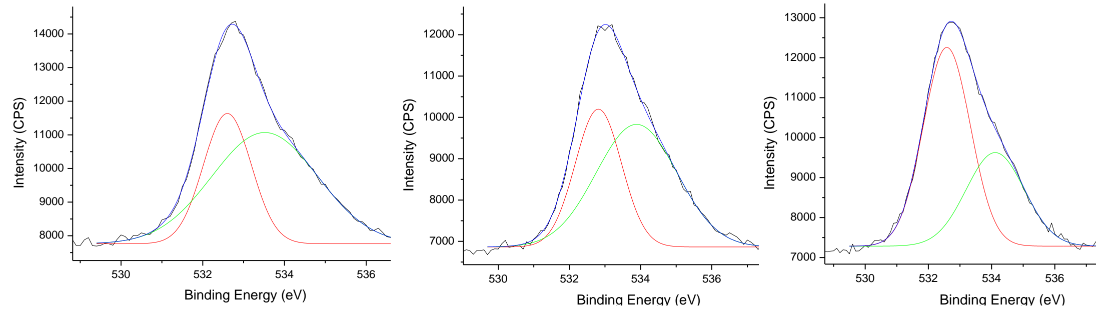

Figure 76: XPS of O 1s components for a) 0 at.%, b) 4.8 at.%, and c) 9.1 at.% doped films. The blue line shows the measured peak, the red line is the fitted line for O_I, and the green line for O_{II}.

In the current study, both O_I and O_{II} components shift to higher BE as doping increases, suggesting an increase in oxidation and indicating that more oxygen bonded to metal ions. This is similar to a study regarding n-type co-doped Ga-Al and Ga-B ZnO films [351].

Table 9: BE of the two oxygen components as found in XPS.

Zr content (at.%)	O_I (eV)	O_{II} (eV)
0	530.1	531.0
4.8	530.4	531.5
9.1	530.4	531.9

5.4.2 Chemical shift

In order to evaluate the chemical state changes due to doping without the effect of surface charging, the Auger parameters for Zn (α_{Zn}) can be calculated using Equation

56 [352]. The relation derived by Wagner [353] is based on the binding energy of Zn ($2p_{3/2}$) and the kinetic energy deduced using the Auger transition line of Zn ($L_3M_{45}M_{45}$) at ~498 eV. The connection was derived using the relation of Auger chemical shifts to photoelectron chemical shifts [353]. As a result, this quantity is often used for referencing as it neglects the effects of work function and surface dipole [354], which are the main causes of shifts in XPS. The presented relation is the one formatted by Gaarenstroom and Winograd [355], who suggested using the sum of line energies in contrast to the kinetic energies subtraction suggested by Wagner, in order to avoid the effects of X-rays on the electron binding energies (e.g. Zn $2p_{3/2}$). Note that the Auger emission occurs when an electron relaxes to a lower energy level to fill in a vacancy, a recombination resulting to photon emission (i.e. vacancy created after X-rays ionised an electron).

Equation 56

$$\alpha_{Zn} = E_{B\,Zn(2p_{3/2})} + E_{K\,Zn(L_3M_{45}M_{45})}$$

The Auger parameter change is also known to equal the relaxation energies in the element, consisting of extra-atomic relaxation R^{ea} or polarisation energy (i.e. $\Delta\alpha_{Zn} = 2R^{ea}$) [356]. As a result, an increase of the shift in the Auger parameter is related to the increase of the electronic polarisation induced by the effect of neighbouring ions in the solid [357].

In ZnO the Auger parameter shift is 3.9 eV [353],[355] in relation to the metallic energies (i.e. α_{Zn}=2014.1 eV). The same reference point was used in the current study's calculations (Table 10), which resulted in slightly higher parameter even for the un-doped film (i.e. 4.16 eV).The Auger parameter of 2009.9 eV for the un-doped film matches the reference of 2009.8-2009.9 eV set by Wagner for ZnO films [357].

Additionally it is consistent with ALD deposited thin films of 3 nm thickness (α_{Zn}=2009.7 eV), which had a slightly lower value due to the chemical changes by the dominant Zn $(OH)_2$ in the initial monolayers [358]. The parameter in the current study does not shift much as doping is added (i.e. in Table 10 $\Delta\alpha_{Zn}$ was in the order of 10^{-2}) indicating the formation of stoichiometric ZnO films. This is in contrast to other dopants such as F (α_{Zn}=2012.6 eV [352]), In (α_{Zn}=2011.48 eV [352]) and Al (α_{Zn}=2009.1 eV [359]) showing higher Auger parameter. However, the Auger parameter difference increases at 6.7 at.% doping in the current films. Nonetheless, the shift is small compared to other doped systems mentioned earlier indicating almost negligible changes. On the other hand, the 9.1 at.% film show no increase as the number of free electrons (charge) was reduced at that point.

Table 10: Auger Parameter and chemical shifts calculated for Zr-doped films.

Zr contents (at.%)	α_{Zn} (eV)	$\Delta\alpha_{Zn}$ (eV) Ref	$\Delta\alpha_{Zn}$ (eV) Doping	Chemical shift (eV)
0	2009.94	-4.16	0.00	2.70
1	2009.92	-4.18	0.02	2.24
2.7	2009.99	-4.11	-0.05	2.47
4.8	2009.93	-4.17	0.01	2.22
6.7	2010.18	-3.92	-0.24	2.31
9.1	2009.95	-4.15	-0.01	2.47

The 250 nm doped film shows the greater Auger energy shift of α_{Zn}=2010.42 eV. The increase was related to mobility, crystallinity and absorption increase as thickness was higher, which are reported to affect the Auger parameters [357]. The increase of polarizability leads to greater Auger shifts, which is believed to be the case for the thicker film due to its increased charge from the dopants.

The Auger parameter was used to calculate the corrected value of chemical shift (Δε) related to the kinetic energy difference to literature (ΔEk) and the relaxation energy (ΔR), which is equal to half auger parameter [356]. The relation is shown in Equation 57 [357] and the calculated values for the current films are shown in Table 10. The relation to doping follows the same relation of polarisation and charge in the films as stated earlier.

Equation 57

$$\Delta\varepsilon = -\Delta Ek + 3\Delta R$$

5.6 Conclusion

The electrical properties of the Zr-doped ZnO films were evaluated, indicating conductivity of a good TCO material. The conductivity was controlled by ALD growth through the deposition temperature, the doping concentration, and the thickness of the films set by the number of ALD cycles. In more detail, the growth temperature of 200°C was found to result in most conductive ZnO films, and since it was within the ALD window it was selected as the standard parameter set for all subsequent runs. The Zr doping percentage was found to reduce the resistivity reaching a minimum at 4.8 at.% Zr concentration, before increased again. The reduction was attributed to the extra ions provided by Zr^{4+} as they substituted Zn^{2+}. The high carrier density led to degenerate films, as shown by the small ratio of Bohr radius to electrons average distance. This resulted in Fermi level shifts at higher energy. The experimental reduction of carrier density compared to the theoretical

ones, was mainly attributed to the mobility scattering by ionized impurities. On the other hand, the increase of resistivity from 6.7 at.% Zr doping was attributed to the formation of zinc vacancies (acceptors) at the boundaries that cause neutralization of the extra donors also located at the grain boundaries. The case was supported by the small Auger parameter shift, suggesting minimum effect from charged particles at the heavier doped film. All films were shown to have Zr^{4+} incorporated in the lattice based on the XPS measurements.

The lowest resistivity was obtained with 4.8 at.% Zr concentration that showed the higher carrier density. Therefore, to overcome the scattering issues such as interfacial, dislocation and grain boundary scattering, thicker films having large grains were deposited up to 250 nm. The resistivity decreased exponentially and the mobility increased linearly as the film thickness was increased. The carrier density was found to be increased with thickness attributed to the tensile strain affecting the electron band structure of the films. As a result, the resistivity was decreased due to the increased carrier density and mobility, reaching the minimum value of 7.5×10^{-4} $\Omega\cdot$cm with film thickness 250 nm (carrier density = 4.16×10^{20} cm^{-3} and mobility = 19.6 cm^{2}V^{-1}s^{-1}).

Another important finding was the relationship between the refractive index and carrier density due to the degenerate character of the films. The relation showed that the more conductive films resulted in decreased refractive index. This effect suggested that carrier density will affect the bandgap and transparency of the films, as it will be analysed in the following chapter.

Chapter 6

Optical properties of ZnO and Zr-doped ZnO films

6.1 Introduction

This chapter focused on the optical properties of Zr-doped ZnO, such as the transparency that is of high importance for TCOs. The transparency of TCO for photovoltaic applications must be as high as possible across the working spectral range of the devices in order to maximise the photocurrent, which typically means transparency higher than 80% in the visible region [35]-[145]. For commercial ITO, transparency of at least 85% [15],[18],[20],[149] can be achieved and hence it is desirable to match or exceed this value for any replacement of TCO. For degenerate materials the absorption may occur in the visible range, something considered as a disadvantage for TCOs in PVs, since the full visible spectrum has to pass through to the absorber. As a result, for TCO applications it is required to have the plasma edge at near IR wavelength [39].

In this chapter, the optical properties such as transmittance, optical gap and defect states are investigated using spectrophotometry and photoluminescence (PL). The analysis will focus on the effects of doping on the optical gap, while the Drude model will be used to estimate the carrier concentration.

6.2 Spectrophotometry

6.2.1 Transmittance

The optical transmittance spectra of the Zr-doped ZnO films are shown in Figure 77 for full range (300-2600 nm) and for visible range data (380-780 nm). The plots include the transmittance line of an un-coated glass used to normalise the transmittance values of the films.

The figures show high transparency for the un-doped and doped ZnO films in the visible and short wave IR range (380-2000 nm). The decrease observed from that point onwards indicates plasma frequency changes. This was expected from the direct relationship between the carrier density and plasma frequency, suggesting that the more conductive films will show increased plasma frequency (greater line slope). The trend is consistent with the Hall measurements (Chapter 5), in which the carriers increased up to 4.8 at.% before decreased again.

The other observation from Figure 77 is the blue-shift of the absorption edge as doping increased. This indicates increase of the optical gap with doping up to 4.8 at.% Zr. The films with 4.8-9.1 at.% doping show absorption edge at similar wavelength hence indicate small variation of the optical gap. The optical gaps for all films are estimated using the Tauc relation as shown in part 6.2.3.

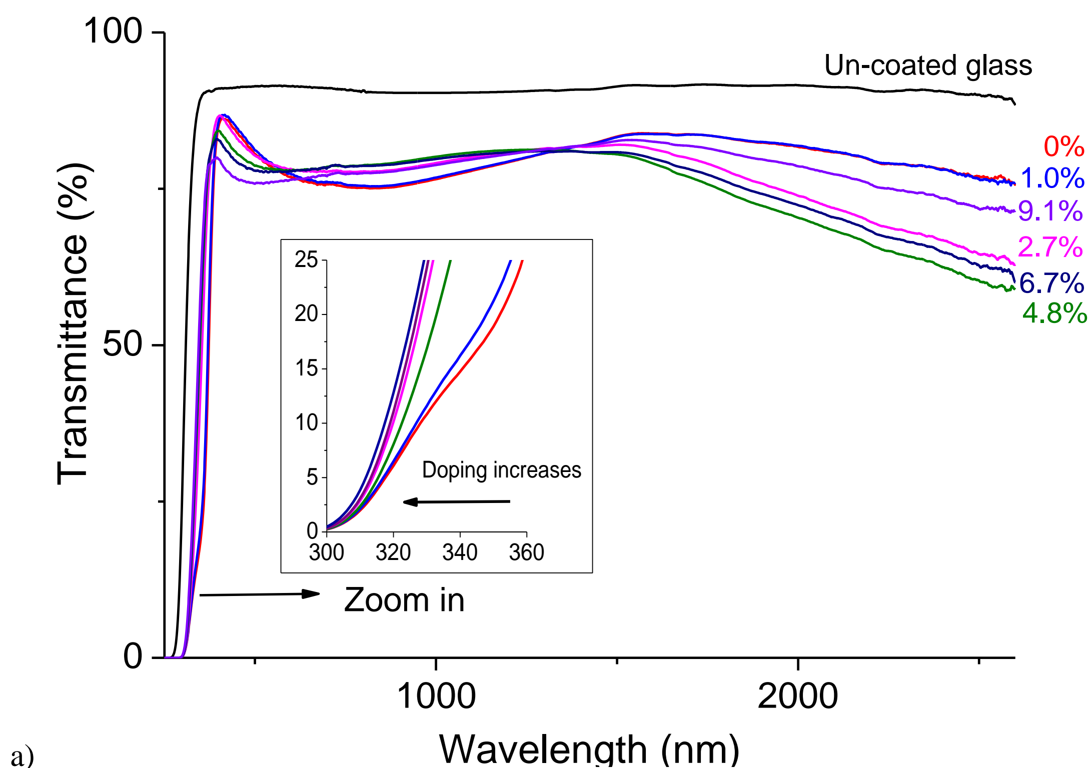

a)

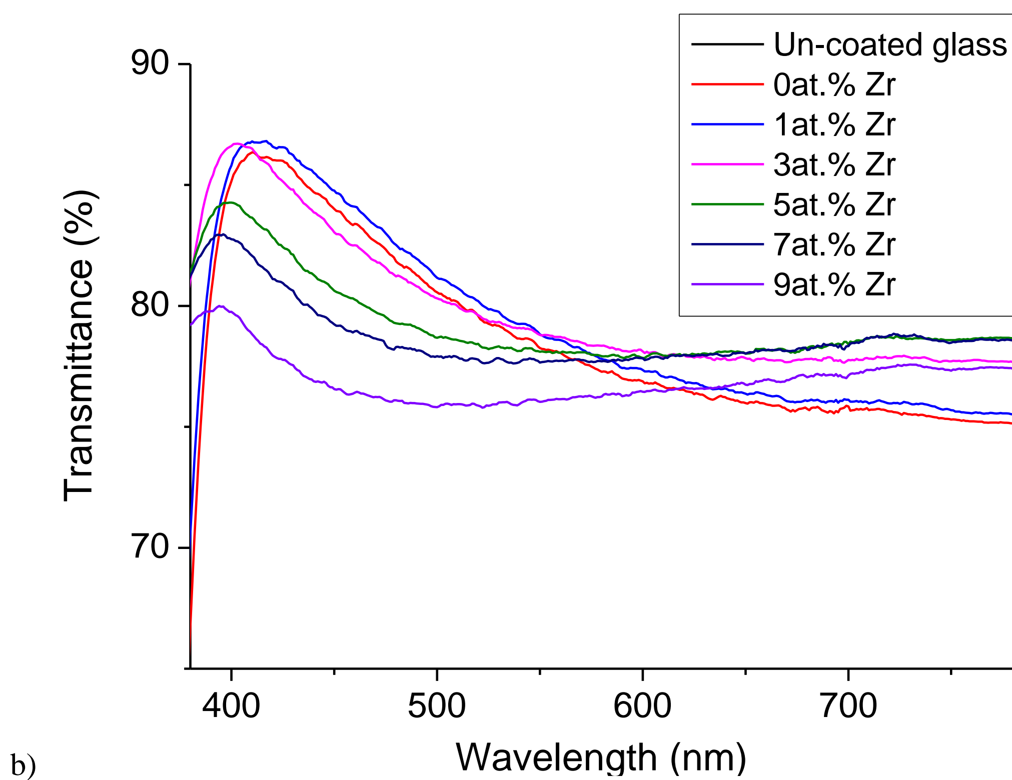

b)

Figure 77: a) Full range transmittance spectra, b) visible range transmittance of ~85 nm thick Zr-doped ZnO films as a function of the atomic concentration of Zr.

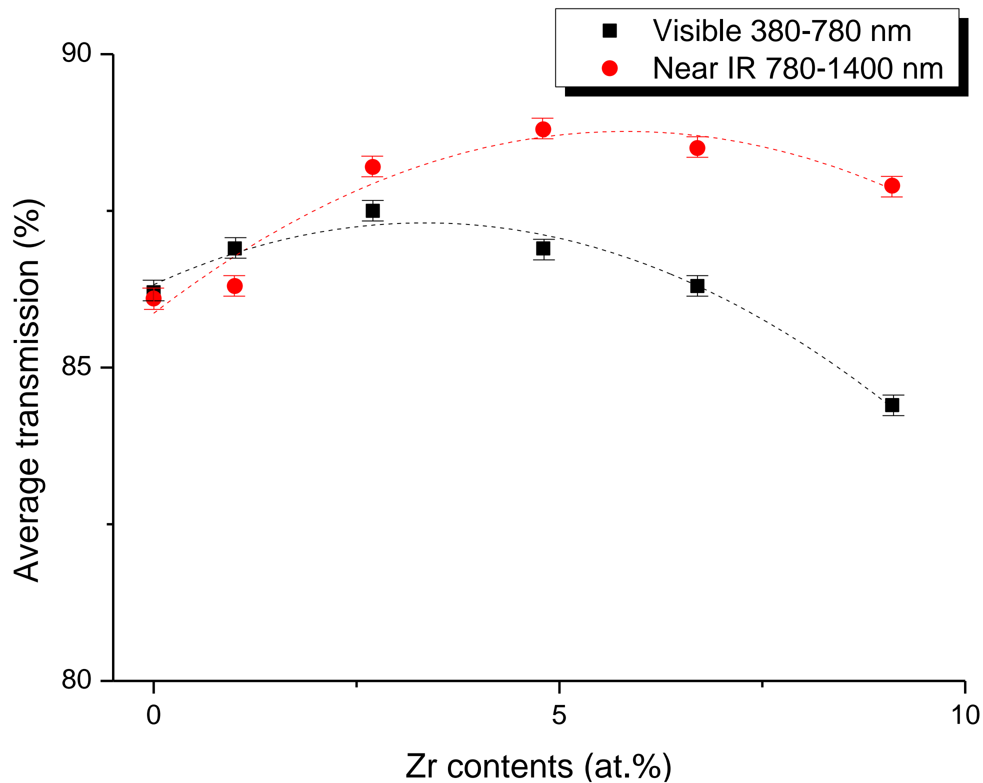

Figure 78: Zr doping dependence of the average normalised transparency (±0.3% error) for films ~85 nm thick.

The average transmittance for the Zr-doped films is shown in Figure 78. In the visible region all the films show transmittance above 84%, with the lowest value being the one with 9.1 at.% Zr. The samples of 1-4.8 at.% Zr doping show increased transmittance of 87-88% in comparison to the un-doped sample of 86%. The data show that the more conductive films (1-4.8 at.%) are the more transparent ones. The transmittance in the near IR spectrum is high for the doped samples with values up to 89% (4.8 at.%) compared to the un-doped sample of 86%. The transmittance average is related to the optical gap changes occurring at degenerate films. The optical gap increases at high carrier density due to the band filling effects (Burstein-Moss), causing reduction of the absorption. The absorption is inversely proportional to transmittance, thus the absorption reduction leads to the transparency increase. As a result, the degeneracy of films allows control over the optical gap and transmittance.

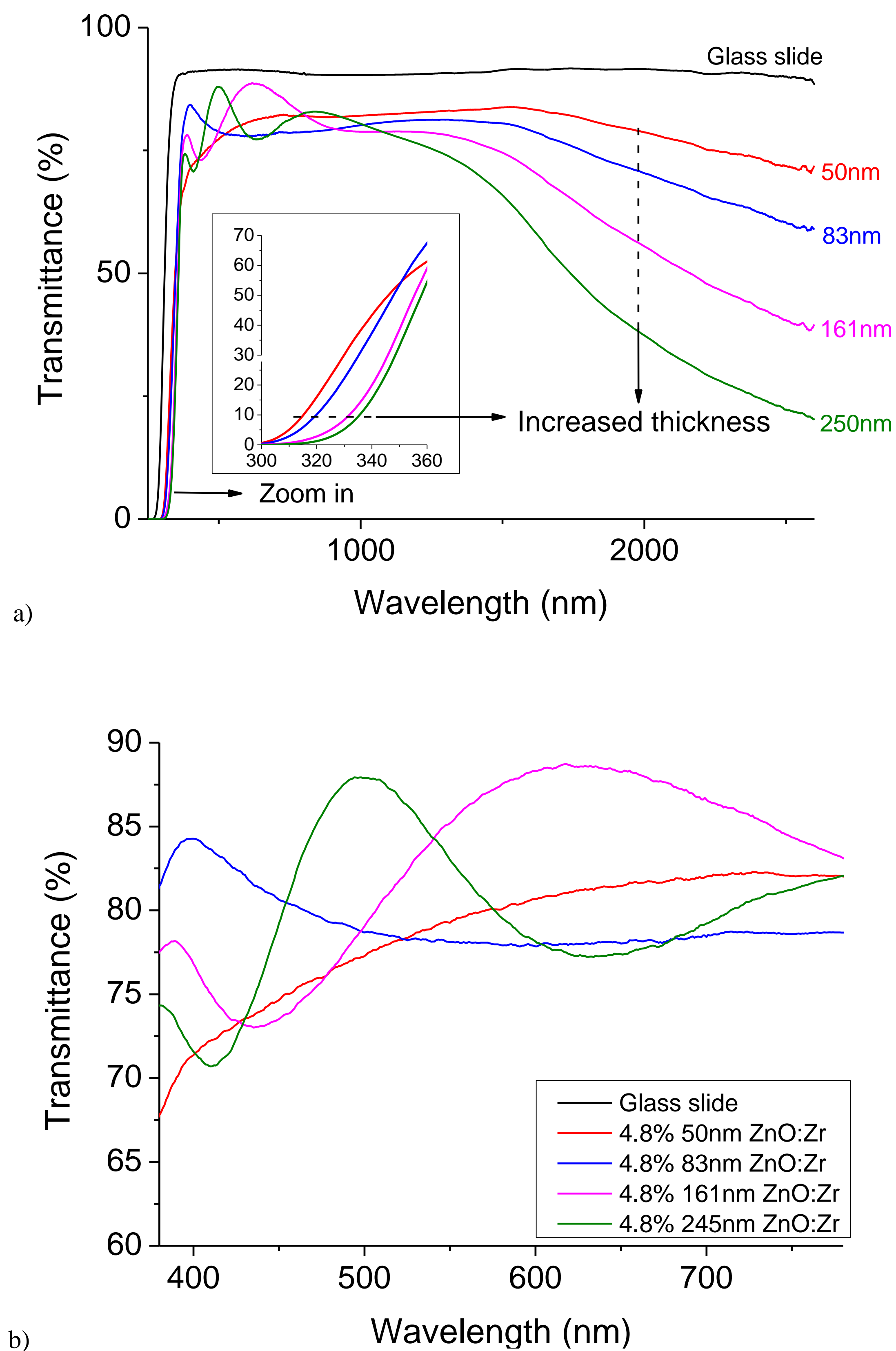

Figure 79: a) Full range transmittance spectra, b) visible range transmittance of 4.8 at.% Zr-doped ZnO films as a function of the overall film thickness.

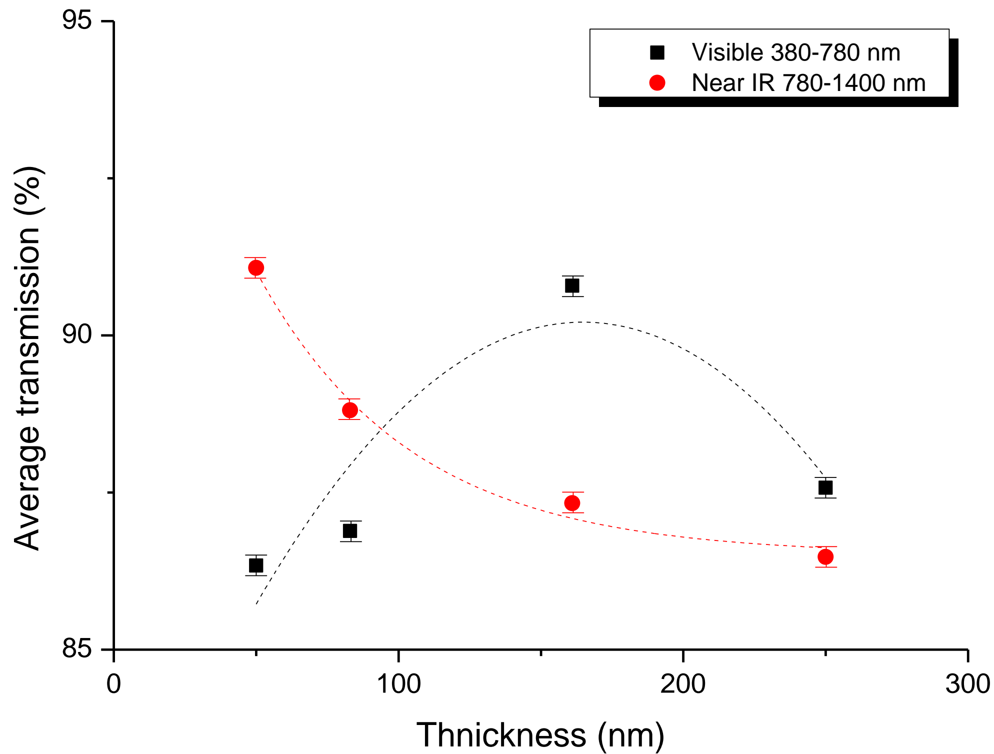

Figure 80: Thickness dependence of the average normalised transparency (±0.3% error) for films doped with 4.8 at.% Zr.

The transmittance of the thicker films with fixed 4.8 at.% doping is shown in Figure 79. Again the transparency is high for all films in the visible and near IR spectrum, showing a decrease at short wave IR range (1400-2000 nm). The absorption edge is red-shifting with thickness increase, indicating reduction of the optical gap. This is due to the increased tensile strain as the film thickness increases, which causes bandgap reduction. The plasma frequency is increased due to the carrier concentration increase, similarly to the samples in Figure 77. The position of the plasma frequency for all samples at short wave IR range complies with the requirement of a wide transparent range for TCOs. Consistent to the theory discussed in section 3.7.1, the oscillations become denser as the film thickness increases due to the increased internal reflections and higher interference between the two interfaces.

The average transparency at each region is shown in Figure 80. As thickness increases, the transparency in the visible region increases up to 91% for the 161 nm film and then decreases to 88% for the thicker film. The near IR region on the other hand shows increased values for the thinner films, reaching 91% for the 50 nm film. The transparency is then decreased to 87% for the 250 nm film. Therefore, the transparency in the visible spectrum can be enhanced with thickness increase, while if high near IR transparency is required then it will be more effective to use thinner films. In comparison to previous studies with Zr-doped ZnO films, the values are comparable of the reported 86% [50], 90% [51],[56], 91% [29], and even 92% [25],[26],[53].

The performance of TCOs is express by the figure of merit, which is calculated by Haacle's formula [146] (Equation 58). The values close to unity are considered as the best performance [360]. An indication of the target value for a competitive TCO is $4\times10^{-2}\ \Omega^{-1}$ resulting from at least 90% transparency and 10 Ω/square sheet resistance [361].

Equation 58

$$F_{TC} = \frac{{T_r}^{10}}{Rs}$$

where T_r is the average transmittance in the visible region and Rs is the sheet resistance. The current films show improved value as the thickness of the 4.8 at.% doped films increased from 83 nm ($F_{TC}=0.14\times10^{-2}\ \Omega^{-1}$) to 250 nm film ($F_{TC}= 0.93\times10^{-2}\ \Omega^{-1}$). These values were relatively low compared to the best performance for TCOs, but are close to figures of ITO films grown by spin coating of $1.19\times10^{-2}\ \Omega^{-1}$ [362]. The results of the current study are promising compared to other doped ZnO films deposited by ALD, such 100 nm Al-doped ZnO ($F_{TC}= 0.10\times10^{-2}\ \Omega^{-1}$) [187], 180 nm In-doped ZnO ($F_{TC}=0.12\times10^{-2}\ \Omega^{-1}$) [192], 100 nm Ti-

doped ZnO (F_{TC}=0.12×10^{-2} Ω^{-1}) [171], and 200 nm Hf-doped ZnO (F_{TC}=0.36×10^{-2} Ω^{-1}) [28].

6.2.2 Drude model calculations

The carrier concentration (Figure 81) and the film resistivity (Figure 82) could be estimated using the transmittance data and the Drude model. The carrier density estimated by the Drude model is higher than the experimental Hall effect values. A similar difference is shown between the Drude model values and the ones measured by four-point-probe and Hall effect.

The difference between the data was previously reported and it was attributed to the non-electrically homogeneous films measured, in contrary to the theoretical conditions of Drude model [363]. This was supported by Kim et al. who reported that films with large grain boundaries showed greater difference in carrier density measured by the Hall effect and the Drude model [364]. Therefore, the difference is based on the fact that no scattering mechanisms are taken into account in this theoretical model. Those mechanisms for the current films were identified in chapter 5 as ionised impurity, interfacial, dislocation and grain boundary scattering. Another effect of the difference is the use of a fixed number for the effective mass (0.4 m_0) for all the films, which in reality changes in relation to the carrier density changes. Therefore, the theoretical values could be improved and match other experimentally measured values by using a modified effective mass. This is further analysed along with the PL data in section 6.3.2.4.

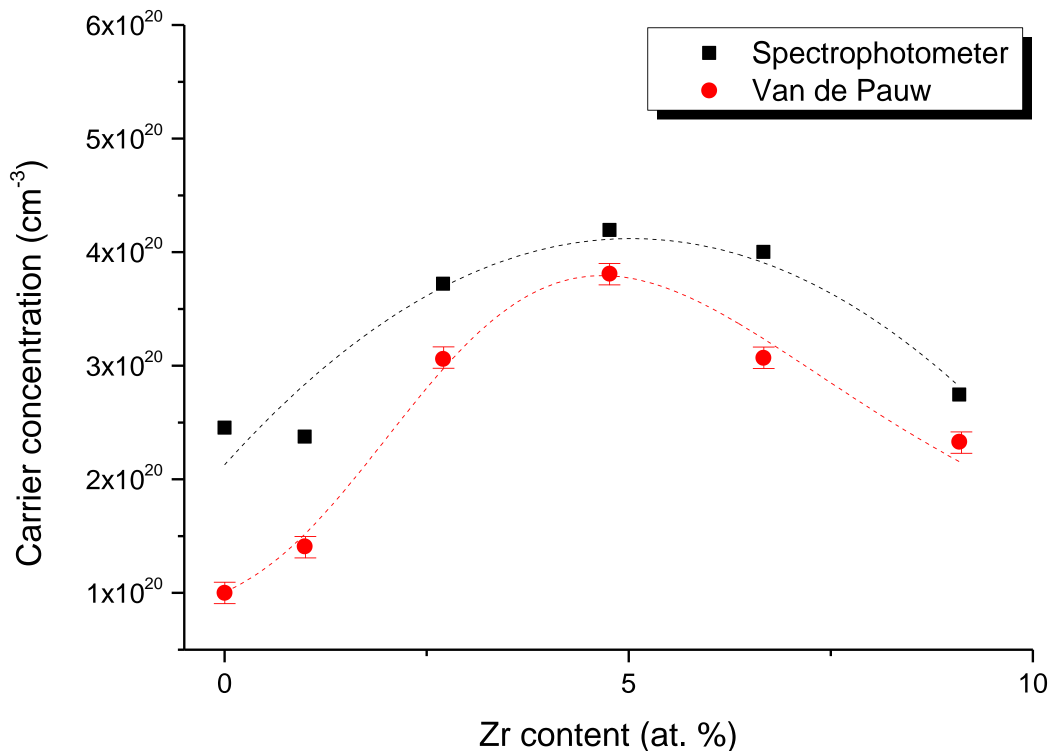

Figure 81: Carrier density comparison between the spectrophotometer data and Hall effect measurements.

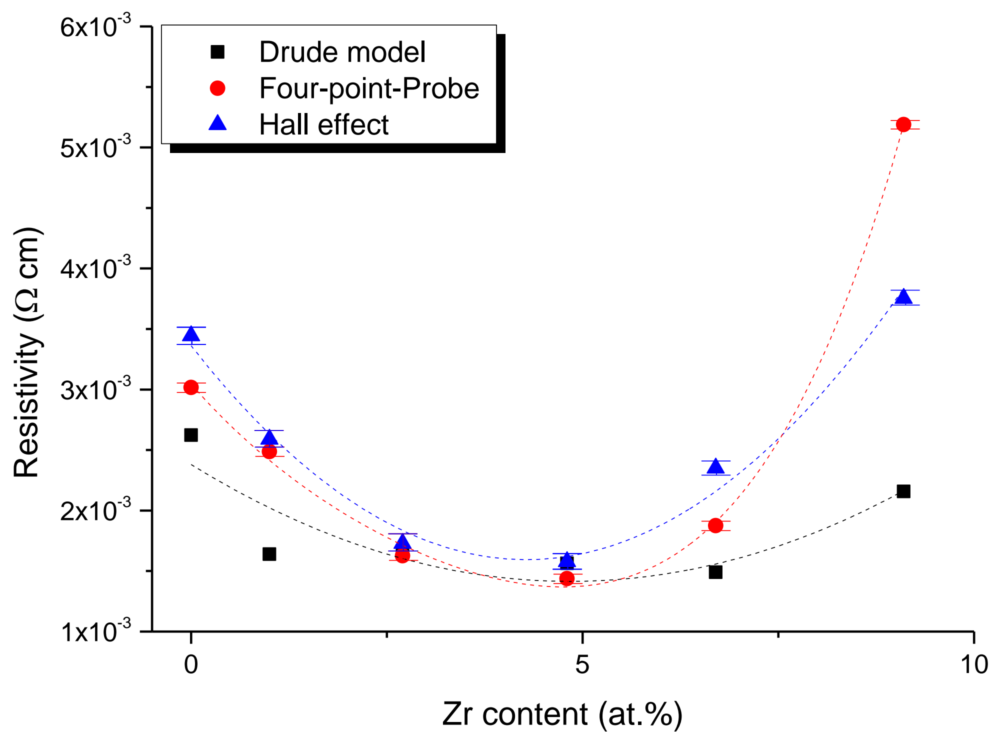

Figure 82: Resistivity comparison between experimental (Hall effect and four-point-probe) and theoretical values (Drude model).

6.2.3 Optical bandgap calculation

The transmittance (T_r) data can also provide information about the light absorption in a wide range of photon energies (hv). The absorption coefficient (α) can be calculated by the inverse application of Lambert-Beer's law (Equation 59) [351], where t is the film thickness.

Equation 59

$$\alpha = \frac{1}{t}\ln\left[\frac{1}{T_r}\right]$$

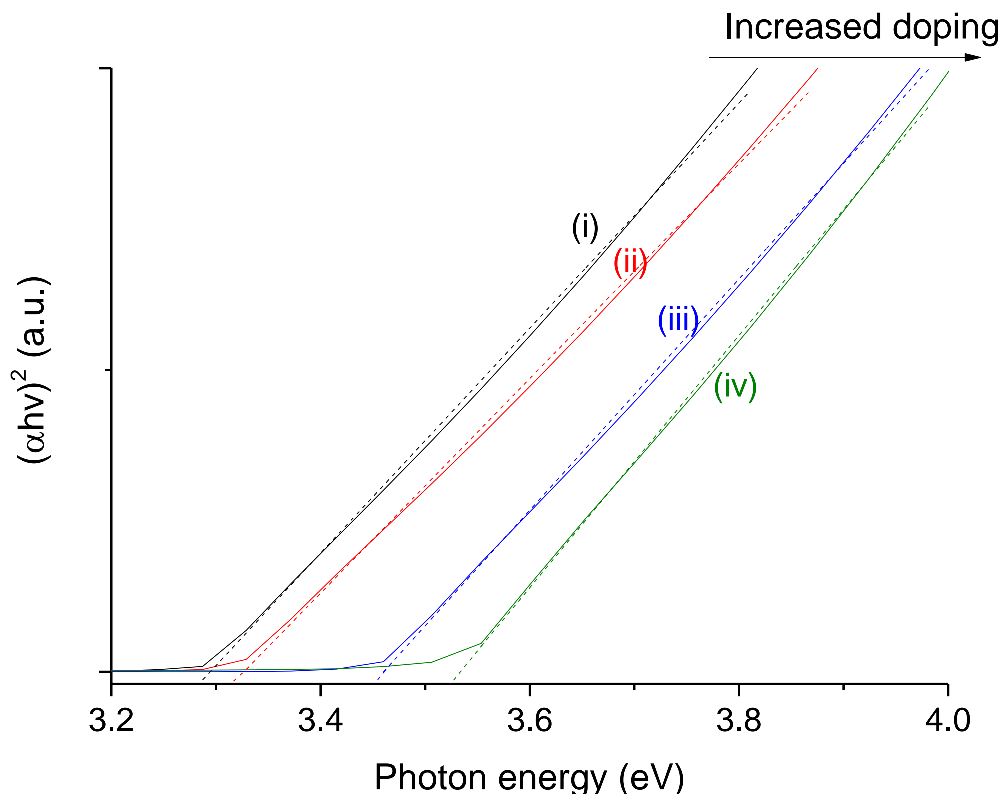

Figure 83: Tauc plots for (i) 0 at.%, (ii) 1.0 at.%, (iii) 2.7 at.%, and (iv) 4.8 at.% Zr-doped films.

The values of absorption coefficient were estimated with the use of SCOUT 3.0 spectrum simulation software, and were later on used to calculate the optical gap (E_g) over the range of photon energies (*hv)* as given in Equation 2 [73].

Equation 60

$$(\alpha hv)^2 = B(hv - E_g)$$

where B is a constant based on the electron-hole mobility. Tauc plots are then plotted as *(ahv)*^{2} *vs. hv*, in order to estimate the optical gap by the intersection of the graph to the y-axis. Fitted lines were used to the linear part of the curves, as shown in Figure 83.

Table 11: Optical gap values taken from Tauc plots with ±0.04 nm uncertainty.

Zr contents (at. %)	Optical gap (eV)
0	3.29
1	3.33
2.7	3.46
4.8	3.53
6.7	3.50
9.1	3.50

The optical gap values for the doped films are presented in Table 11. The data showed that as doping increases the gap is increasing, which is consistent with a study on Zr-doped films that attributed the effect to the grain size reduction due to doping [48]. However, this cannot be the case in the current study as the same shift was also observed for films having larger grains and same doping concentration (i.e. thicker films). This blue-shift was also confirmed by PL measurements. Hence, the shift is attributed to Burstein-Moss and many-body effects, resulting in optical gap

enlargement and narrowing respectively. This gap increase is consistent with the carrier density increase up to 4.8 at.% Zr doping (3.53 eV), which then is reduced for the two heavily doped films with lower carrier density.

6.2.4 Conclusion of the Spectrophotometry results

In conclusion, the high visible and near infrared transmittance of the ZnO: Zr films provide good properties for TCOs, in addition to the previously measured low resistivity values. The transparency was found at its maximum for the more conductive films (88%), and the optical gap was increased consistent with the carrier density increase at low Zr doping. The optical gap increase up to 3.53 eV is attributed to band filling effects. Further carrier density increase with thickness increase, showed even higher transparency up to 91% in the visible spectrum, and up to 91% in the near IR for the 50 nm thick film.

6.3 Photoluminescence

6.3.1 PL on un-doped ZnO films

6.3.1.1 Growth Temperature effect on the un-doped ZnO films

The PL data shown in Figure 84 are from the un-doped films on glass substrates, grown at different temperatures. The measurements were carried out with the lower

available excitation intensity (1.49 MW/cm^2 as determined in section 3.6.2) in order to obtain a full range of intensity data (i.e. at higher intensity the PL peaks were saturated).

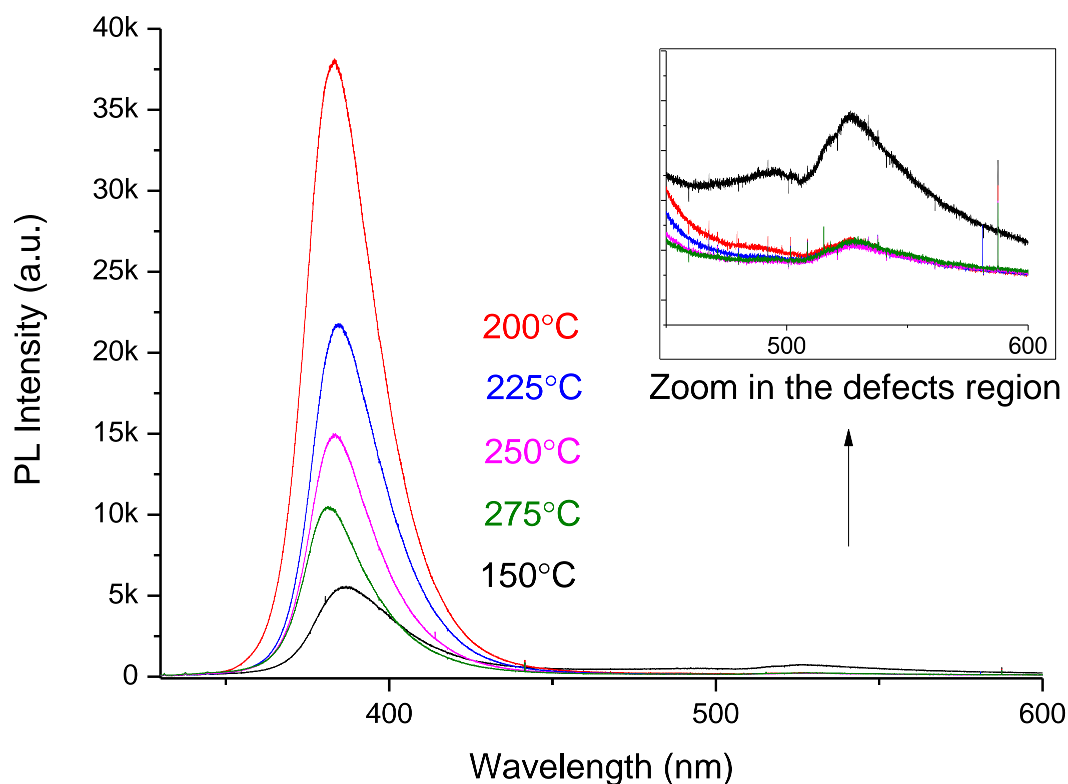

Figure 84: Growth temperature dependence of PL emission for ZnO films on glass.

The dominant emission is located at ~3.18-3.22 eV (i.e. 385-390 nm), which is consistent with the NBE reported in literature at 3.21-3.26 eV [99],[101]. All films show strong emission in the blue-green band (i.e. UV region below 400 nm) and weak defect-related emission in the region above 400 nm. The weak defect-related emission usually indicates low defect concentration and high quality films, but in the current measurements the use of high excitation intensity may be the cause of the defects passivation. The weak emission presented at ~2.36 eV (525 nm), corresponds

to oxygen defect emission from the recombination of electrons trapped in oxygen vacancy defect states to holes in the VBM [105]. As shown in the magnification graph, the sample grown at 150°C has higher defect peak, indicating the creation of defects due to the lack of thermal energy and thus caused the formation of incomplete bonds (increase of oxygen vacancies).

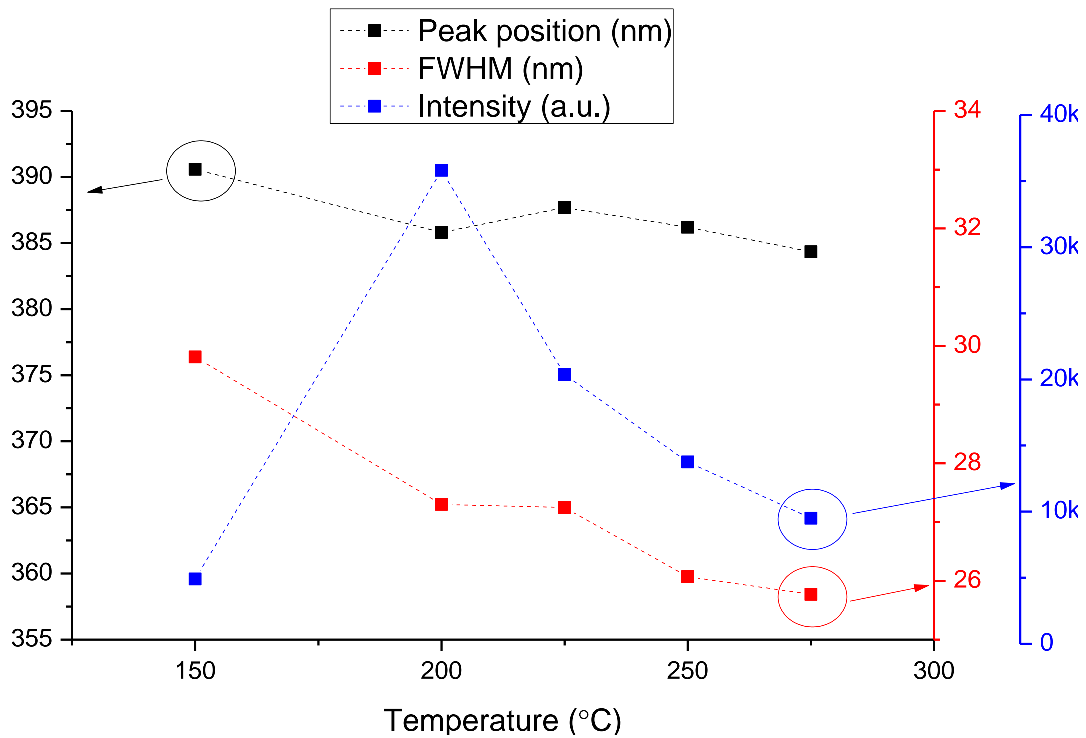

Figure 85: Growth temperature dependence of PL peaks for ZnO films 60-100 nm thick on glass.

For further analysis the peak position, the FWHM and the peak intensity are plotted in Figure 85. The peak position shows energy increase with growth temperature. The emission energy reduction (red-shifting) is related to the tensile strain induced in the films, while the compressive strain induces energy increase (blue-shifting) [73]. This phenomenon is more intense in very small structures (i.e. smaller than 12 Å [365]),

due to the quantum effect, but it is also valid for larger structures. This was suggested by Glinka et al. [366], who showed that the blue-shifting in PL was due to the decreased size of material fragments causing increased scattering in grain boundaries. Therefore, the blue shifting of the bandgap observed in the current measurements is associated with the compressive strain increase as the grain size reduces (lower thickness) for high temperature grown films (see section 4.2).

The FWHM on the other hand, is used as an indication of the good quality of the films crystals [367]. It is reduced as growth temperature increases showing improved crystal formation. However, the intensity of those peaks is different than the broadness trend, with the sample grown at 200°C showing the highest peak intensity. The peak intensity is related to the conductivity of the samples as it expresses the amount of electron-hole recombinations. In more detail, the radiative recombination rate (R) is directly proportional to the electron (n_e) and hole (n_p) concentration (i.e. $R=B\times n_e\times n_p$ where B is a constant [73]), expressing the rate of photons generated per unit volume [73]. Hence, in a degenerate semiconductor were $n_e >> n_p$, an increase of n_e will lead to more radiative recombinations in PL. Therefore, the stronger PL signal at 200°C is consistent with the higher carrier density shown in section 5.2.1, leading to more photo-excited electrons.

6.3.1.2 Excitation energy dependence on the PL signal of the un-doped films

The changes in emissions with different excitation intensity could reveal the origin of the recombination. Based on that, the un-doped film on glass substrate grown at

200°C was tested by varying the excitation energy at room temperature, as shown in Figure 86.

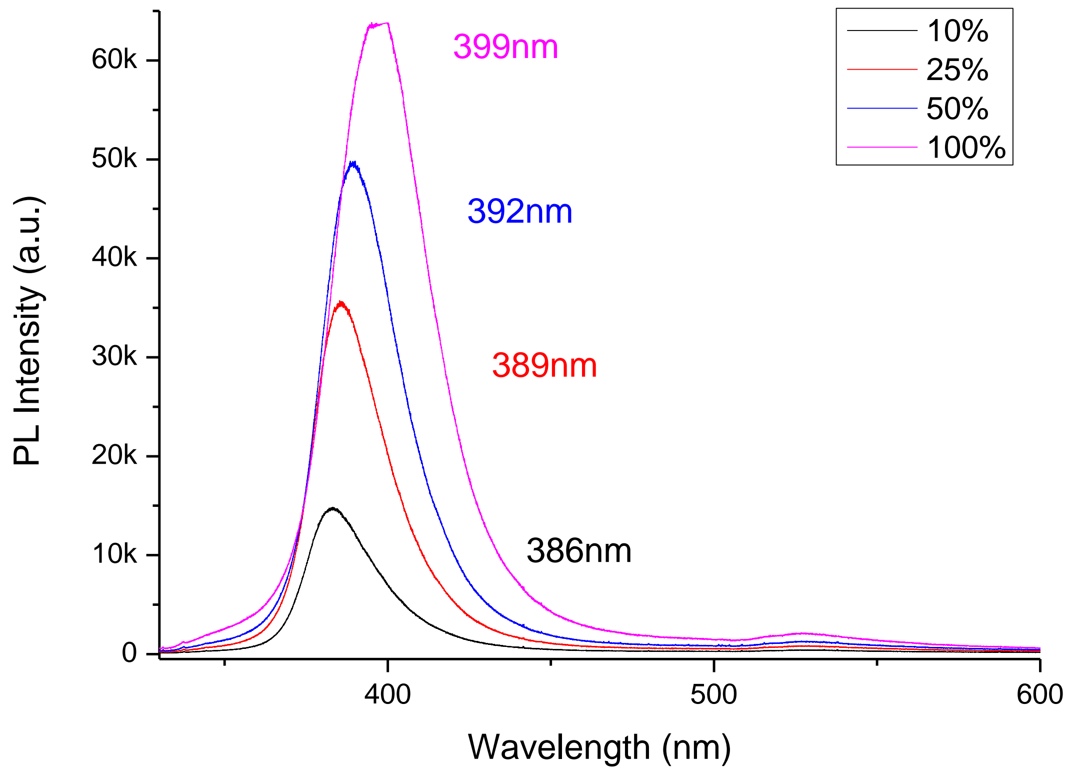

Figure 86: Excitation energy dependence of PL emission for ZnO film grown at 200°C on glass.

The emission peak is shown to be red-shifted (i.e. 3.21-3.11 eV) and broader as the excitation intensity increases. This indicates a stimulated emission, which could be separated into three phases according to the intensity used. The three possible phases are shown in Figure 87 and are based on Zhang's et al. study [368]. Firstly, the super-linear increase of the emission intensity (I) indicates a spontaneous emission, the linear shows a stimulated emission, and the sub-linear shows a stimulated emission at very high excitation intensity (I_{EXC}). The phase is estimated by calculating the exponential using Equation 61 [369].

Equation 61

$$I = \beta {I_{EXC}}^{k}$$

where β is a constant and k is an exponential. According to Schmidt and Lischka [370], k varies between 1 and 2 for energies of excitonic transitions (i.e. linear and super-linear). For bandgap recombination k=2 [371], and for free to bound and donor-acceptor pair transitions k is smaller than unity [370]. At high excitation intensity, electron-hole plasma emissions also occur showing k<1 [372].

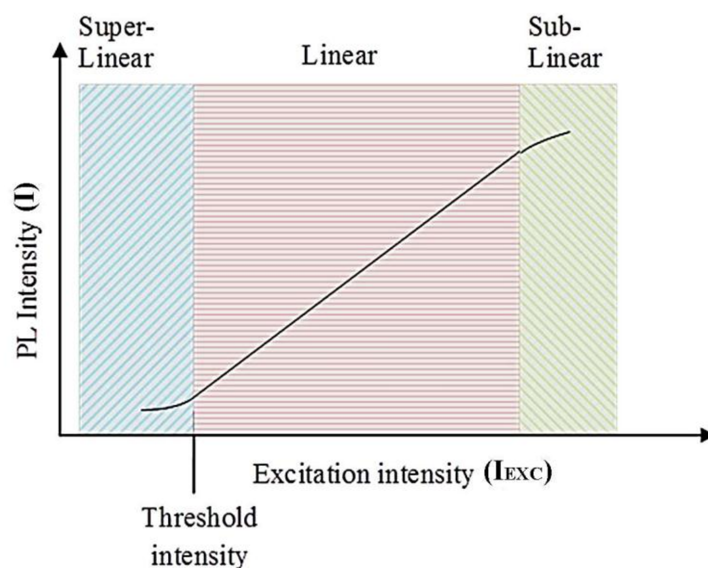

Figure 87: Schematic example of the excitation and emitted intensity relation [368],[270].

The relation of the excitation and emitted intensity of the un-doped film is plotted in Figure 88. The increasing relation indicated stimulated emission with sub-linear increase, and the exponential was estimated as k = 0.54. This suggested that the excitation intensity used was very high (1.49-14.87 MW/cm^2) leading to saturation of the emission. This is consistent with a study on transparent substrates with

excitation intensity up to 480 kW/cm^2 [368]. Therefore, for the current study it is not possible to specify the threshold intensity. The threshold intensity is useful to evaluate the optical quality of the film, which indicates high optical quality when the value is low [368]. For ZnO the threshold intensity was reported as low as 35 kW/cm^2 [113], reduced to this value by using Al_2O_3 passivation layer. In order to specify the threshold intensity for future measurements, it is suggested to use lower magnification objective with high focal length. An example would be the use of LMU-5×-NUV with *f*=40 mm, that will result in intensity range of 23-232 kW/cm^2.

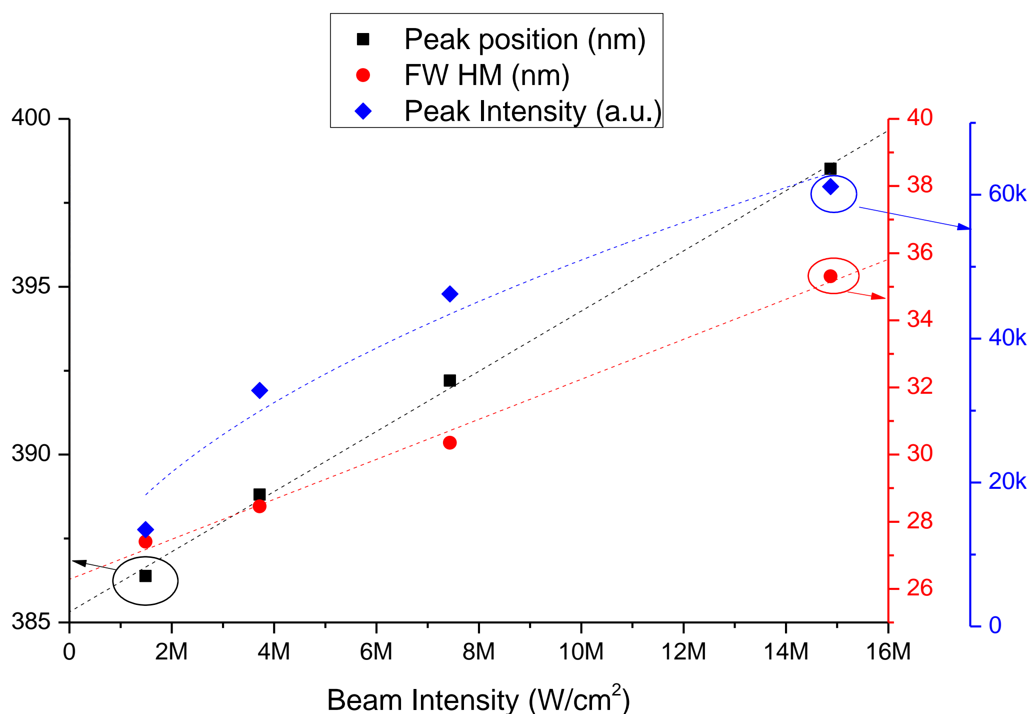

Figure 88: Excitation energy dependence of PL peaks for un-doped ZnO film grown at 200°C on glass.

The saturation of the emission at high excitation intensity is attributed to the damage to the film, which leads to the creation of defect related traps that capture the carriers

and reduce the emission intensity. Those defects would be expected to exist even if the irradiation is reduced, although due to the low excitation energy their effect will be reduced. The other possibility of Auger recombination is rejected as no second radiative recombination at higher energy was observed.

Figure 88 also shows the emission energy and FWHM of the peaks as the excitation intensity increases. The emission is linearly reduced in energy and in broadness as the excitation intensity increases. This indicates non-linear optics, which is a transitional phase of the linear optics (single electron-hole recombinations from excitons or free carriers) [373]. The transition occurs for degenerate materials and for high excitation intensities, which is the case for the current measurements.

Klingshirn studied the linear and nonlinear optics [372], in which the linear optics occur at low excitation intensities below 1 kW/cm^2, resulting in recombination types such as bound excitons (~3.35-3.37 eV at < 70 K [100]), and recombinations between excitons and free carriers. The non-linear optics occurred at intermediate and high intensities in the range of 10^3-10^6 W/cm^2. At intermediate level, the excitons scattered elastically and inelastically with each other due to the extra energy obtained (~3.32 eV at low temperature [17]). At high excitation intensity, the excitons form a different phase, the electron-hole plasma (EHP). This is a metallic state of the pairs formed when the exciton concentration reaches the Mott density. At that point, the excitons overlap with each other and Coulomb interaction is weakening [373]. As a result, excitons lose their individual character as quasiparticles and change to EHP [113]. The Mott density is reported by many studies at room temperature with values such as 3×10^{17} cm^{-3} [113], 5×10^{17} cm^{-3} [100], 1.5×10^{18} cm^{-3} [344], and 4×10^{18} cm^{-3} [17]. The EHP emission for ZnO is usually observed at 3.14-3.15 eV [17],[374], and for ALD grown films is at 3.12-3.16 eV [107],[113].

The intensity used in the current experiments is at the maximum end of the non-linear phase, suggesting that the emission observed is an EHP emission. In order to verify this, the exciton concentration is calculated using Equation 62 [100].

Equation 62

$$n_p = \frac{I_{EXC}\tau}{\hbar\omega_{EXC}t}$$

where τ is the exciton lifetime (typically 300 ps for bulk ZnO), $\hbar\omega_{EXC}$ is the photons energy, and t is the film thickness. The calculated exciton concentration for the un-doped film ranges from 8×10^{19} cm^{-3} to 8×10^{20} cm^{-3}. The concentration is orders of magnitude higher than the Mott density suggesting EHP emission. Thus, the EHP will result in renormalisation of the bandgap (narrowing), and thus the further increase of the exciton concentration at higher intensity will lead to further reduction of the energy emission [113]. In addition, the bandgap narrowing and the high excitation intensity will induce more recombination channels and hence the emission will become broader. This is consistent with the current data that showed increased FWHM and red-shift of the emission as the intensity increased.

The lower intensity at 1.49 MW/cm^2 is used for the rest of the measurements to limit the damage to the films at such high intensities. The emission is EHP for all the films presented (un-doped and doped ones), and the reference point of the optical gap is set at 3.21 eV (un-doped ZnO at 1.49 MW/cm^2) in order to observe any shifts due to doping.

6.3.1.3 Low temperature measurements on ZnO films

The temperature dependence measurements provide information about the thermally induced bandgap shifts and the activation energy of the thermal quenching. The results for the temperature at 83-293 K (-190°C until 20°C) are shown in Figure 89.

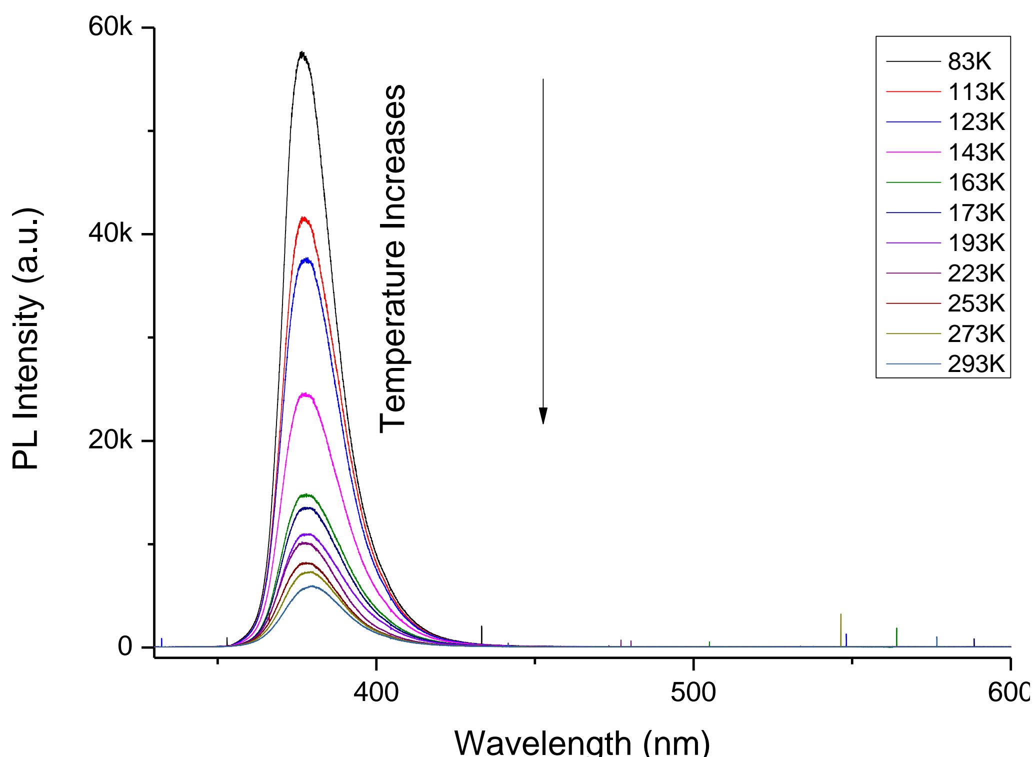

Figure 89: Low temperature PL measurements for un-doped ZnO film grown at 200°C on Si.

The results show a reduction of the peak intensity and red-shift of the emission as the temperature increases. The reduction of the PL intensity is part of the temperature quenching, expressed by Equation 63 [375]. Figure 90 shows the experimental data in relation to this formula.

Equation 63

$$I(T) = \frac{I_0}{1 + A\exp\left(-\frac{E_a}{k_B T}\right)}$$

where A is a constant, k_B is the Boltzman constant, I_0 is the intensity at 0 K, and E_α is the activation energy in thermal quenching process. E_α is the energy required for the thermal escape of carriers from the ground state [376]. Therefore, lower thermal quenching (higher E_α) implies decrease of the thermal escape to non-radiative recombination centres [377]. The activation energies from thermal and negative thermal quenching are in the range of 10-70 meV for ZnO, which consists of the binding energy of excitons to defects, the exciton-binding energy itself and the LO-phonon energy [61].

From the resulted equation in Figure 90, the activation energy (E_α) is found at 33.65 meV. E_α of un-doped ZnO was at 30 meV for deep level emissions [378], at 61 meV for free exciton emission [379], at 53 meV for (D^0X) transition [380], and at 17 meV for NBE emission for films grown by ALD [381]. Hence, the activation energy in the current films is higher than the ones reported in literature, indicating that more excitons are confined in the un-doped film. This could be related to neutral defects formed by intrinsic acceptors and free carriers.

The shift to lower energy as temperature increases is related to the lattice distortions that cause changes in the position of the bands [382]. As a result, the thermal energy within the lattice is increased and provides the electrons with higher energy to move. The increased electron mobility results to more populate energy states leading to thermally induced gap reduction. This is expressed by Varshni’s formula (Equation

64) [383], which shows that the gap at high temperature has lower energy than the fundamental bandgap at near zero temperature.

Equation 64

$$E_g(T) = E_g(0) - \frac{\alpha T^2}{T + \beta}$$

where Eg (T) is the measured gap at a certain temperature T, Eg (0) is the gap value at 0 K (i.e. 3.44 eV [Z7]), α and β are constants. The constant α is in the order of 10^{-4} eVK^{-1} and β is proportional to Debye temperature (i.e. 305-1050 K) [384].

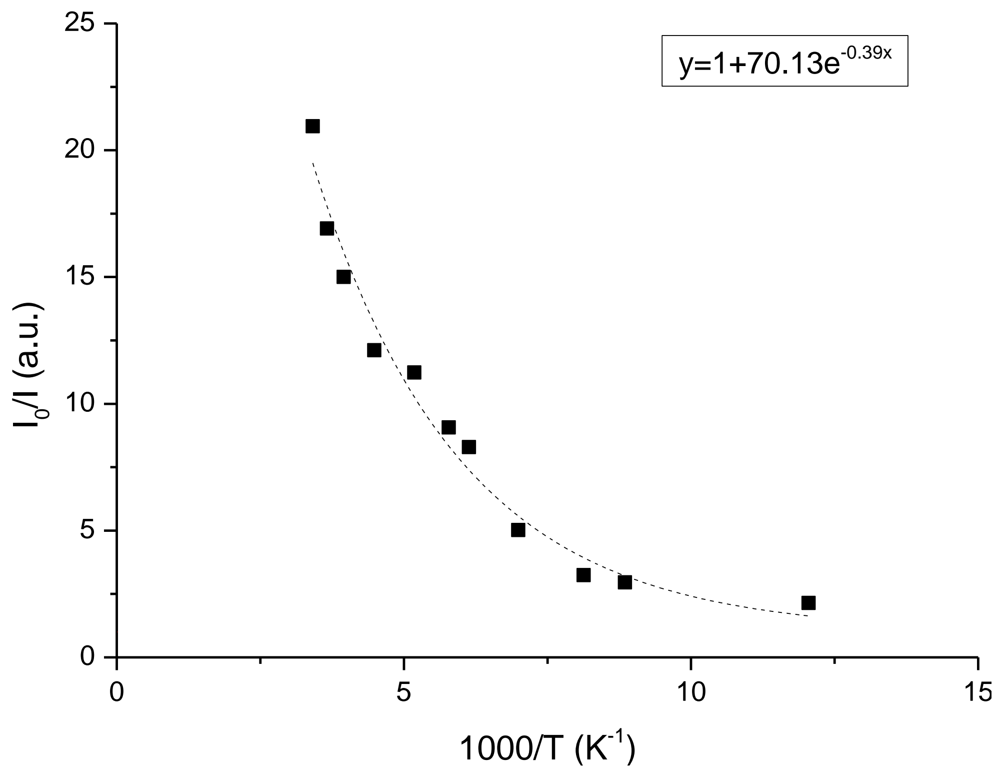

Figure 90: Low temperature dependence of integral intensity for un-doped film grown at 200°C on Si.

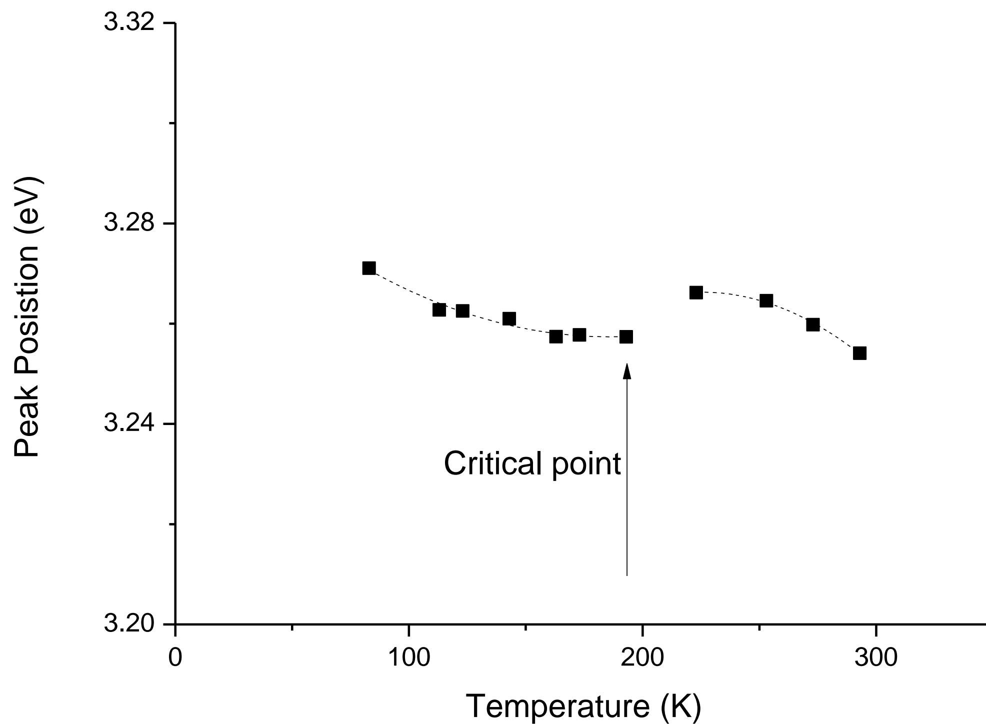

Figure 91: Low temperature dependence of the peak position for un-doped ZnO film on Si substrate.

The relationship between the emission energy to the temperature is shown in Figure 91. The results show a reduction of the energy emission as the temperature increases up to 193 K when the trend is changing. Immediately above the transition point the emission energy is shown to be increased. The transition point around 200 K is consistent with literature for ZnO films [106],[385]. The study [385] reported that carriers are randomly distributed before recombining at low temperatures, and as the temperature rises up to the transition point the carrier lifetime increases. In this case the carriers relax to lower localised states and recombine at lower energy. At temperatures beyond the critical point and up to 210 K, the carriers have enough energy to overcome the localisation states and recombine at higher energies [385]. In the current films, the increased point is at 223 K, which is very close to the reported

value in [385]. At higher temperatures, the carriers gain more thermal energy and can recombine at lower energy.

6.3.1.4 Substrate effect on the PL signal

In order to specify the substrate effect on the emission shifts, the un-doped ZnO film was measured at fixed excitation intensity on both Si and glass substrates as shown in Figure 92. For the Si substrate the intensity is much higher than the one for glass, as more PL signal is reflected from an opaque substrate such as the silicon wafer. The transparent substrate (glass) leads to penetration of the light through the sample and thus reduces the PL signal. The plots also show peak shifting between the two substrates, with the peak corresponding to Si at 3.24 eV and the one corresponding to glass at 3.21 eV (i.e. difference of 27 meV).

The effect of the substrate thermal mismatch of Si and glass could cause changes in the bandgap due to strain. The main cause of extrinsic strain for thin films is the difference of thermal expansion coefficient between the film and the substrate. This is due to the cooling phase when the film is brought to room temperature after it was deposited at higher temperature, causing in-plane strain (i.e. thermal strain) in the film. The strain can alter the bandgap, with the tensile strain causing reduction of the emission energy and the compressive strain causing an increase in energy.

The strain for each substrate and for the two different grain orientations identified for the current films is calculated using their thermal expansion coefficients. The thermal expansion coefficient is $\alpha_a = 4.31\times10^{-6}$ K^{-1} and $\alpha_c = 2.49\times10^{-6}$ K^{-1} for a-axis and c-axis respectively [72]. From the supplier's specifications, the single crystal Si

wafer has α_{Si} =2.5×10^{-6} K^{-1} and the microscope glass slide has α_{Glass}=9×10^{-6} K^{-1}. The thermal strain is calculated using Equation 65 [386] and the results are shown in Table 12. The results show compressive strain for the glass substrates for both grains orientations. The c-axis oriented films on Si substrates show less compression compared to glass, and the a-axis films on Si substrates show tensile strain.

Equation 65

$$\varepsilon_i^{film} = \int_{T_{Growth}}^{T_{RT}} \left(a^{film} - a^{substrate}\right) dT$$

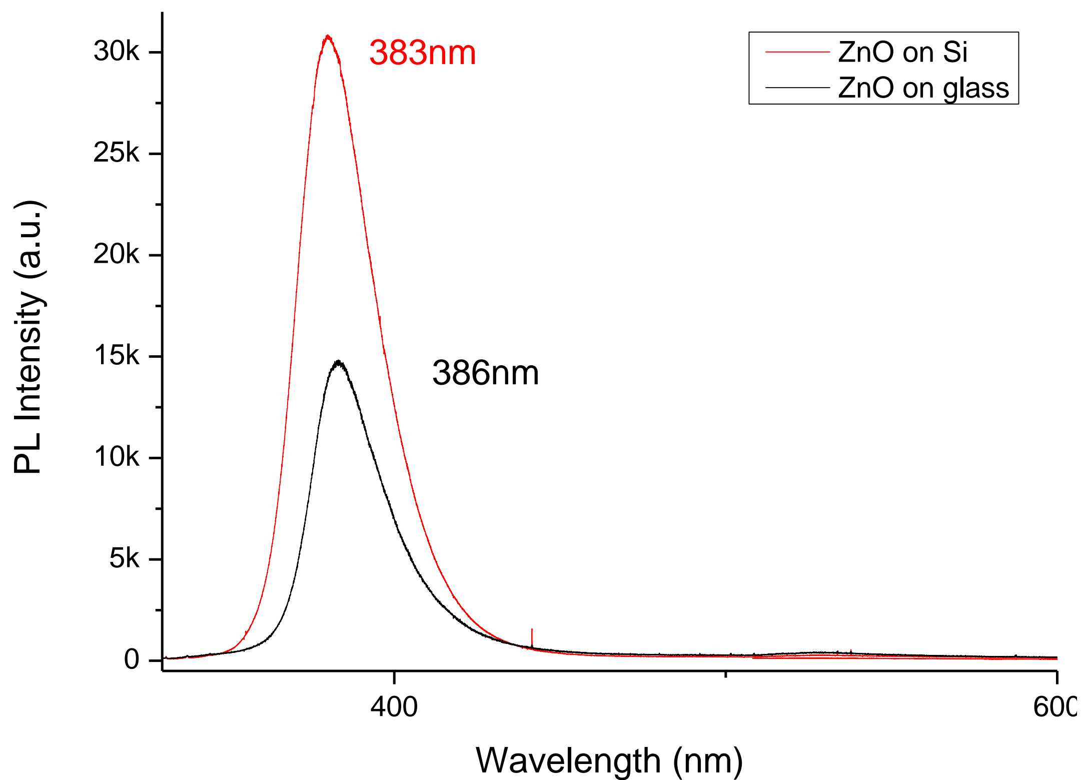

Figure 92: Substrate effect dependence of PL emission for un-doped ZnO film.

Table 12: Thermal strain on glass and Si substrates.

Thermal strain (%)	a-axis	c-axis
Microscope glass slides (1.2mm)	-0.084	-0.117
Si wafers	0.033	-0.0002

The thermal in-plane strain is isotropic as it only depends on the thermal expansion coefficients [386]. Thus, the out-of-plane strain (ε_o) could be calculated in relation to the in-plane strain (ε_i) by Equation 66 [340], where C is the elastic stiffness of ZnO, with C_{13}=105.1 GPa and C_{33}=209.7 GPa [386]. Due to its hexagonal structure the strains ε_{xx} and ε_{yy} are the same and equivalent to the thermal in-plane strain, while the ε_{zz} is equal to the out-of-plane strain. However, due to the dual orientation of the films both directions were taken into account for this theoretical model.

Equation 66

$$\varepsilon_o^{film} = -\frac{2C_{13}}{C_{33}}\varepsilon_i^{film}$$

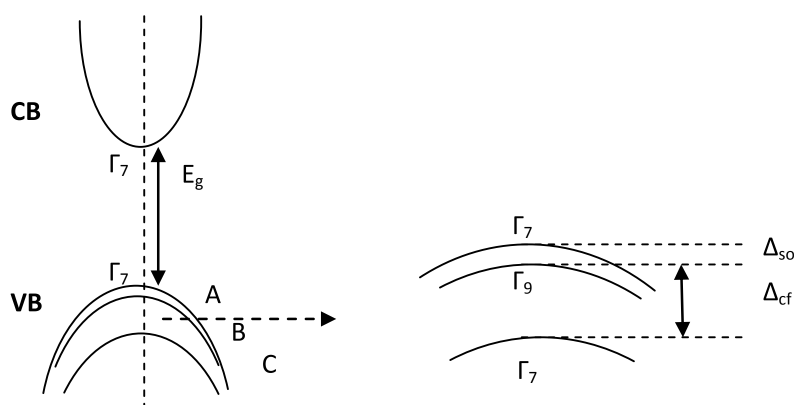

Figure 93: a) Schematic diagram of the CB and VB; b) VB sub-bands.

The total thermal mismatch is calculated using Equation 67, in relation to the thermal strain calculated earlier and the position of the highest VB sub-band. The VB has symmetry Γ_7 (band edge) and consists of three sub-bands due to spin by the hexagonal crystal field [17] as shown by the schematic in Figure 93. The sub-bands are named as A, B and C, with symmetries Γ_7, Γ_9 and Γ_7 respectively. The shift between A and B is the energy difference due to spin orbital splitting (Δ_{so}) and between B and C is the difference by the crystal field splitting. The spin orbital splitting denotes that A and B correspond to heavily and light hole bands respectively [78].

Equation 67

$$\Delta E_v(A) = \delta_1 + \frac{\delta_2}{2} \times \left(1 + \frac{\Delta_{cf} - \left(\frac{\Delta_{so}}{3}\right)}{\sqrt{\left(\Delta_{cf} - \left(\frac{\Delta_{so}}{3}\right)\right)^2 + 8 \times \left(\frac{\Delta_{so}}{3}\right)^2}} \right)$$

where Δcf is the crystal field splitting equal to 54 meV and Δso is the spin orbital splitting equal to -3.5 meV [387]. The δ constants can be calculated using Equation 68, with the deformation potentials being equal to C1=-2.66 eV, C2=2.82 eV, C3=-1.34 eV and C4=1.0 eV [388].

Equation 68

$$\delta_1 = C_1 \varepsilon_{zz} + C_2(\varepsilon_{xx} + \varepsilon_{yy})$$

$$\delta_2 = C_3 \varepsilon_{zz} + C_4(\varepsilon_{xx} + \varepsilon_{yy})$$

The calculations show -11.7 meV shift for the c-axis film on glass substrate, and as the grains orientation shifts to a-axis at the top layers of the film, the additional strain

is calculated at -8.4 meV (calculated as an interface with glass). For the Si substrates the total shift is calculated at 3.3 meV. Therefore, a total difference of 23.4 meV between the two substrates can be attributed to the thermal mismatch. Nevertheless, the experimental difference is found at 27 meV. This difference could be partially due to the error margin during calibration (±0.3 meV), and the strain differences between the interface of the c-axis and a-axis oriented grains. The thermal mismatch is very small, hence, both substrates are used for PL measurements. However, most of the analysis is carried out using glass substrates in order to be comparable with the transmittance and electrical measurements.

6.3.2 PL on ZnO: Zr samples

The PL measurements for Zr-doped ZnO films are shown in this section, and focus on the effect of doping and film thickness variation. Note that the dominant emission is an EHP for all the doped films, based on the exciton concentration showing an increase as doping increases (9.2×10^{19} cm^{-3}). For the thicker 4.8 at.% doped film the exciton concentration (2.92×10^{19} cm^{-3}) is again higher than the Mott density and thus shows an EHP emission.

The results of different doped films on glass substrates are shown in Figure 94. The primary emission is shown to be reduced in intensity as doping increases, especially for films doped higher than 2.7 at.%. This is attributed to the carrier mobility reduction by increasing the doping level, leading to electron scattering and hence to the emission drop. In the UV region, it is shown two peaks separated by ~0.3 eV. Their exact energy is found after peak fitting a Lorenzian function and the data are

shown in Table 13. The deep-level emission is significantly low showing the passivation of the defects due to the high excitation intensity.

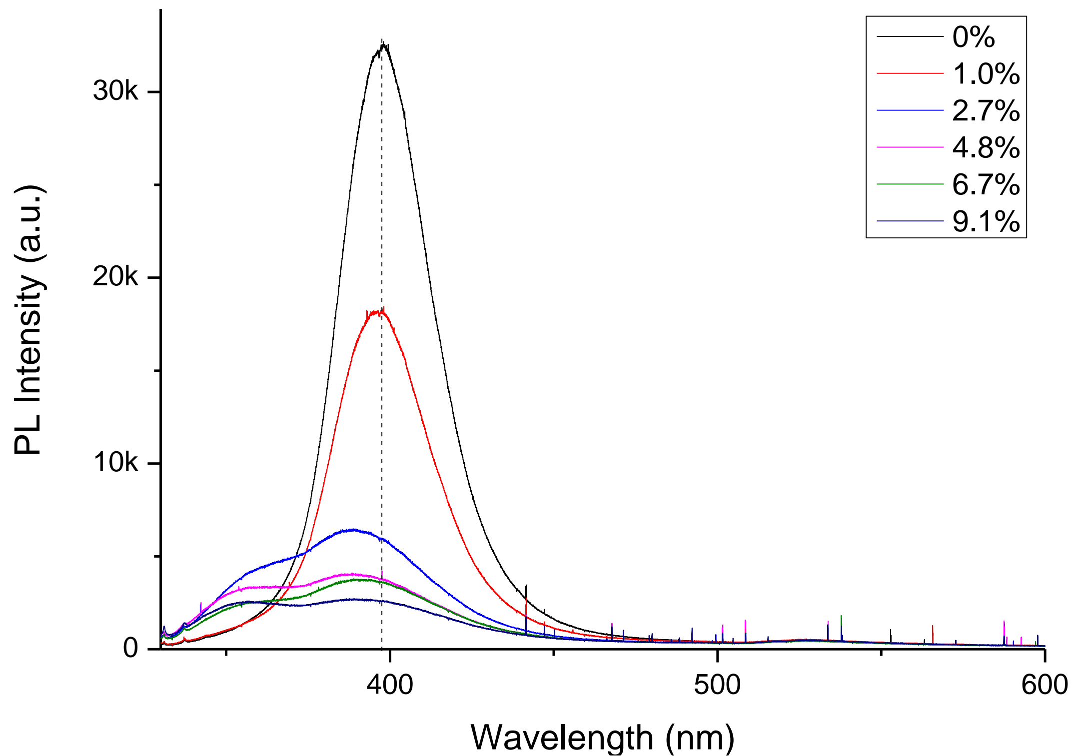

Figure 94: Zr doping dependence of PL emission for films ~85 nm thick grown on glass substrates.

The appearance of the two peaks at ~3.14 eV (395 nm) and ~3.5 eV (354 nm) suggests recombination between more than two different states, or is showing a phenomenon of peak separation. Peaks separation could occur either under magnetic fields causing Zeeman effects [389], or when measurements are carried out under low temperature (10 K) and different exciton recombinations are observed [17]. However, the measurements presented here were at room temperature and without the influence of any external field (magnetic or electric). Therefore, the following discussion is examining firstly which of the two peaks is the dominant one

corresponding to the EHP emission, and then what is the reason of the second emission appearance.

Table 13: Peak position of the high and low energy emissions for the ZnO: Zr films.

Peak position (eV)	
High energy emission	Low energy emission
-	3.21
-	3.24
3.49	3.15
3.52	3.14
3.49	3.15
3.50	3.14

The films deposited on Si substrates (Figure 95) were tested in order to specify the dominant peak. The energy reduction of the dominant emission as the doping increases and the existence of two emissions suggest that their appearance is not affected by the substrate. Also, the highest intensity peak is the one with high energy emission. This comes in contrast to the data obtained for glass, hence, further tests were carried out.

Measurements taken ten months apart on the same samples (glass) showed different dominant peak as shown in Figure 96. The initial scans show the high energy peak as the most dominant, while 10 months later the scans show the low energy peak as the dominant one. Several explanations were considered, including degradation over time. However, this explanation could be valid only if the electrical properties altered as well. This case was excluded after resistivity measurements were consistent with the initial measurements values.

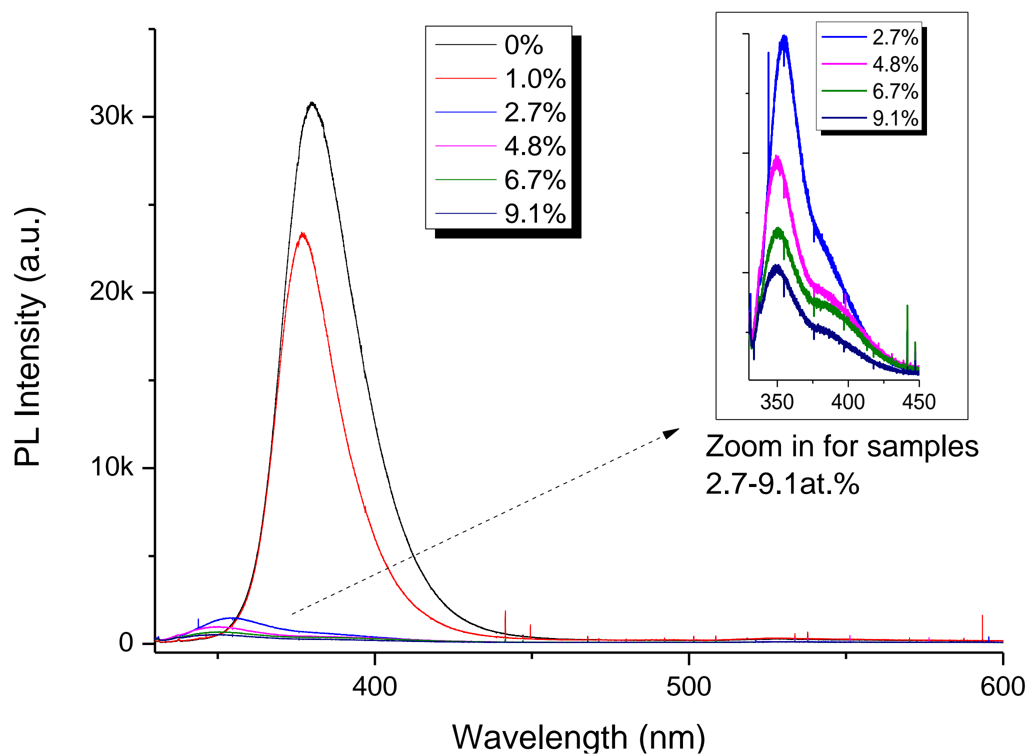

Figure 95: Zr doping dependence of PL emission for films ~85 nm thick grown on Si substrates.

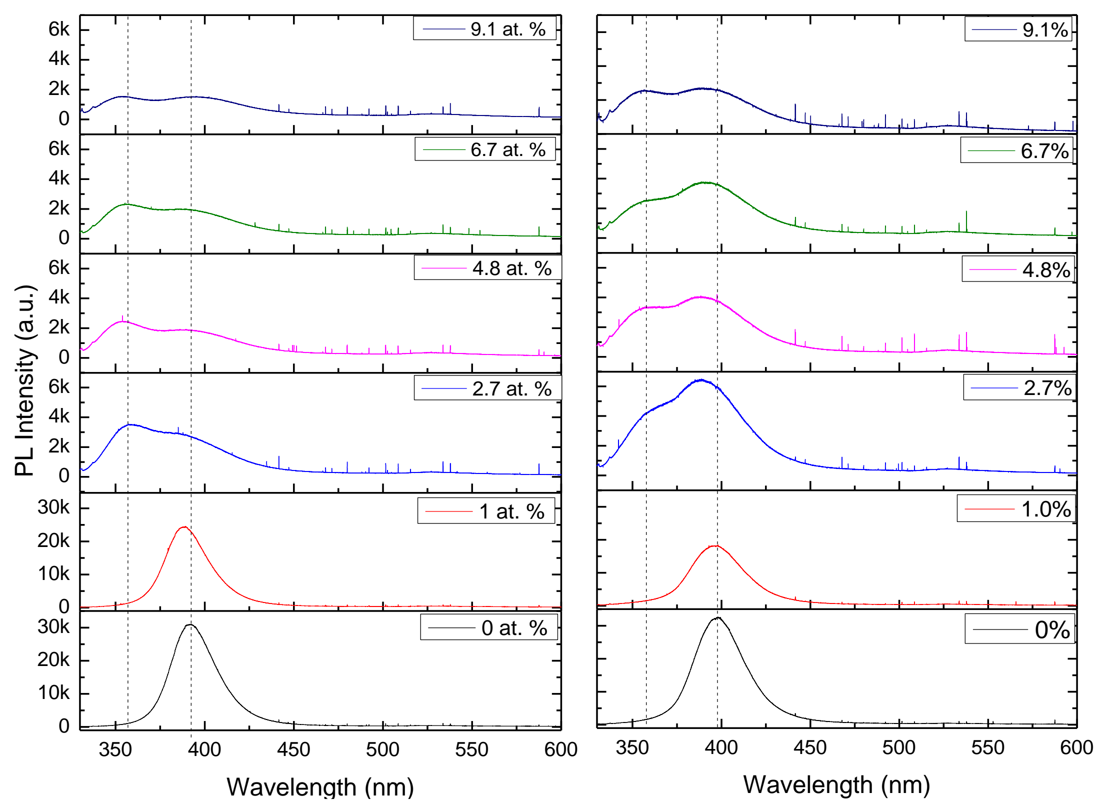

Figure 96: PL stack comparison of the a) initial testing, b) after 10 months testing

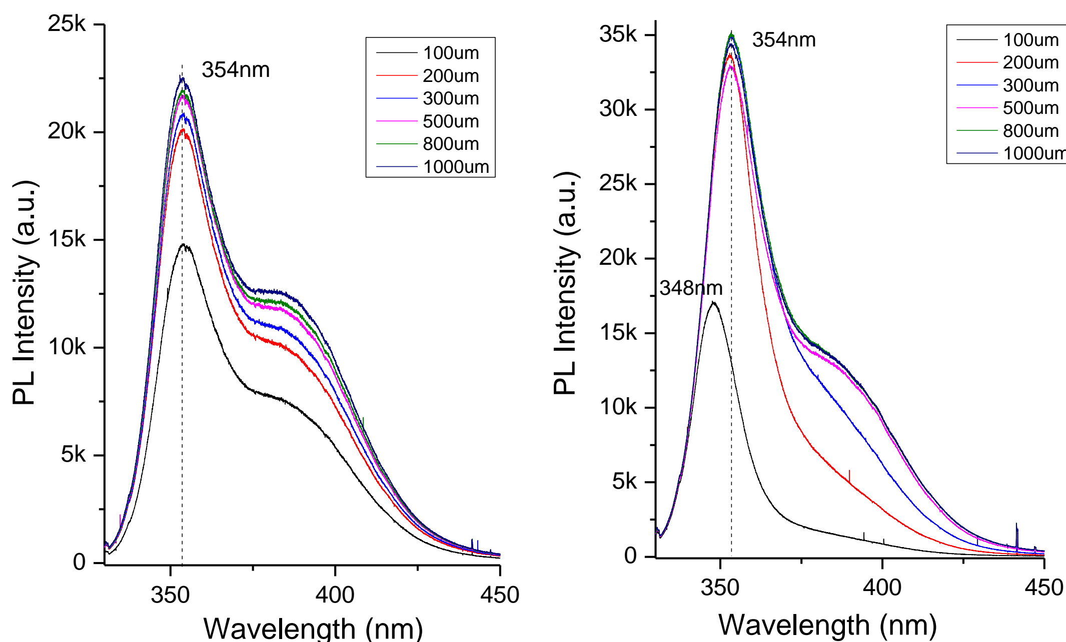

Figure 97: Confocal hole dependence of PL emission for 250 nm thick film with 4.8 at.% doping on Si wafer, using a) 40×-NUV lens, b) 15×-NUV lens.

A confocal test was carried out to investigate further the changes in intensity. Figure 97 shows the confocal test carried out for 250 nm thick film with 4.8 at.% Zr doping. Two different microscope objectives were used in order to compare the magnification effect on the changing of the confocal hole. The test shows that at smaller hole diameter the intensity is proportional to the diameter increase. At larger diameter (500 µm) the intensity is fixed as the hole is larger than the reflected beam diameter. With the LMU-15×-NUV lens and low confocal hole (100 µm) the high energy emission is shifted at higher energy, indicating that the reflected signal was out-of-focus and that the light passing through the hole was attenuated. The disappearance of the low energy emission suggests that its existence is relevant to the focus of the laser to the surface.

A stage position test was also carried out using 100 µm confocal hole and LMU-15×-NUV lens for Si and glass substrates (Figure 98). As the stage moved closer or

further from the focus point the high energy peak decreases in intensity. Therefore, the focus to the surface affects the intensity, and it is the cause of the difference between the scans shown in Figure 96. The high energy peak shows the highest intensity of both emissions. As a result, the high energy emission is considered as the dominant one corresponding to the EHP emission.

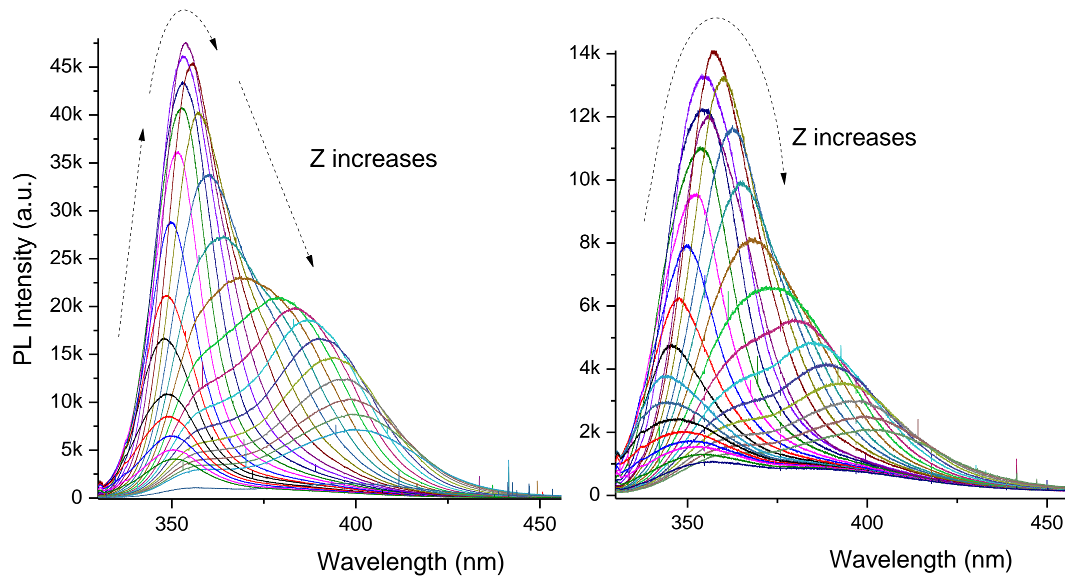

Figure 98: Focus test of 250 nm thick films with 4.8 at.% Zr doping on a) Si and b) glass, with LMU-15×-NUV objective lenses, 100 μm confocal Hole and full excitation energy.

The optical gap of the films is shown to be increased up to ~3.5 eV with doping. The increase occurs gradually up to 4.8 at.% doping, at which point it is slightly reduced possibly due to the reduction of the carrier density for the two heavily doped films. In order to confirm the origin of the high energy peak and define the recombination occurred for the low energy emission, the analysis in section 6.3.2.1 was carried out.

6.3.2.1 The PL peaks origin

In order to identify if the peaks are induced by the high excitation intensity, the excitation intensity was altered for the 250 nm thick film with 4.8 at.% doping as shown in Figure 99. As the excitation intensity increases, both peaks are reduced in energy (Figure 100) and increased in intensity (Figure 101). When this intensity relation is applied to Equation 61, the exponential component *k* is ~0.5 for the higher energy peak. This is consistent with the un-doped film emission in part 6.3.1.2, thus it indicates that the high energy emission corresponds to an EHP emission (non-linear optics). The lower energy peak follows an almost linear relation between the excitation intensity and the PL intensity signal, resulting in *k*=~0.91. The lower than unity exponential shows that the lower energy emission is not excitonic (i.e. should have been higher than 1).

The trend similarity between the high energy emission and the un-doped emission supports that this is an EHP emission. This intensity increase rejects the possibility of having an EHP emission and an exciton-exciton emission observed at high excitation intensity. In this case, the EHP emission (3.14 eV) is expected to have lower energy than the exciton emission (3.18 eV) [390], and as the excitation intensity increases the EHP emission is expected to be amplified and the exciton emission to be reduced in intensity.

The 250 nm thick film on Si substrate with 4.8 at.% doping was used for low temperature PL measurements as shown in Figure 102. The first observation is that the two peaks are still distinct at low temperatures. Also, the high energy peak is shown to increase more compared to the low energy peak. Therefore, again the low energy peak is shown to be induced at high energy conditions (thermal energy).

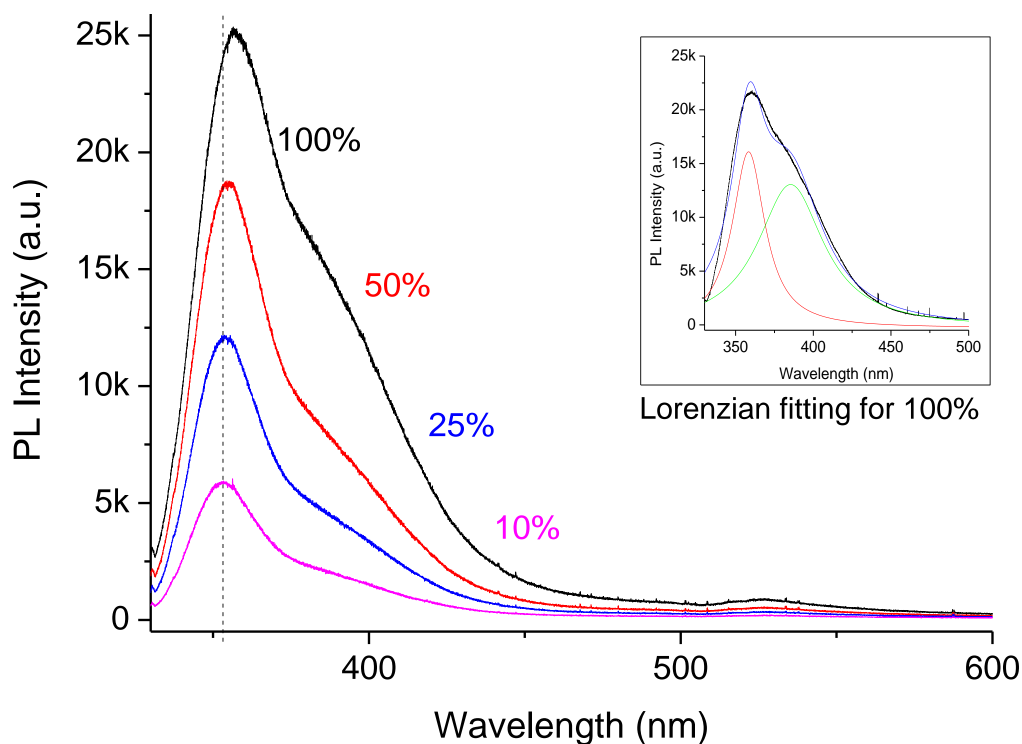

Figure 99: Excitation energy dependence of PL emission for ZnO films 250 nm thick doped with 4.8 at.% on glass substrate.

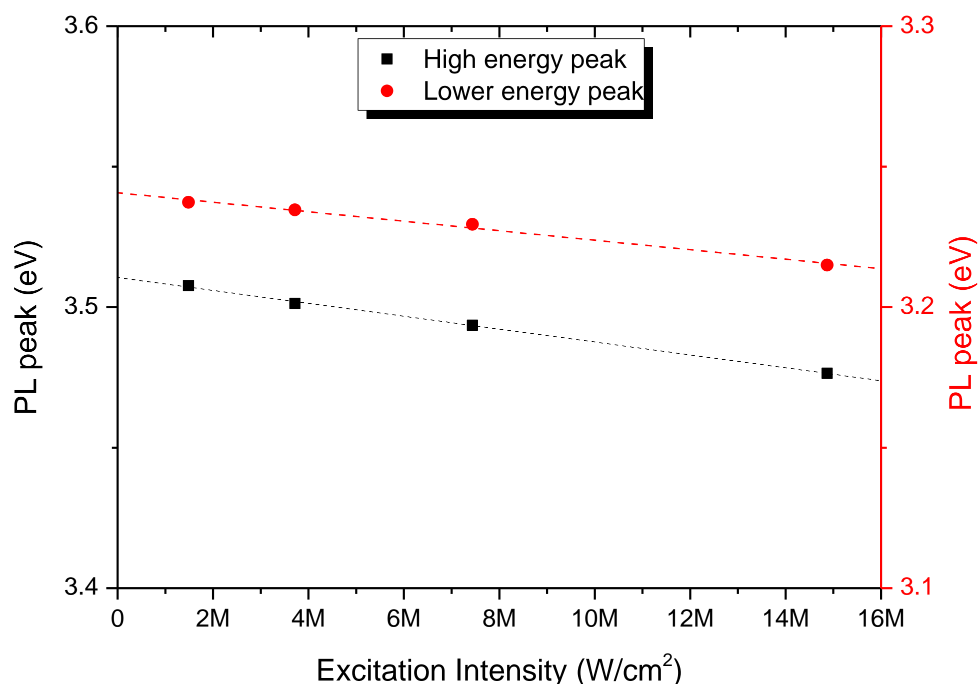

Figure 100: Excitation energy dependence of PL peak position for ZnO films 250 nm thick doped with 4.8 at.% on glass substrate.

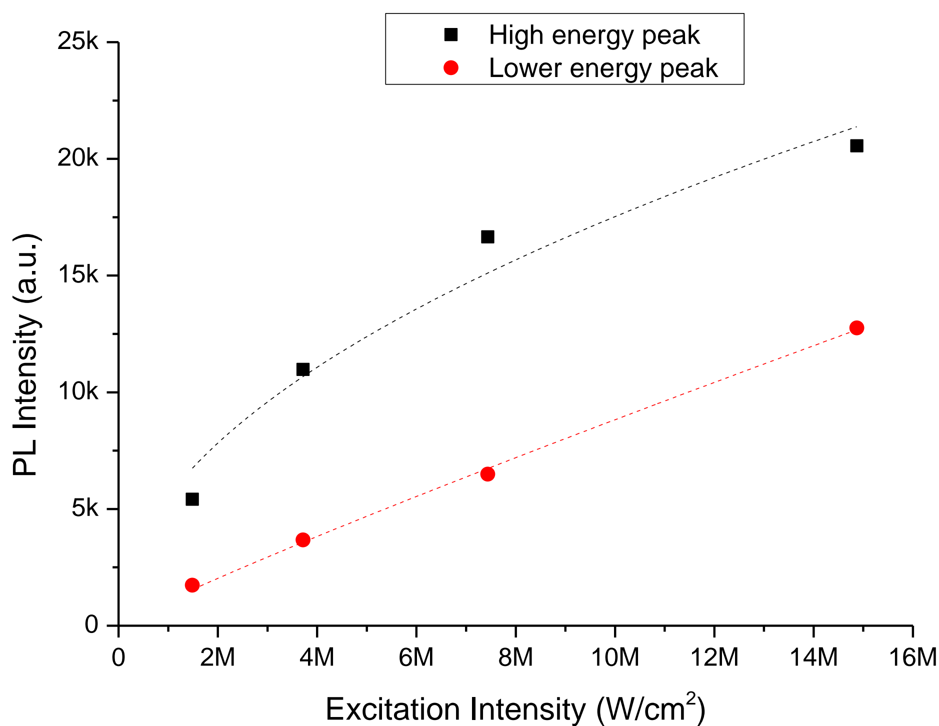

Figure 101: Excitation energy dependence of PL peak intensity for ZnO films 250 nm thick doped with 4.8 at.% on glass substrate.

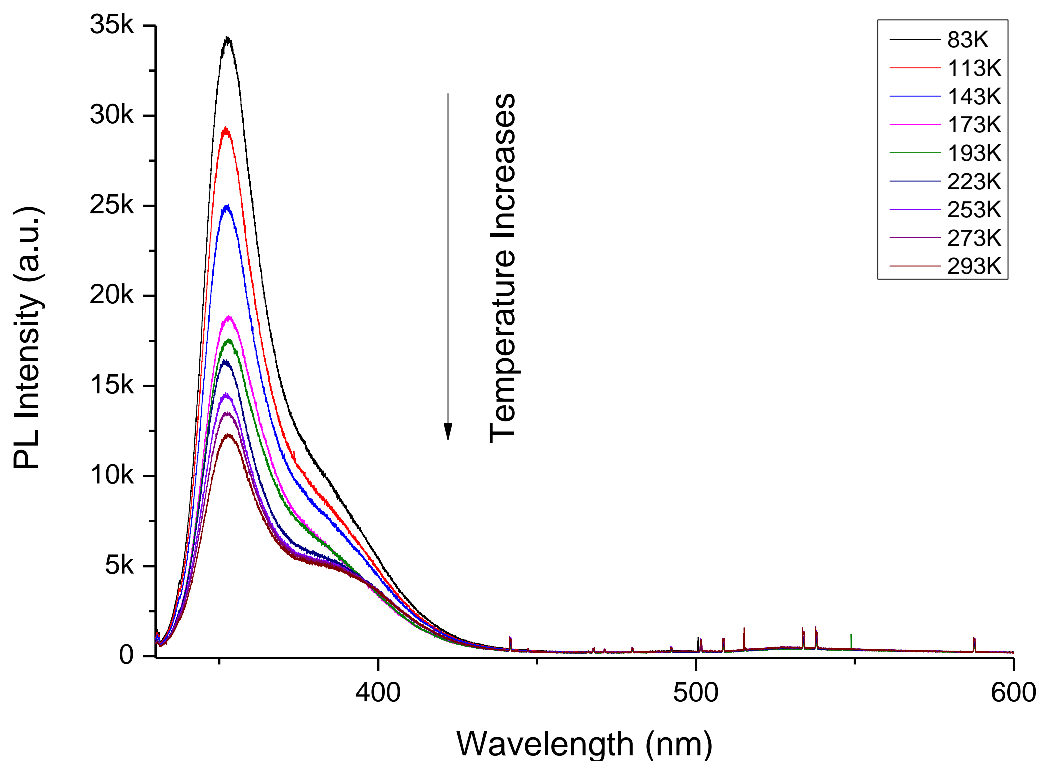

Figure 102: Low temperature PL measurements by using nitrogen filled chamber, for ZnO films 250 nm thick doped with 4.8 at.% on Si wafer substrate.

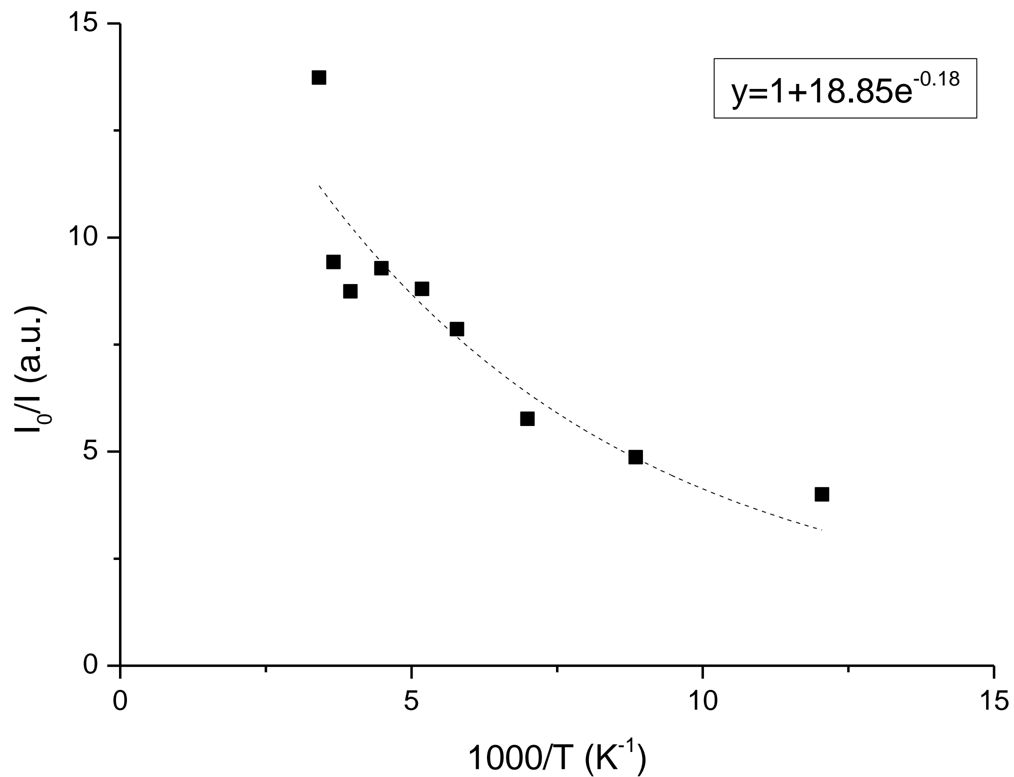

Figure 103: Low temperature dependence of integral intensity for ZnO films 250 nm thick doped with 4.8 at.% on Si wafer substrate.

The relation of the high energy emission intensity to the temperature is shown in Figure 103. By applying Equation 63, the thermal activation energy is calculated at 15.7 meV, which is much smaller than the energy found for the un-doped film at 33.65 meV. Therefore, the thermal quenching process is shown to be increased, indicating that fewer excitons are confined with Zr doping. This is in contrast to Mg doped ZnO films, where the activation energy was increased with doping (from 17 meV to 48 meV), showing that the excitons were restrained by the potential differences induced by Mg doping [381].

The peak position as temperature changed is shown in Figure 104. The trend shows an initial decrease up to the critical point and then increases up to 253 K before decrease again. This is similar to the un-doped film in section 6.3.1.3, showing that

with doping the carriers gain enough energy to overcome the localised states at higher temperature (255 K) compared to the un-doped film (223 K). This is expected due to the higher carrier density of the doped film, which led to more localised states.

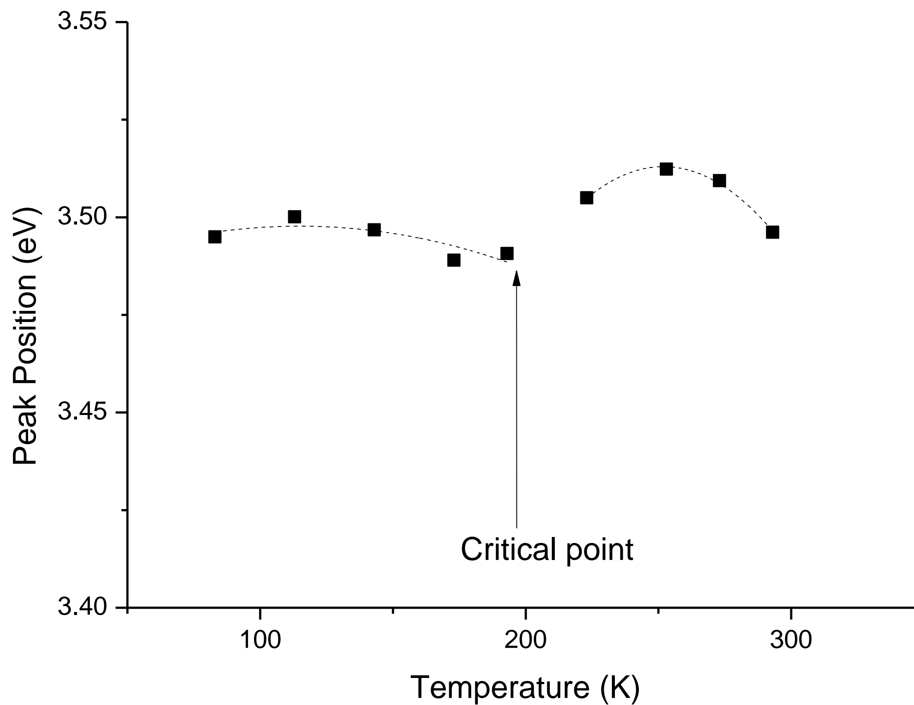

Figure 104: Temperature dependence of peak position for ZnO films 250 nm thick doped with 4.8 at.% on Si substrate.

Based on the temperature and excitation intensity tests, the low energy emission is shown to be induced at high excitation intensity and high temperature, suggesting that it can be related to sub-lattice damage at high irradiation. In this case, the formation of defect states is expected. Also, intensity reduction at low temperatures is often related to defect emissions, as the carriers trapped at defect states are frozen

and cannot recombine and emit photons. Therefore, the low energy emission is probably emerging from defect related recombinations.

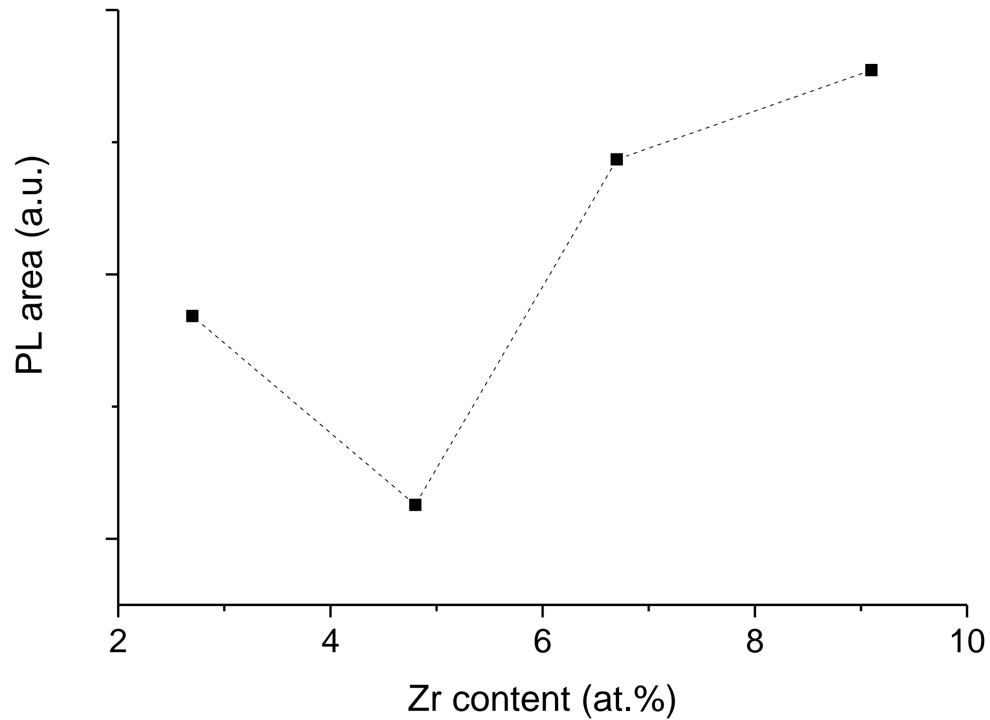

Figure 105: PL low energy emission peak area for ZnO films doped with 2.7-9.1 at.% on glass

The increase of irradiation was reported to induce more zinc vacancies, which act as intrinsic acceptors. Knutsen et al. [97] observed electron density reduction at high irradiation in the order of MeV, showing that the cause could be the increase of zinc vacancies concentration due to the sub-lattice damage. Therefore, the formation of more zinc vacancies acting as deep level acceptors increased the electron trapping effects at high irradiation [97].

The defect state identified in the current study (3.14 eV-3.15 eV) is consistent with the defect state of neutral zinc vacancies (V_{Zn}^0) acting as a deep acceptor at 0.3 eV

above the VBM [101]. The emission is from the recombination of carries from the CBM to the V_{Zn}^{0} state, emitting photons at 3.02-3.14 eV [99],[101]. The identification of the zinc vacancies related emissions for the doped films supports the formation of neutral defects at high doping concentration, as discussed in section 5.2.3. It is possible that the same defect related transition occurred in the un-doped films, but it was not identified due to its energy similarity to the EHP emission.

The vacancies concentration as doping increases is reflected by the changes in PL peak area. Figure 105 shows those changes, with the 4.8 at.% film having the lowest area in comparison to 6.7-9.1a.t% doped films. This is consistent with the carrier density reduction at the heavier doped films, attributed to the neutralisation of the donors by the increased concentration of zinc vacancies.

6.3.2.2 Thickness effect in the PL emissions

For better understanding of the doping induced effects, different thickness films with 4.8 at.% doping are shown in Figure 106. The results show the higher energy peak appearing for all films at approximately the same position (~3.5 eV). The lack of changes between the emissions energy of different oriented films suggests that the orientation in either c-axis (50 nm film) or a-axis (250 nm) does not affect the PL emissions. This is consistent with a study suggesting that the polarity of the crystals is negligible on the bandgap narrowing [391]. The peak intensity increase for the thicker films is due to the higher carrier density that allows more recombination channels.

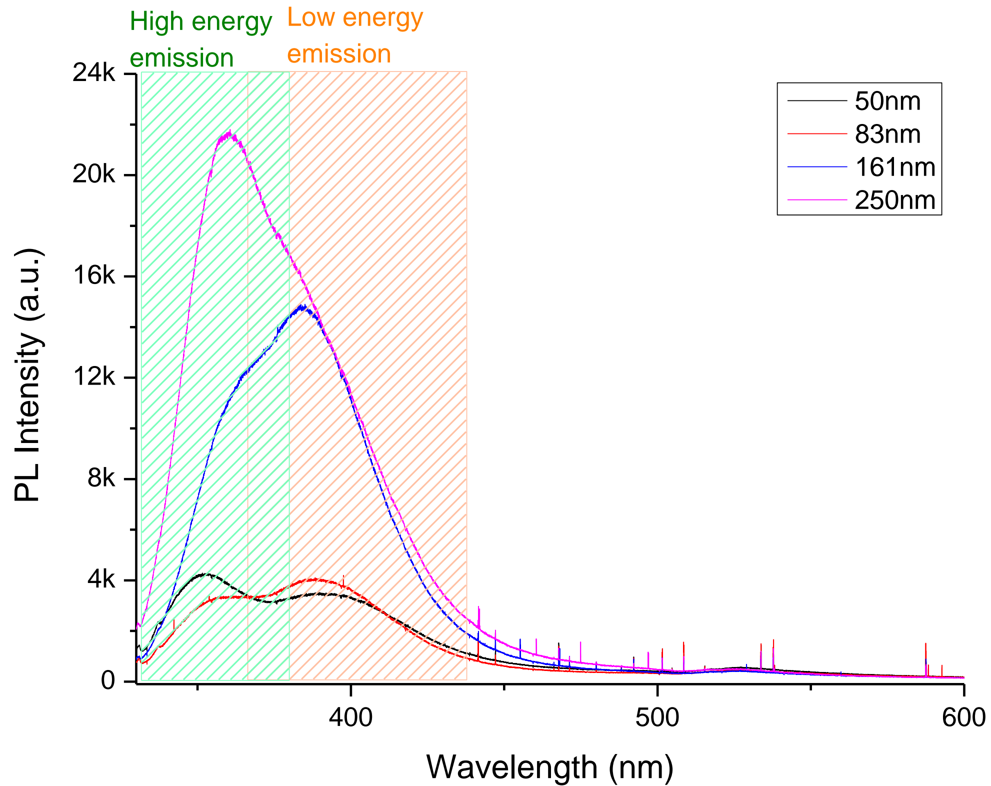

Figure 106: Thickness dependence of PL emission for ZnO films with 4.8 at.% doping on glass.

6.3.2.3 Energy increase of the dominant emission in doped films

The identification of the peaks as EHP emission at high energy and defect related emission at low energy, suggested that the dominant emission increases in energy as doping increased, from 3.21 eV of the un-doped up to 3.52 eV for the 4.8 at.% doped film. Possibilities for this increase include an amplified spontaneous emission (ASE), recombination of hot electrons, strain that induces bandgap changes, size-quantized effect, and band filling effect.

ASE is usually observed at 380-385 nm [113],[255] for ZnO, at high excitation pump intensity in the order of MW/cm^2. Although the excitation intensity used in the

current measurements is comparable with the ones reporting that effect, it is not possible to cause it as the excitation source is not an ultra-pulse laser of a few ns [113],[255],[392]. Therefore, the ASE is not the cause of the high energy emission.

Hot electrons are created when a photon absorbed has not enough energy to excite an electron from the VB to the CB, and so when two such electrons collide a phonon is transferred from one electron to the other, with the one gaining the extra phonon be a hot electron [73]. The hot electron has more than enough energy to reach the CBM, and so is excited at higher energy and emits photons of higher energy. Phonon exchanges that create the hot electrons can only occur in energy boost conditions, such as temperature increase or applied electric field [73]. Therefore, in the current study it is unlikely of having hot electrons only in the doped films due to the fixed measurement conditions. To further support that, the high energy emission was observed at low temperatures and low irradiation.

The bandgap shifts due to the lattice strain were calculated by applying the lattice strain values obtained by XRD in Equation 67. The results show that the VB downshifts by a maximum of 40 meV when doping was added to the films. The shift of ~350 meV is therefore one order of magnitude higher than the strain induced shift, suggesting that this is not the reason of the energy shift.

The reduction of grain size by the addition of Zr^{4+} atoms can lead to size-quantized effect that can increase the bandgap due to the induced compressive strain [48],[393]. However, broadening of the bandgap due to the quantum confinement is only observed for grains of a few Å diameters, which is much smaller than the current grains of 40-90 nm. The large grain size also rejects the possibility for band bending effects, in which a periodic potential is created in the large grain boundaries leading to optical transitions between tail states [386]. The band filling effects are the most

likely cause for the optical gap increase, as discussed in the following section (6.3.2.4).

6.3.2.4 Optical gap modification

The band filling effects include the Burstein-Moss effect (BM) that increases the optical gap, and the generation of many body effects that cause narrowing (BGN) of the bandgap in degenerate films. In order to calculate the energy shifts by those effects, the effective mass for each film has to be first calculated, as it is directly related to the band structure changes by the increased number of carriers.

The term effective mass used in this study refers to the particle mass when located at the CB minimum, and it is the relative mass to the true electron mass (m_0) of $9.10^9 \times 10^{-31}$ kg [394]. The value is never equal to m_0 due to forces affecting electrons mobility, thus values are less than unity (e.g. 0.4 m_0) [73]. The effective mass represents the inverse of the band curvature, thus the larger the curvature the lower the effective mass. For example high number of electrons will require a flatter band in order to occupy more states and accelerate from the band minima/maxima. As a result, n-type doping will reduce the curvature of the CB (band is flatter) and so the effective mass will be increased relative to the carrier density increase [395]. This deformation causes the CB to transform from a parabolic to a non-parabolic band. Therefore, the direct bandgap semiconductors are considered to have parabolic bands, but for wide bandgap degenerate semiconductors the CB is non-parabolic [395]. The VB is considered parabolic in the n-type material as it is not affected by the high electron concentration [342].

Often the band model used for the calculation of band filling effects uses the assumption that both bands are parabolic (parabolic model). As a result, the effective mass (m*) equals the effective mass at the bottom of the parabolic CB (m_0*) [395]. The reported values of m_0* in ZnO are between $0.24m_0$ and $0.48m_0$ [17],[62],[346],[397]. The value of $0.28m_0$ is used as m_0* in the current work, as it is the most popular value in many studies [17],[62],[84],[145],[364],[398].

For the non-parabolic model the m* is calculated using Equation 69 [395]. The values for the current films are shown in Table 14.

Equation 69

$$m^* = m_0^* \left(1 + 2a_{np} \frac{\hbar^2}{m_0^*} (3\pi^2 n_e)^{\frac{2}{3}}\right)^{1/2}$$

where α_{np} is the non-parabolicity parameter equal to 0.29 eV^{-1} [145], ħ is the reduced Planck constant (1.05×10^{-34} Js [394]), and n_e is the carrier density obtained by the Hall effect measurements. Based on this relation, the m* is higher for the non-parabolic model in comparison to the parabolic model (m*= $0.28m_0$). Thus, BM shift is often overestimated when the parabolic model is used.

Table 14: Calculated effective mass for each doped film using the non-parabolic m model.*

Zr content (at. %)	Effective mass m* ($\times m_0$)
0	0.32
1	0.33
2.7	0.36
4.8	0.38
6.7	0.36
9.1	0.35

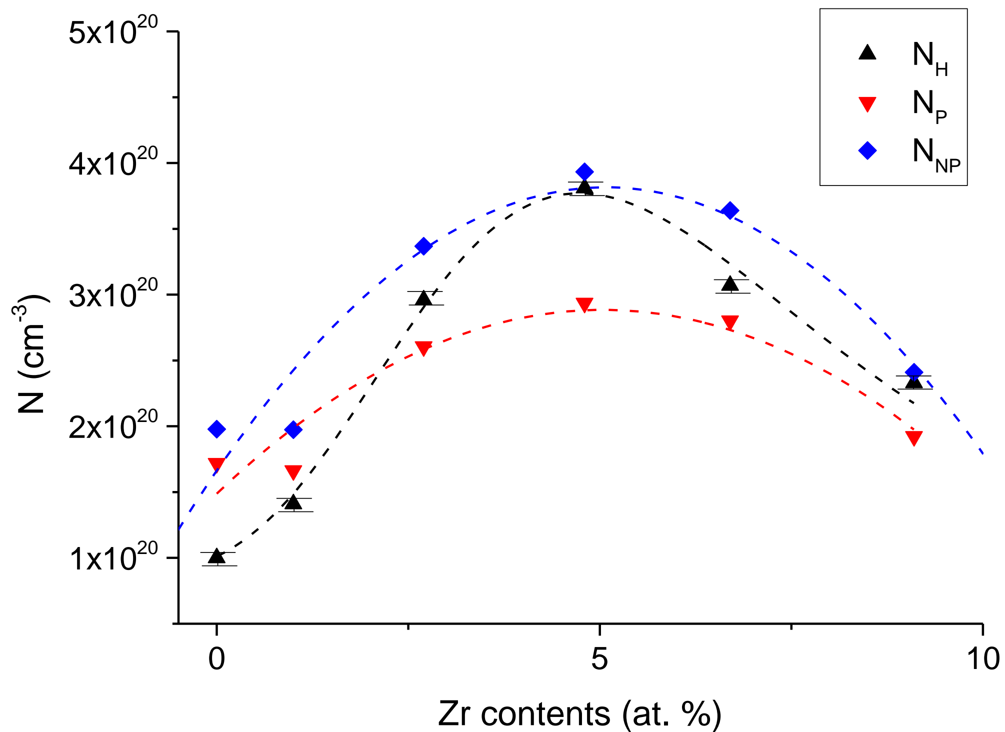

Figure 107: Comparison of the estimated optical (parabolic and non-parabolic) and Hall effect measured carrier concentration.

The modified effective mass can be applied to Drude model used for the spectrophotometer data analysis, in order to recalculate the carrier concentration. The carrier density measured by three different methods is shown in Figure 107, such as the Hall effect measurements (N_H), the parabolic model (N_P) and non-parabolic model (N_{NP}) using the Drude model. For the parabolic model the $m_0^* = 0.28m_0$ is applied and for the non-parabolic carriers the values from Table 14 are applied. The experimental data are shown to be closer to the parabolic carriers up to 1 at.% Zr, and at higher doping the carriers are much closer to the non-parabolic values. However, the carrier densities of 0-1 at.% are not identical to the predicted parabolic values, suggesting that it is not definite that the samples have parabolic bands. Therefore, due to the degeneracy of all the films it could be said that the CB in the un-doped and doped films can be considered as non-parabolic CB.

To evaluate the optical gap shift observed in transmittance and PL measurements as doping increases, a theoretical model is applied including BM and BGN effects for parabolic and non-parabolic CB. The BM shift is estimated using Equation 70 [391], and the BGN using Equation 71 [342]. The shifts in relation to the un-doped film are shown in Figure 108 in comparison to the experimental shifts measured by PL and spectrophotometer. The error bars for the model are based on the range of the reported effective masses at the bottom of the CB ($0.24m_0$ and $0.48m_0$).

Equation 70

$$\Delta E_{BM} = \frac{\hbar^2}{2m^*}(3\pi^2 n_e)^{2/3}$$

Equation 71

$$\Delta E_{BGN} = \frac{e^2}{2\pi\varepsilon_0\varepsilon_r}\left(\frac{3}{\pi}n_e\right)^{1/3}$$

where ε_0 is the vacuum permittivity (8.85×10^{-12} F m^{-1} [394]), and ε_r is the dielectric constant of ZnO equal to 8.49 (unit-less) [340].

The results show greater shift for the parabolic model, while the BM shift is higher than its combination with BGN shift. The experimental data by both methods fall within the range of the non-parabolic model having both BM and BGN effects. The 1 at.% doped sample is now clearly specified of having a non-parabolic CB as it follows the same trend. The energy shift of that film is slightly lower than the range covered by the error bars, suggesting that the model is less accurate for small energy shifts. The plot confirms the overestimation of BM shifts when using parabolic model and when the BGN effect is not taken into account. Consequently, the high

energy emission in PL is shown to shift due to the Burstein-Moss effect and the bandgap renormalisation caused by the high carrier density.

The optical gap increase is considered an advantage for optoelectronic devices as it wideners the transmittance range and improves the effectiveness of PVs by increasing the gap to the absorber material. Hence, the tuned optical gap of ~3.5 eV with Zr doping found in this study, in addition to the low resistivity in the order of 10^{-4} Ω cm, provided an advantage towards the replacement of ITO with bandgap 3.8 eV [399]. The optical gap increase is consistent with Si doped ZnO films grown by ALD [400], which showed increase from 3.25 eV to 3.55 eV caused by BM effect.

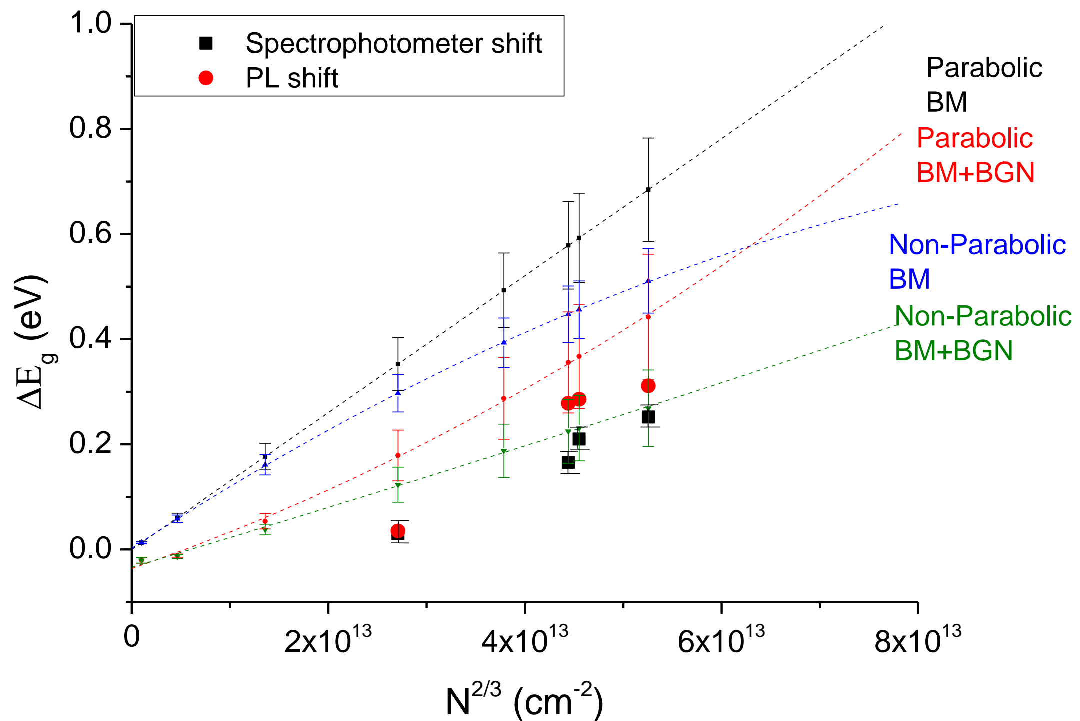

Figure 108: Optical gap difference between the doped and un-doped films as a function of carrier density, using parabolic and non-parabolic models for BM and BGN effects.

6.3.3 PL Conclusion

Based on the analysis carried out for PL and transmittance data, the optical gap of the un-doped and doped ZnO films was determined. The use of theoretical models showed that the CB is non-parabolic for all the doped films and possibly for the un-doped film, due to the high calculated effective mass that results in Drude model values consistent with the experimental carrier density. The models also showed that the optical gap increase observed as doping increased was due to Burstein-Moss effect and many-body effects. Those effects led to the optical gap increase due to the filling of the CB by the high number of carriers. The optical gap increased from 3.21 eV for the un-doped film to a maximum of 3.52 eV for 4.8 at.% doped film.

Regarding the PL emission, the main peak of the films originated from EHP recombination due to the high excitation intensity used and the high carrier density of the films. As doping increased (from 2.7 at.%), the EHP emission was blue-shifted due to the band filling effects, and an additional emission with similar intensity was observed. The emission was attributed to recombinations between the CB and the neutral zinc vacancies defect state. Those defects were observed at high excitation intensity and high temperature. Also, V_{Zn} had higher concentration for the heavily doped films, which is consistent with the carrier density reduction for those films attributed to the formation of neutral defects.

Chapter 7

Conclusion

7.1 Main outcome

Zr-doped ZnO thin films were deposited by ALD, in order to improve the n-type properties for TCO applications. The precursors used were diethylzinc and tetrakis-ethylmethylamino zirconium as Zn and Zr sources respectively, along with H_2O as the co-reactant. The lowest possible resistivity was targeted, hence, the growth temperature at 200°C was selected for all films after showing the lowest resistivity compared to higher temperatures, and also showed self-limiting growth within the ALD window. The resistivity reduction observed at this temperature was attributed to the high hydrogen concentration, which act as shallow donors.

The effect in microstructure as the Zr doping increased was examined. It was found that doping suppressed the grain growth and so reduced the grain size due to segregation of Zr in the grain boundaries. This led to neutralisation of the donors at the boundaries, as zinc vacancies acting as intrinsic acceptors combined to them. Hence, the carrier mobility and carrier density reduced at high doping levels above the most effective doping of 4.8 at.% Zr. The existence of zinc vacancies was supported by a defect-related emission in photoluminescence at 3.14 eV (395 nm), occurring from the recombination between the CB and the neutral zinc vacancies

defect state. This emission increased in intensity for the 6.7-9.1 at.% films indicating higher defect concentration. The minimum resistivity was found at 4.8 at.% Zr doping of 1.44×10^{-3} Ω·cm and carrier density of 3.81×10^{20} cm^{-3} for <100 nm film. This carrier density was almost four times greater than the un-doped film of 1.0×10^{20} cm^{-3}, attributed to the extra carriers added for each Zr^{4+} substituting to Zn^{2+}. The ionic state of zirconium and thus its incorporation to the lattice in all the doped samples was shown by its binding energy during the XPS measurements.

The effect of degenerate doping showed band filling effects that caused increase of the optical gap from 3.21 eV of the un-doped film to 3.52 eV of the 4.8 at.% Zr-doped film. Mathematical models were used to identify the effects, and showed that the net effect of the Burstein-Moss and many-body effects was consistent with the experimental optical gap shifts measured by absorption (spectrophotometer) and emission (photoluminescence) methods. From the same models it was shown that the CB was non-parabolic for the un-doped and doped films, as the high carrier density caused widening of the CB.

The transparency was measured at high percentage with the normalised to the substrate values reaching up to 91% in the visible region (161 nm with 4.8 at.% doping) and 91% in the near IR region (50 nm with 4.8 at.% doping). The transparency was found at maximum for the most conductive films, as the larger optical gap induced reduction of absorption.

The lowest point in resistivity was used to grow thicker films in order to reduce the interfacial, dislocation and grain boundary scattering and achieve even lower resistivity. The dislocation and grain boundary scattering were reduced since the grains were shown to be increased in size as the film thickness increased, possibly due to the deposition of the layers around the initial grains. As a result, the resistivity

recorded for the 250 nm thick film was at 7.5×10^{-4} Ω·cm with carrier density of 4.2×10^{20} cm^{-3} and carrier mobility of 19.6 $cm^2V^{-1}s^{-1}$. The carrier density showed an increase as thickness increased, which was related to the strain effects as thickness increased. The strain can induce shifts in the distribution of the density of states and thus cause a shift of the conduction band to a lower energy level, leading to bandgap reduction. Hence, the increased tensile strain in the thicker films as the grains increased induced bandgap reduction that resulted in higher carrier concentration in the CB.

The increased strain also induced changes in the preferred orientation. As the strain increased with thickness, the driven force shifted from being surface energy driven to strain energy driven. In the first case the system has low strain and so in order to reduce the total systems energy it forces the film to grow in an orientation with the minimum surface energy, which in the case of ZnO this is the (0002) direction in c-axis. As the strain increased, the strain energy becomes the most dominant energy in the system and so to reduce the system energy a low strain energy orientation is preferred, which is the $(10\bar{1}0)$ in a-axis. Therefore, the current films showed c-axis oriented grains up to 70 nm thickness, and then the grains preferred growing in the a-axis orientation. The shifting point changed with the doping level due to the different strain in the system.

In conclusion, Zr-doped ZnO thin films were deposited by ALD with thickness 50-250 nm and doping concentration of 0-9.1 at.% Zr. The controlled thickness can effectively control the carrier mobility and grains preferred orientation, while the Zr doping can control the carrier density, optical gap and transparency of the films. The low resistivity and high transparency obtained by doping the films with Zr atoms indicated that the films can find applications as TCOs grown on sodalime glass.

7.2 Future work

In order to further understand the effect of Zr doping in the current films, a few more experiments are of interest to be carried out. One such experiment will be the use of QCM in order to determine the cause of the thickness reduction as more doping is added to the film. Its use can reveal the weight gain during each cycle and therefore it can determine which cycle offers lower than the expected weight gain due to nucleation issues (e.g. after the doping cycle or during the doping cycle).

Another experiment could be the deposition of very thin films with different level of doping for XPS measurements. The thickness of such films will correspond to very thin crystallites based on the thickness to grains relationship established in the current work. The small crystallites will result in smoother surfaces, which will allow the quantitative element composition as the scattering of photoelectrons will be avoided.

A different method for the composition of the films is the preparation of polished TEM samples for different doped films. Their use in the TEM will then allow EDS measurements that can reveal the composition of the films. This method of polished TEM samples could also reveal more information regarding the preferred orientation shift above 70 nm in thickness, and how the grains are formed at such thickness.

An extensive study using high resolution Super-STEM will be also of interest in order to observe the lattice in atom resolution, which will allow determining the position of the dopants within the lattice and observing any defects created. This could support the case for the neutral defects formation at heavily doped films and show the uniformity of the deposited dopants across the film.

Another test that can be carried out using the current films, is the use of lower excitation intensity PL than the current work, in order to obtain more detailed defect related emissions (i.e. not passivated), and to determine the threshold intensity of the films. This can be done by using the lens LMU-5×-NUV with *f*=40 mm, which will result to the intensity range of 23-232 kW/cm^2.

In the case of depositing new samples using the same precursors, technique and depositing parameters, it would be of interest to use sapphire substrates in order to get more conductive films. Sapphire substrates are transparent and were reported to result in more conductive films compared to sodalime glass [34]. The deposition of 250 nm thick doped films at higher temperature (e.g. 275°C) will be also interesting in order to observe if the same effect of preferred orientation shift occurs similarly to the 200°C deposited films, and if this is the case identify the thickness shifting point.

It will be also interesting if more dopants are used following the same deposition method in order to directly compare Zr-doped films with films such as Al-doped ZnO and Ga-doped ZnO. This could reveal how much the grain size is affected by Zr doping (i.e. reduced) compared to Al and Ga doping, determine if it is more conductive and more transparent, and also show if the optical gap increases as much as the current films (i.e. 0.3 eV increase).

Last but not least, it would be of great interest to apply the current films in devices such as TCOs in thin film solar cells in order to measure their efficiency. In addition, due to their low growth temperature the films could be also grow on polymer substrates for flexible thin films photovoltaics.

References

[1] Bae, H. S., & Im, S. (2004). Ultraviolet detecting properties of ZnO-based thin film transistors. Thin Solid Films, 469-470 (SPEC. ISS.), 75-79.

[2] Carcia, P. F., McLean, R. S., Reilly, M. H., & Nunes Jr., G. (2003). Transparent ZnO thin-film transistor fabricated by RF magnetron sputtering. Applied Physics Letters, 82(7), 1117-1119.

[3] Kim, W., Moon, Y., Kim, K., Shin, S., Du Ahn, B., Lee, J., & Park, J. (2011). The influence of hafnium doping on bias stability in zinc oxide thin film transistors. Thin Solid Films, 519(15), 5161-5164.

[4] Huang, J., Chu, S., Liu, J., et al. (2013). ZnO p-n homojunction random laser diode based on nitrogen-doped p-type nanowires. Advanced Optical Materials, 1(2), 179-185.

[5] Ryu, Y. R., Lubguban, J. A., Lee, T. S., White, H. W., Jeong, T. S., Youn, C. J., & Kim, B. J. (2007). Excitonic ultraviolet lasing in ZnO-based light emitting devices. Applied Physics Letters, 90(13).

[6] Lupan, O., Pauporté, T., Le Bahers, T., Viana, B., & Ciofini, I. (2011). Wavelength-emission tuning of ZnO nanowire-based light-emitting diodes by Cu doping: Experimental and computational insights. Advanced Functional Materials, 21(18), 3564-3572.

[7] Chen, C. , Chang, S. , Chang, S. , Li, M., Chen, I., Hsueh, T., & Hsu, C. (2010). Fabrication of a white-light-emitting diode by doping gallium into ZnO nanowire on a p-GaN substrate. Journal of Physical Chemistry C, 114(29), 12422-12426.

[8] Iwan, S., Bambang, S., Zhao, J. L., Tan, S. T., Fan, H. M., Sun, L., & Sun, X. W. (2012). Green electroluminescence from an n-ZnO: Er/p-Si heterostructured light-emitting diode. Physica B: Condensed Matter, 407(14), 2721-2724.

[9] Sato, H., Minami, T., Miyata, T., Takata, S., & Ishii, M. (1994). Transparent conducting ZnO thin films prepared on low temperature substrates by chemical vapour deposition using Zn $(C_5H_7O_2)_2$. Thin Solid Films, 246(1-2), 65-70.

[10] Faÿ, S., Steinhauser, J., Nicolay, S., & Ballif, C. (2010). Polycrystalline ZnO: B grown by LPCVD as TCO for thin film silicon solar cells. Thin Solid Films, 518(11), 2961-2966.

[11] Sun, H. D., Makino, T., Segawa, Y., Kawasaki, M., Ohtomo, A., Tamura, K., & Koinuma, H. (2002). Enhancement of exciton binding energies in ZnO/ZnMgO multiquantum wells. Journal of Applied Physics, 91(4), 1993.

[12] Martinson, A. B. F., Elam, J. W., Hupp, J. T., & Pellin, M. J. (2007). ZnO nanotube based dye-sensitized solar cells. Nano Letters, 7(8), 2183-2187.

[13] Müller, J., Rech, B., Springer, J., & Vanecek, M. (2004). TCO and light trapping in silicon thin film solar cells. Solar Energy, 77(6), 917-930.

[14] Minami, T. (2005). Transparent conducting oxide semiconductors for transparent electrodes. Semiconductor Science and Technology, 20(4), S35-S44.

[15] Sohn, S., & Kim, H.-M. (2011). Transparent Conductive Oxide (TCO) Films for Organic Light Emissive Devices (OLEDs). In S. H. Ko, Organic Light Emitting Diode - Material, Process and Devices pp. 233-274. InTech.

[16] Ozgur, U., Hofstetter, D., & Morkoc, H. (2010). ZnO devices and applications: A review of current status and future prospects, 98. (7) pp. 1255-1268.

[17] Klingshirn, C. (2007). ZnO: From basics towards applications. Physica Status Solidi (B) Basic Research, 244(9), 3027-3073.

[18] Guillén, C., & Herrero, J. (2011). TCO/metal/TCO structures for energy and flexible electronics. Thin Solid Films, 520(1), 1-17.

[19] Ellmer, K., Klein, A., & Rech, B. (2008). Transparent Conductive Zinc Oxide, Basics and Applications in Thin Film Solar Cells. Heidelberg: Springer.

[20] Bernède, J. C. (2008). Organic photovoltaic cells: History, principle and techniques. Journal of the Chilean Chemical Society, 53(3), 1549-1564.

[21] Faÿ, S., Steinhauser, J., Oliveira, N., Vallat-Sauvain, E., & Ballif, C. (2007). Opto-electronic properties of rough LP-CVD ZnO:B for use as TCO in thin-film silicon solar cells. Thin Solid Films, 515 (24 SPEC. ISS.), 8558-8561.

[22] Ilican, S., Caglar, Y., Caglar, M., & Demirci, B. (2008). Polycrystalline indium-doped ZnO thin films: Preparation and characterization. Journal of Optoelectronics and Advanced Materials, 10(10), 2592-2598.

[23] Huang, C., Wang, M., Deng, Z., Cao, Y., Liu, Q., Huang, Z., & Huang, Q. (2010). Low content indium-doped zinc oxide films with tunable work function fabricated through magnetron sputtering. Semiconductor Science and Technology, 25(4).

[24] Wang, C.C., Man, B.Y., Liu, M., Chen, C.S., Jiang, S.Z., Yang, S.Y., Xu, S.C., Gao, X.G., & Hu, B. (2012). The intrinsic room-temperature ferromagnetism in ZnO:Co thin films deposited by PLD. Advances in Condensed Matter Physics, 2012.

[25] Lin, M., Chang, Y., Chen, M., & Chu, C. (2011). Characteristics of Zr-doped ZnO thin films grown by atomic layer deposition. Journal of the Electrochemical Society, 158(6), D395-D399.

[26] Gokulakrishnan, V., Parthiban, S., Jeganathan, K., & Ramamurthi, K. (2011). Investigation on the effect of Zr doping in ZnO thin films by spray pyrolysis. Applied Surface Science, 257(21), 9068-9072.

[27] Chalker, P. R., Marshall, P. A., King, et al. (2012). Atomic layer deposition of germanium-doped zinc oxide films with tuneable ultraviolet emission. Journal of Materials Chemistry, 22(25), 12824-12829.

[28] Ahn, C. H., Kim, J. H., & Cho, H. K. (2012). Tunable electrical and optical properties in composition controlled Hf:ZnO thin films grown by atomic layer deposition. Journal of the Electrochemical Society, 159(4), H384-H387.

[29] Tsay, C., & Lee, W. (2013). Effect of dopants on the structural, optical and electrical properties of sol-gel derived ZnO semiconductor thin films. Current Applied Physics, 13(1), 60-65.

[30] Lee, D., Kim, H., Kwon, J., Choi, H., Kim, S., & Kim, K. (2011). Structural and electrical properties of atomic layer deposited Al-doped ZnO films. Advanced Functional Materials, 21(3), 448-455.

[31] Geng, Y., Guo, L., Xu, S., Sun, Q., Ding, S., Lu, H., et al. (2011). Influence of Al doping on the properties of ZnO thin films grown by atomic layer deposition. Journal of Physical Chemistry C, 115(25), 12317-12321.

[32] Dhakal, T., Vanhart, D., Christian, R., Nandur, A., Sharma, A., & Westgate, C. R. (2012). Growth morphology and electrical/optical properties of Al-doped ZnO thin films grown by atomic layer deposition. Journal of Vacuum Science and Technology A: Vacuum, Surfaces and Films, 30(2).

[33] Lee, D., Kim, H., Kwon, J., Choi, H., Kim, S., & Kim, K. (2011). Structural and electrical properties of atomic layer deposited Al-doped ZnO films. Advanced Functional Materials, 21(3), 448-455.

[34] Dasgupta, N. P., Neubert, S., Lee, W., Trejo, O., Lee, J., & Prinz, F. B. (2010). Atomic layer deposition of Al-doped ZnO films: Effect of grain orientation on conductivity. Chemistry of Materials, 22(16), 4769-4775.

[35] Walsh, A., Da Silva, J. L. F., & Wei, S. (2011). Multi-component transparent conducting oxides: Progress in materials modelling. Journal of Physics Condensed Matter, 23(33).

[36] Chalker, P. R., Marshall, P. A., Romani, S., et al. (2012). Atomic layer deposition of gallium-doped zinc oxide transparent conducting oxide films. Paper presented at the Materials Research Society Symposium Proceedings, 1315 39-44.

[37] Chalker, P. R., Marshall, P. A., Romani, S., et al. (2013). Atomic layer deposition of Ga-doped ZnO transparent conducting oxide substrates for CdTe-based photovoltaics. Journal of Vacuum Science and Technology A: Vacuum, Surfaces and Films, 31(1).

[38] Saito, K., Hiratsuka, Y., Omata, A., Makino, H., Kishimoto, S., Yamamoto, T., & Hirayama, H. (2007). Atomic layer deposition and characterization of Ga-doped ZnO thin films. Superlattices and Microstructures, 42(1-6), 172-175.

[39] Fortunato, E., Ginley, D., Hosono, H., & Paine, D. C. (2007). Transparent conducting oxides for photovoltaics. MRS Bulletin, 32(3), 242-247.

[40] Gabás, M., Landa-Cánovas, A., Luis Costa-Krämer, J., Agulló-Rueda, F., González-Elipe, A. R., Díaz-Carrasco, P., & Ramón Ramos-Barrado, J. (2013). Differences in n-type doping efficiency between Al- and Ga-ZnO films. Journal of Applied Physics, 113(16).

[41] Liu, Y., Li, Y., & Zeng, H. (2013). ZnO-based transparent conductive thin films: Doping, performance, and processing. Journal of Nanomaterials, 2013.

[42] Duan, X. M., Stampfl, C., Bilek, M. M. M., McKenzie, D. R., & Wei, S. (2011). Design of shallow acceptors in ZnO through early transition metals codoped with N acceptors. Physical Review B - Condensed Matter and Materials Physics, 83(8).

[43] Wang, F., Lv, M., Pang, Z., Yang, T., Dai, Y., & Han, S. (2008). Theoretical study of structural, optical and electrical properties of zirconium-doped zinc oxide. Applied Surface Science, 254(21), 6983-6986.

[44] Subash, B., Krishnakumar, B., Swaminathan, M., & Shanthi, M. (2013). Highly efficient, solar active, and reusable photocatalyst: Zr-loaded Ag-ZnO for reactive red 120 dye degradation with synergistic effect and dye-sensitized mechanism. Langmuir, 29(3), 939-949.

[45] Bahedi, K., Addou, M., El Jouad, M., Bayoud, S., & Sofiani, Z. (2009). Effects of deposition temperature on the surface roughness and the nonlinear optical susceptibility of sprayed deposited ZnO:Zr thin films. Applied Surface Science, 255(22), 9054-9057.

[46] Bahedi, K., Addou, M., El Jouad, M., et al. (2009). Diagnostic study of the roughness surface effect of zirconium on the third-order nonlinear-optical properties of thin films based on zinc oxide nanomaterials. Applied Surface Science, 255(8), 4693-4695.

[47] Bahedia, K., Addoua, M., El Jouada, M., Sofiania, Z., Bayouda, S., Sahraoui, B., & Essaïdi, Z. (2008). Study of nonlinear-optical properties and roughness surface of ZnO:Zr thin films. Paper presented at the ICTON-MW 2008 - International Conference on Transparent Optical Networks "Mediterranean Winter" 2008 - Conference Proceedings.

[48] Clament Sagaya Selvam, N., Vijaya, J. J., & Kennedy, L. J. (2012). Effects of morphology and Zr doping on structural, optical, and photocatalytic properties of ZnO nanostructures. Industrial and Engineering Chemistry Research, 51(50), 16333-16345.

[49] Paul, G. K., Bandyopadhyay, S., Sen, S. K., & Sen, S. (2003). Structural, optical and electrical studies on sol-gel deposited Zr-doped ZnO films. Materials Chemistry and Physics, 79(1), 71-75.

[50] Tsay, C., & Fan, K. (2008). Optimization of Zr-doped ZnO thin films prepared by sol-gel method. Materials Transactions, 49(8), 1900-1904.

[51] Zhang, H., Lei, C., Liu, H., & Yuan, C. (2009). Low-temperature deposition of transparent conducting ZnO:Zr films on PET substrates by DC magnetron sputtering. Applied Surface Science, 255(11), 6054-6056.

[52] Yadav, S. K., Vyas, S., Chandra, R., Chaudhary, G. P., & Nath, S. K. (2009). Study of electrical and optical properties of Zr-doped ZnO thin films prepared by DC reactive magnetron sputtering. Advanced Materials Research, 67, 161-166.

[53] Zhang, H., Liu, H., & Feng, L. (2010). Influence of annealing temperature on the properties of ZnO:Zr films deposited by direct current magnetron sputtering. Vacuum, 84(6), 833-836.

[54] Zhang, H., Liu, H., & Yuan, C. (2011). Comparative study of the properties between transparent conducting ZnO:Zr and ZnO:Al films deposited by DC magnetron sputtering. Advanced Materials Research, 284-286, 2182-2186.

[55] Pisitsaka, P., & Magaraphanb, R. (2008). Influences of Zr^{4+} and polyacrylamide on structural and optical properties of ZnO nanoparticles prepared via microwave irradiation. Advanced Materials Research, 55-57, 613-616.

[56] Wang, J., Zhang, C. Y., Wu, Z. G., & Yan, P. X. (2011). Effect of annealing on structural and optical properties of Zr-doped ZnO film grown by RF magnetic sputtering. Materials Science Forum, 686, 696-705.

[57] Lv, M., Xiu, X., Pang, Z., Dai, Y., Ye, L., Cheng, C., & Han, S. (2008). Structural, electrical and optical properties of zirconium-doped zinc oxide films prepared by radio frequency magnetron sputtering. Thin Solid Films,516(8), 2017-2021.

[58] Kim, H., Horwitz, J. S., Kim, W. H., Qadri, S. B., & Kafafi, Z. H. (2003). Anode material based on Zr-doped ZnO thin films for organic light-emitting diodes. Applied Physics Letters, 83(18), 3809-3811.

[59] Aborn, B. H., & Davidson, E. L. (1930). An X-ray investigation of the structure of copper-zinc oxide catalysts. Journal of Physical Chemistry, 34(3), 521-530.

[60] Bunn, C. W. (1935). The lattice-dimensions of zinc oxide. Proceedings of the Physical Society, 47(5), 835-842.

[61] Klingshirn, C. F., Meyer, B. K., Waag, A., Hoffmann, A., & Geurts, J. (2010). Zinc Oxide From Fundamental Properties Towards Novel Applications. Heidelberg: Springer.

[62] Morkoç, H., & Özgür, Ü. (2009). Zinc Oxide: Fundamentals, Materials and Device Technology. WILEY-VCH.

[63] Ashrafi, A., & Jagadish, C. (2007). Review of zincblende ZnO: Stability of metastable ZnO phases. Journal of Applied Physics, 102(7).

[64] Decremps, F., Zhang, J., & Lieberman, R. C. (2000). New phase boundary and high-pressure thermoelasticity of ZnO. Europhys. Lett., 51 (3), pp. 268-274.

[65] Özgür, Ü., Alivov, Y. I., Liu, C., Teke, A., Reshchikov, M. A., Doğan, S., & Morkọ, H. (2005). A comprehensive review of ZnO materials and devices. Journal of Applied Physics, 98(4), 1-103.

[66] Pauling, L. (1960). The nature of the chemical bond and the structure of molecules and crystals: an introduction to modern structural chemistry. Ithaca (N.Y.) : Cornell University Press.

[67] Phillips, J. C. (1970). The chemical bond and solid state physics. Phys. Today 23(2), 23 (1970); doi: 10.1063/1.3021959.

[68] Catlow, C. R. A., & Stoneham, A. M. (1983). Ionicity in solids. Journal of Physics C: Solid State Physics, 16(22), 4321-4338.

[69] Pauling, L., & Phillips, J. C. (1971) Discussion on the chemical bond. Phys. Today 24(2), 9 (1971); doi: 10.1063/1.3022610.

[70] Hidaka, T. (1977). Pauling's Ionicity and Phillips' Ionicity. Journal of the Physical Society of Japan 44 (4), pp. 1204-1207.

[71] [Z8] Hosford, W. F. (2006). Materials Science, An Intermediate Text. Cambridge University Press.

[72] Jagadish, C., & Pearton, S. (2006). Zinc Oxide Bulk, Thin Films and Nanostructures; Processing, Properties and Applications. Oxford: Elsevier.

[73] Pankove, J. I. (1971). Optical Processes in Semiconductors. London: Constable and Company Ltd.

[74] Liu, J.M. (2005). Photonic Devices. Cambridge: Cambridge University Press.

[75] Taguchi, S., Saruyama, M., Teranishi, T., & Kanemitsu, Y. (2011). Quantized Auger recombination of biexcitons in CdSe nanorods studied by time-resolved photoluminescence and transient-absorption spectroscopy. Physical Review B - Condensed Matter and Materials Physics, 83(15).

[76] Hung-Chun Lai, H., Basheer, T., Kuznetsov, V. L., Egdell, R. G., Jacobs, R. M. J., Pepper, M., & Edwards, P. P. (2012). Dopant-induced bandgap shift in Al-doped ZnO thin films prepared by spray pyrolysis. Journal of Applied Physics, 112(8).

[77] Dvorak, M., Wei, S., & Wu, Z. (2013). Origin of the variation of exciton binding energy in semiconductors. Physical Review Letters, 110(1).

[78] Wagner, M. R., Kunert, H. W., Machatine, A. G. J., Hoffmann, A., Niyongabo, P., Malherbe, J., & Barnas, J. (2009). Bound and free excitons in ZnO. optical selection rules in the absence and presence of time reversal symmetry.Microelectronics Journal, 40(2), 289-292.

[79] Bogardus, E. H., & Bebb, H. B. (1968). Bound-exciton, free-exciton, band-acceptor, donor-acceptor, and auger recombination in GaAs. Physical Review, 176(3), 993-1002.

[80] Burstein, E. (1954). Anomalous optical absorption limit in InSb [4]. Physical Review, 93(3), 632-633.

[81] Wolff, P. A. (1962). Theory of the band structure of very degenerate semiconductors. Physical Review, 126(2), 405-412.

[82] Lu, J. G., Fujita, S., Kawaharamura, T., Nishinaka, H., Kamada, Y., Ohshima, T. & Zhao, B. H. (2007). Carrier concentration dependence of band gap shift in n-type ZnO:Al films. Journal of Applied Physics, 101(8).

[83] Roth, A. P., Webb, J. B., & Williams, D. F. (1982). Band-gap narrowing in heavily defect-doped ZnO. Physical Review B, 25(12), 7836-7839.

[84] Meyer, B. K., Alves, H., Hofmann, D. M., Kriegseis, W., Forster, D., Bertram, F, Rodina, A. V. (2004). Bound exciton and donor-acceptor pair recombinations in ZnO. Physica Status Solidi (B) Basic Research, 241(2), 231-260.

[85] Janotti, A., & Van De Walle, C. G. (2009). Fundamentals of zinc oxide as a semiconductor. Reports on Progress in Physics, 72(12).

[86] Glossary of Terms. (n.d.). Retrieved 2014, from U energy: http://www.uenergysolar.co.uk/faq/glossary-of-terms.

[87] Wu, J., & Xue, D. (2011). Progress of science and technology of ZnO as advanced material. Science of Advanced Materials, 3(2), 127-149.

[88] Vinodkumar, R., Lethy, K.J., Arunkumar, P.R., Krishnan, R.R., Venugopalan Pillai, N., Mahadevan Pillai, V.P., & Philip, R. (2010). Effect of cadmium oxide incorporation on the microstructural and optical properties of pulsed laser deposited nanostructured zinc oxide thin films. Materials Chemistry and Physics, 121(3), 406-413.

[89] Van de Walle, C. G., & Neugebauer, J. (2003). Universal alignment of hydrogen levels in semiconductors, insulators and solutions. Nature, 423(6940), 626-628.

[90] Lany, S., & Zunger, A. (2007). Dopability, intrinsic conductivity, and nonstoichiometry of transparent conducting oxides. Physical Review Letters, 98(4)

[91] Kohan, A. F., Ceder, G., Morgan, D., & Van De Walle, C. G. (2000). First-principles study of native point defects in ZnO. Physical Review B - Condensed Matter and Materials Physics, 61(22), 15019-15027.

[92] Kim, Y. -., & Park, C. H. (2009). Rich variety of defects in ZnO via an attractive interaction between O vacancies and Zn interstitials: Origin of n-type doping. Physical Review Letters, 102(8).

[93] Nickel, N. H., & Gluba, M. A. (2011). Properties of nitrogen molecules in ZnO. Journal of Electronic Materials, 40(4), 440-445.

[94] Thomas, D.G. (1957). Interstitial zinc in zinc oxide. Journal of Physics and Chemistry of Solids, 3(3-4), pp. 229-237.

[95] McCluskey, M. D., & Jokela, S. J. (2009). Defects in ZnO. Journal of Applied Physics, 106(7).

[96] Gu, Q. L., Ling, C. C., Chen, X. D., Cheng, C. K., Ng, A. M. C., Beling, C. D., & Ong, H. C. (2007). Hydrogen peroxide treatment induced rectifying behavior of Aun-ZnO contact. Applied Physics Letters, 90(12).

[97] Knutsen, K.E., Galeckas, A., Zubiaga, A., Tuomisto, F., Farlow, G.C., Svensson, B.G., & Kuznetsov, A.Y. (2012). Zinc vacancy and oxygen interstitial in ZnO revealed by sequential annealing and electron irradiation. Physical Review B - Condensed Matter and Materials Physics, 86(12).

[98] Mishra, S. K., Srivastava, R. K., & Prakash, S. G. (2013). Photoluminescence and photoconductivity studies of ZnO nanoparticles prepared by solid state reaction method. Journal of Materials Science: Materials in Electronics, 24(1), 125-134.

[99] Srivastava, A. K., & Kumar, J. (2013). Effect of zinc addition and vacuum annealing time on the properties of spin-coated low-cost transparent conducting 1 at% Ga-ZnO thin films. Science and Technology of Advanced Materials, 14(6).

[100] Klingshirn, C., Hauschild, R., Fallert, J., & Kalt, H. (2007). Room-temperature stimulated emission of ZnO: Alternatives to excitonic lasing. Physical Review B - Condensed Matter and Materials Physics, 75(11).

[101] Chaaya, A. A., Viter, R., Bechelany, M., Alute, Z., Erts, D., Zalesskaya, A., Miele, P. (2013). Evolution of microstructure and related optical properties of ZnO grown by atomic layer deposition. Beilstein Journal of Nanotechnology, 4(1), 690-698.

[102] Ozawa, K., Oba, Y., Edamoto, K., et al. (2009). Valence-band structure of the polar ZnO surfaces studied by angle-resolved photoelectron spectroscopy. Physical Review B - Condensed Matter and Materials Physics, 79(7).

[103] Lu, Y. M., Li, X. P., Cao, P. J., et al. (2013). Study of ultraviolet emission spectra in ZnO thin films. Journal of Spectroscopy, 1(1).

[104] Wang, Y. G., Lau, S. P., Zhang, X. H., Hng, H. H., Lee, H. W., Yu, S. F., & Tay, B. K. (2003). Enhancement of near-band-edge photoluminescence from ZnO films by face-to-face annealing. Journal of Crystal Growth, 259(4), 335-342.

[105] Moazzami, K., Murphy, T. E., Phillips, J. D., Cheung, M. C., & Cartwright, A. N. (2006). Sub-bandgap photoconductivity in ZnO epilayers and extraction of trap density spectra. Semiconductor Science and Technology,21(6), 717-723.

[106] Chen, Y., Bagnall, D., & Yao, T. (2000). ZnO as a novel photonic material for the UV region. Materials Science and Engineering B: Solid-State Materials for Advanced Technology, 75(2-3), 190-198.

[107] Chen, H. C., Chen, M. J., Liu, T. C., Yang, J. R., & Shiojiri, M. (2010). Structure and stimulated emission of a high-quality zinc oxide epilayer grown by atomic layer deposition on the sapphire substrate. Thin Solid Films,519(1), 536-540.

[108] Yamamoto, A., Kido, T., Goto, T., Chen, Y., & Yao, T. (2002). Bandgap renormalization of ZnO epitaxial thin films. Solid State Communications, 122(1-2), 29-32.

[109] Wagner, M. R., Callsen, G., Reparaz, J. S., et al. (2011). Bound excitons in ZnO: Structural defect complexes versus shallow impurity centers. Physical Review B - Condensed Matter and Materials Physics, 84(3).

[110] Schirra, M., Schneider, R., Reiser, A., Prinz, G. M., Feneberg, M., Biskupek, J., & Sauer, R. (2008). Stacking fault related 3.31 eV luminescence at 130 meV acceptors in zinc oxide. Physical Review B - Condensed Matter and Materials Physics, 77(12).

[111] Yang, S., Kuo, C. C., Liu, W., Lin, B. H., Hsu, H., Hsu, C., & Hsieh, W. F. (2012). Photoluminescence associated with basal stacking faults in c-plane ZnO epitaxial film grown by atomic layer deposition. Applied Physics Letters, 100(10).

[112] Lin, J. M., Lin, H. Y., Cheng, C. L., & Chen, Y. F. (2006). Giant enhancement of bandgap emission of ZnO nanorods by platinum nanoparticles. Nanotechnology, 17(17), 4391-4394.

[113] Chen, H., Chen, M., Wu, M., Cheng, Y., & Tsai, F. (2008). Low-threshold stimulated emission in ZnO thin films grown by atomic layer deposition. IEEE Journal on Selected Topics in Quantum Electronics, 14(4), 1053-1057.

[114] Hickernell, F. S. (1976). Zinc oxide thin film surface wave transducers. Proceedings of the IEEE, 64(5), 631-635.

[115] Kuoni, A., Holzherr, R., Boillat, M., & De Rooij, N. F. (2003). Polyimide membrane with ZnO piezoelectric thin film pressure transducers as a differential pressure liquid flow sensor. Journal of Micromechanics and Microengineering, 13(4), S103-S107.

[116] Kon, S., Oldham, K., & Horowitz, R. (2007). Piezoresistive and piezoelectric MEMS strain sensors for vibration detection. Paper presented at the Proceedings of SPIE - the International Society for Optical Engineering, , 6529 PART 2.

[117] Kuo, H., Guo, J., & Ko, W. H. (2007). High performance piezoresistive micro strain sensors. Paper presented at the Proceedings of the 2nd IEEE International Conference on Nano/Micro Engineered and Molecular Systems, IEEE NEMS 2007, 1052-1055.

[118] Gullapalli, H., Vemuru, V. S. M., Kumar, A., Botello-Mendez, A., Vajtai, R., Terrones, M., & Ajayan, P. M. (2010). Flexible piezoelectric ZnO-paper nanocomposite strain sensor. Small, 6(15), 1641-1646.

[119] Bueno, P. R., Varela, J. A., & Longo, E. (2008). SnO2, ZnO and related polycrystalline compound semiconductors: An overview and review on the voltage-dependent resistance (non-ohmic) feature. Journal of the European Ceramic Society, 28(3), 505-529.

[120] Matsuoka, M. (1971). Nonohmic Properties of Zinc Oxide Ceramics. Japanese Journal of Applied Physics, 10(6), 736-746.

[121] Levinson, L. M., & Philipp, H. R. (1975). The physics of metal oxide varistors. Journal of Applied Physics, 46(3), 1332-1341.

[122] Look, D. C. (2001). Recent advances in ZnO materials and devices. Materials Science and Engineering B: Solid-State Materials for Advanced Technology, 80(1-3), 383-387.

[123] Yang, F., Ma, S., Zhang, X., Zhang, M., Li, F., Liu, J., & Zhao, Q. (2012). Blue-green and red luminescence from ZnO/porous silicon and ZnO:Cu/porous silicon nanocomposite films. Superlattices and Microstructures, 52(2), 210-220.

[124] Tsukazaki, A., Ohtomo, A., Onuma, T., Ohtani, M., Makino, T., Sumiya, M., & Kawasaki, M. (2005). Repeated temperature modulation epitaxy for p-type doping and light-emitting diode based on ZnO. Nature Materials, 4(1), 42-45.

[125] Liu, W., Gu, S. L., Ye, J. D., Zhu, S. M., Liu, S. M., Zhou, X., & Zhang, C. L. (2006). Blue-yellow ZnO homostructural light-emitting diode realized by metalorganic chemical vapor deposition technique. Applied Physics Letters, 88(9).

[126] Nakahara, K., Akasaka, S., Yuji, H., Tamura, K., Fujii, T., Nishimoto, Y., Kawasaki, M. (2010). Nitrogen doped mg x zn 1-x O/ZnO single heterostructure ultraviolet light-emitting diodes on ZnO substrates. Applied Physics Letters, 97(1).

[127] Ryu, Y. R., Lee, T. S., Lubguban, J. A., White, H. W., Park, Y. S., & Youn, C. J. (2005). ZnO devices: Photodiodes and p-type field-effect transistors. Applied Physics Letters, 87(15), 1-3.

[128] Kind, H., Yan, H., Messer, B., Law, M., & Yang, P. (2002). Nanowire ultraviolet photodetectors and optical switches. Advanced Materials, 14(2), 158-160.

[129] Djuriić, A. B., Ng, A. M. C., & Chen, X. Y. (2010). ZnO nanostructures for optoelectronics: Material properties and device applications. Progress in Quantum Electronics, 34(4), 191-259.

[130] Liu, Y., Gorla, C. R., Liang, S., Emanetoglu, N., Lu, Y., Shen, H., & Wraback, M. (2000). Ultraviolet detectors based on epitaxial ZnO films grown by MOCVD. Journal of Electronic Materials, 29(1), 69-74.

[131] Soci, C., Zhang, A., Xiang, B., Dayeh, S. A., Aplin, D. P. R., Park, J., & Wang, D. (2007). ZnO nanowire UV photodetectors with high internal gain. Nano Letters, 7(4), 1003-1009.

[132] Young, S. J., Ji, L. W., Chang, S. J., Liang, S. H., Lam, K. T., Fang, T. H., & Xue, Q. K. (2007). ZnO-based MIS photodetectors. Sensors and Actuators, A: Physical, 135(2), 529-533.

[133] Hwang, D., Oh, M., Lim, J., Choi, Y., & Park, S. (2007). ZnO-based light-emitting metal-insulator-semiconductor diodes. Applied Physics Letters, 91(12).

[134] Ali, G. M., & Chakrabarti, P. (2010). Effect of thermal treatment on the performance of ZnO based metal-insulator-semiconductor ultraviolet photodetectors. Applied Physics Letters, 97(3).

[135] Liang, S., Sheng, H., Liu, Y., Huo, Z., Lu, Y., & Shen, H. (2001). ZnO schottky ultraviolet photodetectors. Journal of Crystal Growth, 225(2-4), 110-113.

[136] Ali, G. M., & Chakrabarti, P. (2010). ZnO-based interdigitated MSM and MISIM ultraviolet photodetectors. Journal of Physics D: Applied Physics, 43(41).

[137] Schmidt-Mende, L., & MacManus-Driscoll, J. L. (2007). ZnO-nanostructures, defects, and devices. Materials Today, 10(5), 40-48.

[138] Gonzalez-Valls, I., & Lira-Cantu, M. (2009). Vertically-aligned nanostructures of ZnO for excitonic solar cells: A review. Energy and Environmental Science, 2(1), 19-34.

[139] Beek, W. J. E., Wienk, M. M., & Janssen, R. A. J. (2004). Efficient hybrid solar cells from zinc oxide nanoparticles and a conjugated polymer. Advanced Materials, 16(12), 1009-1013.

[140] Baxter, J. B., & Aydil, E. S. (2005). Nanowire-based dye-sensitized solar cells. Applied Physics Letters, 86(5), 1-3.

[141] Labat, F., Ciofini, I., Hratchian, H. P., Frisch, M., Raghavachari, K., & Adamo, C. (2009). First principles modeling of eosin-loaded ZnO films: A step toward the understanding of dye-sensitized solar cell performances. Journal of the American Chemical Society, 131(40), 14290-14298.

[142] O'Regan, B., & Grätzel, M. (1991).A low-cost, high-efficiency solar cell based on dye-sensitised colloidal TiO2 films. Nature, 335, 737-740.

[143] Leschkies, K. S., Divakar, R., Basu, J., Enache-Pommer, E., Boercker, J. E., Carter, C. B., & Aydil, E. S. (2007). Photosensitization of ZnO nanowires with CdSe quantum dots for photovoltaic devices. Nano Letters, 7(6), 1793-1798.

[144] Lewis, B. G., & Paine, D. C. (2000). Applications and processing of transparent conducting oxides. MRS Bulletin, 25(8), 22-27.

[145] Ellmer, K. (2001). Resistivity of polycrystalline zinc oxide films: Current status and physical limit. Journal of Physics D: Applied Physics, 34(21), 3097-3108.

[146] Haacke, G. (1976). New figure of merit for transparent conductors. Journal of Applied Physics, 47(9), 4086-4089.

[147] Kim, H., Pique, A., Horwitz, J. S., Merritt, C. D., Schlaf, R., Kafafi, Z. H., Gilmore, C. M., & Chrisey, D. B. (1999). Transparent conducting electrode materials grown by pulsed laser deposition for organic light-emitting devices. Proc. SPIE 3797, Organic Light-Emitting Materials and Devices III, 290.

[148] Hosono, H. (2007). Recent progress in transparent oxide semiconductors: Materials and device application. Thin Solid Films, 515(15 SPEC. ISS.), 6000-6014.

[149] Granqvist, C. G. (1993). Transparent conductive electrodes for electrochromic devices: A review. Applied Physics A Solids and Surfaces, 57(1), 19-24.

[150] Klein, A., Körber, C., Wachau, A., Säuberlich, F., Gassenbauer, Y., Harvey, S. P., & Mason, T. O. (2010). Transparent conducting oxides for photovoltaics: Manipulation of fermi level,work function and energy band alignment. Materials, 3(11), 4892-4914.

[151] Würfel, P. (2005). Physics of Solar Cells: From Principles to New Concepts. WILEY-VCH Verlag GmbH & Co.

[152] Rabinovich, E., & Hodes, G. (2013). Effective bandgap lowering of CdS deposited by successive ionic layer adsorption and reaction. Journal of Physical Chemistry C, 117(4), 1611-1620.

[153] MKS Technology for Productivity. (n.d.). Chemical Vapor Deposition. Retrieved 2012, from MKS Technology for productivity; Process solutions: http://www.mksinst.com/docs/ur/CVDps.pdf.

[154] Wu, J., & Liu, S. (2002). Catalyst-free growth and characterization of ZnO nanorods. Journal of Physical Chemistry B, 106(37), 9546-9551.

[155] Zhang, B. P., Wakatsuki, K., Binh, N. T., Usami, N., & Segawa, Y. (2004). Effects of growth temperature on the characteristics of ZnO epitaxial films deposited by metalorganic chemical vapor deposition. Thin Solid Films, 449(1-2), 12-19.

[156] Kelly, P. J., & Arnell, R. D. (2000). Magnetron sputtering: A review of recent developments and applications. Vacuum, 56(3), 159-172.

[157] Cebulla, R., Wendt, R., & Ellmer, K. (1998). Al-doped zinc oxide films deposited by simultaneous RF and DC excitation of a magnetron plasma: Relationships between plasma parameters and structural and electrical film properties. Journal of Applied Physics, 83(2), 1087-1095.

[158] Chen, W., Wang, J., &Wang, M. (2007). Influence of doping concentration on the properties of ZnO:Mn thin films by sol-gel method. Vacuum, 81(7), 894-898.

[159] Vispute, R. D., Choopun, S., Enck, R., Patel, A., Talyansky, V., Sharma, R. P. & Jones, K. A. (1999). Pulsed laser deposition and processing of wide band gap semiconductors and related materials. Journal of Electronic Materials, 28(3), 275-286.

[160] Liu, Y., Zhao, L., & Lian, J. (2006). Al-doped ZnO films by pulsed laser deposition at room temperature. Vacuum, 81(1), 18-21.

[161] Agura, H., Suzuki, A., Matsushita, T., Aoki, T., & Okuda, M. (2003). Low resistivity transparent conducting Al-doped ZnO films prepared by pulsed laser deposition. Thin Solid Films, 445(2), 263-267.

[162] Park, S., Ikegami, T., & Ebihara, K. (2006). Effects of substrate temperature on the properties of Ga-doped ZnO by pulsed laser deposition. Thin Solid Films, 513(1-2), 90-94.

[163] Kuo, F. L., Lin, M., Mensah, B. A., Scharf, T. W., & Shepherd, N. D. (2010). A comparative study of the photoluminescence and conduction mechanisms of low temperature pulsed laser deposited and atomic layer deposited zinc oxide thin films. Physica Status Solidi (A) Applications and Materials Science, 207(11), 2487-2491.

[164] Gupta, M. K., Sinha, N., & Kumar, B. (2011). P-type K-doped ZnO nanorods for optoelectronic applications. Journal of Applied Physics, 109(8).

[165] Stoehr, M., Juillaguet, S., Kyaw, T.M., & Wen, J.G. (2007). Doping effect on the optical properties of ZnO nanostructures. Physica Status Solidi (C) Current Topics in Solid State Physics, 4(4), 1432-1437.

[166] Lyons, J. L., Janotti, A., & Van De Walle, C. G. (2009). Why nitrogen cannot lead to p -type conductivity in ZnO. Applied Physics Letters, 95(25).

[167] Na, J., Peng, Q., Scarel, G., & Parsons, G. N. (2009). Role of gas doping sequence in surface reactions and dopant incorporation during atomic layer deposition of Al-doped ZnO. Chemistry of Materials, 21(23), 5585-5593.

[168] Schmitt, S. W., Gamez, G., Sivakov, V., Schubert, M., Christiansen, S. H., & Michler, J. (2011). Chemical and optical characterisation of atomic layer deposition aluminium doped ZnO films for photovoltaics by glow discharge optical emission spectrometry. Journal of Analytical Atomic Spectrometry, 26(4), 822-827.

[169] Cheng, Y. (2011). Effects of post-deposition rapid thermal annealing on aluminum-doped ZnO thin films grown by atomic layer deposition. Applied Surface Science, 258(1), 604-607.

[170] Lyons, J. L., Janotti, A., & Van De Walle, C. G. (2009). Role of Si and Ge as impurities in ZnO. Physical Review B - Condensed Matter and Materials Physics, 80(20).

[171] Ye, Z., Lu, H., Geng, Y., et al. (2013). Structural, electrical, and optical properties of Ti-doped ZnO films fabricated by atomic layer deposition. Nanoscale Research Letters 8:108.

[172] Zhang, B., Zhang, X., Gong, H., Wu, Z., Zhou, S., & Du, Z. (2008). Ni-doped zinc oxide nanocombs and phonon spectra properties. Physics Letters, Section A: General, Atomic and Solid State Physics, 372(13), 2300-2303.

[173] Kim, K., Kim, G., Woo, J., & Kim, C. (2008). Characteristics of nickel-doped zinc oxide thin films prepared by sol-gel method. Surface and Coatings Technology, 202(22-23), 5650-5653.

[174] Khomchenko, V. S., Kryshtab, T. G., Savin, A. K., Zavyalova, L. V., Roshchina, N. N., Rodionov, V. E., & Andraca-Adame, J. A. (2007). Fabrication and properties of ZnO:Cu and ZnO:Ag thin films. Superlattices and Microstructures, 42(1-6), 94-98.

[175] Kim, W., Moon, Y., Kim, K., Shin, S., Ahn, B. D., Lee, J., & Park, J. (2011). Improvement in the negative bias temperature stability of ZnO based thin film transistors by Hf and Sn doping. Thin Solid Films, 519(20), 6849-6852.

[176] Fu, E., Zhuang, D., Zhang, G., Ming, Z., Yang, W., & Liu, J. (2004). Properties of transparent conductive ZnO:Al thin films prepared by magnetron sputtering. Microelectronics Journal, 35(4),. 383-387.

[177] Oh, B., Jeong, M., Kim, D., Lee, W., & Myoung, J. (2005). Post-annealing of Al-doped ZnO films in hydrogen atmosphere. Journal of Crystal Growth, 281(2-4), 475-480.

[178] Zhu, Y., Wang, Y., Wan, P., Li, H., & Wang, S. (2012). Optical and mechanical properties of transparent conductive Al-doped ZnO films deposited by the sputtering method. Chinese Physics Letters, 29(3).

[179] Suchea, M., Christoulakis, S., Katsarakis, N., Kitsopoulos, T., & Kiriakidis, G. (2007). Comparative study of zinc oxide and aluminum doped zinc oxide transparent thin films grown by direct current magnetron sputtering. Thin Solid Films, 515(16 SPEC. ISS.), 6562-6566.

[180] Kim, D., Yun, I., & Kim, H. (2010). Fabrication of rough Al-doped ZnO films deposited by low pressure chemical vapor deposition for high efficiency thin film solar cells. Current Applied Physics, 10 (SUPPL. 3), S459-S462.

[181] Wang, X.H., Li, R.B., & Fan, D.H. (2011). Study on synthesis and optical properties of Al-doped ZnO hierarchical nanostructures. AIP Advances, 1(1).

[182] Kuo, S., Chen, W., Lai, F., Cheng, C., Kuo, H., Wang, S., & Hsieh, W. (2006). Effects of doping concentration and annealing temperature on properties of highly-oriented Al-doped ZnO films. Journal of Crystal Growth, 287(1), 78-84.

[183] Kuroyanagi, A. (1989). Crystallographic characteristics and electrical properties of Al-doped ZnO thin films prepared by ionized deposition. Journal of Applied Physics, 66(11), 5492-5497.

[184] Lee, J., & Park, B. (2003). Transparent conducting ZnO:Al, In and Sn thin films deposited by the sol-gel method. Thin Solid Films, 426(1-2), 94-99.

[185] Inamdar, D., Agashe, C., Kadam, P., & Mahamuni, S. (2012). Doping optimization and surface modification of aluminum doped zinc oxide films as transparent conductive coating. Thin Solid Films, 520(11), 3871-3877.

[186] Hou, Q., Meng, F., & Sun, J. (2013). Electrical and optical properties of Al-doped ZnO and $ZnAl_2O_4$ films prepared by atomic layer deposition. Nanoscale Research Letters, 8(1), 1-8.

[187] Banerjee, P., Lee, W. Bae, K., Lee, S.B., & Rubloff, G.W. (2010). Structural, electrical, and optical properties of atomic layer deposition Al-doped ZnO films. Journal of Applied Physics, 108(4).

[188] Genevée, P., Donsanti, F., Renou, G., & Lincot, D. (2013). Study of the aluminum doping of zinc oxide films prepared by atomic layer deposition at low temperature. Applied Surface Science, 264, 464-469.

[189] Nahm, C., Shin, S., Lee, W., et al. (2013). Electronic transport and carrier concentration in conductive ZnO:Ga thin films. Current Applied Physics, 13(2), 415-418.

[190] Nunes, P., Fortunato, E., Tonello, P., Braz Fernandes, F., Vilarinho, P., & Martins, R (2002). Effect of different dopant elements on the properties of ZnO thin films. Vacuum, 64(3-4), 281-285.

[191] Zhao, L., Shao, G., Song, Q., Xiujuan, S., & Han, S. (2011). Development on transparent conductive ZnO thin films doped with various impurity elements. Rare Metals, 30(2), 175-182.

[192] Illiberi, A., Scherpenborg, R., Roozeboom, F., & Poodt, P. (2014). Atmospheric spatial atomic layer deposition of In-doped ZnO. ECS Journal of Solid State Science and Technology, 3(5), P111-P114.

[193] Dai, L. P., Deng, H., Mao, F. Y., & Zang, J. D. (2008). The recent advances of research on p-type ZnO thin film. Journal of Materials Science: Materials in Electronics, 19(8-9), 727-734.

[194] Kim, Y., Jeong, K., Yun, H., Yang, S., Lee, S., Lee, H., & Lee, G. (2012). P-type conductive behavior of AlN co-doped ZnO films deposited by the atomic layer deposition. Paper presented at the TMS Annual Meeting, , 2 19-25.

[195] Kumar, E. S., Chatterjee, J., Rama, N., Gupta, N. D., & Rao, M. S. R. (2011). A codoping route to realize low resistive and stable p-type conduction in (Li,Ni):ZnO Thin films grown by pulsed laser deposition. ACS Applied Materials and Interfaces, 3(6), 1974-1979.

[196] Jung, Y., Yang, W., Koo, C. Y., Song, K., & Moon, J. (2012). High performance and high stability low temperature aqueous solution-derived Li-Zr co-doped ZnO thin film transistors. Journal of Materials Chemistry, 22(12), 5390-5397.

[197] Le, H. Q., & Chua, S. J. (2011). Gallium and indium co-doping of epitaxial zinc oxide thin films grown in water at 90°C. Journal of Physics D: Applied Physics, 44(12).

[198] Lu, Z.L., Miao, W., Zou, W.Q., Xu, M.X., & Zhang, F.M. (2010). Enhanced ferromagnetism in single crystalline Co-doped ZnO thin films by Al codoping. Journal of Alloys and Compounds, 494(1-2), 392-395.

[199] Lu, Z., Hsu, H., Tzeng, Y., & Huang, J. (2009). Carrier-mediated ferromagnetism in single crystalline (Co, Ga)-codoped ZnO films. Applied Physics Letters, 94(15).

[200] Zhang, J., Gao, D., Yang, G., et al. (2011). Synthesis and magnetic properties of Zr-doped ZnO nanoparticles. Nanoscale Research Letters, 6, 1-21.

[201] Khan, I., Khan, S., Nongjai, R., Ahmed, H., & Khan, W. (2013). Structural and optical properties of gel-combustion synthesized Zr-doped ZnO nanoparticles. Optical Materials, 35(6), 1189-1193.

[202] Puurunen, R. L. (2005). Surface chemistry of atomic layer deposition: A case study for the trimethylaluminum/water process. Journal of Applied Physics, 97(12).

[203] George, S. M., Ott, A. W., & Klaus, J. W. (1996). Surface chemistry for atomic layer growth. Journal of Physical Chemistry, 100(31), 13121-13131.

[204] Ahonen, M., Pessa, M., & Suntola, T. (1980). A study of ZnTe films grown on glass substrates using an atomic layer evaporation method. Thin Solid Films, 65(3), 301-307.

[205] George, S. M. (2010). Atomic layer deposition: An overview. Chemical Reviews, 110(1), 111-131.

[206] Kim, H., Lee, H., & Maeng, W. (2009). Applications of atomic layer deposition to nanofabrication and emerging nanodevices. Thin Solid Films, 517(8), 2563-2580.

[207] ALD 2010 Workshop. (2010). 10th International Conference on Atomic Layer Deposition (pp. 3-64). Seoul: Dielectric Thin film Laboratory Seoul National University.

[208] Guziewicz, E., Godlewski, M., Wachnicki, L., et al. (2012). ALD grown zinc oxide with controllable electrical properties. Semiconductor Science and Technology, 27(7).

[209] Leskelä, M., & Ritala, M. (2002). Atomic layer deposition (ALD): From precursors to thin film structures. Thin Solid Films, 409(1), 138-146.

[210] Profijt, H. B., Potts, S. E., Van De Sanden, M. C. M., & Kessels, W. M. M. (2011). Plasma-assisted atomic layer deposition: Basics, opportunities, and challenges. Journal of Vacuum Science and Technology A: Vacuum, Surfaces and Films, 29(5).

[211] Chang, C., & Tsai, F. (2011). Efficient and air-stable plastics-based polymer solar cells enabled by atomic layer deposition. Journal of Materials Chemistry, 21(15), 5710-5715.

[212] Tanskanen, J. T., Bakke, J. R., Pakkanen, T. A., & Bent, S. F. (2011). Influence of organozinc ligand design on growth and material properties of ZnS and ZnO deposited by

atomic layer deposition. Journal of Vacuum Science and Technology A: Vacuum, Surfaces and Films, 29(3).

[213] Mousa, M. B. M., Oldham, C. J., Jur, J. S., & Parsons, G. N. (2012). Effect of temperature and gas velocity on growth per cycle during Al_2O_3 and ZnO atomic layer deposition at atmospheric pressure. Journal of Vacuum Science and Technology A: Vacuum, Surfaces and Films, 30(1).

[214] Krajewski, T. A., Luka, G., Wachnicki, L., et al. (2010). Growth conditions and structural properties as limiting factors of electrical parameters of ZnO thin films grown by atomic layer deposition with diethylzinc and water precursors. 14th International Conference on II-VI Compounds, II-VI 2009, August 23, 2009 - August 28, 7. (6) pp. 1550-1552.

[215] Ott, A. W., & Chang, R. P. H. (1999). Atomic layer-controlled growth of transparent conducting ZnO on plastic substrates. Materials Chemistry and Physics, 58(2), 132-138.

[216] Park, S. K., & Lee, Y. E. (2004). Controlling preferred orientation of ZnO thin films by atomic layer deposition. Journal of Materials Science, 39(6), 2195-2197.

[217] Kim, D., Kang, H., Kim, J., & Kim, H. (2011). Erratum: The properties of plasma-enhanced atomic layer deposition (ALD) ZnO thin films and comparison with thermal ALD (applied surface science (2011) 257 (3776-3779)).Applied Surface Science, 257(17), 7905.

[218] Malm, J., Sahramo, E., Perälä, J., Sajavaara, T., & Karppinen, M. (2011). Low-temperature atomic layer deposition of ZnO thin films: Control of crystallinity and orientation. Thin Solid Films, 519(16), 5319-5322.

[219] Kim, J., Bae, S., Yang, H., & Hwang, J. (2010). Electrical and optical properties of zinc oxide thin films deposited using atomic layer deposition. Journal of the Korean Ceramic Society, 47(4), 353-356.

[220] Guziewicz, E., Godlewski, M., Krajewski, T. A., et al. (2009). ZnO by ALD - advantages of the material grown at low temperature. Acta Physica Polonica A, 116(5), 814-817.

[221] Chiang, T., Dai, C., & Lian, D. (2011). Influence of growth temperature on the optical and structural properties of ultrathin ZnO films. Journal of Alloys and Compounds, 509(18), 5623-5626.

[222] Yen, C., Jian, S., Chen, G., Lin, C., Lee, H., Ke, W., et al. (2011). Influence of annealing temperature on the structural, optical and mechanical properties of ALD-derived ZnO thin films. Applied Surface Science, 257(17), 7900-7905.

[223] Shih, Y. T., Chiu, C. Y., Chang, C. W., Yang, J. R., Shiojiri, M., & Chen, M. J. (2010). Stimulated emission in highly (0001)-oriented ZnO films grown by atomic layer deposition on the amorphous glass substrates. Journal of the Electrochemical Society, 157(9), H879-H883.

[224] Illiberi, A., Roozeboom, F., & Poodt, P. (2012). Spatial atomic layer deposition of zinc oxide thin films. ACS Applied Materials and Interfaces, 4(1), 268-272.

[225] Pung, S., Choy, K., Hou, X., & Shan, C. (2008). Preferential growth of ZnO thin films by the atomic layer deposition technique. Nanotechnology, 19(43).

[226] Singh, T., Lehnen, T., Leuning, T., Sahu, D., & Mathur, S. (2014). Thickness dependence of optoelectronic properties in ALD grown ZnO thin films. Applied Surface Science, 289, 27-32.

[227] Makino, H., Kishimoto, S., Yamada, T., Miyake, A., Yamamoto, N., & Yamamoto, T. (2008). Effects of surface pretreatment on growth of ZnO on glass substrate. Physica Status Solidi (A) Applications and Materials Science,205(8), 1971-1974.

[228] Pant, P., Budai, J. D., & Narayan, J. (2010). Nonpolar ZnO film growth and mechanism for anisotropic in-plane strain relaxation. Acta Materialia, 58(3), 1097-1103.

[229] Mun Wong, K., Alay-E-Abbas, S. M., Shaukat, A., Fang, Y., & Lei, Y. (2013). First-principles investigation of the size-dependent structural stability and electronic properties of O-vacancies at the ZnO polar and non-polar surfaces. Journal of Applied Physics, 113(1).

[230] Lu, B., Ma, M. J., Ye, Y. H., Lu, J. G., He, H. P., & Ye, Z. Z. (2013). Rational growth of semi-polar ZnO texture on a glass substrate for optoelectronic applications. Journal of Physics D: Applied Physics, 46(5).

[231] Fujimura, N., Nishihara, T., Goto, S., Xu, J., & Ito, T. (1993). Control of preferred orientation for ZnO_x films: Control of self-texture. Journal of Crystal Growth, 130(1-2), 269-279.

[232] Illy, B. N., Cruickshank, A. C., Schumann, S., et al. (2011). Electrodeposition of ZnO layers for photovoltaic applications: Controlling film thickness and orientation. Journal of Materials Chemistry, 21(34), 12949-12957.

[233] Gieraltowska, S., Wachnicki, L., Witkowski, B. S., Godlewski, M., & Guziewicz, E. (2012). Atomic layer deposition grown composite dielectric oxides and ZnO for transparent electronic applications. Thin Solid Films, 520(14), 4694-4697.

[234] Law, M., Greene, L. E., Radenovic, A., Kuykendall, T., Liphardt, J., & Yang, P. (2006). ZnO-Al_2O_3 and ZnO-TiO_2 core-shell nanowire dye-sensitized solar cells. Journal of Physical Chemistry B, 110(45), 22652-22663.

[235] Kang, J. H., Kim, C. E., Kim, M., Myoung, J., & Yun, I. (2009). Material characterization and process modeling issues of high-k dielectrics for FET applications. 2009 IEEE Nanotechnology Materials and Devices Conference, NMDC 2009, June 2, 2009 - June 5, pp. 237-240.

[236] Martinson, A. B. F., Elam, J. W., Hupp, J. T., & Pellin, M. J. (2007). ZnO nanotube based dye-sensitized solar cells. Nano Letters, 7(8), 2183-2187.

[237] King, D. M., Liang, X., Carney, C. S., Hakim, L. F., Li, P., & Weimer, A. W. (2008). Atomic layer deposition of UV-absorbing ZnO films on SiO_2 and TiO_2 nanoparticles using a fluidized bed reactor. Advanced Functional Materials, 18(4), 607-615.

[238] King, D. M., Liang, X., Li, P., & Weimer, A. W. (2008). Low-temperature atomic layer deposition of ZnO films on particles in a fluidized bed reactor. Thin Solid Films, 516(23), 8517-8523.

[239] Li, X. L., Li, C., Zhang, Y., Chu, D. P., Milne, W. I., & Fan, H. J. (2010). Atomic layer deposition of ZnO on multi-walled carbon nanotubes and its use for synthesis of CNT-ZnO heterostructures. Nanoscale Research Letters, 5(11), 1836-1840.

[240] Libera, J. A., Elam, J. W., & Pellin, M. J. (2008). Conformal ZnO coatings on high surface area silica gel using atomic layer deposition. Thin Solid Films, 516(18), 6158-6166.

[241] Ladanov, M., Algarin-Amaris, P., Villalba, P., Emirov, Y., Matthews, G., Thomas, S., & Wang, J. (2013). Effects of the physical properties of atomic layer deposition grown seeding layers on the preparation of ZnO nanowires. Journal of Physics and Chemistry of Solids, 74(11), 1578-1588.

[242] Kwon, S. J. (2005). Effect of precursor-pulse on properties of Al-doped ZnO films grown by atomic layer deposition. Japanese Journal of Applied Physics, Part 1: Regular Papers and Short Notes and Review Papers, 44(2), 1062-1066.

[243] Song, J., Mu, H., Jiang, L., Yin, G., Yu, Z., & He, D. (2011). The electrical and optical properties of Al-doped ZnO thin films prepared by atomic layer deposition. Advanced Materials Research, 306-307, p. 1402-1405.

[244] Oh, B., Kim, J., Han, J., Seo, D., Jang, H. S., Choi, H., et al. (2012). Transparent conductive ZnO:Al films grown by atomic layer deposition for Si-wire-based solar cells. Current Applied Physics, 12(1), 273-279.

[245] Yousfi, E. B., Weinberger, B., Donsanti, F., Cowache, P., & Lincot, D. (2001). Atomic layer deposition of zinc oxide and indium sulfide layers for Cu (In,Ga)Se_2 thin-film solar cells. Thin Solid Films, 387(1-2), 29-32.

[246] Čeh, M., Chen, H., Chen, M., Yang, J., & Shiojiri, M. (2010). Structure and electro-optical properties of thin films grown by alternate atomic layer deposition of ZnO and Al_2O_3 on the sapphire substrate. Materials Transactions, 51(2), 219-226.

[247] Yamamoto, Y., Saito, K., Takahashi, K., & Konagai, M. (2001). Preperation of boron-doped ZnO thin films by photo-atomic layer deposition. Solar Energy Materials and Solar Cells, 65(1), 125-132.

[248] Niilisk, A., Aarik, J., Uustare, T., Mandar, H., Tkachev, S., & Manghnani, M. (2005). Structural study of ZrO_2 and HfO_2 thin films grown by atomic layer deposition. Optical Materials and Applications, July 6, 2004 - July 9, 5946. pp. 1-8.

[249] Niinistö, J., Kukli, K., Kariniemi, M., Ritala, M., Leskelä, M., Blasco, N., & Dussarrat, C. (2008). Novel mixed alkylamido-cyclopentadienyl precursors for ALD of ZrO_2 thin films. Journal of Materials Chemistry, 18(43), 5243-5247.

[250] Lee, B., Choi, K.J., Hande, A., Kim, M.J., Wallace, R.M., Kim, J., Senzaki, Y., Shenai, D., Li, H., Rousseau, M., & Suydam, J., (2009). A novel thermally-stable zirconium amidinate ALD precursor for ZrO_2 thin films.Microelectronic Engineering, 86(3), pp. 272-276.

[251] Yun, S. J., Lim, J. W., & Lee, J. (2004). PEALD of zirconium oxide using tetrakis(ethylmethylamino)zirconium and oxygen. Electrochemical and Solid-State Letters, 7(12), F81-F84.

[252] Losurdo, M., & Hingerl, K. (2013). Ellipsometry at the Nanoscale. Berlin Heidelberg: Springer Berlin Heidelberg.

[253] ELLIPSHEET: Spreadsheet Ellipsometry (Excel Ellipsometer). (n.d.). Retrieved from EXCEL Worksheets for Basic Ellipsometry Calculation: http://www.ccn.yamanashi.ac.jp/~kondoh/ellips_e.html.

[254] Krajewski, T., Guziewicz, E., Godlewski, M., Wachnicki, L., Kowalik, I.A., Wojcik-Glodowska, A., Lukasiewicz, M., Kopalko, K., Osinniy, V., & Guziewicz, M. (2009). The influence of growth temperature and precursors' doses on electrical parameters of ZnO thin films grown by atomic layer deposition technique. Microelectronics Journal, 40(2), 293-295.

[255] Yu, S. F., Yuen, C., Lau, S. P., Wang, Y. G., Lee, H. W., & Tay, B. K. (2003). Ultraviolet amplified spontaneous emission from zinc oxide ridge waveguides on silicon substrate. Applied Physics Letters, 83(21), 4288-4290.

[256] Rueter, M. A., & Vohs, J. M. (1992). The surface reactions of ethyl groups on Si(100) formed via dissociation of adsorbed diethylzinc. Surface Science, 262(1-2), 42-50.

[257] Zhang, J., Yang, H., Zhang, Q., Dong, S., & Luo, J. K. (2013). Structural, optical, electrical and resistive switching properties of ZnO thin films deposited by thermal and plasma-enhanced atomic layer deposition.Applied Surface Science, 282, 390-395.

[258] Becker, J. S., Kim, E., & Gordon, R. G. (2004). Atomic layer deposition of insulating hafnium and zirconium nitrides. Chemistry of Materials, 16(18), 3497-3501.

[259] Gallino, F., Di Valentin, C., & Pacchioni, G. (2011). Band gap engineering of bulk ZrO_2 by Ti doping. Phys. Chem. Chem. Phys., 2011,13, 17667–17675.

[260] Four-Point Probe Manual. (n.d.). Retrieved from Four-Point Probes; A division of Bridge technology: http://four-point-probes.com/four-point-probe-manual/.

[261] Sze, S., & Lee, M.K. (2013). Semiconducotr Devices: Physics and Technology. John Wiley and Sons Singapore Pte. Ltd.

[262] Van der Pauw, L. J., (1958). A method of measuring specific resistivity and Hall effect of discs of arbitrary shape. Philips Res.Rept.,13,1.

[263] Chwang, R., Smith, B.J., & Crowell, C.R. (1974). Contact size effects on the van der Pauw method for resistivity and Hall coefficient measurement. Solid State Electronics, 17(12), pp. 1217-1227.

[264] Pekker, Á., & Kamarás, K. (2010). A general figure of merit for thick and thin transparent conductive carbon nanotube coatings. Journal of Applied Physics, 108(5).

[265] Li, S. S. (2006). Semiconductor Physical Electronics. New York: Springer.

[266] P. Atkins, & de Paula, J. (2006). Atkins' Physical Chemistry [Eighth Edition]. New York: W. H. Freeman and Company.

[267] Patane, A., & Balkan, N. (2012). Semiconductor Research: Experimental Techniques. Berlin Heidelberg: Springer Series in Materials Science.

[268] Jobin Yvon Horiba HR800 User Manual.

[269] Raman Spectroscopy: Raman Academy. (n.d.). Retrieved 2013, from Horiba Scientific: http://www.horiba.com/uk/scientific/.

[270] Gfroerer, T. H. (2006). Photoluminescence in Analysis of Surfaces and Interfaces. Encyclopedia of Analytical Chemistry.

[271] Olympus Miscroscope Componetns Quide.

[272] Kevin, M., & Ho, G. W. (2013). Transmission/absorption measurements for in situ monitoring of transparent conducting Ga:ZnO films grown via aqueous methods. Journal of Materials Chemistry A, 1(45), 14239-14245.

[273] Mulvaney, P. (1996). Surface plasmon spectroscopy of nanosized metal particles. Langmuir, 12(3), 788-800.

[274] Lapedes, D. (1978) Dictionary of Scientific & Technical Terms: Second Edition. New York: McGraw Hill.

[275] Shimadzu SolidSpec-3700/3700DUV UV-VIS-NIR Spectrophotometer. (n.d.). Retrieved from SHIMADZU Analytical and Measuring Instruments: http://www.shimadzu.com/an/spectro/uv/solidspec/solid.html.

[276] Singh, J. (1995). Semiconductor Optoelectronics Physics and Technology. Singapore: McGraw-Hill Book Co.

[277] Rohrer, G. S. (2001). Structure and Bonding in Crystalline Materials. Cambridge: Cambridge university press.

[278] Cullity, B. D., & Stock, S. R. (2001). Elements of X-ray Diffraction. New Jersey: Prentice Hall.

[279] Suryanarayana, C., & Grant Norton, M. (1998). X-ray Diffraction: A practical Approach. New York: Plenum Publishing Corporation.

[280] International Tables for Crystallography (2006), Vol. C, Chapter 6.1, pp/ 554-595.

[281] Henke, B. L., Gullikson, E. M., & Davis, J. C. (1993). X-ray interactions: Photoabsorption, scattering, transmission, and reflection at E = 50-30,000 eV, Z = 1-92. Atomic Data and Nuclear Data Tables, 54(2), 181-342.

[282] Nordling, C., Sokolowski, E., & Siegbahn, K. (1957). Precision method for obtaining absolute values of atomic binding energies. Physical Review, 105(5), 1676-1677.

[283] Karlsson, E., & Siegbahn, K. (1960). A new design for a beta-ray spectrograph for relative measurements. Nuclear Instruments and Methods, 7(2), 113-123.

[284] K. Siegbahn, C. Nordling, A. Fahlman, R. et al. (1967). ESCA: Atomic, Molecular and Solid State Structure by mans of Electron Spectroscopy. Uppsala, Sweden: Almqvist snd Wiksells.

[285] Tougaard, S. (1988). Quantitative analysis of the inelastic background in surface electron spectroscopy. Surface and Interface Analysis, 11(9), 453-472.

[286] Introduction into X-ray and UV Photoelectron Spectroscopy (XPS/UPS). Berlin: Helmholtz Zentrum Berlin for Materials and Energy.

[287] Seah, M. P., & Dench, W. A. (1979). Quantitative electron spectroscopy of surfaces: A standard data base for electron inelastic mean free paths in solids. Surface and Interface Analysis, 1(1), 2-11.

[288] Jablonski, A., Olejnik, K., & Zemek, J. (2006). Elastic electron backscattering from flat and rough si surfaces. Journal of Electron Spectroscopy and Related Phenomena, 152(1-2), 100-106.

[289] Cumpson, P. J., & Seah, M. P. (1997). Elastic scattering corrections in AES and XPS. II. estimating attenuation lengths and conditions required for their valid use in overlayer/substrate experiments. Surface and Interface Analysis, 25(6), 430-446.

[290] Sojka, Z., & Klier, K. (1992). High resolution XPS analysis of binary and ternary Cu and Fe doped ZnO catalysts for methane oxidation to formaldehyde. Journal of Electron Spectroscopy and Related Phenomena, 60(3), 155-174.

[291] Scofield, J. H. (1976). Hartree-slater subshell photoionization cross-sections at 1254 and 1487 eV. Journal of Electron Spectroscopy and Related Phenomena, 8(2), 129-137.

[292] Fadley, C. S., Baird, R. J., Siekhaus, W., Novakov, T., & Bergström, S. Å. L. (1974). Surface analysis and angular distributions in X-ray photoelectron spectroscopy. Journal of Electron Spectroscopy and Related Phenomena,4(2), 93-137.

[293] Yan, Y. L., Helfand, M. A., & Clayton, C. R. (1989). Evaluation of the effect of surface roughness on thin film thickness measurements using variable angle XPS. Applied Surface Science, 37(4), 395-405.

[294] Kuhn, W. K., & Andermann, G. (2001). Effects of surface roughness on surface analysis via soft and ultrasoft X-ray fluorescence spectroscopy. Applied Surface Science, 185(1-2), 84-91.

[295] Abou-Ras, D., Kirchartz, T., & Rau, U. (2011). Advanced Characterization Techniques for Thin Film Solar Cells. Weinheim, Germany: Wiley-VCH.

[296] Kim, Y., Jeong, J., Kim, J., Kim, Y., & Lim, Y.S. (2006). Image processing of atomic resolution transmission electron microscope images. Journal of the Korean Physical Society, 48(2), pp. 250-255.

[297] Hammond, C. (2009). The basics of Crystallography and Diffraction (Third edition). New York: Oxford University Press.

[298] Fultz, B., & Howe, J. M. (2008). Transmission Electron Microscopy and Diffractometry of Materials. Berlin Heidelberg: Springer Berlin Heidelberg.

[299] Yearian, H. J. (1935). Intensity of diffraction of electrons by ZnO. Physical Review, 48(7), 631-639.

[300] Binnig, G., Quate, C. F., & Gerber, C. (1986). Atomic force microscope. Physical Review Letters, 56(9), 930-933.

[301] Hutter, J. L., & Bechhoefer, J. (1993). Calibration of atomic-force microscope tips. Review of Scientific Instruments, 64(7), 1868-1873.

[302] Hong, S., Woo, J., Shin, H., et al. (2001). Principle of ferroelectric domain imaging using atomic force microscope. Journal of Applied Physics, 89(2), 1377-1386.

[303] Atomic Force Microscopy Products. (n.d.). Retrieved from Bruker: www.bruker.com.

[304] Raposo, M., Ferreira, Q., & Ribeiro, P. (2007). A Guide for Atomic Force Microscopy Analysis of Soft-Condensed Matter. In A. Méndez-Vilas, & J. Díaz, Modern Research and Educational Topics in Microscopy (pp. 758-769).

[305] S. C. Abrahams, J. L. (n.d.). Database from ICSD (entry 26170), Acta Cryst. B, 25 (1969), 1233.

[306] Callister, Jr., W. D. (2007). Materials science and engineering: An introduction. New York: John Wiley & Sons, Inc.

[307] Chai, Z., Lu, X., & He, D. (2012). Atomic layer deposition of zinc oxide films: Effects of nanocrystalline characteristics on tribological performance. Surface and Coatings Technology, 207, 361-366.

[308] Xu, M.A , Zhang, Y.A , & Wei, L.A (2013). Group III dopant segregation and semiconductor-to-metal transition in ZnO nanowires: A first principles study. RSC Advances, 13(3), 19793-19797.

[309] Tapily, K., Gu, D., & Baumgart, H. (2010). Growth mechanism of ALD ZnO films investigated by physical characterization. Paper presented at the ECS Transactions, 33(2) 355-363.

[310] Ohyama, M., Kozuka, H., & Yoko, T. (1998). Sol-gel preparation of transparent and conductive aluminum-doped zinc oxide films with highly preferential crystal orientation. Journal of the American Ceramic Society, 81(6), 1622-1632.

[311] Lee, J. -., & Park, B. -. (2003). Transparent conducting ZnO:Al, In and Sn thin films deposited by the sol-gel method. Thin Solid Films, 426(1-2), 94-99.

[312] Warren, B. E. (1941). X-ray diffraction in random layer lattices. Physical Review, 59(9), 693-698.

[313] Pala, R. G. S., & Metiu, H. (2007). Modification of the oxidative power of ZnO($10\bar{1}0$) surface by substituting some surface Zn atoms with other metals. Journal of Physical Chemistry C, 111(24), 8617-8622.

[314] Murti, D. K., & Bluhm, T. L. (1982). Preferred orientation of ZnO films controlled by R.F. sputtering. Thin Solid Films, 87(1), 57-61.

[315] Nam, K. H., Lee, P. J., & Lee, J. J. (2010). Texture control of ZnO films by inductively coupled plasma assisted chemical vapor deposition. Thin Solid Films, 518(23), 7029-7032.

[316] Xu, Y., Goto, M., Kato, R., Tanaka, Y., & Kagawa, Y. (2012). Thermal conductivity of ZnO thin film produced by reactive sputtering. Journal of Applied Physics, 111(8).

[317] Przezdziecka, E., Wachnicki, ?., Paszkowicz, W., Lusakowska, E., Krajewski, T., Luka, G., et al. (2009). Photoluminescence, electrical and structural properties of ZnO films, grown by ALD at low temperature. Semiconductor Science and Technology, 24(10)

[318] Wang, T., Wu, H., Chen, C., & Liu, C. (2012). Growth, optical, and electrical properties of nonpolar m-plane ZnO on p-Si substrates with Al2O3 buffer layers. Applied Physics Letters, 100(1).

[319] Solís-Pomar, F., Martínez, E., Meléndrez, M. F., & Pérez-Tijerina, E. (2011). Growth of vertically aligned ZnO nanorods using textured ZnO films. Nanoscale Research Letters, 6, 1-11.

[320] Henrich, V. E., & Cox, P. A. (1994). The Surface of Metal Oxides. Cambridge: Cambridge University Press.

[321] Lee, Y. E., Kim, Y. J., & Kim, H. J. (1998). Thickness dependence of microstructural evolution of ZnO films deposited by RF magnetron sputtering. Journal of Materials Research, 13(5), 1260-1265.

[322] Carel, R., Thompson, C. V., & Frost, H. J. (1996). Computer simulation of strain energy effects vs surface and interface energy effects on grain growth in thin films. Acta Materialia, 44(6), 2479-2494.

[323] Thompson, C. V., & Carel, R. (1995). Texture development in polycrystalline thin films. Materials Science and Engineering B, 32(3), 211-219.

[324] Pelleg, J., Zevin, L. Z., Lungo, S., & Croitoru, N. (1991). Reactive-sputter-deposited TiN films on glass substrates. Thin Solid Films, 197(1-2), 117-128.

[325] Thompson, C. V., & Carel, R. (1996). Stress and grain growth in thin films. Journal of the Mechanics and Physics of Solids, 44(5), 657-673.

[326] Barnham, K., & Vvedensky, D. (2001). Low-Dimensional semiconductor structures. Cambridge: Cambridge Univesity Press.

[327] Van de Walle, C.G., 2000. Hydrogen as a cause of doping in zinc oxide. Physical Review Letters, 85(5), 1012-1015.

[328] Bang, J., & Chang, K.J. (2008). Diffusion and thermal stability of hydrogen in ZnO. Applied Physics Letters, 92(13).

[329] Bang, J., & Chang, K.J. (2008). Atomic structure and Diffusion of hydrogen in ZnO. Journal of the Korean Physical Society, 55 (1), 98-102.

[330] Eisermann, S., Kronenberger, A., Dietrich, M., Petznick, S., Laufer, A., Polity, A., & Meyer, B.K. (2009). Hydrogen and nitrogen incorporation in ZnO thin films grown by radio-frequency (RF) sputtering. Thin Solid Films, 518(4), 1099-1102.

[331] Thomas, M.A., Armstrong, J.C., & Cui, J. (2013). New approach toward transparent and conductive ZnO by atomic layer deposition: Hydrogen plasma doping. Journal of Vacuum Science and Technology A: Vacuum, Surfaces and Films, 31(1).

[332] Li, F., Wang, L., Dai, J., Pu, Y., Fang, W., & Jiang, F. (2007.) Photoluminescence observations of hydrogen incorporation and outdiffusion in ZnO thin films. Journal of Luminescence, 124(1), 162-166.

[333] Wang, Y., Quillian, B., Wannere, C.S., Wei, P., Schleyer, P.V.R., & Robinson, G.H. (2007). A Trimetallic compound containing Zn-Zr bonds: $Cp_2Zr(ZnR)_2$ ($Cp=C_5H_5$; $R=C_6H_3$-2, 6-(2,4,6-i-$Pr_3C_6H_2)_2$)).Organometallics, 26(12), 3054-3056.

[334] Erhart, P., Klein, A. & Albe, K. (2005). First-principles study of the structure and stability of oxygen defects in zinc oxide. Physical Review B - Condensed Matter and Materials Physics, 72(8).

[335] Bennett, B. R., Soref, R. A., & Del Alamo, J. A. (1990). Carrier-induced change in refractive index of InP, GaAs, and InGaAsP. IEEE Journal of Quantum Electronics, 26(1), 113-122.

[336] Vancea, J., Pukowietz, S., Reiss, G., & Hoffmann, H. (1987). Electrical conduction in low-resistivity (quasiamorphous) $Ag_{1-x}Cu_x$ alloys. Physical Review B, 35(17), 9067-9072.

[337] Rossnagel, S. M., & Kuan, T. S. (2004). Alteration of Cu conductivity in the size effect regime. Journal of Vacuum Science and Technology B: Microelectronics and Nanometer Structures, 22(1), 240-247.

[338] Kwok, S., Tsang, K., Chow, Y.L. & Wu, K. (2003). Synthetic asymptote formula for surface-printed resistor. IEE Proceedings: Microwaves, Antennas and Propagation, 150(5), 396-399.

[339] Hendry, E., Koeberg, M., & Bonn, M. (2007). Exciton and electron-hole plasma formation dynamics in ZnO. Physical Review B - Condensed Matter and Materials Physics, 76(4).

[340] Hanada, T. (2009). Basic Properties of ZnO, GaN, and Related Materials. In T. Yao, & S.-K. Hong, Advances in Materials Research, Vol. 12: Oxide and Nitride Semiconductors (pp. 1-19). Berlin Heidelberg: Springer.

[341] Natsume, Y., & Sakata, H. (2000). Zinc oxide films prepared by sol-gel spin-coating. Thin Solid Films, 372(1), 30-36.

[342] Kim, W. M., Kim, J. S., Jeong, J., Park, J., Baik, Y., & Seong, T. (2013). Analysis of optical band-gap shift in impurity doped ZnO thin films by using nonparabolic conduction band parameters. Thin Solid Films, 531, 430-435.

[343] Feng, D., & Jin, G. (2005). Introduction to Condensed Matter Physics. Hackensack, NJ: World Scientific.

[344] Versteegh, M. A. M., Kuis, T., Stoof, H. T. C., & Dijkhuis, J. I. (2011). Ultrafast screening and carrier dynamics in ZnO: Theory and experiment. Physical Review B - Condensed Matter and Materials Physics, 84(3).

[345] Wilk, G. D., Wallace, R. M., & Anthony, J. M. (2001). High-κ gate dielectrics: Current status and materials properties considerations. Journal of Applied Physics, 89(10), 5243-5275.

[346] Young, D. L., Coutts, T. J., Kaydanov, V. I., Gilmore, A. S., & Mulligan, W. P. (2000). Direct measurement of density-of-states effective mass and scattering parameter in transparent conducting oxides using second-order transport phenomena. Journal of Vacuum Science and Technology A: Vacuum, Surfaces and Films, 18(6), 2978-2985.

[347] Chen, M., Pei, Z. L., Wang, X., Sun, C., & Wen, L. S. (2001). Structural, electrical, and optical properties of transparent conductive oxide ZnO:Al films prepared by DC magnetron reactive sputtering. Journal of Vacuum Science and Technology, Part A: Vacuum, Surfaces and Films, 19(3), 963-970.

[348] FISONS Instruments Surface Science, XPS and Auger Hanbook

[349] Chen, M., Wang, X., Yu, Y. H., Pei, Z. L., Bai, X. D., Sun, C., & Wen, L. S. (2000). X-ray photoelectron spectroscopy and auger electron spectroscopy studies of Al-doped ZnO films. Applied Surface Science, 158(1), 134-140.

[350] Bakradze, G., Jeurgens, L.P.H. and Mittemeijer, E.J., 2011. Valence-band and chemical-state analyses of Zr and O in thermally grown thin zirconium-oxide films: An XPS study. Journal of Physical Chemistry C,115(40), 19841-19848.

[351] Tsay, C., & Yu, S. (2014). Optoelectronic characteristics of UV photodetectors based on sol-gel synthesized GZO semiconductor thin films. Journal of Alloys and Compounds, 596, 145-150.

[352] Shinde, S.S. & Rajpure, K.Y. (2011). X-ray photoelectron spectroscopic study of catalyst based zinc oxide thin films. Journal of Alloys and Compounds, 509(13), 4603-4607.

[353] Wagner, C.D., (1975). Chemical shifts of Auger lines, and the Auger parameter. Faraday discussions of the Chemical Society, 60, 291-300.

[354] Cole, R.J., Gregory, D.A.C., & Weightman, P. (1994). Analysis of Auger-parameter and XPS shifts: Application of potential models. Physical Review B, 49(8), 5657-5661.

[355] Gaarenstroom, S.W., & Winograd, N. (1977). Initial and final state effects in the ESCA spectra of cadmium and silver oxides. The Journal of chemical physics, 67(8), 3500-3506.

[356] Moretti, G. (2013). The Wagner plot and the Auger parameter as tools to separate initial and final state contributions in X-ray photoemission spectroscopy. Surface Science, 618, 3-11.

[357] Wagner, C.D., & Joshi, A. (1988). The auger parameter, its utility and advantages: a review. Journal of Electron Spectroscopy and Related Phenomena, 47(C), 283-313.

[358] Janocha, E., & Pettenkofer, C. (2011). ALD of ZnO using diethylzinc as metal-precursor and oxygen as oxidizing agent. Applied Surface Science, 257(23), 10031-10035.

[359] Martin-Concepción, A.I., Yubero, F., Espinós, J.P., González-Elipe, A.R., & Tougaard, S. (2003). X-ray photoelectron spectroscopy study of the first stages of ZnO growth and nanostructure dependence of the effects of polarization at ZnO/SiO_2 and ZnO/Al_2O_3 interfaces. Journal of Vacuum Science and Technology A: Vacuum, Surfaces and Films, 21(4), 1393-1398.

[360] Tvarožek, V., Šutta, P., Novotný, I., et al. (2008). Preparation of transparent conductive AZO thin films for solar cells. Paper presented at the ASDAM 2008 - Conference

Proceedings of the 7th International Conference on Advanced Semiconductor Devices and Microsystems, 275-278.

[361] Rowell, M.W., & Mcgehee, M.D. (2011). Transparent electrode requirements for thin film solar cell modules. Energy and Environmental Science, 4(1), 131-134.

[362] Chen, Z., Li, W., Li, R., Zhang, Y., Xu, G., & Cheng, H. (2013). Fabrication of highly transparent and conductive indium-tin oxide thin films with a high figure of merit via solution processing. Langmuir, 29(45), 13836-13842.

[363] Qiao, Z., Agashe, C., & Mergel, D. (2006). Dielectric modeling of transmittance spectra of thin ZnO:Al films. Thin Solid Films, 496(2), 520-525.

[364] Kim, J. S., Jeong, J., Park, J. K., Baik, Y. J., Kim, I. H., Seong, T., & Kim, W. M. (2012). Optical analysis of doped ZnO thin films using nonparabolic conduction-band parameters. Journal of Applied Physics, 111(12).

[365] Logan, P., & Peng, X. (2009). Strain-modulated electronic properties of ge nanowires: A first-principles study. Physical Review B - Condensed Matter and Materials Physics, 80(11).

[366] Glinka, Y. D., Lin, S., Hwang, L., Chen, Y., & Tolk, N. H. (2001). Size effect in self-trapped exciton photoluminescence from SiO_2-based nanoscale materials. Physical Review B - Condensed Matter and Materials Physics, 64(8), 854211-8542111.

[367] Yao, B., Guan, L. X., Xing, G. Z., Zhang, Z. Z., Li, B. H., Wei, Z. P., & Shen, D. Z. (2007). P-type conductivity and stability of nitrogen-doped zinc oxide prepared by magnetron sputtering. Journal of Luminescence, 122-123(1-2), 191-194.

[368] Zhang, X. Q., Suemune, I., Kumano, H., Wang, J., & Huang, S. H. (2004). Surface-emitting stimulated emission in high-quality ZnO thin films. Journal of Applied Physics, 96(7), 3733-3736.

[369] Sánchez Zeferino, R., Barboza Flores, M., & Pal, U. (2011). Photoluminescence and Raman scattering in Ag-doped ZnO nanoparticles. Journal of Applied Physics, 109(1).

[370] Schmidt, T., Lischka, K., & Zulehner, W. (1992). Excitation-power dependence of the near-band-edge photoluminescence of semiconductors. Physical Review B, 45(16), 8989-8994.

[371] Cheng, B., Yu, X., Liu, H., Fang, M., & Zhang, L. (2009). Enhanced effect of electron-hole plasma emission in Dy, Li codoped ZnO nanostructures. Journal of Applied Physics, 105(1).

[372] Klingshirn, C. F. (2005). Semiconductor Optics. Verlag Berlin Heidelberg: Springer.

[373] House, R. L., Kirschbrown, J. R., Mehl, B. P., Gabriel, M. M., Puccio, J. A., Parker, J. K., & Papanikolas, J. M. (2011). Characterizing electron-hole plasma dynamics at different points in individual ZnO rods. Journal of Physical Chemistry C, 115(43), 21436-21442.

[374] Teng, X., Fan, H., Pan, S., Ye, C., & Li, G. (2007). Abnormal photoluminescence of ZnO thin film on ITO glass. Materials Letters, 61(1), 201-204.

[375] Sentosa, D., Liu, B., Wong, L. M., Lim, Y. V., Wong, T. I., Foo, Y. L., & Wang, S. J. (2011). Temperature dependent photoluminescence studies of ZnO thin film grown on (1 1 1) YSZ substrate. Journal of Crystal Growth,319(1), 8-12.

[376] Lee, S., So, W., Jung, J. H., Nam, G., Yoon, H., Park, H., Leem, J. (2012). Temperature-dependent photoluminescence of ZnO thin films deposited by using the sol-gel dip-coating method. Journal of the Korean Physical Society, 61(8), 1171-1176.

[377] Yoo, J., Chon, B., Tang, W., Joo, T., Dang, L. S., & Yi, G. (2012). Excitonic origin of enhanced luminescence quantum efficiency in MgZnO/ZnO coaxial nanowire heterostructures. Applied Physics Letters, 100(22).

[378] Ye, H. B., Kong, J. F., Shen, W. Z., Zhao, J. L., & Li, X. M. (2007). Temperature-dependent photoluminescence of undoped, N-doped and N-In codoped ZnO thin films. Journal of Physics D: Applied Physics, 40(18), 5588-5591.

[379] Nam, G., Park, H., Yoon, H., Kim, J. S., & Leem, J. (2013). Studies on temperature- and excitation-power-dependent photoluminescence of ZnO thin film grown by plasma-assisted molecular beam epitaxy. Current Applied Physics, 13(4 SUPPL.2), S168-S171.

[380] Lee, S. Y., Shin, Y. H., Park, Y. H., & Kim, Y. (2011). Temperature dependence of the optical quenching behavior of ZnO nanorods. Journal of the Korean Physical Society, 58(5), 1174-1177.

[381] Chien, J., Huang, Y., Chang, Y., Shyue, J., Yang, J., Shiojiri, M., & Chen, M. (2013). Tunable optical and structural properties of $Mg_xZn_{1-x}O$ films prepared by in situ atomic layer doping technique. ECS Journal of Solid State Science and Technology, 2(1), P31-P35.

[382] Medved, D. B. (1958). Photodesorption in zinc oxide semiconductor. The Journal of Chemical Physics, 28(5), 870-873.

[383] Varshni, Y. P. (1967). Temperature dependence of the energy gap in semiconductors. Physica, 34(1), 149-154.

[384] Zhao, D., Zhang, C., Zhang, X., et al. (2014). Substrate-induced effects on the optical properties of individual ZnO nanorods with different diameters. Nanoscale, 6(1), 483-491.

[385] Zhu, L., Gu, X., He, H., Huang, F., Qui, M., Ye, Z., Zhang, Y., Zhao, B. (2008). Temperature-dependent Photoluminescence from ZnO/ZnMgO heterostructure grown on Si (111) substrates. Journal of Korean Physical Society, 53 (5), 2985-2988.

[386] Srikant, V., & Clarke, D. R. (1997). Optical absorption edge of ZnO thin films: The effect of substrate. Journal of Applied Physics, 81(9), 6357-6364.

[387] Schleife, A., Rödl, C., Fuchs, F., Furthmüller, J., & Bechstedt, F. (2007). Strain influence on valence-band ordering and excitons in ZnO: An ab initio study. Applied Physics Letters, 91(24).

[388] Rowe, J. E., Cardona, M., & Pollak, F. H. (1968). Valence band symmetry and deformation potentials of ZnO. Solid State Communications, 6(4), 239-242.

[389] Reynolds, D. C., Litton, C. W., & Collins, T. C. (1965). Zeeman effects in the edge emission and absorption of ZnO. Physical Review, 140(5A), A1726-A1734.

[390] Bagnall, D. M., Chen, Y. F., Shen, M. Y., Zhu, Z., Goto, T., & Yao, T. (1998). Room temperature excitonic stimulated emission from zinc oxide epilayers grown by plasma-assisted MBE. Journal of Crystal Growth, 184-185, 605-609.

[391] Jain, A., Sagar, P., & Mehra, R. M. (2006). Band gap widening and narrowing in moderately and heavily doped n-ZnO films. Solid-State Electronics, 50(7-8), 1420-1424.

[392] Lee, G. J., Lee, Y., Lim, H., et al. (2010). Photoluminescence and lasing properties of ZnO nanorods. Journal of the Korean Physical Society, 57(61), 1624-1629.

[393] Makino, T., Chia, C. H., Tuan, N. T., Sun, H. D., Segawa, Y., Kawasaki, M., & Koinuma, H. (2000). Room-temperature luminescence of excitons in ZnO/(Mg,Zn)O multiple quantum wells on lattice-matched substrates.Applied Physics Letters, 77(7), 975-977.

[394] Mohr, P. J., Taylor, B. N., & Newell, D. B. (2008). CODATA recommended values of the fundamental physical constants: 2006. Reviews of Modern Physics, 80(2), 633-730.

[395] Abdolahzadeh Ziabari, A., & Rozati, S. M. (2012). Carrier transport and bandgap shift in n-type degenerate ZnO thin films: The effect of band edge nonparabolicity. Physica B: Condensed Matter, 407(23), 4512-4517.

[396] Pisarkiewicz, T., Zakrzewska, K., & Leja, E. (1989). Scattering of charge carriers in transparent and conducting thin oxide films with a non-parabolic conduction band. Thin Solid Films, 174(PART 1), 217-223.

[397] Oshikiri, M., Imanaka, Y., Aryasetiawan, F., & Kido, G. (2001). Comparison of the electron effective mass of the n-type ZnO in the wurtzite structure measured by cyclotron resonance and calculated from first principle theory. Physica B: Condensed Matter, 298(1-4), 472-476.

[398] Ye, J. D., Gu, S. L., Zhu, S. M., Liu, S. M., Zheng, Y. D., Zhang, R., & Shi, Y. (2005). Fermi-level band filling and band-gap renormalization in Ga-doped ZnO. Applied Physics Letters, 86(19), 1-3.

[399] Liu, H., Avrutin, V., Izyumskaya, N., Özgr, Ü., & Morkoç, H. (2010). Transparent conducting oxides for electrode applications in light emitting and absorbing devices. Superlattices and Microstructures, 48(5), 458-484.

[400] Yuan, H. (2012). Structural, electrical and optical properties of Si doped ZnO films grown by atomic layer deposition. Journal of Materials Science: Materials in Electronics, 23(11), 2075-2081.